



Garibaldi Geothermal Energy Project

Mount Meager 2019 - Field Report

Geoscience BC Report 2020-09

Grasby, S.E., Ansari, S.M., Bryant, R., Calahorrano-DiPatre, A., Chen, Z., Craven, J.A., Dettmer, J., Gilbert, H., Hanneson, C., Harris, M., Hormozzade, F., Liu, J., Montezadian, D., Muhammad, M., Russell, J.K., Salvage, R.O., Savard, G., Tschirhart, V., Unsworth, M.J., Vigouroux-Caillibot, N., Williams-Jones, G., Williamson, A.R.

The Garibaldi Volcanic Belt Geothermal Energy Project – Mount Meager 2019 Field Program

Grasby, S.E., Ansari, S.M., Bryant, R., Calahorrano-DiPatre, A., Chen, Z., Craven, J.A., Dettmer, J., Gilbert, H., Hanneson, C., Harris, M., Hormozzade, F., Liu, J., Muhammad, M., Russell, J.K., Salvage, R.O., Savard, G., Tschirhart, V., Unsworth, M.J., Vigouroux-Caillibot, N., Williams Jones, G., and Williamson, A.R.

INDEX

Chapter 1 – The Garibaldi Volcanic Belt Geothermal Energy Project – Mount Meager 2019 Field Program.....	1
Grasby, S.E., Ansari, S.M., Bryant, R., Calahorrano-DiPatre, A., Chen, Z., Craven, J.A., Dettmer, J., Gilbert, H., Hanneson, C., Harris, M., Hormozzade, F., Liu, J., Muhammad, M., Russell, J.K., Salvage, R.O., Savard, G., Tschirhart, V., Unsworth, M.J., Vigouroux-Caillibot, N., Williams Jones, G. and Williamson, A.R.	
Chapter 2 – Bedrock mapping for Mount Meager Geothermal Research Initiative.....	6
Harris, M., Muhammad, M., Williams Jones, G. and Russell, J.K.	
Chapter 2 – Appendix	30
Chapter 3 -- Fracture system analyses of the Mount Meager area.....	36
Chen, Z., Grasby, S.E., Liu, X.	
Chapter 4 -- Gravity Mapping of the Mount Meager Volcanic Complex: Preliminary Results.....	50
Calahorrano-Di Patre, A.E.; Williams-Jones, G.	
Chapter 5 -- Broadband magnetotelluric study at Mount Meager to investigate the hydrothermal and magmatic system.....	77
Unsworth, M.J.; Hanneson, C.S.1, Williamson A.R.	
Chapter 6 -- Overview of the 2019 Audiomagnetotelluric Survey of the Mount Meager Geothermal Reservoir.....	126
Craven, J.A.; Hormozzade, F., Tschirhart, V.; Ansari, M., Bryant, R. and Montezadian, D.	
Chapter 7-- Mount Meager Passive Seismic Monitoring.....	148
Gilbert, H.; Dettmer, J.; Savard, G. and Su, H.	

Chapter 1 – The Garibaldi Volcanic Belt Geothermal Energy Project – Mount Meager 2019 Field Program

Grasby, S.E.¹, Ansari, S.M.¹, Bryant, R.¹, Calahorrano-DiPatre, A.², Chen, Z.¹, Craven, J.A.¹,
Dettmer, J.³, Gilbert, H.³, Hanneson, C.⁴, Harris, M.⁵, Hormozzade, F.⁶, Liu, J.¹, Muhammad, M.²,
Russell, J.K.⁵, Salvage, R.O.³, Savard, G.³, Tschirhart, V.¹, Unsworth, M.J.⁴, Vigouroux-Caillibot, N.⁷,
Williams Jones, G.², and Williamson, A.R.⁴

¹Geological Survey of Canada, ²Simon Fraser University³, University of Calgary, ⁴University of Alberta,
⁵University of British Columbia, ⁶Carleton University, ⁷Douglas College

Introduction

Canada seeks to meet a climate target of net zero CO₂ emissions by 2050, requiring developing new renewable-energy resources. Compared to other renewables, geothermal energy has numerous advantages, the most important of which is the ability to provide a stable baseload-power supply without the need for energy-storage solutions, as compared to intermittent sources such as wind or solar. However, this greater reliability of supply comes with much greater exploration risk. While it is relatively easy to determine where it is windy and sunny, defining a hot aquifer in the deep subsurface ultimately requires expensive drilling operations. Geoscience research is essential to develop new approaches to help reduce this exploration risk.

In response to the Energy Crises of the 1970's, Canada initiated a Geothermal Energy Program that ran from 1975–1985, and provided the first insight into the thermal regime of Canada (Jessop, 2008; Grasby et al., 2011). This work included defining some of the highest temperature geothermal systems in Canada, those related to hot sedimentary basins (found in the Northwest Territories, Yukon, British Columbia [BC], Alberta and Saskatchewan), as well as volcanic belts (Yukon and BC). As part of this earlier program, geothermal-exploration wells were drilled in the Garibaldi volcanic belt of southwestern BC, near active thermal springs on the southern flank of Mount Meager. This drilling defined high-temperature geothermal resources, exceeding 250 °C (Jessop, 2008; Witter, 2019). However, the project was never economically viable because flow rates were too low to justify the power-transition cost over the distance required. While a technical success, in that the exploration program discovered a world-class thermal reservoir, development of the site was limited by the low permeability rocks at depth.

With renewed interest in geothermal potential in Canada, a new research project was initiated to help reduce exploration risk for geothermal energy associated with volcanic systems in Canada. The main aim of this work is to develop new techniques and tools that can be employed to predict the occurrence of hot and permeable aquifers in the sub-surface. To this end, a multidisciplinary geoscience field program was conducted at Mount Meager in the summer of 2019. This report summarises the field program and data collected.

Methods

Access to the Mount Meager area has been limited since a 53-million-cubic-meter landslide in 2010 (Canada's largest historic event) destroyed bridges on old logging roads. Given this, a mainly helicopter-supported field program was operated from July 2 to 24, along with subsequent visits through August and September for instrument maintenance and final removal. A total of 375 person days were spent in the field, including one field camp and with the remainder of the field crew conducted daily set-outs by helicopter as well as work from logging roads. The field program focused on establishing an array of seismometers (UofC), an array of MT stations focused on the shallow geothermal system (GSC) as well as the deeper volcanic plumbing (UofA), a gravity survey (SFU), bedrock mapping (UBC), fracture and rock-property studies (GSC), and thermal-spring geochemistry (DC and GSC; Figure 1).

Detailed bedrock mapping was conducted to enhance understanding of the nature of the spatial distribution of volcanic rocks that form the Mount Meager Volcanic Complex, with a particular focus on rock types with preferential reservoir properties (Chapter 2). Field mapping included recording rock-property observations at 848 field stations. These results will support the development of hydrogeological models for bulk-rock permeability to better characterize potential fluid flow at depth.

In order to develop an understanding of the nature of fracture systems and their potential influence on bulk-rock permeability, fieldwork was conducted to measure spatial distribution and variability in fracture orientation and fracture density (Chapter 3). This was combined with remote-sensing image analyses and artificial intelligence to define trends, orientations and densities of lineaments through the study area. Identified lineaments were ground-truthed as part of the geological and geophysical mapping program to assess if they represent higher permeability fracture systems. Determination of the regional stress fields is more complex in areas of high topographic relief, as the free surface cannot be assumed to be flat. Methods being used for stress-field determination include well-borehole breakout analyses and bedding slip, etc. Regional data will assist in refinement of the tensile portion of the regional-stress field, which would provide insight into preferred fluid-flow directions. The current stress system will be incorporated using geoscience information (magnitude, location and sense of motion) from historical records of earthquakes in the study area and surrounding vicinities, and constrained by deformation patterns and additional geoscience information from previously drilled boreholes.

Gravity measurements were taken at 79 stations around the Mount Meager Volcanic Complex (Chapter 4), with the aim of mapping its internal structure. The network comprises both a dense distribution of sites near the volcanic edifice and more broadly spaced stations with increasing distance from the mountain. This distribution seeks to investigate the deep magmatic structures (depth >10 km) by comparing data from distal stations with data from the proximal dense network of stations. Smaller scale structures, such as the hydrothermal system of Mount Meager, will be mapped by analyzing gravity change between stations closer to the edifice.

Collection of magnetotelluric (MT) data was aimed at greatly expanding coverage beyond that collected in the 1980s (Jones and Dumas, 1993), using modern and more field-portable instruments (Chapters 5&6). The MT data collection in 2019 at the Mount Meager Volcanic Complex was performed on two spatial scales. A set of 23 MT measurements was taken by the UofA MT group to understand the deeper structure of the system, which requires longer recording time and consequently reduced the total number of measurement locations (Chapter 5). The deeper focus MT survey was designed to image pathways that carry fluids to the geothermal reservoir and the fumaroles on Job Glacier. These deep MT measurements will also define the size and content of any magma bodies beneath the volcano. In the region of the geothermal reservoir on the south side of Pylon Peak, MT measurements were made in a dense grid of 84 stations by the GSC MT group to study the details of the geothermal reservoir (Chapter 6). The goal of the survey was to use the new MT data to determine permeability variations in the subsurface and link these to flow rates observed at the surface.

Fifty-nine passive-seismic sites, each consisting of a Hawk field-station unit (INOVA Geophysical) connected to 10 Hz three-component geophones, were established (Chapter 7) for characterizing crustal structures associated with the area of high geothermal heat and how those vary within the geothermal system. The observations from this array will be used to identify the distribution of low seismic-wave speeds, which can mark the distribution of fractures that serve as pathways for geothermal fluids, as well as magma chambers. Detecting and locating the local seismicity during this brief seismic deployment will provide constraints on the pattern of faults and fractures within Mount Meager that allow for fluid circulation through this geothermal system. The Hawk systems are also being tested for their ability to record more distant earthquakes and whether those signals can be used to measure structures within the Garibaldi volcanic belt.

Beyond the main project activities, the field camp also supported establishment of landslide monitoring equipment in addition to examination of volcanic fumaroles in the ice caves on Job Glacier. As these are not directly part of the research activity they are not reported on further.

Acknowledgements

The authors gratefully acknowledge the support of T. Jenkins and M. Bruce of Lil'wat First Nation in providing guidance in the field and logistical planning and wildlife monitoring. Pilots M. Accurso, D. Vincent and R. Slinger of No Limits Helicopters provided expert service. Innergex Renewable Energy Inc. provided significant support to the field program through access to their field bunkhouse. Wayne Russell on Innergex was of great assistance throughout our field stay. Field assistance was provided by K. Biegel, R. Bryant, J. Smale, H. Su, A. Williamson and A. Wilson. Funding for this project was provided by Geoscience BC and Natural Resources Canada. The University of Alberta group was supported by funding from the Natural Sciences and Engineering Council of Canada (NSERC) through a Canada First Research Excellence Fund (CFREF) award (Future Energy Systems) and a Discovery Grant to M. Unsworth. The University of Calgary group was supported by funding from the Canada Research Co-ordinating Committee through a New Frontiers in Research Fund award and a Discovery Grant to J. Dettmer. Financial assistance was provided to R. Salvage by the Microseismic Industry Consortium.

References

- Grasby, S.E., Allen, D.M., Bell, S., Chen, Z., Ferguson, G., Jessop, A., Kelman, M., Ko, M., Majorowicz, J., Moore, M., Raymond, J. and Therrien, R. (2011): Geothermal energy resource potential of Canada; Geological Survey of Canada, Open File 6914, 322 p., <<https://doi.org/10.4095/288745>> [October 2019].
- Jessop, A. (2008): Review of National Geothermal Energy Program, Phase 2 – geothermal potential of the Cordillera; Geological Survey of Canada, Open File 5906, 86 p., <<https://doi.org/10.4095/225917>> [October 2019].
- Jones, A.G. and Dumas, I. (1993): Electromagnetic images of a volcanic zone; Physics of the Earth and Planetary Interiors, v. 81, no. 1–4, p. 289–314, <[https://doi.org/10.1016/0031-9201\(93\)90137-X](https://doi.org/10.1016/0031-9201(93)90137-X)> [October 2019].
- Witter, J. (2019): South Meager geothermal project – new perspectives from recently unearthed data; Geoscience BC, Report 2019-07, 5 p., URL <<http://www.geosciencebc.com/i/pdf/Report-2019-07-Innovate-Geothermal.pdf>> [November 2019].

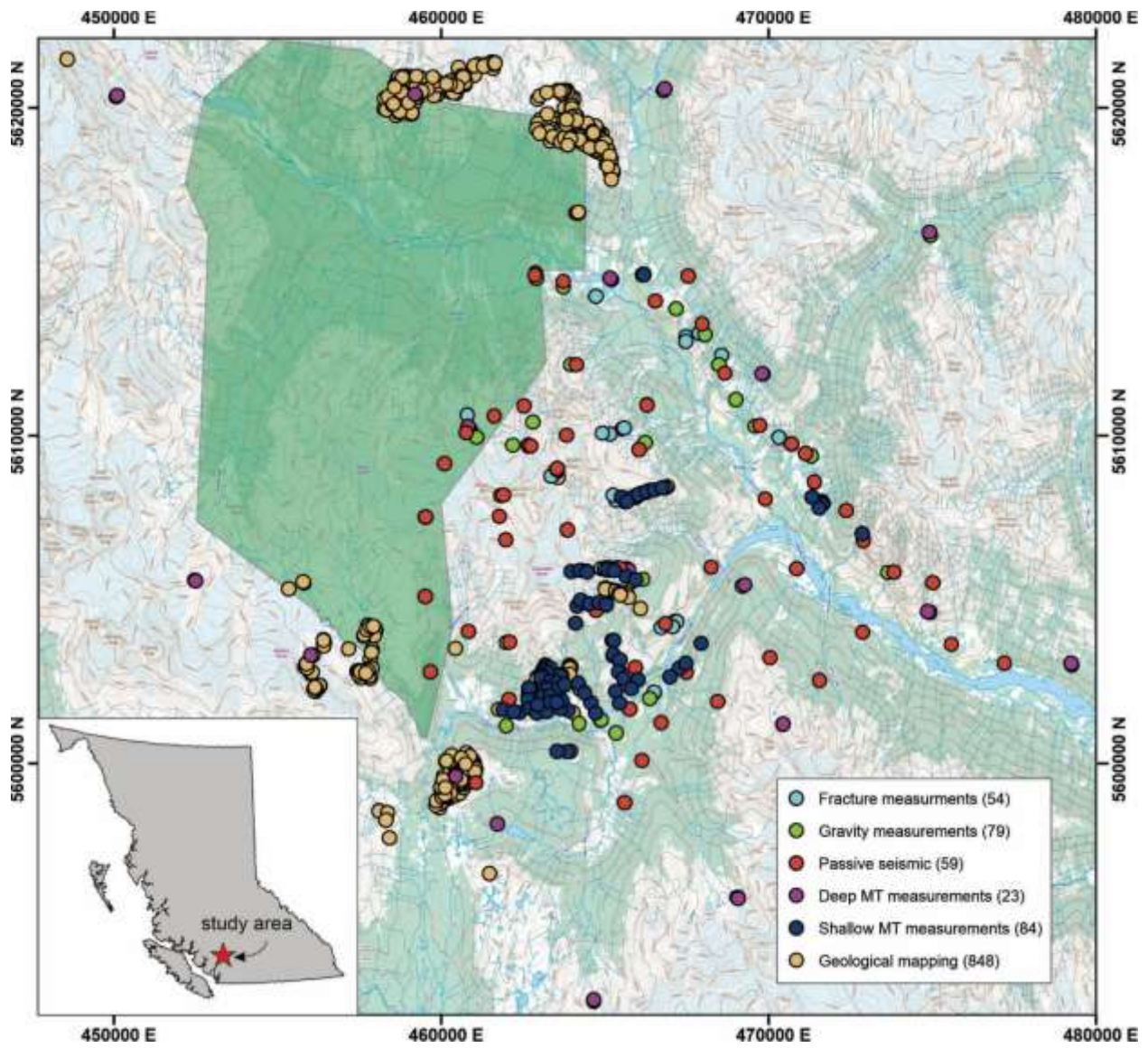


Figure 1: Map of the Mount Meager study area and field locations visited.

Chapter 2 - Bedrock mapping for Mount Meager Geothermal Research Initiative

Harris, M.¹, Muhammad, M.², Williams Jones, G.² and Russell, J.K.¹

¹Earth, Ocean and Atmospheric Sciences, the University of British Columbia

²Earth Sciences, Simon Fraser University

Introduction

Exploring geothermal energy as a source of renewable energy is appealing due to its limited environmental impact; however, there is substantial economic risk due to development costs and large uncertainties in the properties of the subsurface reservoir rocks. Subsurface models of geology are paramount for evaluating reservoir capacity, zones of permeability, fracture or fault patterns, and ultimately reducing the exploration risk. The overarching goal for this work is to contribute information that can be used to assess the geothermal potential underlying Mount Meager of Southwest British Columbia (BC) (Fig. 1). Mount Meager (Fig. 1) is a volcanic complex situated 160 km N of Vancouver and is part of the Garibaldi Volcanic belt (GVB) which, itself, represents a northern segment of the Cascade Volcanic Arc into Canada.

This specific contribution comprises a large-scale field mapping campaign focussed on bedrock structural analysis and expansion of the regional mapping to include unmapped young volcanic centres on the peripheral margins of Mount Meager. Our work expands on two previous major mapping campaigns conducted by Woodsworth (1977) and Read (1977). Woodsworth mapped the entire Pemberton region including the coastal plutonic and metasedimentary uplifted basement rocks and episodic volcanic deposits. The scale of Woodsworth's map was large and, thus, volcanic units around Mount Meager were only distinguished by age between Miocene to Pleistocene. In contrast, Read's map was finer scale and focused exclusively on the geology of the Mount Meager massif; he identified more than thirty map units comprising intrusive or extrusive igneous deposits, which were assigned to "assemblages" based on relative and absolute age relationships. Subsequent work by Green et al. (1988), and Stasiuk and Russell (1989, 1990) built upon the mapping by Woodsworth and Read and produced petrologic and geochemical classifications for the eruptive rocks of Mt Meager, with correlating age constraints ranging from 2.2 to less than 0.1 Ma (Green et al., 1988). Our work here builds upon these previous studies.

Methods

The 2019 mapping campaign was designed to inform on the subsurface rock types and structures underlying the Mount Meager volcanic complex and to better characterize the peripheral volcanic centres. To do this we traversed the terrain by foot, locating outcrops, recording lithological field descriptions, collecting samples, taking structural measurements, and following discernable unit contacts. We spent six weeks mapping in the field, compiling rock measurements, descriptions, and samples.

Classic structural geology techniques were used including plotting attitude of structures on stereonet, analyzing structural trends, and spatial correlation between rock units versus structural

features including fractures/veins, faults, folds, and the attitudes of basement and young volcanic units. We also considered syn- (i.e., intrusion and extrusion) and post- (i.e., faulting, mass movement, and glaciation) depositional processes. The data and field observations were used to study the potential kinematic compatibility of the mapped structures: 1) relative to spatial and cross-cutting relationship of structures such as faults, folds and attitude of rock units, and 2) relative to the modern regional tectonic trend within Garibaldi Volcanic belt including Mount Meager Volcanic Complex (MMVC).

Our fieldwork employed various field tools such as the Fieldmove Clino mapping application for recording bedding, joint and fracture orientations, dike trends and dips, and fault slickensides. Additionally, Gaia GPS was used to pinpoint site and sample locations with detail tagged descriptions for each locality. Both field technologies enabled the expeditious transfer of field data to laboratory computers. Petrographic descriptions were compiled using polarizing microscopes after the field season at the laboratories of the University of British Columbia and Simon Fraser University, BC. Maps and models were digitized using ArcGIS and Leapfrog software. A small suite of samples was used for physical property measurement, returning values for bulk density, total porosity, and connected porosity. The samples were analyzed at the Centre for Experimental Study of the Lithosphere, University of British Columbia using the buoyancy methods from ISRM (1979).

Data Collection

The Mount Meager terrain is extremely rugged, covered by thick forests and vegetation at lower elevations and steep and unstable topography at higher elevations. Helicopter support was used to access remote locations, which helped extend the mapping. The mapping campaign produced 846 GPS site locations at which data were collected including: outcrop descriptions, contact relationships, sample locations, and structural measurements (e.g., foliations, fault orientations, etc.). We collected 130 rock samples for further petrologic, geochemical, geochronological, and physical property characterization.

Our mapping included three areas outside the bounds of the Read (1979) map (Fig. 2): Cracked Mountain (Fig. 3), North Lillooet Ridge (Fig. 4), and Southwestern Meager (Fig. 2c). Two new ancillary volcanic outcrops were also mapped (Figs. 2a,b). A summary of volcanic and basement rocks is presented in the following map area subsections. Additional lithofacies descriptions are in the supplementary material included in this report.

Cracked Mountain Map Area

Cracked Mountain is a volcano located 2 km SW of the Mount Meager Massif (Figs. 2, 3), and overlies crystalline basement rocks. The edifice lies on the south side of Meager Creek and northeast of the Elaho River Valley and was previously mapped by Read (1977) who assigned it to the Mosaic Assemblage. The volcanic rocks unconformably overlie the Cretaceous Coastal Plutonic basement rocks (Woodsworth, 1977; Read, 1979), biotite and hornblende granodiorites and biotite and muscovite schist, with discernable contacts seen on the south and southeastern edge of Cracked Mountain. Wilson (2015) remapped the edifice and ascribed a glaciovolcanic origin (Wilson and Russell, 2018). An $^{40}\text{Ar}/^{39}\text{Ar}$ age determination for an alkaline basaltic dike from the volcano returned an age of 190 ± 61.0 ka (Wilson, 2019). During the 2019 Geothermal field mapping campaign, we allocated two weeks to remap Cracked Mountain and to expand upon the work of Read (1977) and Wilson (2015). Here we provide a more in-depth description of the volcanic lithofacies and the eruptive sequence.

The Cracked Mountain edifice is roughly elliptical in shape and has a length of ~ 1.5 km and width of ~ 1 km; the height of the edifice (i.e., thickness) above basement is ~ 300 m indicating an approximate total volume of ~ 0.5 km³. Extensional cracks dissect the entirety of Cracked Mountain, ranging from 0.5 to > 10 m width, and up to 20 m depth. The fractures form paralleled clusters that commonly trend perpendicular to the down slope direction, with some cracks forming complimentary angled trends

showing strike slip offset. The cracks along the margins and lower elevations of the volcano show substantial vertical offset, up to 20 metres, while the cracks near the summit show smaller scale offset (1-2 m). The fracture prevalence and depth provide excellent exposure of the intervolved lithofacies of Cracked Mountain.

Volcanic Lithofacies

The volcano is host to four discrete lithofacies: pillow lavas (CMpL), monolithic vitric breccias (CMmB), monolithic vitric lapilli tuffs (CMIT), and intrusive dikes (CMjl) (Fig. 3). Pillow lavas are volumetrically dominant, forming a thin veneer near the top of the mountain and walls (~ 30 m) of thickly stacked pillow lavas along the edges of the edifice (Fig. 3). Monolithic breccias (CMmB) cover the largest surface area of the Cracked Mountain lithofacies, and are exposed at the higher elevations (Fig. 3) as thin 1-2 m thick deposits, interbedded within other lithologies (i.e., CMpL and CMIT), and progressively thicken (<10 m) down slope. Monolithic, vitric lapilli tuff (CMIT) predominately outcrop at the high elevations of Cracked Mountain as the surficial layer (1-2 m) (Fig. 3), however it was also observed interbedded with monolithic breccias and even underlying pillow lavas at the bottom of Cracked Mountain. Forty-eight intrusive dikes (CMjl) (Fig. 3) were mapped across the Cracked Mountain volcano. The dikes cut through all other lithofacies, are predominantly subvertical, and have widths ranging from 0.5 to 3 m. The dominant trends of the dikes strike E-NE and W-NW, and in some cases are more than 200 m in length.

The stratigraphic relationships between the four lithofacies described above is complicated and suggest that the different lithofacies were produced synchronously (i.e., rather than sequentially). Firstly, there are no unconformities or erosional surfaces observed between volcanic lithofacies. Secondly, pillow lavas are seen in close genetic association with late dikes that have intruded the volcanoclastic deposits (i.e., CMmB and CMIT). The transition from dike to pillow lava suggests the dikes were intruding weak, water-saturated piles of fragmental material shortly after the deposits had accumulated. Thirdly, the interbedding of breccias and vitric tuffs with the pillow lavas suggests an alternating eruptive style (i.e., explosive and effusive). For these reasons, our preliminary work is unable to ascribe a unique sequence of events for the Cracked Mountain eruption.

Basement Geology

The biotite hornblende granodiorite (Mgd) (Fig. 3), and quartz biotite-rich schist (uTr-csb) (Fig. 3) unconformably underlie the Cracked Mountain assemblage, and mark a topographic shallowing beneath the pillow lavas. Lithologic designators are the same as Read's (1979) map. The granodiorite is exposed along the southwest to southeast edge of the Cracked Mountain volcano. The granodiorites dip to the SW and SE, and have steeply dipping NE and SW joint orientations. The quartz biotite schist is well exposed along the southeast and eastern edge of the Cracked Mountain volcano. The pillow lava and breccia contact with the schist can be followed along a NW trending extensional crack on the eastern edge of Cracked Mountain.

North Lillooet Ridge Map Area

The North Lillooet Ridge comprises an east-west trending series of outcrops along the Lillooet river valley situated 4 km N of the Mount Meager massif, British Columbia (Figs. 2, 4). The western extent of the ridge is marked by a N-S glacial valley, roughly 4 km downstream from the present-day Lillooet Glacier. The ridge extends ~8 km to the east, terminating at Salal Creek. From the Lillooet River, the ridge rises ~6 km up the north side of the valley reaching an elevation of ~2,200 m.

The region was previously mapped by Woodsworth (1977) who characterized Lillooet Ridge as underlain by quartz-diorite basement rocks, metasedimentary schists and gneisses, quartz monzonites, and Pleistocene volcanic rocks. The large scale of Woodsworth's map led to him combining all the

Pleistocene volcanic rocks into a single map unit. The Read (1979) map overlaps a small section on the north side of the Lillooet River (Fig. 2) containing outcrops of lava which he consigned to the Mosaic Assemblage. A K-Ar age of 0.09 ± 0.06 Ma was reported for the assemblage (Green et al., 1988). Stasiuk and Russell (1989) used thin section and whole rock analyses to determine an alkaline basalt composition for the lava. Stewart et al. (2008) only mapped deposits belonging to the Pebble Creek Formation, which resulted from the 2360 B.P. eruption of Mount Meager. Fallout deposits are shown to extend halfway up the Lillooet Ridge (up to 1,200 m elevation) (Stewart et al., 2008).

The field mapping of the North Lillooet Ridge took place over two weeks. The mapped area was divided into the West Ridge and East Ridge by a present-day glacial valley (Fig. 5b).

Volcanic Lithofacies

Eastern Lillooet Ridge Volcanic Assemblage

The Eastern Lillooet Ridge volcanic assemblage comprises six unique volcanic lithofacies: Hackly jointed aphyric lava (NLhcl), columnar jointed aphyric lava (NLcjL), blocky jointed porphyritic lava (NLbjL), pillow lava (NLpL), monolithic tuff breccia (NLmtB), and monolithic vitric breccia (NLmpB) (Fig. 4). The extent of the volcanic outcroppings span ~ 2 km E-W and ~ 3 km N-S (Fig. 4). The ridge summit is at $\sim 2,080$ m with two adjacent, N-S oriented lava capped peaks. The southernmost peak (NLhcl) (Fig. 4) is elliptical in shape and features steep sides and a flat top. Hackly and irregular columnar joints point outward south and west. The lava extends a few hundred metres S of the summit and roughly 0.5 km west of the summit. The lava was observed in direct contact with the underlying pink-coloured monzonite basement rocks. The northernmost summit hosts well formed columnar jointed aphyric lava (NLcjL) (Fig. 4). The columns are up to 0.5 m in diameter and 15 m in length and are oriented N and NW. Isolated outcrops of NLcjL continue to the west and terminate after ~ 1 km at the edge of a glacial valley (Fig. 4). NLcjL from the northern peak overlies NLhcl from the southern peak.

Southeast of the two summits, there is a small outcrop of vesicular, blocky jointed lava (NLbjL) (Fig. 4). The lava is at $\sim 2,000$ m elevation and extend downslope for 100 m before transitioning into pillow lavas (NLpL). The pillow lavas continue roughly 400 m S and ~ 1 km W (Fig. 4). Monolithic tuff breccias (NLmtB) (Fig. 4) outcrop within the pillow lavas, and are well exposed in a N-S stream cut valley at $\sim 1,900$ m elevation (Fig. 4). A series of subvertical olivine, plagioclase, and augite porphyritic dikes intrude through the tuff breccias. At $\sim 1,700$ m elevation, the pillow lavas transition into monolithic vitric breccias (NLmpB) (Fig. 4) that extend 1.5 km down valley. The outcropping of NLmpB terminates as a steep cliff at roughly 1,060 m elevation immediately above the Lillooet River (Fig. 4). A series of vertical, olivine, augite, and plagioclase glomeroporphyritic dikes crosscut the breccia cliff face. NLmpB directly overlies a basal till at the base of the cliff.

Western Lillooet Ridge Volcanic Assemblage:

The Western Lillooet Ridge volcanic assemblage comprises four unique volcanic lithofacies: columnar jointed porphyritic lava (NLvjL), irregularly jointed aphyric lava (NLijL), monolithic stacked breccia (NLmcb), and blocky to columnar jointed porphyritic lava (NLbcjL) (Fig. 4). The volcanic outcroppings extend ~ 1.5 km east-west from an elevation of $\sim 1,560$ to $\sim 1,950$ m above the Lillooet River valley (Fig. 4).

The southwestern summit is a lava capped landform (NLvjL) (Fig. 4) that stretches ~ 1 km E-W. Large, vertical columnar joints, up to 0.5 m diameter, are exposed along the southward slopes. The topography shallows at the base of the columnar jointed slope, grading into the underlying irregularly jointed aphyric lava (NLijL) (Fig. 4). NLijL stretches ~ 1.5 km E-W (Fig. 4). The eastern outcrops expose irregular to hackly jointed columns (5-10 cm diameter) that point laterally outward. The interior and western exposures display slightly more regular and vertical columnar joints. A narrow outcropping of monolithic stacked breccia (NLmcb) (Fig. 4) is exposed within a N-S valley roughly 50 m SE of the NLvjL, and is exposed directly

east of the NLijL. The breccia outcrops as 'spire' like landforms reaching roughly 10 m high. The extent of the breccia is limited to ~100 m within the valley.

Along the western end of the North Lilloet Ridge, a thin outcropping of plagioclase, biotite, hornblende, and alkali feldspar porphyritic lava (NLbcjL) (Fig. 4) is exposed at ~1,700 m elevation. The lava is crudely columnar jointed but locally shows radially oriented columnar jointing.

Basement Geology

East Lilloet Basement Geology

The eastern Lilloet ridge basement rocks are predominantly monolithic, with the entirety of the East Lilloet Ridge volcanic assemblage overlying the pink, coarse grained monzonite (Mqm) (Fig. 4). South-southwest dipping monzonite outcrops along the southward edge of the ridge and continues east, paralleling Salal Creek. To the NW, the monzonite is in contact with coarse-grained quartz and biotite-rich gneiss (uTrcsb) (Fig. 4); the contact with the monzonite dips S-SE whilst the fabric in the gneiss dips N-NW. The contact can be traced ~1.5 km before the monzonite is truncated by a glacial valley, while the gneiss continues northwest, partially overlain by portions of the present-day glaciers.

West Lilloet Basement Geology

The western Lilloet ridge basement rocks begin on the west side of the glacial valley that divides the ridge into eastern and western segments. East-southeast dipping coarse grained gneiss (uTrcsb) (Fig. 4) overlies E-SE dipping coarse grained granodiorite (Mgd) (Fig. 4). Stream cut incisions through the granodiorite expose thin outcroppings of the underlying, medium grained, platy fractured amphibolite (Hpa) (Fig. 4). The granodiorite extends ~ 5 km west, reaching the glacial valley that bounds the North Lilloet ridge. Two east-west trending outcroppings of white marble (uTrcc) (Fig. 4) are thrust up through the granodiorite along small localized-folds. Medium grained biotite, hornblende, and quartz rich diorite (Mqd) (Fig. 4) occurs along the western edge of the ridge, bordering the westward glacial valley. Medium to coarse grained hornblende, pyroxene, and plagioclase rich amphibolite (Hpa) outcrops in a large section of the western edge of the ridge, unconformably underlies the NLvjL (Fig. 4).

North Lilloet Ridge Structure

The main structural feature observed was the presence of a potential major E-W striking strike-slip fault between the western and eastern ridges (Figs. 5a,c). It is difficult to constrain the timing of deformation and/or timing of strike-slip movement due to the lack of clear offset of the young volcanic rocks. However, an approximate age based on the presence of other kinematic indicators mapped on both ridges can be provided. The kinematic indicators include: bedding attitudes, minor folds, faults, veins and joints, and spatial relationship between outcrops of intact volcanic rocks and displaced volcanic rocks.

East Lilloet Ridge Structure

On the eastern ridge, two faults were mapped – the first is an ~ 33 m long left-lateral strike-slip fault, striking E-W with a few metres of offset. The second fault, cut by the first fault, is ~300 m long striking N-S, with signs of multiple deformation including normal, reverse and strike-slip. Additionally, nine minor folds were mapped, mostly with a general trending E-W direction except for one minor fold trending NE-SW (Fig. 6). Three sets of joints/fractures were mapped striking NW-SE, E-W, and NNE-SSW. The overall strike of beddings of the basement rocks are E-W and ENE-WSW (Fig. 6).

Spatially, the 300 m long N-S striking fault appears to cut through the young volcanic rocks. However, the fault surface predominantly crops out at the centre of the ridge and ends at the north side between the beginning of intact young volcanic rocks and most likely displaced volcanic rocks; the fault surface outcrops further south in an area covered with air-fall pumice deposits (Fig. 6).

West Lillooet Ridge Structure

Four minor faults (two fault sets) were mapped from along the west Lillooet ridge, striking NNE-SSW (reverse), NE-SW (normal), NE-SW (reverse), and NE-SW (reverse) respectively (Fig. 7b). Additionally, two minor folds were mapped trending N-S and NNE-SSW. Trends for three sets of joints and veins strike NNW-SSE, NE-SW and ENE-WSW (Fig. 7b). In general, three striking trends were identified for the beddings of basement rocks on the west ridge, which include NNW-SSE, NE-SW and ENE-WSW (Fig. 7b).

Southwest Meager Map Area

The Southwestern Meager map area comprises volcanic and basement rocks situated ~5 km west of Devastator Creek and ~6 km NW of Meager Creek (Fig. 2). We also extended our mapping eastward along the southern flank of Mount Meager, beneath Pylon Peak, where we traversed the roads built between the original geothermal drill pads, and re-mapped the exposed basement rocks across this region (Fig. 2).

Southwest Meager Volcanic Lithofacies

A previously unmapped lava flow (DCcJL) (Fig. 2c) was identified ~6 km west of Pylon Peak and ~6 km S-SW of Mount Job, exposed on the flat lying western edge of the Devastator Creek stream cut valley. Unconformably overlying basement granodiorite, the lava outcrops in a narrow depression at the lip of the steep sloped valley below, forming vertically oriented columnar joints 5 to 10 m high. The flow continues southward, following the valley edge for roughly 1 km before wrapping around westward forming a discernable lava toe. The front of the lava is exposed in places, under ~0.5 m of alluvium, and is topographically shallower than the underlying basement rocks.

Southwest Meager Basement Geology

At ~1,800 m elevation NW of Meager Creek, S-SW dipping coarse-grained gneiss (uTrcsb) overlies S-SW dipping granodiorite (Mgd) (Fig. 2). Small outcroppings of medium to coarse-grained augite and hornblende amphibolite (Hpa) are exposed in stream cut incisions through the granodiorite. Discordant contacts with platy to blocky jointed amphibolite and the overlying granodiorite were observed. Northeast of the Upper Lillooet Provincial Park boundary, the basement rocks show a change in dip direction, with the granodiorite dipping to NE and gneiss dipping SE. Minor folding was mapped in a narrow stream cut valley just east of the Park boundary, with thin, 20-30 m wide blocks of amphibolite and white marble (uTrcc) (Fig. 2) thrust up through the overlying granodiorite.

Southwest Meager Structure

The structural data recorded in the field include bedding of basement units, joints, fractures, veins and fault and fold data. The relative crosscutting relations were interpreted in the field where feasible. We cannot assign timing of deformation for the rock units due to lack of age constraints of the different basement rocks. Instead, a relative timing of deformation based on the kinematic compatibility of the crosscutting relationship was assigned to different structural features. Two major sets of joints/veins, striking NE-SW and ENE-WSW, and a few NW-SE striking veins have been identified in the field (Fig. 8b2). The NW-SE striking veins, where found, cut the major sets striking NE-SW and ENE-WSW (Fig. 8). Different types of faulting were mapped including reverse, oblique-slip normal and strike-slip. The faults strike N-S, NE-SW and NW-SE, respectively.

Ancillary Volcanics

During our helicopter set outs and reconnaissance, we identified two additional unmapped volcanic landforms that, based on relative weathering and stratigraphic positioning, may be Quaternary in age.

Perkins Pillar Lava

Our 2019 mapping campaign included new mapping of a lava (PPbjL) (Fig. 2a) situated ~1 km west of the Mount Meager summit. The lava is visible at an elevation of 2,360 m on the west side of the glacial valley beneath Perkins Pillar, and was first described by Roberti (2019) during fieldwork. The lava is dark grey, plagioclase, biotite, and hornblende porphyritic, and is exposed by recent glacial retreat near the Mount Meager summit. The lava is roughly 200 m wide, 500 m long, and 40 m thick and extends southward down a glacial valley on the south side of Perkins Pillar. An associated quartz and biotite rich block and ash autobreccia (PPbmtB) outcrops up-slope from PPbjL (Fig. 2a) and extends roughly 50 m S-SE before PPbjL begins. At the time of mapping, the lower portion of the lava was underlying snowpack and therefore the full extent of the unit is not known.

Elaho Valley Lava

Previous mapping by Woodsworth (1977) traced a long section of alkaline basalts within the Elaho Valley for ~20 km, starting ~10 km S of the Mount Meager massif. The source of the Elaho lavas was not determined. The age of the lava, based on whole rock K-Ar, is 0.14 ± 0.10 Ma (Green et al., 1988). During our 2019 mapping campaign, we mapped a section comprising multiple light grey, plagioclase, olivine, and augite porphyritic lavas (EVbjL) (Fig. 2b) at the mouth of the Elaho Valley ~5 km north of Woodsworth's locations, and ~5 km S of the Mount Meager massif (Fig. 2b). We traced the lavas above a waterfall that sits on the west side of the Elaho Valley where Meager Creek flows down into the valley. No vent was found, but columnar to blocky jointed lava outcrops are visible on both sides of the upper Meager Creek tributary. At the waterfall exposure, more than seven discrete lava layers of vertically jointed colonnades were observed. The lava was traced roughly 1 km S at the same elevation (~1,080 m) to the top of the waterfall, to a series of small lakes where blocky jointed outcrops of the lava were mapped on both east and west sides of the lakes (Fig. 2b).

Physical Properties of Mount Meager Basement Rocks

A preliminary set of physical property measurements were made on Mount Meager basement rocks and these data are shown in Table 1. The reported values are for bulk density and total porosity. The isolated and connected porosity of the rocks were also measured, however all samples returned values of approximately zero isolated porosity and therefore the connected porosity and total porosity values were determined to be essentially equal.

Results

Volcanology Synthesis

The 2019 mapping program focussed on the Neogene-Quaternary volcanic rocks with an aim of contributing knowledge relevant to the geothermal exploration campaign. The relation of young volcanics to geothermal potential lies in the understanding of magmatic storage and conduit systems throughout a volcanic complex. Additionally, their petrologic characteristics and volume inform on the nature of the subsurface geology for a region.

The MMVC is one of the largest and most recently active volcanic centres in the Garibaldi Volcanic Belt, with four discernable eruptions spanning the Pliocene to the Pleistocene (Green et al., 1988). The eruptive compositions of Mount Meager range from alkaline basalts to rhyolites (Green et al., 1988; Stasiuk and Russell, 1989; Read, 1990), which is indicative of magmatic differentiation during subsurface storage in young, active magma chambers.

Despite the breadth of mapping and research done on Mount Meager volcanic deposits, there are substantial portions of the volcanic complex that are undocumented or unstudied. The volcanic stratigraphy, eruptive ages, volumes, and durations of volcanism are not known on peripheral ridges and peaks relative to Read's (1977) map of the Mount Meager massif. However, even volcanic lithofacies

originally described by Read (1977, 1979) require further study by modern methods in order to properly assess the local volcanic and magmatic history and its import for geothermal resources.

Cracked Mountain volcanic synthesis

The Cracked Mountain volcano is substantially more complex than indicated by Read's (1977) initial mapping. The anomalous lithofacies of pillow lavas, pillow breccias, and vitric tuffs alone are revealing of the paleoclimate in which this volcano formed, as a subaqueous environment is necessary for such lithofacies. The situation of these lithofacies at high elevation above valleys to the north and west make a river or lake paleoenvironment highly unlikely. A subglacial environment is favored from our own observations and research on the volcano. The lack of erosional features between lithofacies indicate they erupted in a monogenetic event. The age of the eruptions was previously reported as 190 ± 61.0 ka ($^{40}\text{Ar}/^{39}\text{Ar}$) (Wilson, 2019). However, we aim to improve upon this date with new samples of our own. The eruptive volume for Cracked Mountain is non-trivial with the present-day edifice comprising roughly 0.5 km^3 of lava and pyroclastic ejecta. This volume, coupled with the high-density dike swarms across the volcano, affirms substantial magmatic activity in recent geologic history. Our identification of the Elaho Valley lavas, another series of voluminous flows situated less than 2 km SW of Cracked Mountain support our interpretation that the southwest MMVC is a young, active volcanic centre, and should be further explored for its geothermal potential.

North Lillooet Ridge volcanic synthesis

The West Lillooet Ridge volcanic assemblage comprises at least four petrographically unique eruptive units. Unconformities observed between volcanic units indicate a moderately long-lived and discontinuous eruptive history. The initial analysis of the lavas indicates intermediate to felsic compositions, which is suggestive of magmatic differentiation and subsurface storage prior to eruptions along this portion of the ridge.

The East Lillooet Ridge volcanic assemblage marks a change in eruptive occurrence and compositions as compared to the western ridge. Upon initial examination, the two prominent peaks comprise intermediate magmatic compositions while the pillow lavas, vitric breccias, tuff breccias, and dikes are likely mafic. No unconformities were observed between units – rather, gradational transitions were exposed on the slopes of the ridge. This stratigraphy indicates short lapses between the East Ridge eruptions. The overall age for such activity is unknown, however presence of pillow lavas, vitric breccias, and tuff breccias at 2,000 m elevation make this another candidate for glaciovolcanic interactions. The vitric breccias and dikes that directly overlie a basal till at the lower East Ridge exposure, suggests the most recent volcanic activity was concurrent or even post-dating the last period of glaciation.

Our mapping has concluded that there is evidence of voluminous magmatic eruptions along the North Lillooet Ridge. The indications of magmatic storage along the western area and young volcanic activity along the east lead us to the assessment that the North Lillooet Ridge map area should also be further considered for its geothermal potential.

Structural Synthesis

Tectonically, the Garibaldi Volcanic Belt (including the MMVC), coincides with Coast plutonic belt uplift and was produced by episodic accretion of multiple plates. The most recent tectonic phase includes the late Cenozoic subduction of Juan de Fuca plate beneath the continental margins of SW BC and northwestern Washington. This was later accompanied by Neogene-Quaternary volcanism and formed the NW-SE trending Garibaldi Volcanic Belt (Fig. 1).

Additionally, the GVB has recognized geothermal potential (e.g. Ghomshei et al.; Arianpoo, 2009; Ghomshei et al., 2004; Ghomshei et al., 2005) and thus understanding the natural hazards, tectonic evolution and their influences on the quality of the geothermal activity is essential. The current regional

maximum horizontal principle stress within the Coast Plutonic Belt including the GVB is approximately ENE-WSW (Leonard et al., 2010; Balfour et al., 2011), perpendicular to the Juan de Fuca and SW BC subduction front (Fig. 1). Thus, we can expect that trends of regional compressional structures such as the folds and reverse faults within the MMVC should be compatible with the regional horizontal maximum stress; possibly NNW-SSE trending structures.

Considering the proximity of Mount Meager to the Nootka Fault, stress partitioning between the interaction of Juan de Fuca and North American plates and Explorer and North American plates should be recognized (Fig. 1). The subduction rate between Explorer plate and the North American plate is less than that of the Juan de Fuca and North American plates (Riddihough and Hyndman, 1976) and could lead to spatial and temporal stress partitioning. This may lead to volume change of discrete basement blocks through transpression (tri-axial deformation in the case of temporal stress partitioning or pure shear deformation during spatial stress partitioning) or rotation of discrete basement blocks (for simple shear deformation). In either case, it influences the style and geometry of fracture patterns and consequently the flow of subsurface hydrothermal fluids, basement rock stability, and the stability of any shallow magmatic systems. Considering the regional horizontal maximum stress direction, the major regional compressional structures such as folds should trend approximately NNW-SSE to satisfy the kinematic compatibility; major compressional faults should strike parallel to the trend of the folds.

North Lillooet Ridge Structural Synthesis

The potential major left-lateral strike-slip fault structure between the western and eastern Lillooet ridges strikes roughly E-W. On the western ridge, one normal and three reverse faults strike NNE-SSW and NE-SW, oblique and perpendicular to the strike of the strike-slip fault. Additionally, two minor folds trend N-S and NNE-SSW, oblique or perpendicular to the strike of the strike-slip fault. This spatial and kinematic distribution agrees with the strike-slip model. On the eastern ridge, the 300 m long N-S striking fault has a fault surface with dip direction that alternates between east and west direction along strike (Fig. 6d). This fault is cut and offset a few metres by a 33 m long E-W striking fault. The fault offset in the field indicates a left-lateral strike-slip fault. Additionally, 8 minor folds, trend E-W and 1 minor fold trends NE-SW.

The kinematic relationship between these structures relative to the major strike-slip fault is as follows: 1) the 300 m long N-S striking fault is kinematically compatible with the regional maximum horizontal stress direction and the presence of a strike-slip fault between west and east ridges; 2) the 33 m long E-W striking strike-slip fault is also compatible kinematically with other structures and may be considered as a strand of the major strike-slip fault between the east ridge and west ridge; 3) the NE-SW trending minor fold, being oblique to strike of the major strike-slip fault, is also kinematically compatible with the strike-slip model; 4) the other 8 minor folds trending E-W are not kinematically compatible with the other structures and thus not compatible with the modern regional horizontal stress direction. This inconsistency may be due to the rate of uplift, direction of modern plate movement within SW BC, and most importantly, movement of individual basement blocks in the region. The Garibaldi Volcanic Belt is tectonically active with very high rates of uplift (Clague, 1992; Roberti, 2018).

The presence of normal and reverse dip-slip slickenlines along a single fault surface (300 m long N-S striking fault) may suggest the influence of glacial unloading. Our mapping of the attitude of basement beddings between the western ridge and eastern ridge (both ridges are less than 5 km apart) shows more than 50° change in strike (Figs. 7a, 6b); this suggests either tilting of basement units due to glacial unloading or basement block rotation. While this data is insufficient to constrain rotation of individual basement blocks, the change in strike orientation of the basement units (Fig. 9) along with the strike-slip structure makes basement block rotation feasible. Therefore, we consider that the inconsistency in the trend of the minor folds on the eastern ridge may be related to tilting of basement blocks due to glacial unloading and perhaps rotation of individual basement blocks. However, to confirm this, we would need

to study paleo-magnetic inclination of young volcanic rocks to validate any rotation of basement blocks as well as define timing of rotation.

Southwest Meager structural synthesis

A geometrical relationship between bedding of the units and minor folds indicates the presence of a major fold (trending NNW-SSE) (Fig. 8b) within the SW contact of the MMVC. Although we lack stratigraphic evidence, we have assigned this fold to be an anticline based on the patterns and geometry of the minor folds (S-shape, M-shape and Z-shape minor folds) at the limbs of major fold (Figs. 10c-f). Geometrically, buckling within compressional systems can define deformation history and thus aids identifying the hinge zone and limbs. For example, in the case of an anticline, Z-folds represent the left limb, S-folds represent the right limb and M-folds indicate the hinge zone (Fig. 10d).

The coincidence of the fold hinge area with a paleo-glacial valley and the cross-cutting relationship between veins within the major fold hinge zone may indicate that the fold crest has undergone possible erosion by glaciation and outer arc extension (collapse) presumably due to glacial unloading (Fig. 10f). Within the major fold hinge zone, an ESE-WNW striking vein cuts the NE-SW and ENE-WSW striking veins (Fig. 10f). Thus, the ESE-WNW striking set must postdate the formation of folding. In general, three sets of faults were identified within southwest contact of Meager: 1) a reverse fault, which roughly strikes N-S (Fig. 10b); 2) a NE-SW striking normal fault (Fig. 10b) and 3) an approximately NW-SE striking fault with major strike-slip component (Fig. 10a). Adjacent to the NW-SE striking strike-slip fault with a few metres of lateral offset, a ubiquitous (possibly Quaternary age) NE-SW striking fault scarp (possible normal) is mapped (Fig. 10b). Strike-slip and normal faults of southwestern Meager have similar structural trends with strike-slip and normal faults on the North Lillooet Ridge; both are most likely related to structural collapse due to glacial unloading and movement between individual basement blocks.

Summary

The Mount Meager Volcanic Complex, is an ice-clad volcano and part of the NW-SE trending Garibaldi Volcanic Belt which formed as the result of Neogene-Quaternary volcanism in southwestern British Columbia. The GVB, and particularly the MMVC, has identified geothermal potential (e.g., Ghomshei et al 2004; 2005; Arianpo, 2009). Understanding, the nature of the natural hazards, tectonic evolution and their influence on the quality of future geothermal exploration is essential. The presence of landslides and slope instability on ice-clad volcanoes within the GVB is well documented. However, the causation and trigger factors of such instabilities are not well-understood in terms of the level of contribution from deglaciation, rapid uplift and the regional tectonic configuration.

We carried out extensive field geology mapping on the North Lillooet Ridge, north of Mount Meager as well as across the southwest MMVC. We mapped both young volcanic rocks and basement rocks and collected structural data such as faults, folds, fractures and the attitude of beddings and planar features.

We identified three large volcanic centres along the periphery of the MMVC that contain unique lithofacies and eruptive deposits, contributing largely to the expansion of the previously mapped volcanics with the Cracked Mountain assemblage, East Lillooet Ridge volcanic assemblage, and West Lillooet Ridge volcanic assemblage, respectively. Additionally, we identified a new lava in the Southwest Meager map area, the Devastator Creek lava, and two ancillary magmatic occurrences with the Perkins Pillar lavas and Elaho Valley lavas.

Through our basement rock mapping, we obtained substantial bedding, fracture, and fault data that has been used to identify trends across the MMVC. Preliminary analysis of our data from the North Lillooet Ridge indicates the presence of major strike-slip movement, at least two stages of deformation, and basement block tilting or potential rotation. Strike-slip and normal faults on southwestern Meager have similar structural trends with the strike-slip and normal faults on the North Lillooet Ridge. We suggest that

tilting of basement blocks may be related to deglaciation and rapid uplift. Additionally, basement block rotation if proven may be related to the differences of stress rate between subduction of Juan de Fuca and North American plate versus subduction of Explorer plate with North American plate.

Future work will include, but is not limited to: long term (plus 20 years) temporal monitoring of deformation (displacement) across Mount Meager via synthetic aperture radar interferometry, radiometric dating of young volcanic units to constrain different episodes of deformation and eruptive recurrence intervals, geochemical analyses to better characterize the eruptive units and fingerprint their melt sources, paleomagnetism of rock units to trace small scale tilting and/or rotation of discrete basement blocks, and continued geologic mapping for areas that lack present day map coverage.

Data

Table 1: Physical property measurements on samples of basement rocks from Mount Meager. Bulk density (g cm^{-3}) and total porosity (%) are reported for each type of mapped unit.

Rock unit	Sample Local	Bulk Density(g cm^{-3})	\pm	Total Porosity (%)	\pm
Hpa	Southwest Meager	2.635	0.001	1.75	2.02
Hpa	Southwest Meager	2.247	0.000	13.63	0.30
Hpa	North Lilloet Ridge	2.949	0.000	1.38	3.09
Mgd	North Lilloet Ridge	2.700	0.000	0.81	0.04
Mgd	North Lilloet Ridge	2.701	0.002	0.78	4.30
Mgd	Cracked Mountain	9.940	0.003	4.42	0.26
Mgd	East Meager	2.761	0.001	0.78	3.47
Mqd	North Lilloet Ridge	2.875	0.000	0.93	3.40
Mqm	North Lilloet Ridge	2.576	0.002	1.82	1.92
uTrec	Southwest Meager	2.664	0.001	0.90	6.81
uTrec	North Lilloet Ridge	2.679	0.002	1.13	3.77
uTresb	North Lilloet Ridge	2.745	0.000	0.63	0.02
uTresb	Southwest Meager	2.900	0.001	1.23	2.21
uTr-csb	Cracked Mountain	2.841	0.001	1.24	2.55

Acknowledgements

Thanks to Sophie Leiter of UBC for her assistance in the physical property measurements conducted in the CESL laboratory.

References

- Arianpoo, N., 2009, The geothermal potential of Clarke Lake and Milo gas fields in northeast British Columbia (Masters dissertation). British Columbia, Canada: University of British Columbia.
- Balfour, N.J., Cassidy, J.F., Dosso, S.E., and Mazzotti, S., 2011, Mapping crustal stress and strain in southwest British Columbia: *Journal of Geophysical Research: Solid Earth*, 116, B3, doi:10.1029/2010JB008003.

- Ghomshei, M., Sanyal, S.K., Macleod, K., Henneberger, R.C., Ryder, A., and Fainbank, B. 2004, Status of the South Meager Geothermal Project British Columbia, Canada: Resource Evaluation and Plans for Development. *Transactions Geothermal Resources Council*, 28, 339–344.
- Ghomshei, M.M., Meech, T.L.S.J. a, Dakin, R. a, Geopower, W., West, C., Street, H., Granville, S., Canada, B.C., Associates, P., and Vancouver, N., 2005, Canadian Geothermal Energy Poised for Takeoff: Proceedings World Geothermal Congress 2005, 1–4.
- Ghomshei, M.M., Kimball, S.J., and Porkial, S., 2009, Geochemical evidence of a geothermal power resource the Canadian Rockies: Canoe hot springs, British Columbia, *in* *Transactions - Geothermal Resources Council*, 33, 419–423.
- Green, N.L., Harakal, J.E., Souther, I.J.G., and Read, P.B., 1988, Eruptive history and K-Ar geochronology of the late Cenozoic Garibaldi volcanic belt, southwestern British Columbia: *Geological Society of America Bulletin*, 100, 563–579.
- Leonard, L.J., Currie, C.A., Mazzotti, S., and Hyndman, R.D., 2010, Rupture area and displacement of past Cascadia great earthquakes from coastal coseismic subsidence: *Bulletin of the Geological Society of America*, 122, 2079–2096, doi:10.1130/B30108.1.
- Read, P.B., 1977, Meager Creek Volcanic Complex, southwestern British Columbia: *Geological Survey of Canada*, 77-1A, 277–281, doi: 10.4095/102701.
- Read, P.B., 1979, Geology of Meager Creek Geothermal Area, British Columbia: *Geological Survey of Canada Open-File 603*, 1 sheet, doi:10.4095/129507.
- Read, P., 1990, Mt Meager Complex, Garibaldi Belt, Southwestern BC.: *Geoscience Canada*, 17, 167–170.
- Riddihough, R.P., and Hyndnan, R.D., 1976, Canada's Active Western Margin - The Case for Subduction: 3, 269–278.
- Roberti, G., 2019, Mount Meager , a glaciated volcano in a changing cryosphere : hazards and risk challenges (Doctoral Dissertation). British Columbia, Canada: Simon Fraser University.
- Russell, J.K., and Stasiuk, M., 1990, The Bridge River Assemblage in the Meager Mountain volcanic complex, southwestern British Columbia: *Geological Survey of Canada*, 90-1E, 227-233.
- Stasiuk, M., and Russell JK, 1989, Petrography and chemistry of the Meager Mountain volcanic complex, southwestern British Columbia: *Geological Survey of Canada*, 89-1E, 189–196.
- Stewart, M.L., Russell, J.K., and Hickson, C.J., 2008, Geology, Pebble Creek formation, British Columbia: *Geological Survey of Canada*, Open File 5533, 1 sheet, doi:10.4095/225582.
- Wilson*, A.M., and Russell, J.K., 2018, Quaternary glaciovolcanism in the Canadian Cascade volcanic arc—Paleoenvironmental implications: *Field Volcanology: A Tribute to the Distinguished Career of Don Swanson*: *Geological Society of America*, 538, doi:10.1130/2018.2538(06).
- Wilson, A.M., 2019, Glaciovolcanism in the Garibaldi volcanic belt (Doctoral dissertation). British Columbia, Canada: University of British Columbia.

Woodsworth, G., 1977, Geology of Pemberton (92J) Map Area: Geological Survey of Canada, p. 1 sheet,
doi:10.4095/129282.

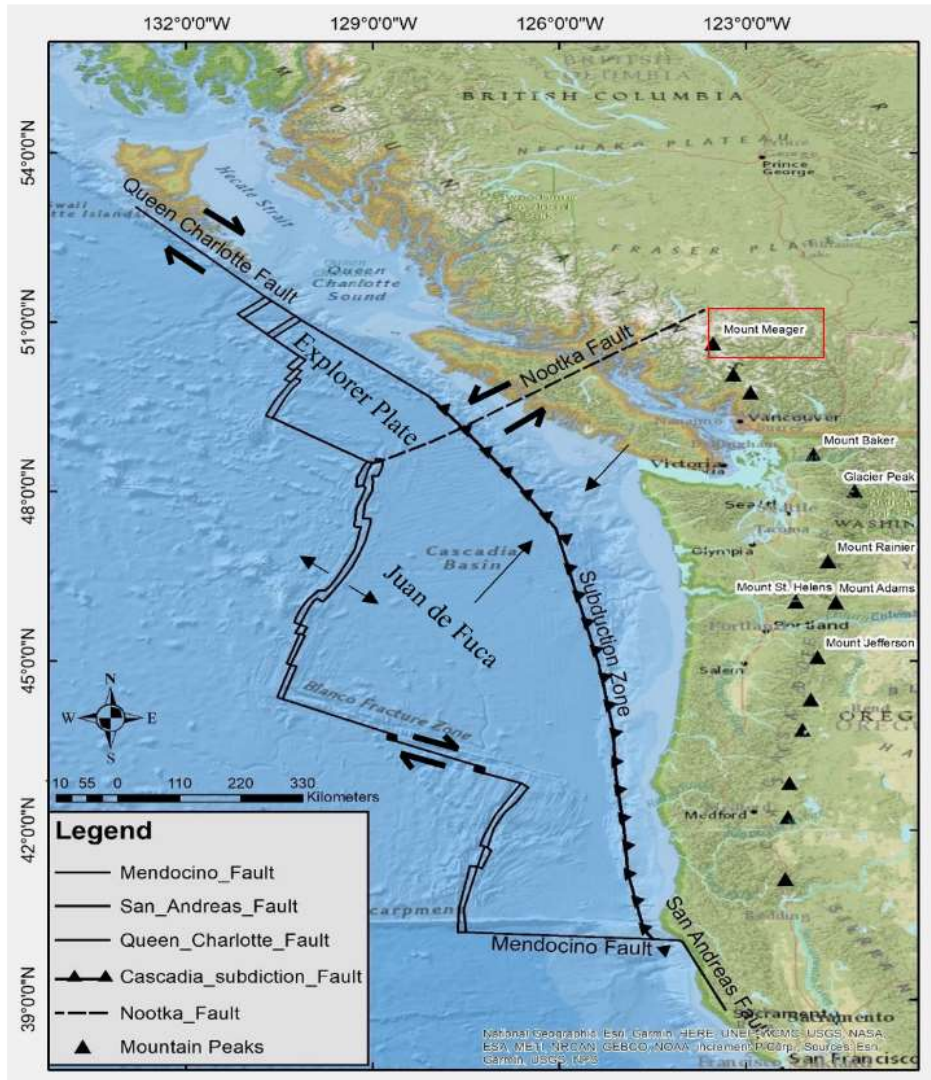
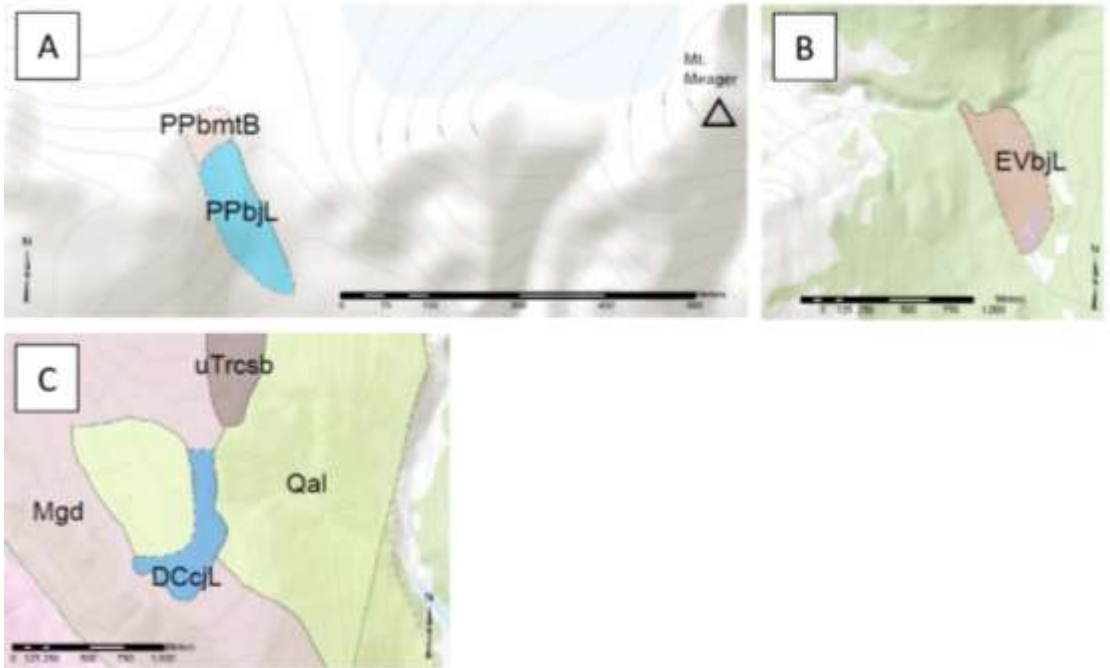
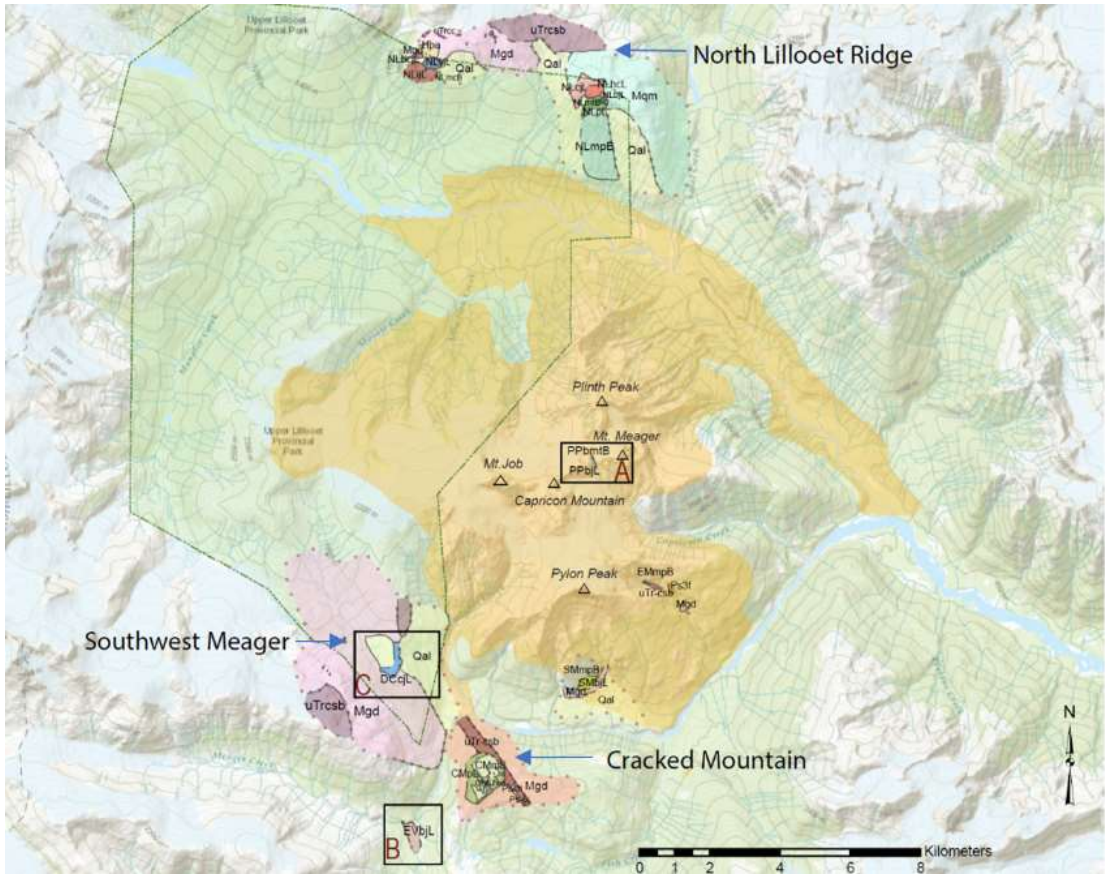


Figure 1: Regional Tectonic Map of the US and Canadian segments of the Cascade Volcanic Arc (Leonard et al., 2010). Note the change of plate boundaries starting from northern California to the northern Garibaldi Volcanic Belt (GVB) north of Mount Meager. The age of subduction changes from 10 Ma south of GVB below Glacier Peak to 5 Ma beneath Mount Meager, the northern most part of the GVB.



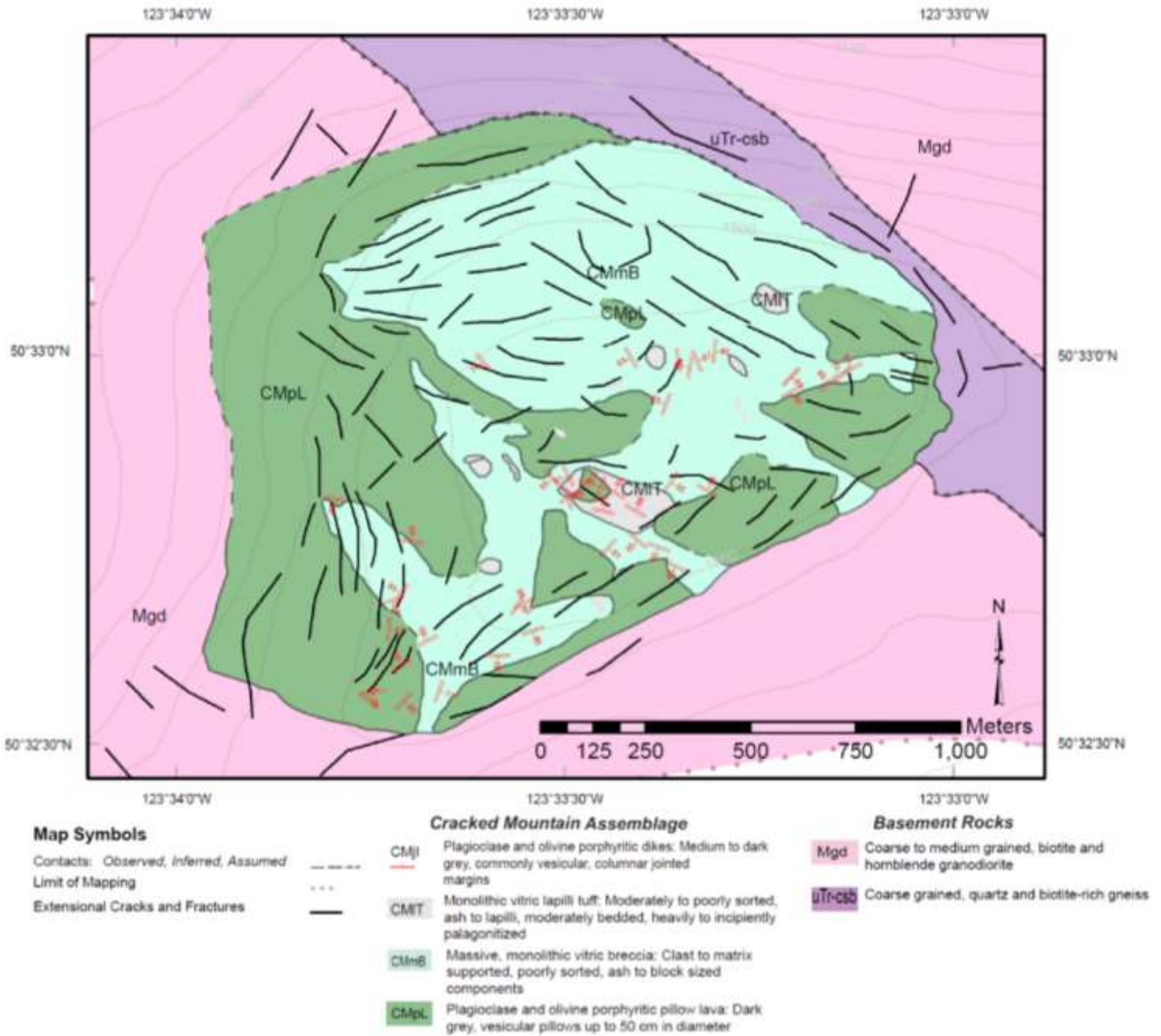


Figure 3: Geologic map of Cracked Mountain, a young volcanic cone mapped as a glaciovolcanic landform with an age date of 190 ± 61.0 ka (Wilson, 2019). Four unique lithofacies are shown across the volcanic edifice, dike location and orientations are shown in red, and extensional cracks are shown in black. The volcanic edifice unconformably overlies basement granodiorites and mica-schists.

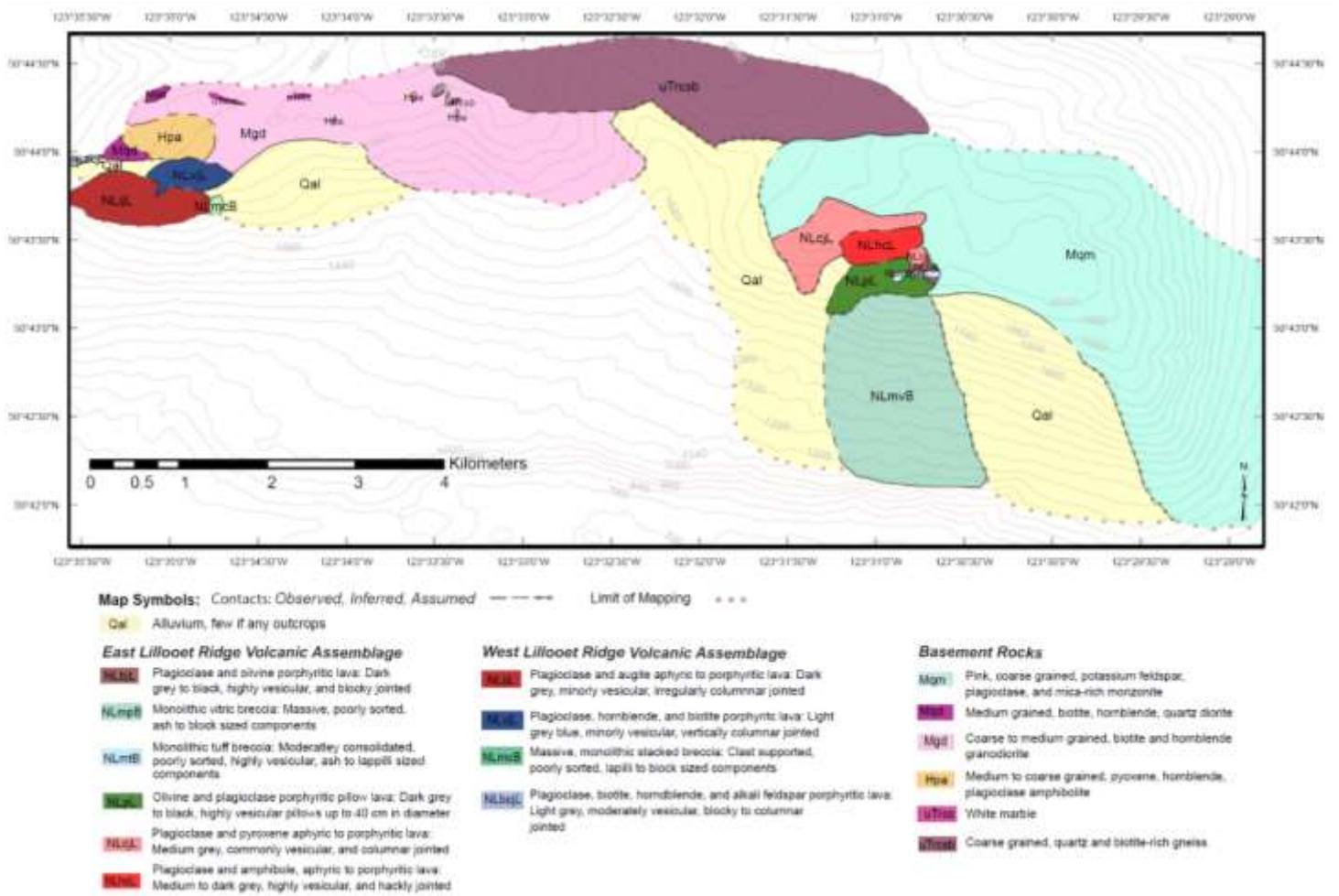


Figure 4: Geologic map of North Lillooet Ridge, showing two newly defined young volcanic centres on the periphery of the Mount Meager Massif: The East Lillooet Ridge volcanic assemblage and West Lillooet Ridge volcanic assemblage, overlying basement monzonite, granodiorite, diorite, amphibolite, marble, and mica-rich gneiss.

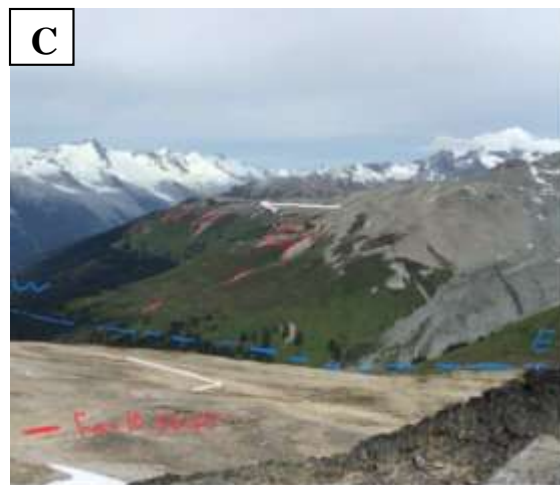
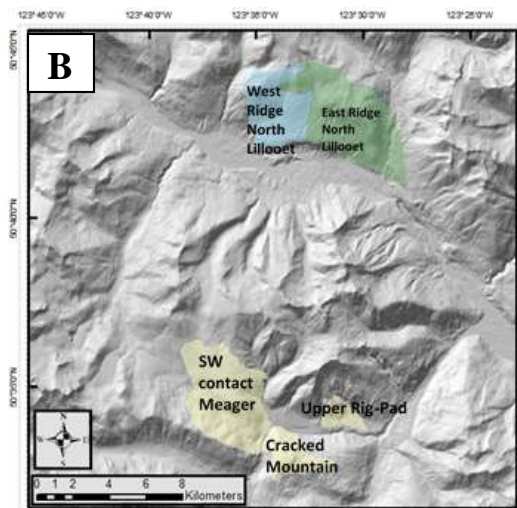
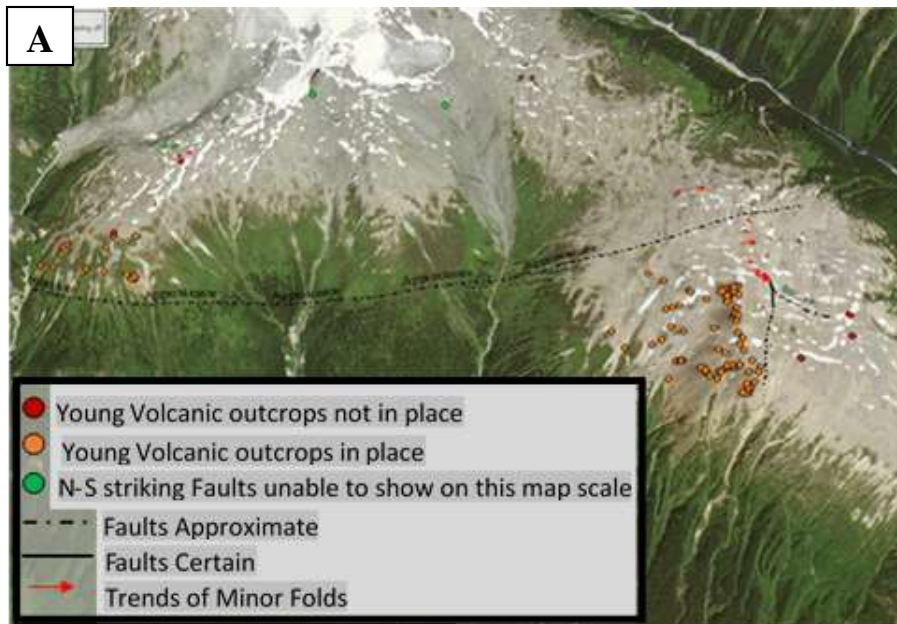


Figure 5: A) 3 m PlanetScope satellite image draped over 1.5 m Digital Elevation Model (from historical aerial photos); orange dots represent outcrops of coherent young volcanic rocks; red dots represent outcrops of young volcanic rocks which most likely not in place; green dots represent locations of N-S striking minor faults on the western ridge; red arrows represent trend of minor folds; solid lines represent certain faults; dash-dot lines represent concealed-approximate fault trace. B) Map shows locations of field mapping. C) A field photograph shows the patterns and geometry of fault steps. Note the geometry and arrangement of the fault steps indicate a left-lateral movement of the fault.

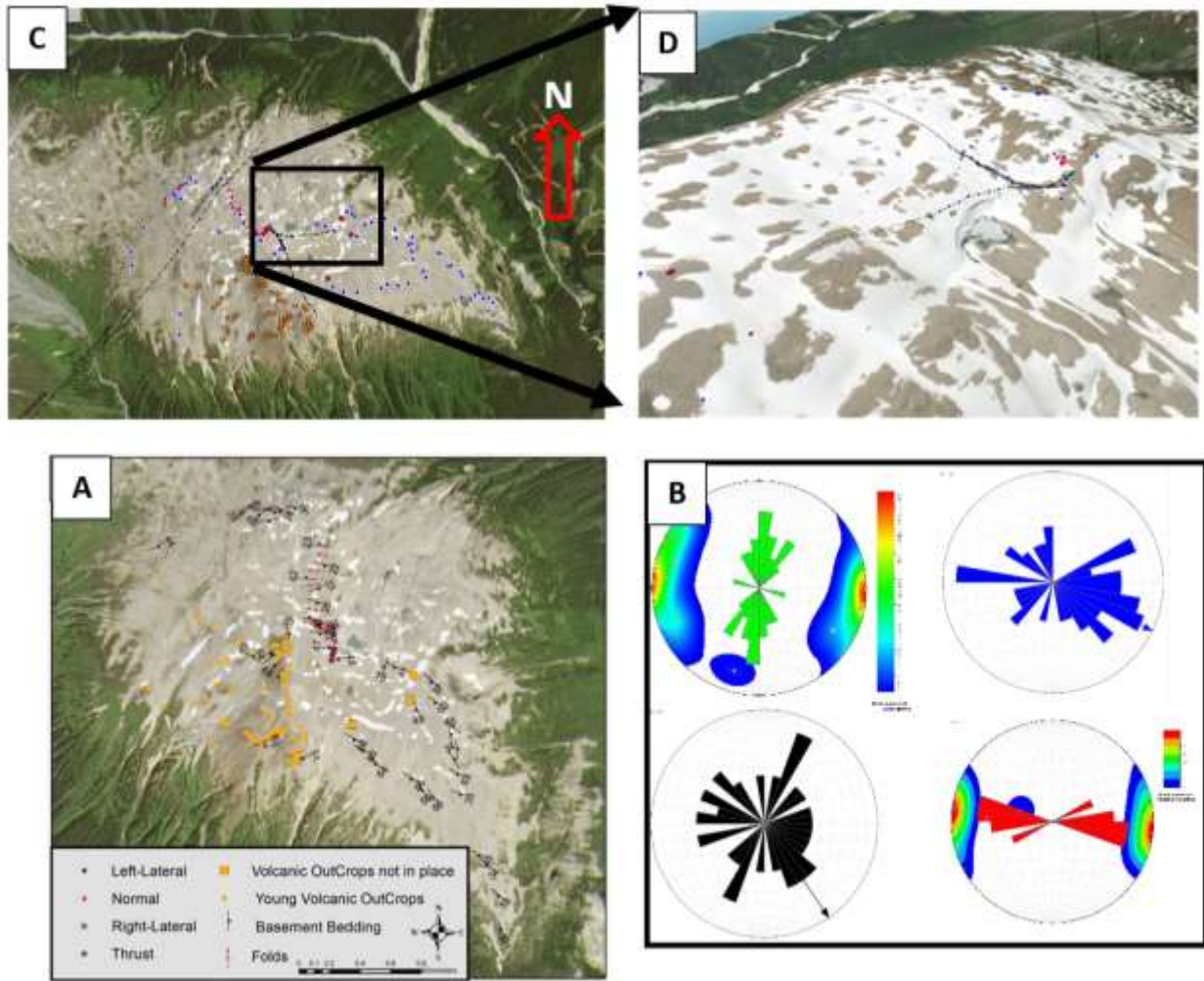


Figure 6: A) Geology Map of eastern Lillooet Ridge show: Outcrops of young volcanic rocks, older basement rocks and location and type of faults on the west ridge. Orange dots represent outcrops of young intact volcanic rocks; orange-square shapes represent outcrops of non-intact young volcanic rocks; black dots represent outcrops of older basement rocks. B) Stereographic plot of structural data of eastern ridge; green, shows strike orientation of faults; blue, strike orientation of basement beddings; black strike orientation of joint, fractures and veins; red trend of minor folds. Stereographic contours show the density of the data per cluster for poles of strike of structural features such as fault, joints/fractures and beddings. C) Planetscope satellite image draped over 1.5 m Digital Elevation Model (constructed from historical aerial photos); orange dots represent outcrops of coherent young volcanic rocks; red dots represent outcrops of young volcanic rocks which most likely not in place solid lines represent certain faults; dash-dot lines represent concealed-approximate fault trace. D) A 3D view constructed from draping 30 cm World imagery over 1.5 m Digital Elevation Model; notice the spatial relationship and topography between outcrops of coherent young volcanic and outcrops of young volcanic most likely not in place relative to the mapped fault structures.

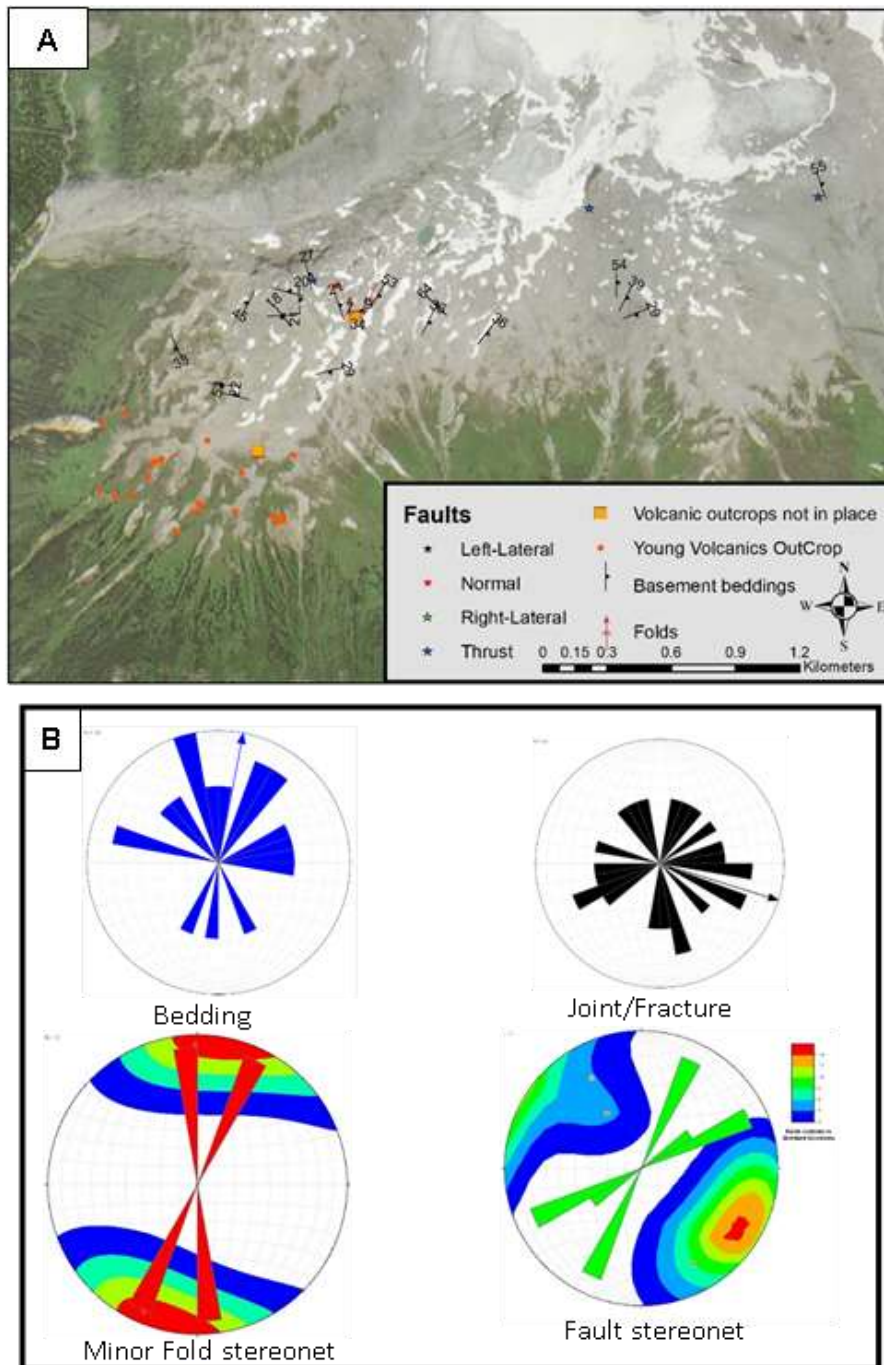


Figure 7: A) Structural map of western Lillooet Ridge show: Outcrops of young volcanic rocks, older basement rocks and location and type of faults on the west ridge. Orange dots represent outcrops of young intact volcanic rocks; orange-square shapes represent outcrops of non-intact young volcanic rocks; black dots represent outcrops of older basement rocks. B) Rose diagram for strike and trend of measured structural data; green, shows strike orientation of faults; blue, strike orientation of basement units; black strike orientation of joint, fractures and veins; red trend of minor folds. Stereographic contours show the density of the data per cluster for poles of strike of structural features such as fault, joints/fractures and beddings.

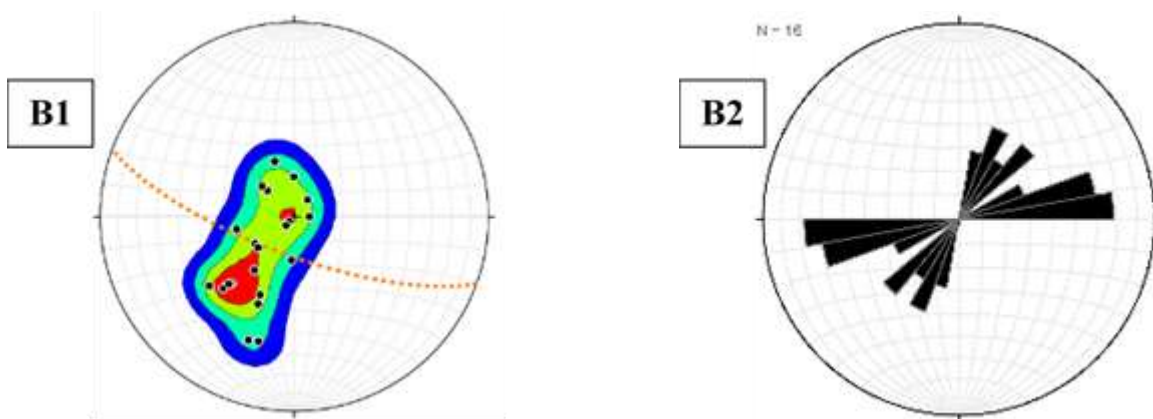
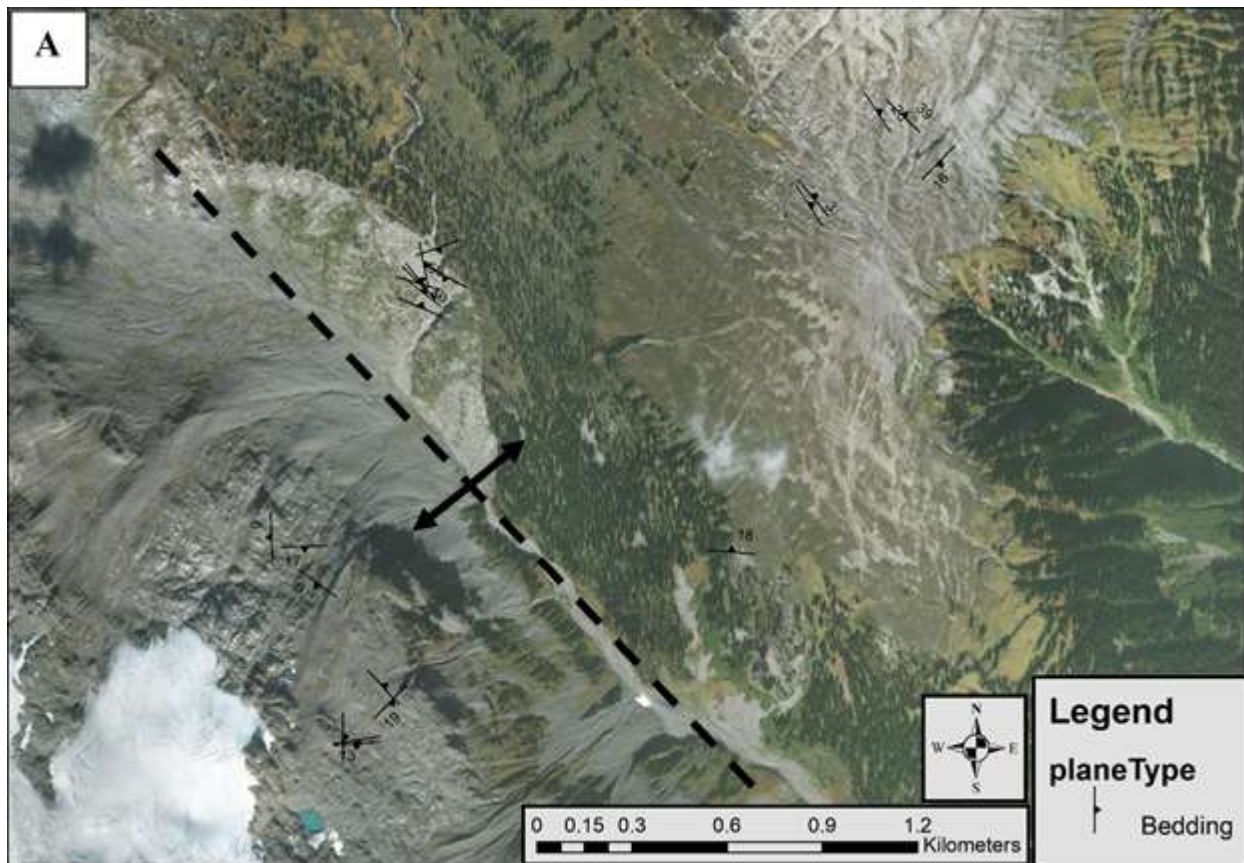
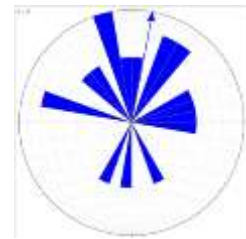
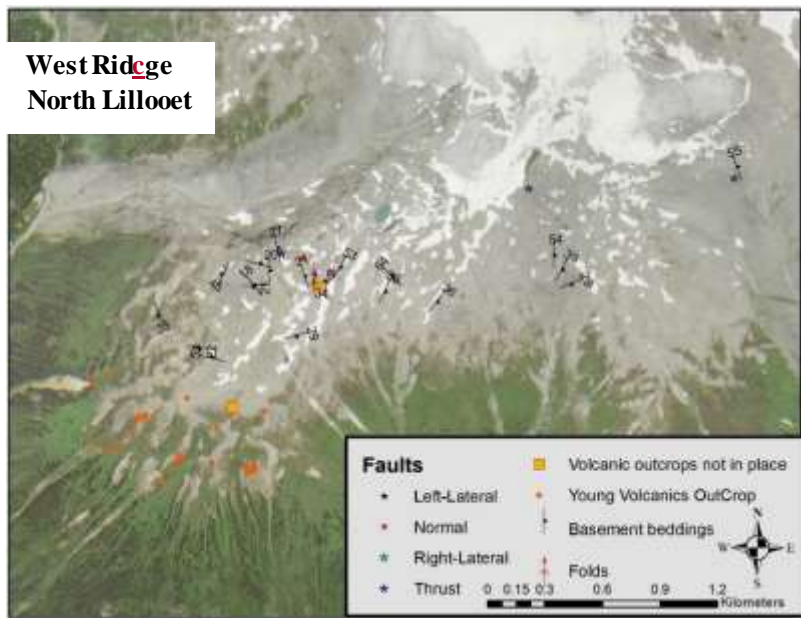
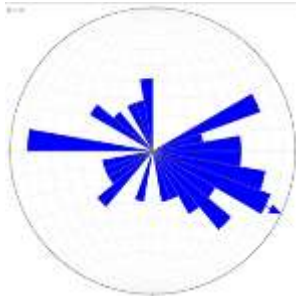
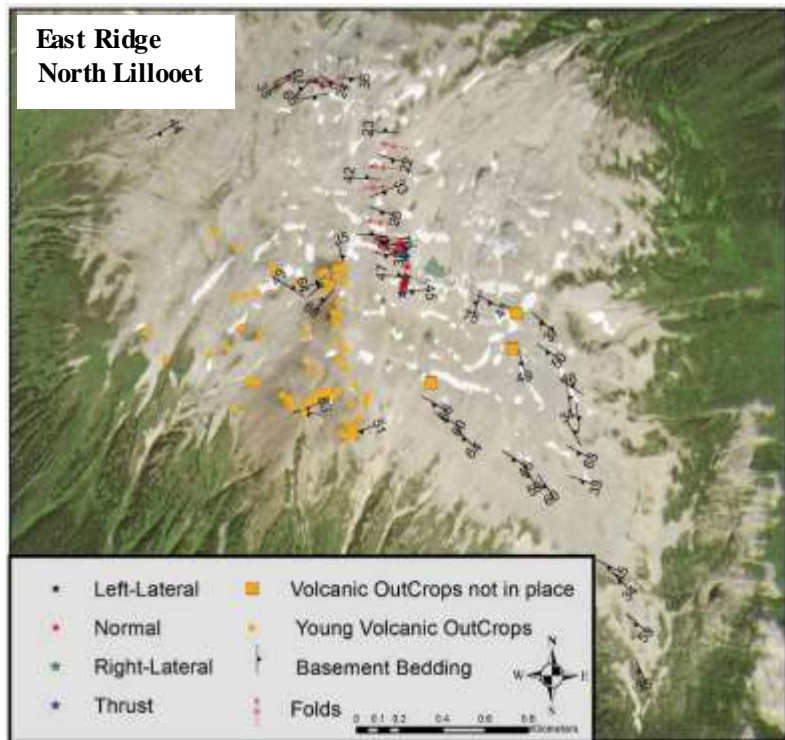


Figure 8. A) Structural map of southwestern contact of Mount Meager. B1) Stereograph of basement beddings of southwestern contact of Mount Meager: Orange dotted plane represents axial plane (striking NW-SE) of calculated fold structure; contours were drawn for poles of bedding planes for the major fold limbs. B2) Rose diagram of veins and fractures southwest of Meager.



Rose Diagram of strike of basement units-Western Ridge



Rose Diagram of strike of basement units-Eastern Ridge

Figure 9. Show comparison of the attitude of basement units in North Lillooet Ridge. Note: on the west ridge basement units strike N-S and WNW-ESE; contrastingly, on the eastern ridge two clusters of basement unit geometry identified; strike of basement units north of young volcanic outcrops are consistent with the western ridge while strike of basement units south of young volcanic outcrops are inconsistent with the western ridge and striking NW-SE.

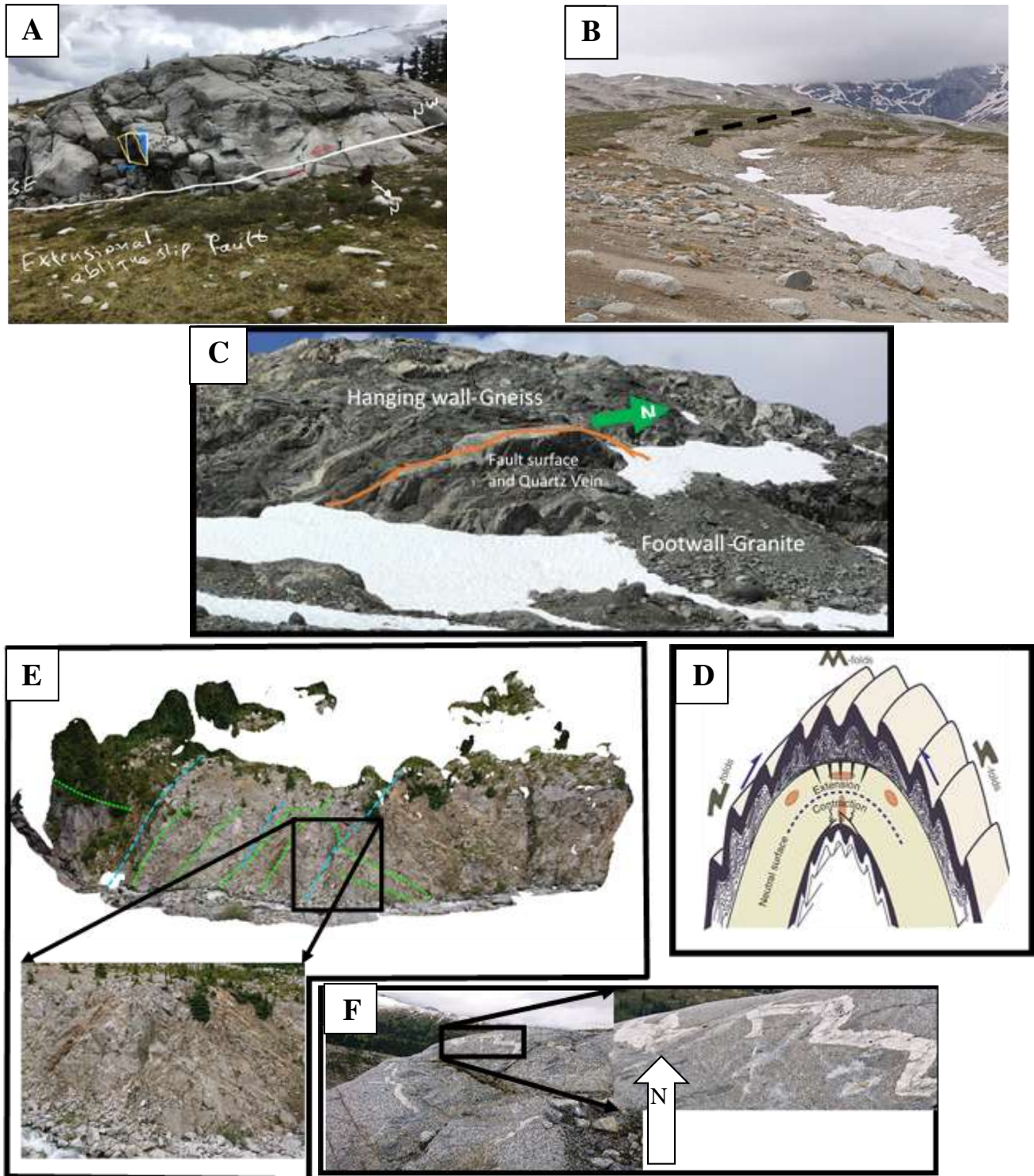


Figure 10. A) NW-SE striking strike-slip fault (approximately 1 m offset). B) NE-SW striking fault scarp (potentially normal fault). C) N-S striking compressional fault and S-shape minor fold. D) A cartoon model explains geometry of buckling fold on limbs of major folds. E) N-S striking compressional fault and Z-shape minor fold. F) NE-SW striking quartz vein folded (M-shape minor fold) within the hinge area of a major fold structure. Note that the folded quartz vein is cut by a NW-SE striking xenolith vein.

Chapter 2 - Appendix 1

Volcanic Lithofacies Descriptions

Cracked Mountain Assemblage

CMpL- Plagioclase and olivine porphyritic pillow lava: Dark grey, vesicular pillows up to 50 cm in diameter

The Cracked Mountain pillow lavas are composed of bulbous pillows up to 50 cm in diameter. Interstitial volcanoclastic sediment fills void spaces between intact pillows in some outcrops, while large radial columnar jointed pods, up to 3 m in diameter, make up a lesser degree of the lithofacies

The pillow lavas show variation in color, texture, and vesicularity when sampled from the interior of the flows as compared to the outer margins. The internal pillow lavas are medium to dark grey in color, and show plagioclase, olivine, and clinopyroxene porphyritic to glomeroporphyritic texture. Plagioclase (10-15%) is the dominant phenocryst, forming subhedral crystal laths ranging from 0.2 to 3 mm in length. Olivine (6-10%) is also common and forms anhedral to subhedral crystals that range from 0.2 to 3 mm in diameter. Clinopyroxene (>1%) is scarce but does occur in some samples as subhedral crystals, up to 2 mm in diameter. The groundmass is medium to coarsely grained, with plagioclase (50-70%) as the dominant mineral. Olivine and clinopyroxene both are present but occur to a lesser degree (both ~10%). Vesicularity is moderate, (10-20%), coarse, up to 3 mm in diameter, and subrounded to angular in shape. Towards the outer margins of the pillow lava outcrops, the color becomes increasingly dark, verging on black, and vesicularity can increase substantially (<50%). Mineralogical and macroscopic textures remain consistent with interior pillow lavas but the exterior pillow groundmasses are notably fine grained and vitric, with only microcrysts of olivine and plagioclase visible.

CMmB- Massive, monolithic vitric breccia: Clast to matrix supported, poorly sorted, block to ash sized components.

The Cracked Mountain monolithic vitric breccias have clast sizes ranging from half metre pillow fragments to lapilli sized vitric clasts. Sorting is poor, and deposits are massive. The partially intact pillow fragments are angular to subrounded, and frequently show quenched margins.

The vitric breccia clasts are dark grey to black and are plagioclase and olivine porphyritic. Plagioclase (10-15%) forms coarse subhedral laths ranging from 0.1 to 4 mm, and olivine (5-10%) occurs as anhedral to conchoidally fractured crystals ranging in size from 0.1 to 2 mm. The clast groundmass is vitric to fine grained with crystals of plagioclase, olivine, and clinopyroxene (>0.1mm). The clasts are highly vesicular (<50%) showing rounded to angular shapes.

The matrix that supports the brecciated clasts is yellow to brown in color, and medium to fine grained. The matrix components are highly angular, conchoidally fractured volcanic glass, and display jigsaw fracture patterns under petrographic microscope inspection. Among the vitric clasts are moderately intact to highly fractured crystals of plagioclase and olivine. Many vitric ash sized fragments are rimmed with dark brown to black alteration, likely palagonite. Microvesicles within the matrix are scattered between vitric clasts and mineral crystals, showing rounded to angular shapes.

CMIT - Monolithic, vitric lapilli tuff: Moderately to poorly sorted, ash to lapilli, moderately bedded, heavily to incipiently palagonitized

The Cracked Mountain vitric lapilli tuff has grain sizes of ash to lapilli (2 mm to 6 cm) and is matrix supported throughout the entire volcano. The lithofacies has varying degrees of palagonitization, ranging from incipiently to heavily altered.

The vitric tuff ranges in color from grey to dark yellow, is crudely bedded to massive, and moderately to poorly sorted. The components of the lapilli tuff breccia are dark, angular, and highly vesicular (<50%) vitric clasts. The clasts are porphyritic with medium to coarse plagioclase (5-10%) and anhedral olivine (3-6%). The shape of the vesicles ranges from subrounded to angular. The clast groundmass is fine grained, and appears nearly extinct under cross polarized light but contains minor microcrysts of plagioclase, olivine, and clinopyroxene. The tuff matrix is composed of angular to subrounded glassy fragments, showing conchoidal to jigsaw type fracture patterns. The vitric crystals range from incipiently to pervasively altered along grain margins by dark brown to black palagonite. Both phenocrysts and microcrysts within the matrix display varying degrees of splintering, where some crystals appear as partially intact pieces of their larger crystal habits and others show jigsaw fragmentation within a pre-existing crystal shape.

CMjI- Plagioclase and olivine porphyritic dikes: Medium to dark grey, commonly vesicular, columnar jointed

Dikes are medium grey in color and often have undulating glassy margins. The interiors display coarsely grained olivine and plagioclase porphyritic to glomeroporphyritic texture. Plagioclase (10-15%) is the most common phenocryst, forming subhedral laths with lengths of 0.2 to 5 mm. Olivine (7-10% forms as subhedral to anhedral crystals with diameters of 0.1 to 2mm. Vesicularity varies from dike to dike (5% to <30%), with the highest concentrations of vesicles along the outer margins of the dikes. The vesicle sizes are coarse, up to 4mm in diameter, with rounded to angular shapes. The groundmass is medium to fine grain, with plagioclase (50-70%), olivine (10-15%), and clinopyroxene (10-15%) present. Microvesicularity is common among most dikes.

Eastern Lillooet Ridge Volcanic Assemblage Lithofacies

NLhcL: Plagioclase and hornblende, aphyric to porphyritic, lava: Medium to dark grey, highly vesicular, and hackly jointed

The colour of the lava is dark to medium grey, with aphyric texture. Hackly and irregular jointed columns propagate in lateral and vertical directions. Small, elongate hornblendes (1-2%) range from 0.5 to 3 mm. Highly pitted plagioclase (1-2%) and augite (>1%) also occur as very minor phenocrysts. The groundmass is dominated by fine grain plagioclase (60%) with very minor augite (>5%). Opaques (~35%) are highly concentrated within the groundmass and also fill in more than 70% of the phenocrysts as pitted inclusions. Planar stretched vesicles (5-15%) are present throughout the unit.

NLcjL: Plagioclase and augite, aphyric to porphyritic lava: Medium grey, commonly vesicular, and columnar jointed

The lava is medium grey, aphyric with very scarce phenocrysts. The few crystals are highly altered augite (2-3%) that form subhedral habits, ranging from 0.5 to 3 mm in diameter. Plagioclase (1-2%) also occurs

as subhedral laths ranging from 0.5 to 1.5 mm in length. Vesicularity ranges from samples to sample (5-15%) forming subrounded to stretched shapes. The groundmass of the lava is fine grained, and plagioclase rich (60%) with very minor augite (>5%) present. Opaques (~45%) are highly concentrated within the groundmass, and are commonly seen as intergrowths within the larger pitted augite and plagioclase crystals.

NLbjL: Plagioclase and olivine porphyritic lava: Dark grey, highly vesicular, and blocky jointed

The lava is dark grey to black, with coarse grained plagioclase, olivine, and augite, porphyritic to glomeroporphyritic texture. Plagioclase (15-20%) is the dominant phenocryst, forming euhedral to subhedral laths ranging from 0.5 to 3 mm in length. Olivine (5-10%) forms as anhedral crystals ranging from 0.5 to 1.5 mm in diameter, and augite (5%) forms as subhedral to anhedral crystals ranging from 0.5 to 1.5 mm in diameter. Vesicularity is moderate to high (15-30%) with coarse sized vesicles up to 3mm in diameter. The groundmass is fine grained and moderately glassy, with plagioclase (60%) dominating and moderate amounts of olivine and augite (both ~10-15%).

NLpL: Olivine, augite, and plagioclase porphyritic pillow lava: Dark grey to black, and highly vesicular, pillows up to 40 cm in diameter

The North Lillooet pillow lavas are composed of small to medium sized bulbous pillow lobes with maximum diameters of 40 cm. Large radially columnar jointed pods of lava up to four meters in diameter are also observed at the eastern most edge of the pillow lava outcrops.

The pillow lava is dark grey to black, plagioclase, olivine, and augite porphyritic to glomeroporphyritic. Plagioclase (15-20%) is the dominant phenocrysts forming euhedral to subhedral laths ranging from 0.5 to 3 mm in length. The larger plagioclase crystals commonly exhibit compositional zoning with moderate to high degrees of pitted alteration. Olivine (5-10%) forms as anhedral crystals ranging from 0.5 to 1.5 mm in diameter. Augite (5%) forms as subhedral to anhedral crystals ranging from 0.5 to 1.5 mm in diameter, and as with plagioclase, commonly shows high degrees of pitted alterations. Vesicularity is moderate to high (15-30%) with coarse sized vesicles up to 3mm in diameter. The groundmass is fine grained and moderately glassy, with plagioclase (60%) dominating, with moderate amounts of olivine and augite (both ~10-15%) as well. The textural fabric is diabasic with plagioclase, olivine, and augite forming interlocking microcrysts.

NLmtB: Monolithic tuff breccia: Moderately consolidated, poorly sorted, highly vesicular, lapilli to ash sized components

The North Lillooet tuff breccia is monolithologic, massive, moderately consolidated, matrix supported, and poorly sorted with clast sizes ranging from block to ash.

The breccia clasts are dark grey to black in color, and occur as angular, monolithic, highly vitric and vesicular fragments of lava. The clasts are olivine, plagioclase, and augite porphyritic. Plagioclase (10-15%), olivine (5-7%), and augite (4-5%) porphyritic. The groundmass of the clasts is glassy, and contains microcrysts of plagioclase (30%) and minor amounts of olivine and augite (>5% for both). As with the pillow lava, the plagioclase phenocrysts commonly show high degrees of zoning, and both plagioclase and augite crystals are moderately to pervasively pitted with opaques and inclusions of microcrysts of olivine and augite. The tuff breccia matrix is yellow to brown in color, and is comprised of angular ash sized glassy

shards showing conchoidal and jig-saw fracture patterns. Anhedral and fragmented pieces of larger plagioclase, olivine, and augite are also seen within the vitric matrix of the tuff breccia.

NLmpB: Monolithic vitric breccia: Massive, poorly sorted, block to ash sized components

The unit is massive, clast to matrix supported, and poorly sorted with block to lapilli sized components. Large radially columnar jointed pods of lava are embedded within the cliff forming walls at the lower waterfall exposure, and plagioclase, olivine and augite glomeroporphyritic dikes intrude through the breccia.

The breccia clasts are dark grey to black, and contain augite (5-7%), plagioclase (1-2%), and olivine (1-2%) porphyritic texture. The groundmass is aphanitic and vitric, with limited plagioclase (10-15%) and very minor olivine and augite (both 1-2%). Clast vesicularity is substantial, ranging from 40-50%, showing both rounded and angular to stretched void shapes. The breccia matrix is composed of angular to conchoidally fractured, ash sized volcanic glass, that commonly shows jig-saw fracture patterns in void spaces. Irregularly shaped and fractured crystals of plagioclase, augite, and olivine are also scattered throughout the ash matrix.

Western Lillooet Ridge Volcanic Assemblage Lithofacies

NLvjL: Plagioclase, hornblende, and biotite porphyritic lava: Light grey blue, minorly vesicular, and vertically columnar jointed

The lava is light grey to light blue, with coarse grained plagioclase, hornblende, and biotite porphyritic texture. Plagioclase (30%) is the dominant phenocryst ranging from 0.5 to 4.5 mm in length, and commonly shows zoning and pitted alterations with opaque inclusions. Hornblende (10%) is common, but occurs as smaller tabular to acicular crystals ranging from 0.5 to 1.5 mm, commonly showing brown alteration rims. Biotite (1-2%) is scarce but does occur as 0.5 to 1 mm subhedral phenocrysts. The groundmass is medium grained, and plagioclase dominant (75%), with moderate hornblende (5-10%) and opaques (10%). The textural fabric is trachytic to pilotaxitic with flow aligned plagioclase laths forming around some of the large phenocrysts. The lava exhibits little to no vesicularity.

NLijL: Plagioclase and augite aphyric to porphyritic lava: Dark grey, minorly vesicular, and irregularly columnar jointed

The lava is dark grey, with medium to fine grained plagioclase and augite aphyric to porphyritic texture. Plagioclase (12%) occurs as subhedral laths ranging from 0.5 to 2 mm in length, and nearly all crystals show moderate to substantial degrees of zoning and pitted alterations with opaque inclusions. Augite (3%) occurs as anhedral crystals ranging from 0.5 to 1 mm in diameter. The groundmass is plagioclase dominant (70%) with lesser amounts of augite (10-15%) and opaques (10-15%). The textural fabric is pilotaxitic. Vesicularity is minor (5-10%) forming subrounded to angular vesicles.

NLmcB: Massive, monolithic stacked breccia: Clast supported, and poorly sorted, block to lapilli sized components

The North Lillooet stacked breccia is massive, clast supported, and poorly sorted with clast sizes ranging from lapilli to bomb size (6 to 50 cm), and occur as rounded to subangular lithic fragments. Little to no matrix is found between interlocking clasts.

The monolithic clasts are plagioclase and hornblende porphyritic. Plagioclase is dominant (25%) but forms small subhedral to fractured laths ranging from 0.2 to 2.5 mm, with the majority of laths less than 1 mm in size. The larger crystals of plagioclase commonly show zoning and moderate degrees of pitted alteration with opaque inclusions. Hornblende (1-2%) is rare but does occur as phenocrysts up to 1.5 mm in length. The groundmass is also dominated by plagioclase (60-70%) with abundant opaques (20%) and minor amounts of a highly altered brownish to red subhedral crystals, possibly augite (5%). The textural fabric is pilotaxitic, and vesicularity ranges from five to ten percent, forming irregular and very angular vesicle shapes.

NLbcjL: Plagioclase, biotite, hornblende, and alkali feldspar porphyritic lava: Light grey, moderately vesicular, blocky to columnar jointed

The lava is light grey, and texture of the blocky jointed lava is porphyritic, with plagioclase (15-20%) as the dominant phenocryst. The plagioclase forms subhedral laths ranging from 0.2 to 3.5 mm in length, and are ubiquitously zoned and pitted with opaques. Biotite (5%) occurs as tabular crystals 0.2 to 1.5 mm in length, while hornblende (1-2%) forms subhedral phenocrysts ranging from 0.5 to 1 mm in diameter. Alkali feldspar (>1%) is very rare, but is observed under petrographic inspection. The groundmass is aphanitic and moderately vitric, with plagioclase (25%) and quartz (25%) as the major components. Biotite (10-15%) and hornblende (5-10%) are both found to lesser degrees. Vesicularity is very minor (>2%).

Devastator Creek Lava

DCcjL: Plagioclase, augite, and hornblende porphyritic lava: Light grey, minorly vesicular, and columnar jointed

The lava is light grey in color, and the texture of the is plagioclase, augite, and hornblende porphyritic. Plagioclase (25%) is dominant, forming medium to coarse grained laths, 0.2 to 5 mm in length. The plagioclase is commonly observed to have compositional zoning and pitted alterations with opaque inclusions in more than 50% of the minerals. Augite (5%) forms fine to medium sized subhedral crystals, ranging from 0.2 to 1 mm in diameter, and show little to no alteration. Likewise, hornblende (3-4%) forms medium sized crystals, ranging from 0.2 to 1 mm in length, and also show little to no alteration. The groundmass is medium to fine grained, with abundant plagioclase (60-70%) and opaques (25%). Augite (5%) is moderate, while hornblende (1-2%) is very minor. The textural fabric is pilotaxitic to trachytic with some flow alignment of plagioclase laths around the larger phenocrysts.

Perkins Pillar Lava

PPbjL: Plagioclase, biotite, and hornblende porphyritic lava and autobreccia (PPbmtB): Dark grey, moderately vesicular, and blocky jointed

An autobreccia is exposed at the base of the lava. The breccia is white to grey in color, massive, and poorly sorted. Clasts are monolithic plagioclase, biotite, and hornblende and have vitric groundmasses. Some show larger clasts show radial jointing. Roughly 5 m above the autobreccia, a coherent plagioclase, biotite, and hornblende porphyritic lava, that is dark grey in color, with moderate vesicularity and blocky jointing, makes up the remainder of the thick lava flow.

The lava is plagioclase, biotite, and hornblende porphyritic. Plagioclase (15-20%) is the dominant phenocryst forming medium to coarse laths 0.5 to 3.5 mm in length. Biotite (5%) and hornblende (2-3%) occur as finer 0.5 to 1 mm crystals. Both augite (1%) and quartz (1%) are observed as phenocrysts but

scarce. The groundmass is moderately vitric, and plagioclase dominant (70%). Opaques (20%) also make up a moderate occurrence within the groundmass, while biotite (2%), hornblende (1%) and augite (1%) are very minor. The textural fabric is trachytic to pilotaxitic, with plagioclase showing flow alignment around some of the larger phenocrysts. Vesicularity (10%) is minor, but coarse in size, up to 3.5 mm in diameter. The vesicle shapes are rounded to subangular and stretched.

Elaho Valley Lava

EVbjL: Plagioclase, olivine, and augite porphyritic lava: Light grey, minorly vesicular, and blocky to columnar jointed

The lava is plagioclase, olivine, and augite porphyritic. Plagioclase (15-20%) is the most abundant phenocryst forming medium to coarse laths ranging from 0.2 to 3.5 mm in length. The plagioclase commonly shows pitted and alteration with opaque intergrowths. Olivine (5%) forms subhedral crystals ranging from 0.2 to 2.5 mm in diameter, showing no alteration. Augite (2-3%) is lesser but does occur as subhedral phenocryst ranging from 1 to 2 mm in diameter. The groundmass is medium grained, and dominated by plagioclase (50%) and opaques (30%) with lesser degrees of olivine and augite (both 10%). The groundmass fabric is diabasic, with discrete crystal boundaries for all minerals. Moderate trachytic flow alignment of plagioclase laths is also observed.

Chapter 3 - Fracture system analyses of the Mount Meager area

Chen, Z.¹, Grasby, S.E.¹, Liu, X.¹

¹Geological Survey of Canada

Introduction

Two weeks of a field geological and fracture study campaign were held in the Mount Meager area in the period of July 7-19, 2019. The main objectives of the study are: 1) to improve our understanding of the fracture systems and their control on geothermal reservoirs in a volcanic belt, and 2) to search for geoscience indicators for geothermal resource 'sweet-spots' in the south Mount Meager geothermal area, and 3) determine the ability to extrapolate such indicators across the Garibaldi Volcanic Belt. The specific aim of the 2019 summer fieldwork was to assess the volcanic geothermal resource potential through field observation and data analysis with following three tasks:

- A) measuring fracture attributes, such as strike, dip direction, dip angle, spacing and density, for fracture reservoir model construction;
- B) collecting rock samples to obtain reservoir parameters (porosity, permeability and density) and rock thermal properties (such as thermal conductivity, thermal capacity and enthalpy); and
- C) collecting geological evidence and indicative features of geothermal anomalies in the Mount Meager volcanic complex.

Methods

Traditional methods for geological fieldwork were used. Field party observed, identified and recorded geological and geomorphologic features, measured attitudes (strike, dip direction, dip angle, density and spacing) of fracture/fault planes, and collected rock samples for further laboratory analysis. The identified geological and geomorphologic features and evidence of geological processes were analyzed in a relation to tectonic and volcanic activities of the region and to assess their association to reservoir development in and around each station. Fracture spacing in this study is defined as the vertical distance between two neighbouring fracture planes from the same fracture set (Fig. 1). Two major fracture sets were recognized in Figure 1 and fracture spacing was measured separately for each fracture set. Sanderson and Peacock (2019) provided details on definition and quantitative methods of spacing data analysis. In addition, a drone was employed to assist the fieldwork by taking aerial photos and searching for suitable sites for setting stations. Figure 2 is an aerial photo of a road cut cross section along the Lillooet River valley, showing a prominent fracture set with strike about parallel to the river. Outcrop photos were used to digitize fracture traces allowing calculations of occurrence, length distribution, density and spacing for construction of fractured reservoir model.

Data analysis methods included statistics of the measured fracture orientation, dip direction and angle, and estimation of fracture density and other parameters useful for geological synthesis and model development. Various graphic methods were applied to reveal geological trends, spatial variation of geological features and fractures, and correlation between geomorphologic and geological features. Laboratory physical and numerical fracture modelling results were used to guide field data interpretation (e.g., Guo, et al., 2017).

Data Collection

The selection of station was based on our work objectives and one of the following criteria: 1) exposure of crystalline basement, or new volcanic bodies allowing observation and study of the rock, and to take samples for laboratory analysis and tests; b) exposure of measurable fracture sets and fault zones; c) exposure of specific geological or geomorphologic features, or sites that help determine the nature and character of the geothermal resource in the region, such as hot spring, evidence of permeable zone and ground-water circulation, and special geomorphologic features. Figure 3 shows some examples of the special feature station.

The study area is in a rain forest climate zone, where forest and vegetation cover the most of the low lying areas, and snow and ice in higher regions, with often poorly exposed bedrock. The topography of the volcanic complex is extremely steep and glaciers cover large portion of the mountain. Figure 4 is a Google Earth map showing topographic characters of the Mount Meager volcanic complex and locations of observation stations. Most observation stations were along major logging roads and on mountain ridges, where fresh bedrock is best exposed. Access to the stations along the logging road was by moto vehicle; while to the mountain ridges, it relied on helicopter for transportation. The 2010 Mount Meager landslide has destroyed the road bridge close to the intersection of Capricorn Creek and Meager Creek. As such, a helicopter had to be used to access the observation stations in the southern Meager geothermal lease area.

We have made 55 observation stations (Table 1) and taken 25 rock specimens for analysis. Depending on the condition of bedrock exposure, we have two types of stations, single outcrop and cross section. Stations #3 and 5 are cross sections, each extent for about 120 meters, and #40, 42, 43, 44, 45, 46, each for about 58 meters. The remaining stations are single outcrops. For fracture study, more than 1207 fracture space data points were measured, 251 attitudes of fracture plane were recorded.

Results

Rock samples have been sent to relevant laboratories for different analysis and tests. Two major categories of analysis are to be conducted: a) petrology, such as type and characteristics of the rock (thin section and mineral composition); and b) petrophysical and thermal properties of the rock, such as density, permeability, porosity, thermal conductivity and heat capacity. The results will be released in a Geological Survey of Canada open file when the analysis and tests are completed. Here in this report, we present the field observation and data collection in the 2019 summer field campaign, and discuss preliminary results of data analysis with emphasis on measured fracture spacing and attitudes.

The fracture measurements (surface attitude, spacing and density) are listed numerically in Appendix 1 as a separate data file, and displayed graphically in various plots (Figs. 6, 7, 8 and 9). The dip-direction and dip-angle cross plot (Fig. 6) shows variation in fracture planes by station, depicting the pertinent trends of dip direction and angle in each site. The rose diagram (Fig. 7) displays the distribution of dip directions of the measured fractures. Fracture planes are projected on a stereo net for each station (Fig. 8) to reveal the spatial association of the fracture planes. It is noteworthy that for the same fracture set, we may have numerous fracture spacing measurements, but only one representative fracture attitude. In this case, when the data were plotted, the same representative fracture attitude was assigned for each spacing data point. This may cause visual inconsistency when comparing different figures of the same station if the number of measurements is involved in the plots.

The statistics of fracture spacing data are shown in Figs 9A and B as a histogram and cumulative distribution curve. Although varying in a large range from about 1 cm to over 200 cm, the majority of the

fracture (>85%) has a spacing less than 50 cm. Fracture spacing measurements in basement rock and volcanic cover are plotted separately in Figs. 9C and D and 9E and F. Comparison of the cumulative distribution curves (Fig. 9F) suggests that fracture spacing is slightly greater in the volcanic cover layers than that in the basement rocks in the studied outcrops.

Discussion

Multiple groups of fracture sets were observed in most bedrock outcrop stations examined. The analysis of the fracture orientation shows interesting variations. Spatially, the orientation of major fracture group(s) varies depending on the location relative to the volcanic eruption center in the margin of the Mount Meager complex. From stations along the Lillooet River in the northwest side of the complex, the fractures striking NW-SE are most common, to the southeast the most apparent fracture orientation is NE-SW, while to the south E-W striking fractures prevail (Fig. 10), although other groups with different orientations coexist. Geographically, the primary circular drainage segments define the margin of the Mount Meager volcanic complex. For example, the Lillooet River marks the northern and northeastern margin and the Meager Creek defines the margin to the south and southeast. The secondary radial drainage segments, representing by a series of creeks, starting from glaciers in the mountain highs, intersect the primary circular branches, forming a typical volcanic drainage system. Geomorphic process study suggests that physical discontinuities in the form of fractures/faults within the rock mass strongly influence bedrock weathering and erosion (e.g., Scott, et al., 2018). Numerical model shows that drainage network patterns are highly sensitive to the mechanical weakness, narrow fracture spacing, and persistent low relief, associated with fault-weakened zones (Roy, et al., 2016). Associated geomorphologic features are the NW segment of the Lillooet River and NE and EW segments of the Meager Creek for the circular fracture group; while small creeks, appearing radial around the volcanic complex, belongs to the second group.

Within the volcanic complex, the E-W striking fractures dominate in the Mount Meager peak and around Perkin's Pillar in the east, coincidence with the general trend of contacts of distinct volcanic assemblages of different ages (See Figure 2 of Reed, 1990). In the western part of the complex, the strike of prominent fracture set appears to be NS to NNW-SSE, where the observed fracture orientation is aligned well with clusters of earthquakes and mapped volcanic eruption centers (Fig. 10).

At least three types of fractures of different origins under distinct geological processes are recognized. The fracture groups related to regional tectonic deformation are consistent in character and are common in basement rocks. Their strikes are often in good spatial alignments with volcanic eruption centers and veins, and earthquake events. Fractures associated with volcanic doming and eruption activities may vary geographically. They are circular/radial segments and the strikes change spatially depending on their location relative to the eruption center. Volcanic activity may overprint tectonic fractures. The pre-existing zones of weakness can be further complicated by reactivation and modification during volcanic activity. The gravitational fracture is common in volcanic areas and commonly appears parallel to slope. This type of fracture causes instability in the mountain ridge and peak, and can lead to slides and rock avalanche.

The southern Meager Creek geothermal reservoir is a fractured crystalline basement consisting of metamorphic rocks and quartz monzonite plutons. A volcanic complex of overlapping andesite, dacite and pyroclastic piles that become progressively younger from south to north overlies on the post-Miocene erosion surface of the basement (Fairbank et al., 1981; Lewis and Souther, 1978). Previous exploration has outlined the potential high temperature geothermal resource prospective area, and subsequent production tests confirmed the presence of a permeable zone that defines the fractured reservoir, although the obtained water flow rate did not justify a commercial power plant (GeothermamEx Inc.,

2004; 2009). Nemcok, et al. (2004) in the study of the Karaha-Telaga Bodas geothermal field in the Java volcanic arc showed that fracture systems in reservoir and cap rock were formed under distinct stress regimes and developed in different stages of the volcanic activities. This study provides insights for a better understanding of the volcanic activities and their relationship with the development of the fault/fracture system in reservoir, helping better define and characterize the geothermal resource prospect with an optimized resource development strategy.

Summary and Future Work

Fractures are common in intrusive and metamorphic basement rocks and volcanic rocks that cover them in the study area. The fracture measurements (attitude, spacing and density) were plotted to depict general strike trends and mechanic relationships among the recorded groups at each station, and to reveal their spatial relationship to volcanic eruption centers, and differences in character between basement rock and volcanic cover collectively. Preliminary analysis suggest at least three types of fractures, each with distinct characters, that are likely related to different geological processes, such as regional deformation, volcanic activity, and slope stability by gravitational forces.

The field fracture observations will be used in conjunction with remotely sensed interpretation, and other newly acquired geophysical/geological data, to generate regional maps that describe spatial variation of fracture properties, such as fracture density, spacing, dip angle and direction of various groups, and to investigate their relationship with regional deformation belts, volcanic activities and hazardous gravitational deformation. The results will provide insights for fractured reservoir modeling, and improve our understanding on the geothermal anomalies in the Mount Meager volcanic complex.

In addition, this field geological campaign provides a valuable dataset for validating remote sensing interpretation. However, there are still several key data and technical gaps for identifying and confirming geothermal anomalies in the region. Future field campaigns at Meager are necessary to address the data and technical gaps, particularly for confirming geothermal anomalies zones identified from remotely sensed physical data.

Data

- 1) Raw data is provided as a separate excel spreadsheet data file for all the fracture measurements.

Acknowledgements

This is an output from Geoscience for New Energy Supply of Natural Resources Canada. Ms. Christine Deblonde of Geological Survey of Canada (Calgary) provided field GIS equipment, preparation of GIS maps for the fieldwork and the Google Earth map for this report.

Citations

Burberry, C.M., Swiatlowski, J.L., Searls, M/L., and Filina, I., 2018. Joint and Lineament Patterns across the Midcontinent Indicate Repeated Reactivation of Basement-Involved Faults, geosciences, <https://www.mdpi.com/2076-3263/8/6/215/pdf>.

Fairbank; B. D. Openshaw; R. E. Souther, J. G. and Stauder, J. J., 1981, Meager Creek geothermal project: an exploration case study, Geothermal Resources Council BULLETIN July 1981, p3-7.

GeothermamEx Inc., 2004. Report on the south meager geothermal resource British Columbia, Canada, for Western Geopower Corp. 156p.

GeothermamEx Inc., 2009. Report on the south meager geothermal resource British Columbia, Canada, for Western Geopower Corp. 20p.

Guo, L., Latham, J. P., and Xiang, J., 2017. A numerical study of fracture spacing and through-going fracture formation in layered rocks, International Journal of Solids and Structures. [Volumes 110–111](#), April 2017, Pages 44-57, <https://doi.org/10.1016/j.ijsolstr.2017.02.004>

Lewis, J.F., and Souther, J.G., 1978, Meager Mt., B.C. -Possible Geothermal Energy Resource: EMR, Earth Physics Branch, Geothermal Series No. 9, Ottawa, 17 pp.

Lewis, J.F., and Jessop, A.M., 1981, Heat Flow in the Garibaldi Volcanic Belt, a Possible Canadian Geothermal Energy Resource Area: Can. J. Earth Sei., Vol. 18, pp 366-375.

Nemcok, M., Moore, J.M., Allis, R. & McCulloch, J, 2004. Fracture development within a stratovolcano: the Karaha-Telaga Bodas geothermal field, Java volcanic arc, in Cosgrove, J. W. & Enget, DER, T. (eds) 2004. The Initiation, Propagation, and Arrest of Joints and Other Fractures. Geological Society, London, Special Publications, 231, 223-242. 0305-8719/04/\$15 ©. The Geological Society of London 2004.

Oakey, G., 1994. A structural fabric defined by topographic lineaments: Correlation with Tertiary deformation of Eilesmere and Axel Heiberg Islands, Canadian Arctic, Journal of Geophysical Research, VOL. 99, NO. B10, Pages 20, 311-20,321, OCTOBER 10, 1994.

Opheim, J. A. and Gudmundsson, A., 1998, Formation and geometry of fractures, and related volcanism, of the Krafla fissure swarm, northeast Iceland, Geological Society of America Bulletin, v. 101, p. 1608-1622, 18 figs., 1 table, December 1989.

Read, P. B. ,1990. Mount Meager Complex, Garibaldi Belt, Southwestern British Columbia. Geosciences Canada 17 (3): 167- 170

Roy, S.G., Tucker, G.E., Koons, P.O., Smith, S.M., and Upton, P., 2016. A fault runs through it: Modeling the influence of rock strength and grain-size distribution in a fault-damaged landscape, Journal of Geophysical Research: Earth Surface, 10.1002/2015JF003662.

Sanderson, D.J., Peacock, D.C.P., 2019., Line sampling of fracture swarms and corridors Journal of Structural Geology 122 (2019) 27–37.

Toprak V., and Goncuoglu, M.C., 1993. Tectonic control on the development of the Neogene-Quaternary Central Anatolian Volcanic Province, Turkey , Geological Journal, VOL. 28, 357-369 (1993).

Table 1. List of observation stations and rock samples of the 2019 fieldwork.

Station #	Type	Lat	long	Sample #	Date	On note book	Location
1	Geology	50.67893	-123.499	20190707 #1	20190707	1	Road to the Pumice mine (blocked by slide)
2	Geology +old well site	50.6405	-123.419	20190707 #2	20190707	2	Road side close to field camp
3	Geology+fract	50.65094	-123.438	20190708 #1	20190708	1	Road side-xsection
4	Geology+fract	50.66806	-123.46	20190709 #1	20190709	1	Hot Spring, Keyhole
5	Geology+fract	50.64842	-123.436		20190709	#22	Road side xsection
6	Geology+fract	50.58818	-123.47	20190711 #1	20190711	1	East Meage geothermal prospect
7	Geology+fract	50.58996	-123.464	20190711 #2	20190711	2	East Meage geothermal prospect
8	Geology+fract	50.58985	-123.463		20190711	3	East Meage geothermal prospect
9	Geology+fract	50.58847	-123.465		20190711	4	East Meage geothermal prospect
10	Geology+fract	50.604	-123.489	20190712 #1	20190712	1	E. of Devasdation Glacier
11	Geology+fract	50.6045	-123.493	20190712 #2	20190712	2	E. of Devasdation Glacier
12	Geology+fract	50.6038	-123.493		20190712	3	E. of Devasdation Glacier
13	Geology+fract	50.6298	-123.517		20190712	4	W. M Meager peak
14	Geology+fract	50.62965	-123.518	20190713 #1	20190713	1	W. M Meager peak
15	Geology+fract	50.64124	-123.493	20190713 #2	20190713	2	NE of M Meager peak
16	Geology+fract	50.64148	-123.496	20190713 #3	20190713	3	NE of M Meager peak
17	Geology+fract	50.64269	-123.487	20190713 #4	20190713	4	NE of M Meager peak
18	Geology+fract	50.64282	-123.487	20190713 #5	20190713	5	NE of M Meager peak
19	Geology+fract	50.64617	-123.554		20190713	6	NE of M Meager peak
20	Geology	50.62361	-123.487	20190714 #1	20190714	1	SE. M. Meager peak Ridge
21	Geology+fract	50.62262	-123.486	20190714 #2	20190714	2	SE. M. Meager peak Ridge
22	Geology	50.62309	-123.49		20190714	3	SE. M. Meager peak Ridge
23	Geology+fract	50.6245	-123.491		20190714	4	SE. M. Meager peak Ridge
24	Geology+fract	50.62402	-123.482		20190714	5	SE. M. Meager peak Ridge
25	Geology+fract	50.62428	-123.481		20190714	7	SE. M. Meager peak Ridge
26	Geology+fract	50.6238	-123.481		20190714	8	SE. M. Meager peak Ridge
27	Geology+fract	50.62579	-123.475		20190714	9	SE. M. Meager peak Ridge
28	Geology+fract	50.62663	-123.469		20190714	10	SE. M. Meager peak Ridge
29	Geology	50.62773	-123.47		20190714	11	SE. M. Meager peak Ridge
30	Geology+fract	50.62664	-123.467		20190714	11	SE. M. Meager peak Ridge
31	Geology+fract	50.60446	-123.494	20190715 #1	20190715	1	E. of Devasdation Glacier
32	Geology	50.60428	-123.496	20190715 #2	20190715	2	E. of Devasdation Glacier
33	Geology	50.604	-123.495		20190715	3	E. of Devasdation Glacier
34	Geology+fract	50.6045	-123.489		20190715	4	E. of Devasdation Glacier
35	Geology+fract	50.60437	-123.488		20190715	5	E. of Devasdation Glacier
36	Geology+fract	50.60434	-123.485		20190715	6	E. of Devasdation Glacier
37	Geology	50.56788	-123.515		20190715	7	MC1-2-3 well pad
38	Geology+fract	50.57021	-123.473		20190715	8	Hot Spring, Meager Creek east
39	Geology	50.57044	-123.473		20190715	9	Hot Spring, Meager Creek east
40	Geology+fract	50.57109	-123.527	20190716 #1	20190716	1	Along S Meager drilling triail
41	Geology+fract	50.5705	-123.523	20190716 #2	20190716	2	Along S Meager drilling triail
42	Geology+fract	50.57059	-123.523		20190716	3	Along S Meager drilling triail
43	Geology+fract	50.57073	-123.522		20190716	4	Along S Meager drilling triail
44	Geology+fract	50.57089	-123.522		20190716	5	Along S Meager drilling triail
45	Geology+fract	50.57132	-123.521		20190716	6	Along S Meager drilling triail
46	Geology	50.57153	-123.52		20190716	7	Along S Meager drilling triail
47	Geology	50.57495	-123.513		20190716	8	M-8 well pad
48	Geology	50.56968	-123.527		20190716	9	Along S Meager drilling triail
49	Geology	50.56975	-123.527		20190716	10	Along S Meager drilling triail
50	Geology+fract	50.66907	-123.454	20190717 #1	20190717	1	Road site bedrock outcrop
51	Geology	50.66301	-123.444	20190717 #2	20190717	2	Road side Pumice exposure
52	Geology	50.64228	-123.554	20190718 #1	20190718	1	N of Mount Job peak
53	Geology+fract	50.64195	-123.553	20190718 #2	20190718	2	N of Mount Job peak
54	Geology	50.68149	-123.513	0190718 #3, #	20190718	3	Pumice mine site
55	Geology	50.67759	-123.475	20190707#1	20190718	4	Keyhole Bridge

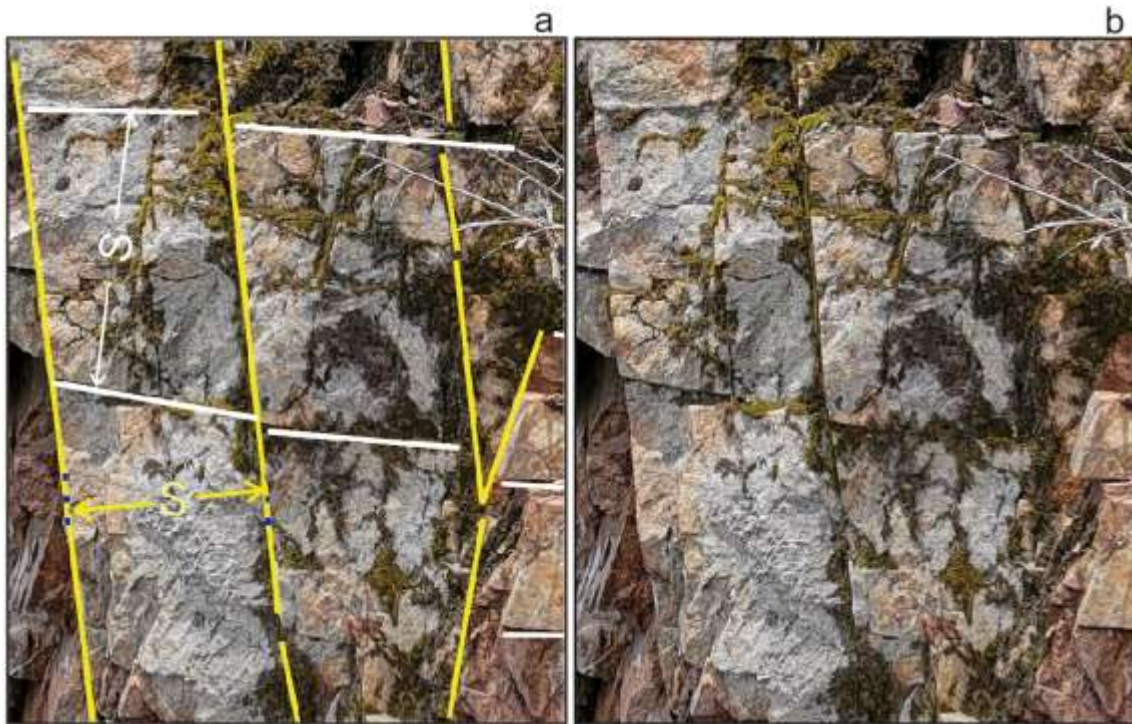


Figure 1. Definition of fracture spacing that measure the vertical distance between two neighbouring fractures of the same fracture set. Left (a): two major fracture sets are recognized and each has its own spacing measures. Right (b): original photo. Photo taken at St. # 5.



Figure 2. A drone photograph showing a bird's-eye view of the roadside cross-section station #3 along the Lillooet River (see location in Figure 3) as well as fracture pattern in the Cretaceous rock complex.



Figure 3. Example feature observation stations: A) the full diamond production test well site (CM-1 well, st. # 37), B) Keyhole hot spring (st. # 4), C) Pumice mine (St.# 54), D) water leaking from permeable intervals between two volcanic layers (photo taken from st. #); E) contact boundaries between volcanic layers (photo from st. #), and F) Keyhole fall cliff consisting of welded breccia of competent portion of the volcanic pile (from st. # 55).

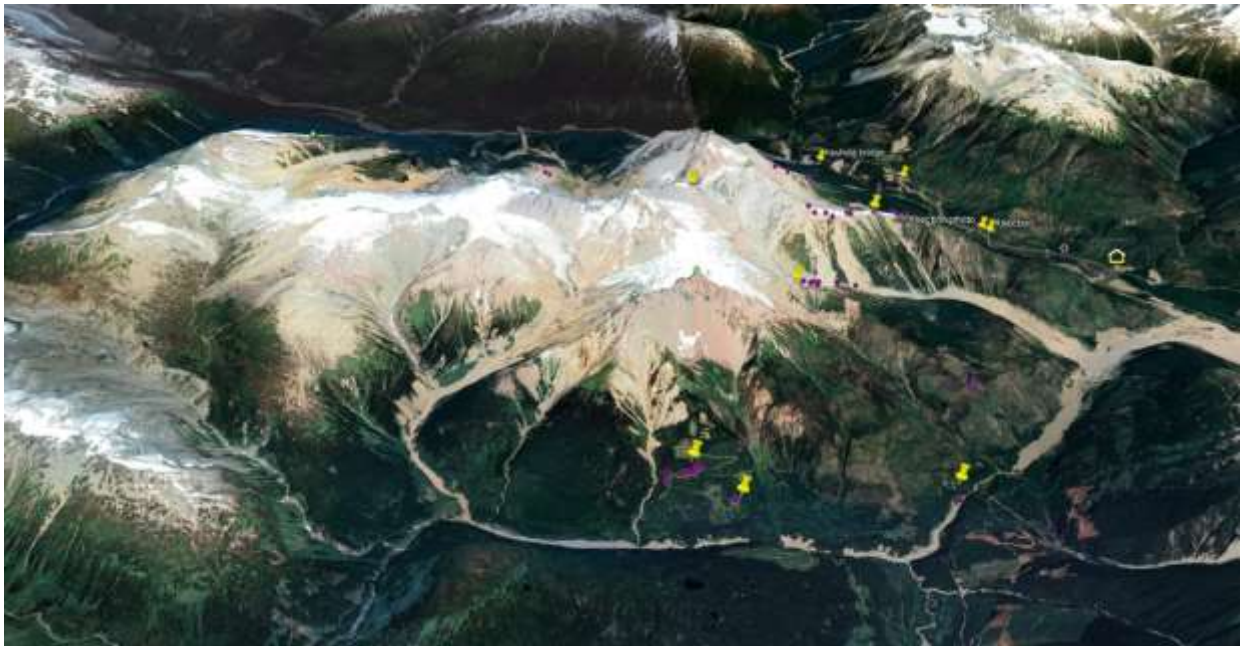


Figure 4 Google Earth view of the study area and locations of observation station (magenta) in the 2019 summer GSC Mount Meager fieldwork. Yellow marker indicates location of photo cross section that will be discussed in the next section.

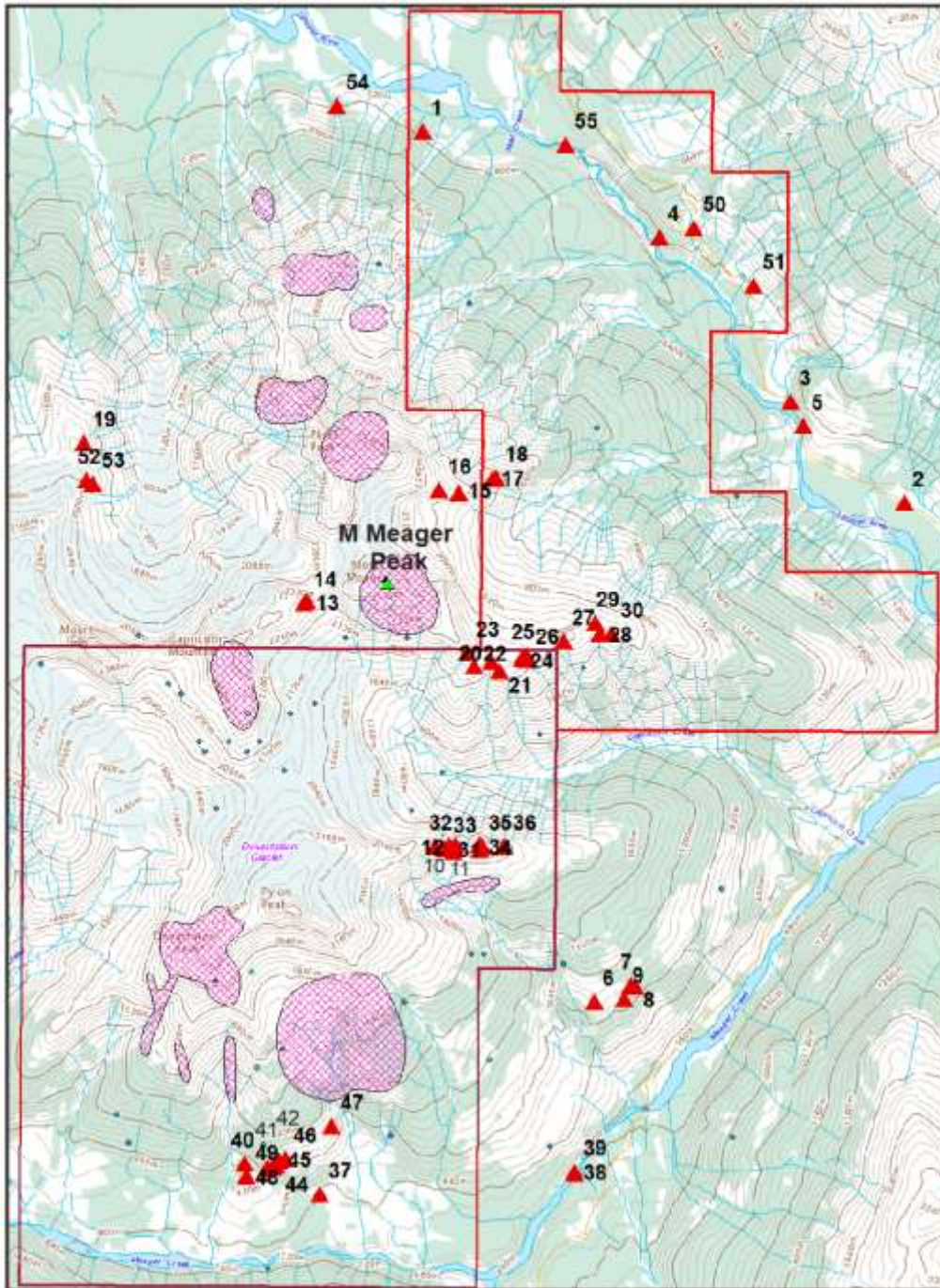


Figure 5. Map showing the locations of the observation station in this study, and regional geological elements and topographic features of the Mount Meager area. (Source of the extent of volcanic complex: GeothermamEx Inc., 2004). Red polygons are geothermal energy resource lease blocks and blue dot indicates earthquake event.

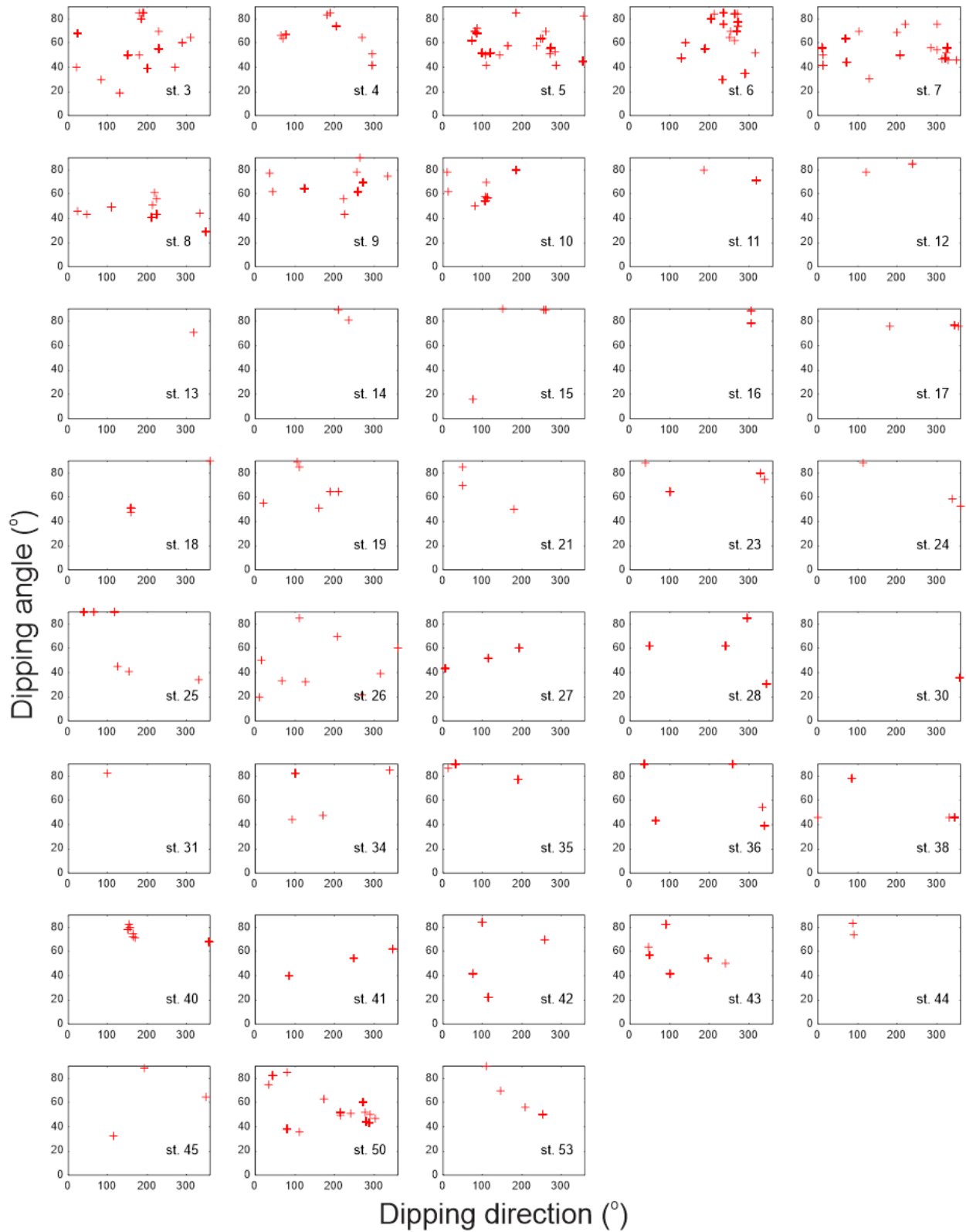


Figure 6. Plots showing the variation of observed fracture dipping direction and angles in various stations. St. in the lower-right is the station number.

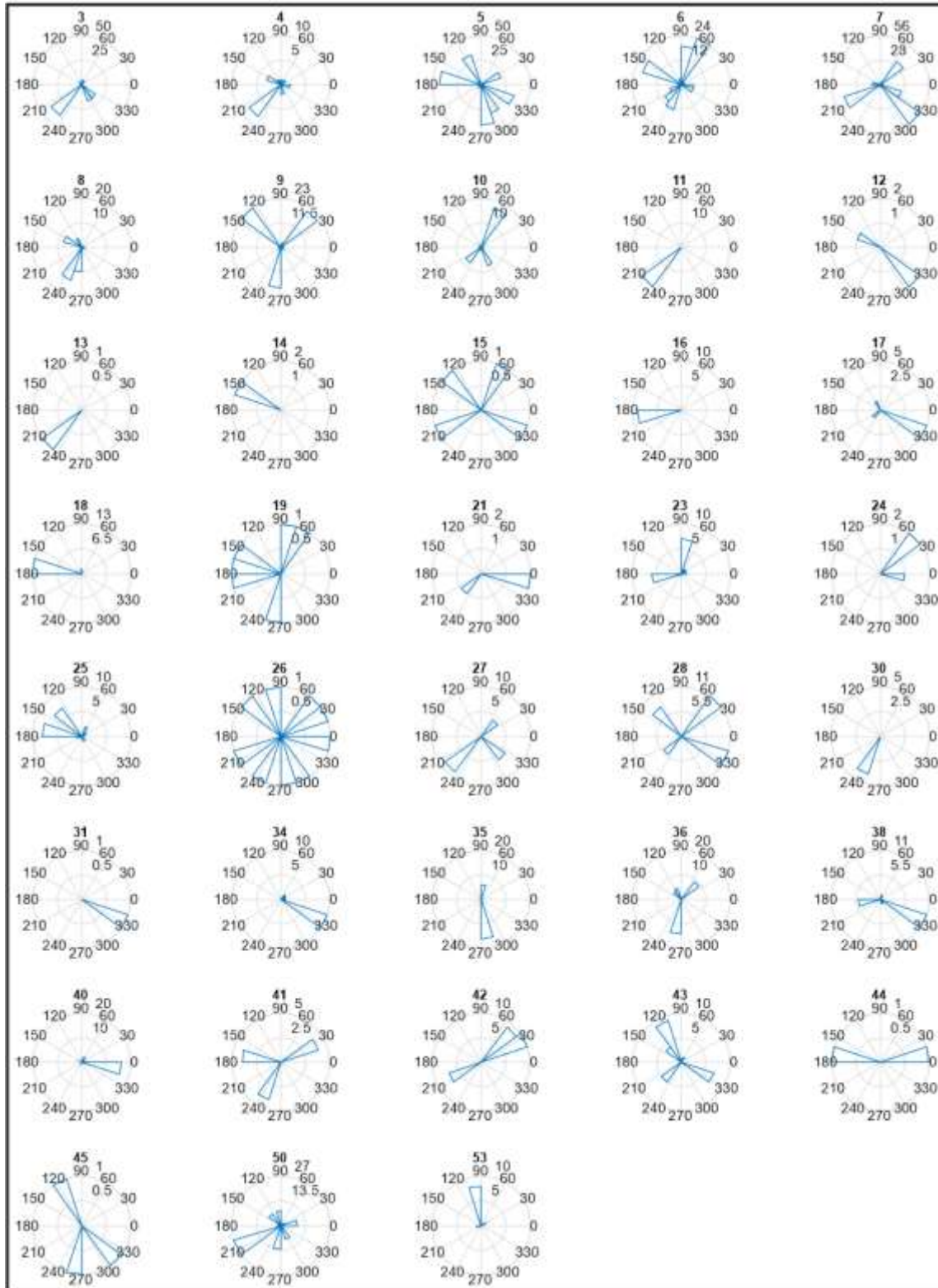


Figure 7. Rose diagrams showing the dip directions of the measured fracture sets in all stations with measurements. Please note that the plots were made directly using Matlab function rose.m, which are not comparable with geographic north with an anticlockwise angular axis.

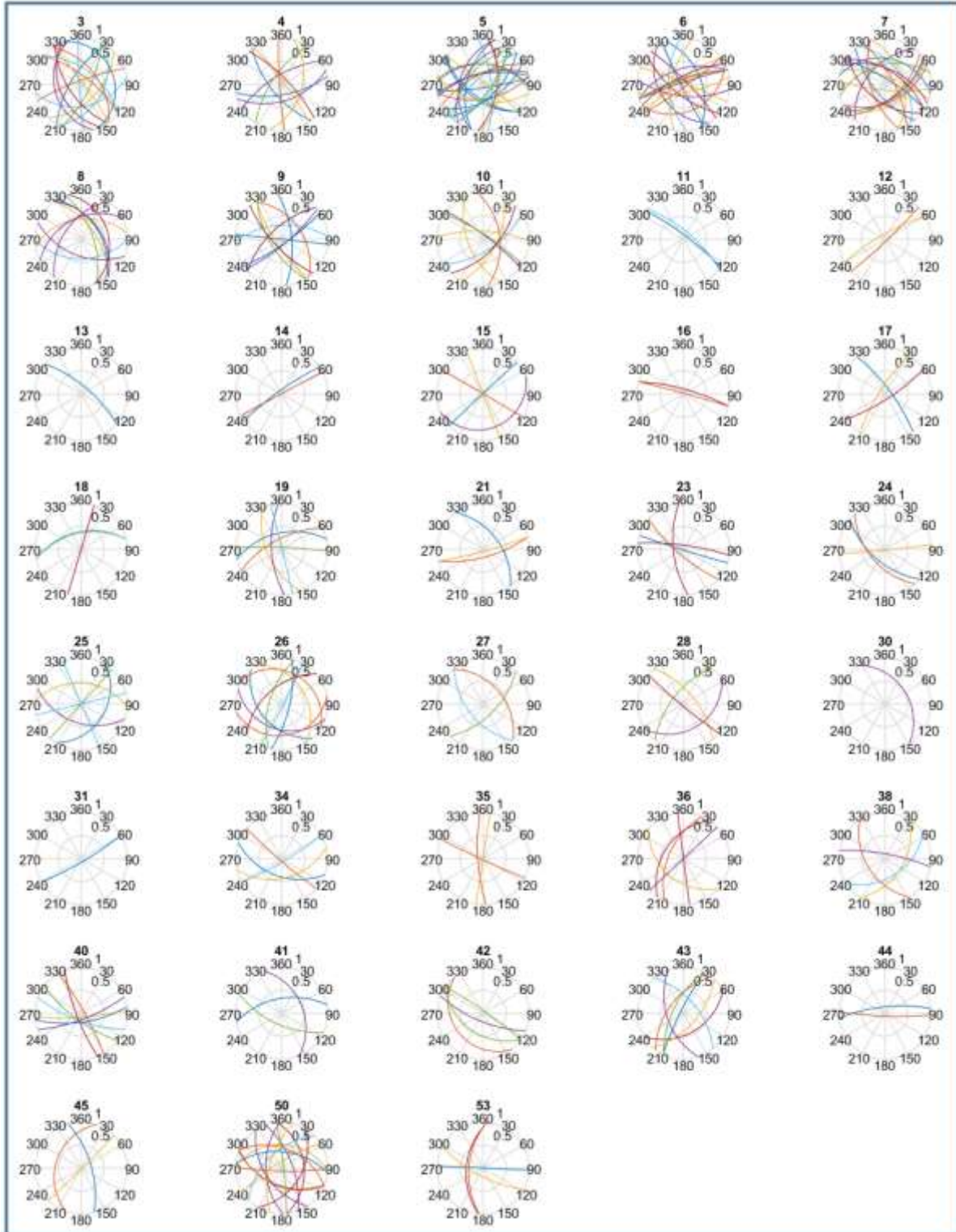


Figure 8. Fracture plane stereo nets for all stations with fracture measurements, showing occurrence and spatial relationship amount the fracture set in each station.

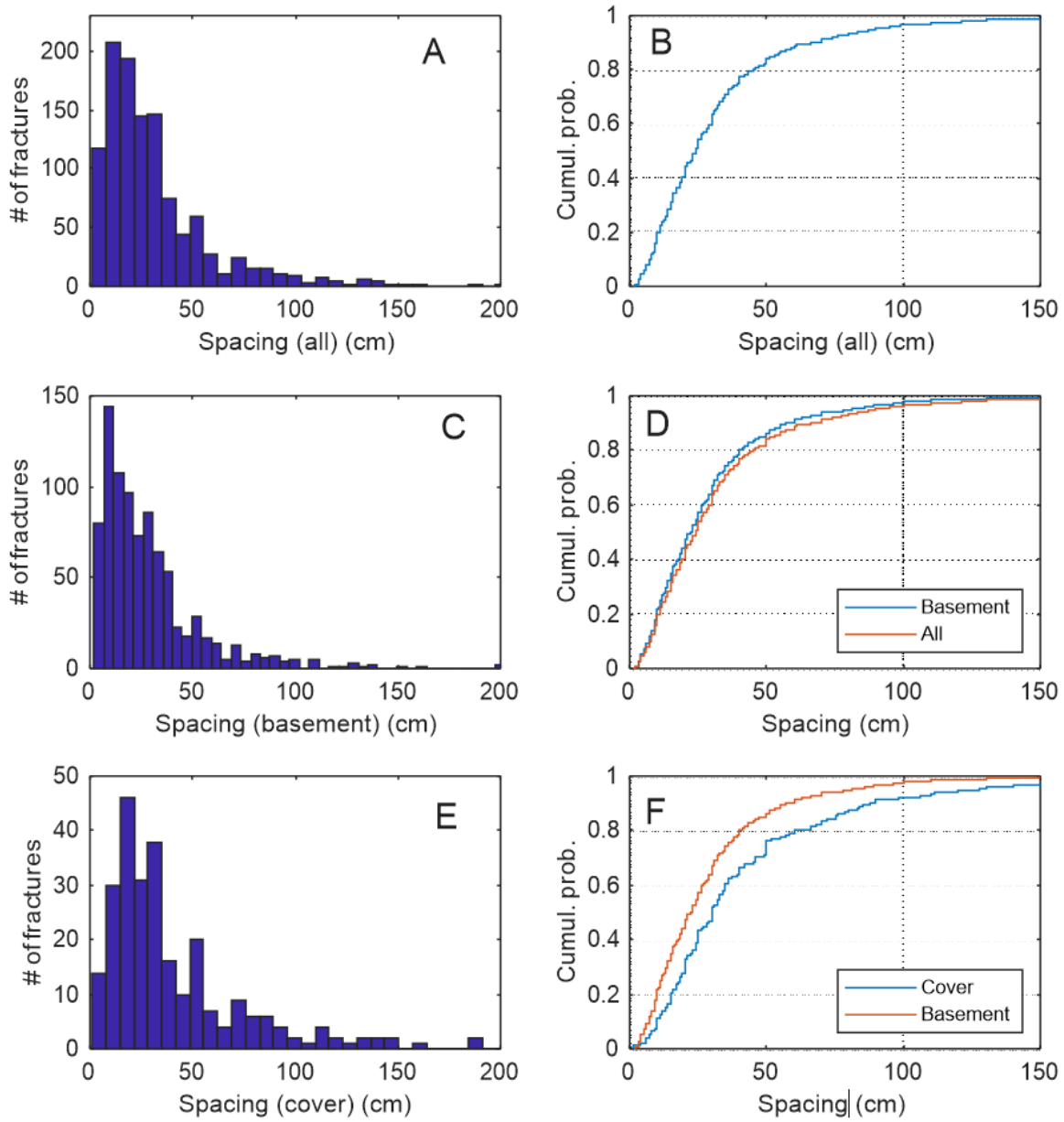


Figure 9. A) histogram of single fracture spacing of all measured fracture group; B) cumulative distribution of all measured single fracture spacing, from which 85% fracture measure have spacing <50 cm; C) histogram of single fracture spacing measured in basement rock; D) cumulative distribution of measured fracture spacing in basement rock; E) histogram of fracture spacing measured in volcanic cover; F) cumulative distribution of measured fracture spacing in volcanic cover.

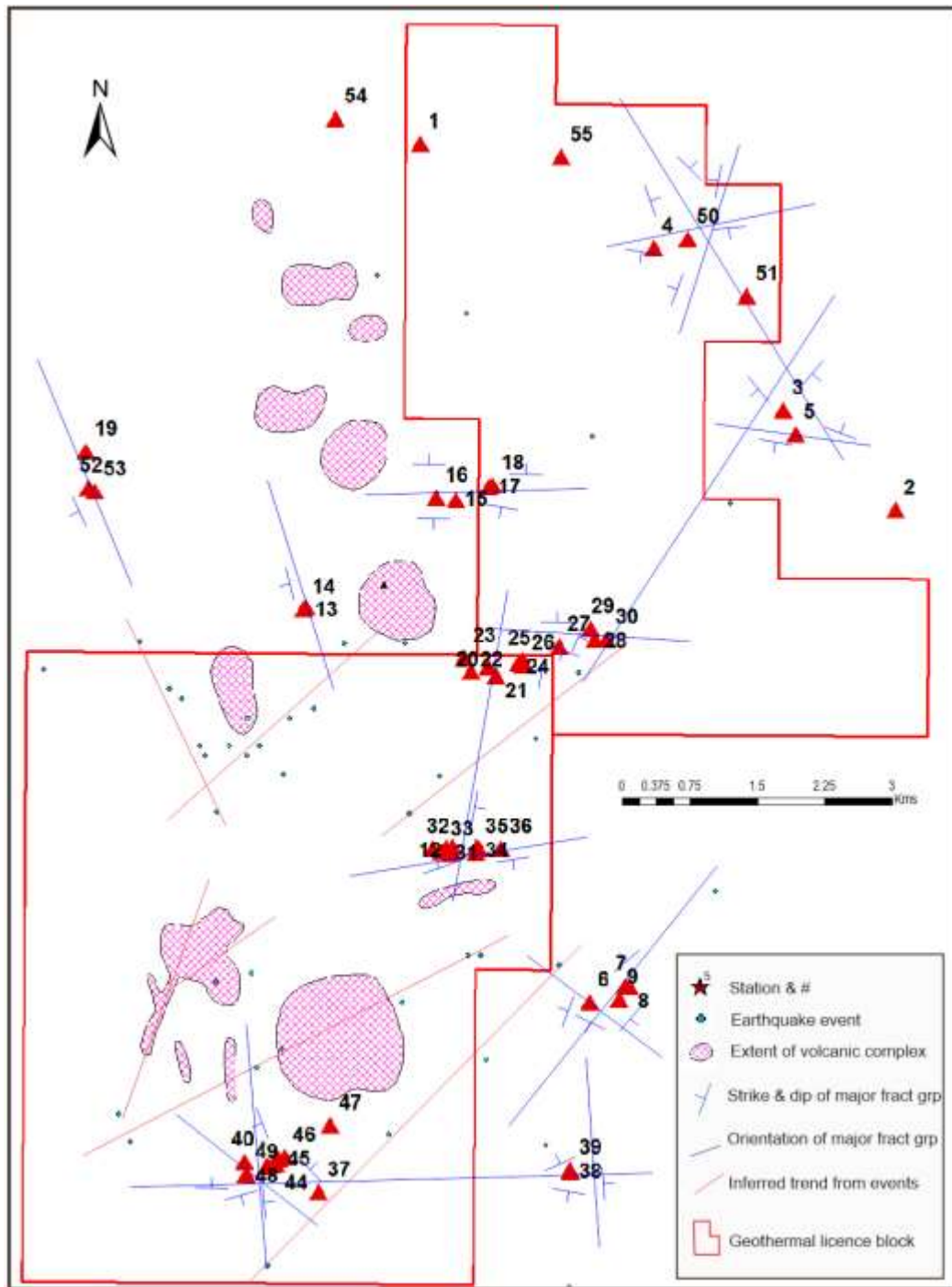


Figure 10. Summary map showing orientation and dip of major fracture groups in the Mount Meager area based on 2019 GSC field observation. The extent of volcanic complex is from GeothermamEx Inc. (2004).

Chapter 4 - Gravity Mapping of the Mount Meager Volcanic Complex: Preliminary Results

Calahorrano-Di Patre, A.E.¹; Williams-Jones, G.¹

¹Physical Volcanology Group, Centre for Natural Hazards Research, Department of Earth Sciences, Simon Fraser University, Burnaby, B.C., Canada

Introduction

In order to investigate the extent of natural resources, and the hazards related to their extraction, it is vital to image the geological subsurface structures of an area. In the case of the Mount Meager Volcanic Complex (MMVC), in which a rich geothermal resource is present in a landslide-prone dormant volcanic complex, it is critical to employ diverse methods (e.g., geophysical and geological) to identify the area's structures, the size and shape of the resource, and the nature of the deposits surrounding it.

Spatial gravity measurements, used in conjunction with other geophysical methods, give valuable insights on subsurface geological structures by detecting mass and density changes underlying the surveyed area (e.g., Miller et al. 2017; Van Camp et al. 2017; Milano et al. 2019). Although other geophysical techniques can also identify subsurface structures, gravity mapping is the only one that discerns variations in subsurface density. Gravity anomalies -differences between the observed gravity at a specific point and the value predicted by a model of the Earth's gravity field- are often represented in Bouguer Gravity maps, which are commonly used in exploration geophysics (e.g., the oil and gas industry (Eckhardt, 1940), geothermal exploration (Atef et al., 2016)) and hazard assessment (e.g., investigating the internal structure of Kilauea volcano (Zurek et al., 2015), evaluating risk zones on karstic terrain (Putiska et al., 2014), or contributing to seismic microzonation maps (Barnaba et al., 2010)).

Bouguer gravity maps are obtained by removing the effect on gravity measurements from elevation change, terrain corrections, and regional density (Lowrie, 2007; Wilcox, 1989). Free-air corrections that consider differences in elevation between stations must be applied to the data, since gravity decreases as the distance of the point from the centre of the Earth increases. Terrain corrections applied to gravity measurements aim to remove the effect from local topography (e.g., a local decrease in gravity due to the proximity of a peak). Finally, removing regional density trends aids in detecting and carefully interpreting the local gravity anomalies. The Bouguer map, therefore, shows relative high-density zones as a positive anomaly, and low-density zones with a negative anomaly. Further analysis of these anomalies (e.g., trend reduction, Fourier filtering, and inverse modelling) allows for determination of the depth, location, and general shape of the source of the detected anomaly (Lowrie, 2007).

The gravity survey at the Mount Meager Volcanic Complex aimed to compile evidence that could complement the results from other geophysical techniques employed in the area. The focus of the survey was, therefore, not only to compile information about specific areas of interest, but also to investigate the overarching structure of the massif and surrounding area, as well as help constrain its tectonic controls. In order to achieve this ambitious goal, specific methodologies and survey specifications were used, as well as diverse processing software and techniques. The results presented here are thus preliminary and will be further refined in the future.

Methods

Relative vs. Absolute Gravity Measurements

Gravity measurements were collected during July and August 2019 at the Mount Meager Volcanic Complex with a LaCoste & Romberg relative gravity meter (G-127). A reference station, to which all other measurements are compared, was established at the Innergex base camp (Lat: 50.63556755°, Long: -123.4055742°). Relative gravity measurements, in comparison with absolute measurements (where the true value of Earth's gravity is measured at a specific point), need to be further corrected for time dependent effects (i.e., daily drift, tide effects, and tares). Moreover, the reference station should be tied to an absolute station of the Canadian Gravity Standardization Network (CGSN): the closest station to our Innergex base station is the North Vancouver absolute station (#9929-2008, N49°21'6", W123°14'57"). In order to properly reference the measurements to the base station, daily loops consisting of repetitions of survey and base station measurements must be performed, taking particular care to repeat the base (reference) station measurement at least at the beginning and end of every daily measurement loop. Given the distance between the North Vancouver absolute station and the Innergex reference station, in order to establish a tie to an absolute gravity station it is necessary to create other intermediate reference stations between Vancouver and Mount Meager. These stations should be located away from gravity noise sources (e.g., roads and rivers, where ground vibrations can affect the measurements), and the locations should not be easily moved or prone to change in the following years. Considering these requirements, two reference stations will be established in the following months: one near the Pemberton well house and one near the RCMP/Squamish EOC.

In order to determine the absolute gravity value of the base station at Mount Meager, two daily loops will be established: one between Mount Meager, Pemberton, and Squamish (consisting of measurements at Squamish-Pemberton-Mount Meager Base-Pemberton-Squamish) and one between Squamish and North Vancouver (consisting of measurements at the absolute gravity station of North Vancouver-Squamish-North Vancouver). These loops will relay the value of the relative gravity between the Squamish and Pemberton stations, the Vancouver absolute station, and the Mount Meager base gravity station. The absolute gravity value at the Mount Meager base station can thus be determined by a simple sum or subtraction of its relative gravity difference from the absolute gravity station at North Vancouver, and by the same method, the absolute gravity value can also be determined for the relative stations measured around the Mount Meager Volcanic Complex.

Time dependent corrections

The collected relative gravity data was corrected using the suite of programs GTOOLS (Battaglia et al., 2012). GTOOLS is an open source interactive suite of modular computer programs developed in Matlab, which allow for consistent processing of gravity data collected by Scintrex CG-5 and LaCoste & Romberg gravity meters. GTOOLS reads the gravity data, computes and corrects the Earth tide effect on measurements, computes and corrects the effect from ocean tides, calculates the linear instrumental drift, and computes the weighted least-square adjusted gravity values as well as the accumulated errors on the data.

- **Earth Tide Correction:** Due to the gravitational pull of the Sun and the Moon, the solid body of the Earth is deformed with a certain periodicity, changing the distribution of its mass and modifying the gravitational potential of the Earth. These body Earth-tides (also called load-tides) can be calculated for any point of the Earth's surface using Longman's formulas for computing the Tidal accelerations due to the Moon and the Sun (Longman, 1959). Longman's model is used by GTOOLS to correct this effect from gravity measurements.

- **Ocean Tide Corrections:** Another consequence of the gravitational attraction of the Sun and Moon, in combination with the Earth-tides, is the formation of tides in the oceans and other marine bodies. The movement of large masses of water can be detected by precise gravity meters, however, these effects are small (less than the average measurement error of 20 μGal) and the correction can be omitted for the present case.
- **Daily Instrumental Drift:** Gravity meters such as the LaCoste & Romberg are subjected to instrumental drift caused by the intrinsic elastic properties of the gravimeter's zero-length spring (Lowrie, 2007; Seigel, 1995). The spring creeps slowly over time; however, this effect is linear and can be corrected by assuming the gravity at certain stations (e.g., the base station) is stable throughout the day, and then applying a linear regression to one loop of gravity data. GTOOLS calculates the instrumental drift by considering all station's repetitions during the day, applies a linear regression, and relays as a final result the weighted least-square gravity values as a gravity difference between the gravity's survey stations and the base/reference station.

An example of GTOOLS corrections on gravity measurements from one daily loop can be seen in Figures 1 to 4. In Figure 1, data from a daily loop is read and stored by station name. Raw gravity measurements are then plotted station by station (In Figure 2, station G001 is shown) in time. GTOOLS then removes any outliers if necessary (data that deviates from the mean by more than 2σ), and presents the plotted filtered data (Fig. 3). After calculating the tide correction for each station, the daily drift is calculated (Fig. 4) and the weighted least-square gravity values are computed.

Spatial Corrections and Gravity anomalies

Once all the temporal dependent corrections have been applied to the data, in order to analyze only the relevant information captured by the gravity measurements, it is necessary to remove the influence of spatial and topological features of the environment. This includes free-air corrections and latitude corrections, as well as Bouguer slab and Terrain corrections. In short, the aim is to remove any gravitational effect that could mask gravity anomalies that relay information about variations in the subsurface density. In order to obtain these anomalies, the open-source program GSOLVE was used. GSOLVE is a Python GUI program, created to calculate gravity anomalies from relative gravity measurements (McCubbin et al., 2018), with different modules that compute sequentially the spatial corrections.

- **Free-air effect:** The free air effect is simply the gravitational change caused by a difference in elevation between stations. It is commonly modelled by the linear formula of change $-0.3086H$ mGal m^{-1} , where H is the station elevation in comparison with the reference. The approximation of gravity change for a 1 m increase in elevation (-0.3086 mGal m^{-1}) is also called the free air gravity gradient. Although it is possible to derive a second order free-air correction (Hackney and Featherstone, 2003), or to measure a more station accurate free-air gravity gradient, for a Bouguer type of survey where a larger uncertainty (in comparison with microgravity surveys) is permitted, the linear formula of change will be used.
- **Latitude correction:** Due to the shape of the Earth, the gravitational attraction is stronger at the poles and weaker at the equator. Even in a relatively reduced area, a change in latitude between stations carries inevitably an intrinsic change in the gravitational attraction due to the eccentricity of the Earth. In order to correct for this effect, the normal gravity (or latitude correction) can be computed using the Somigliana-Pizzetti formula (Moritz, 1980). The Somigliana-Pizzetti formula is used by GSOLVE to calculate the magnitude of normal gravity on the surface of a reference ellipsoid (either GRS80 or GRS67). For these preliminary results, the reference ellipsoid used is GRS80. The ellipsoidal gravity is calculated as

$$\gamma(\varphi) = \gamma_a \frac{1 + k \sin^2(\varphi)}{\sqrt{1 - e^2 \sin^2(\varphi)}}$$

Where φ is the ellipsoidal latitude of the station, γ_a is the normal gravitational acceleration at the equator (978032.67715 (mGal) for GRS80), k is the normal gravity constant (0.001931851353 for GRS80), and e^2 is the square of the first numerical eccentricity of the ellipsoid (0.00669438002290 for GRS80).

- **Bouguer slab correction:** The Bouguer slab correction, or simple Bouguer correction (Bullard A correction), is a model that attempts to remove the gravitational attraction of topographic masses around the measuring site by considering the mass between two stations at different elevations as an infinite plate of constant density. It must be applied in conjunction to the free-air correction to obtain the simple Bouguer gravity anomaly. The Bouguer slab correction in mGal is given by $\delta g_{bs} = -0.0419\rho H$, where H is the observation height (the elevation of the station), and ρ is the rock density in g/cm^3 . The typical value of 2.67 g/cm^3 will be used for the preliminary results, but the rock density will be refined in the future using density data from field samples collected by the geological mapping teams.
- **Terrain Correction:** The terrain (or Bullard C) correction is used to correct other gravitational effects from topography that might have been missed by the simple model of the Bouguer slab (the most obvious examples are hills and valleys adjacent to the survey stations). GSOLVE calculates the terrain correction from a digital elevation model (DEM) by using the Nagy prism formula (Nagy, 1966). GSOLVE allows for calculations of terrain corrections inside a selected range annulus (with a minimum and maximum radius) around several points, therefore giving the option of using different resolution DEMs for near terrain corrections and far terrain corrections. In this case, near terrain corrections (500 m around the stations) are performed using a 1 m resolution DEM (derived from LIDAR), and far terrain corrections (using distances from 500 m to 15 km) are performed with a 30 m resolution DEM. However, there are a number of measured gravity stations that are not included in the LiDAR DEM extension, or that they are located too close to its perimeter. For these stations either a gross correction using the 30 m resolution DEM was applied, or the LiDAR DEM was used for a short terrain (50 m correction) around the station, and from 50 m to 15 km, the larger resolution DEM was used. Different densities, resolutions, and ranges will be experimented and analyzed in the future.

Data Collection

A total of 81 survey gravity stations, aside from the Innergex base station, were measured around the Mount Meager Volcanic Complex during July and August 2019. The survey grid was established considering the desired resolution of the results and, therefore, the size characteristics and presumed approximate depth of the features to image with the gravity data. Shallower and smaller structures like the hydrothermal system, in order to appear in the measured gravity signal, need to be surveyed with a tighter network, while deeper and larger structures can be measured from farther away and by a network comprised of more widely spaced stations. With these considerations in mind, and within the limitations of the topography, distance, and travel time between stations, stations at Meager were located near points of interest (such as the South Meager geothermal area and the ridges below Pylon Peak and Mt Meager) with an average distance between each other of 250 to 500 m, and at an average one to two km distance between stations for points farther away from the edifice (or from points located at sharp topographic features such as the ridge below Capricorn Mountain). The stations were reached mainly via helicopter, except for the ones located along the North Lillooett Forest Service road. This also defined an

additional constraint for the stations: in order to not unreasonably extend travel times, stations were generally close to the measurement sites of other geophysical methods (MT, AMT, and seismic stations). The resulting network is shown in Figure 5.

The Meager network was measured by repeating the base station at Innergex (BASE) at the beginning and the end of the day, and stations were sequentially measured in between these two BASE measurements. In order to acquire higher precision measurements, and to ensure that the measurements reflect reality and tares are averted, a protocol of measurement stabilization was implemented: in each station, measurements were recorded when a difference of less than 10 μGal between 5 consecutive measurements was achieved. Likewise, some stations were measured in different loops to check for repeatability, and in order to avert and detect high drifts in the data, days where more than 5 hours would be spent between the beginning and end of the day had an extra repeated BASE measurement between measurements of survey stations. Repeatability of measurements was achieved within 25 to 30 μGal , and the difference in measurements of the base station within a day generally did not surpass a difference of 40 to 50 μGal . Notable exceptions were two long days with a difference of 100 μGal and 150 μGal , which are still within an acceptable measurement error for a Bouguer gravity survey.

GPS measurements at each station were obtained with a Juniper Geode sub-meter GNSS receiver. The Geode is a novel hand-held GNSS, which uses a SBAS correction signal to achieve a 30 cm horizontal accuracy (Juniper Systems, 2019). The Geode has a receiver type GNSS single frequency with carrier phase tracking, 162 channels, and 3 channel SBAS parallel tracking. The data collected is in NMEA 0183, crescent binary format. In order to improve its line of sight, the Geode was mounted on a one-meter vertical pole beside the gravity meter (except in chosen stations where the usage of the pole was not possible or unnecessary). GNSS measurements were collected at a frequency of 1 Hz and stored for the totality of the gravity reading. The measurements were then post-processed to remove outliers in the data, and the average for each station was used and combined with LiDAR data to achieve the best height accuracy for each station.

Results

A summary of raw gravity measurements alongside the corrections is shown in Tables 1 and 2 in the supplementary materials. Due to weather and logistical constraints, the absolute gravity for the base station is still not currently available (and thus, the “absolute gravity” values presented are actually the relative gravity difference between the BASE station and the survey stations measurements). However, as we are analyzing anomalies, the final result will not be affected as it will be presented relative to the BASE station value (normalized to zero).

Relative gravity measurements, corrected for temporal effects but not for spatial effects, are shown in Figure 7. It is clear that in this form, the free air effect dominates the measured gravity differences. The free air effect can be visualized in Figure 8, while the ellipsoidal gravity (or latitude correction) is plotted in Figure 9. The combined Free Air Anomaly (the ellipsoidal and free air effect) is shown in Figure 10. The Terrain Corrections and complete Bouguer anomaly corrections can be seen in Figures 11 and 12 respectively. Finally, the corrected gravity data is presented in Figure 13. This is the preliminary Bouguer anomaly map, taking into account that the Terrain correction will be improved in the following iterations.

The plots presented in Figures 7 to 12 have been generated by linearly interpolating discrete gravity measurements or corrections at each survey station. Therefore, some artifacts due to the interpolation are bound to appear in areas with low density of points (e.g., the area within the Lillooet Provincial Park, which was not surveyed because of permit limitations). These artifacts can be eliminated by either improving the coverage of the network, or by analyzing data points independently while still referring them to their base station. This; however, is a convenient way to visualize the preliminary results. The

specific gravity corrected values for each station can be individually assessed in Table 3, Table 4, and Table 5 of this report.

Figure 13 presents only a very preliminary view of the gravity anomalies at Mount Meager and the surrounding areas. However, some initial observations can be made from a precursory assessment of this preliminary Bouguer anomaly map:

1. A low gravity region was identified in the South Meager Area, which could indicate a low density region consistent with previous observations of a geothermal source.
2. Another interesting region where negative anomalies were observed is on the northern flank of Mount Meager. Due to the rugged topography, not many stations were surveyed in the general region. However, if these preliminary results are confirmed, it would be an interesting zone to explore in possible future surveys.
3. A number of very strong positive anomalies are visible in the southern extent of the surveyed area. Although these measurements must be re-processed to confirm the certainty of the terrain correction, the high-density area would be consistent with the presence of basement rocks and quartz veins (observed during the survey). These points could serve in the future as constraints for the inversion models, and for interpreting the results.

Summary and Future Work

Gravity measurements were performed at 81 survey stations and one reference station located in the Mount Meager Volcanic Complex and surrounding areas. The network of stations was designed to enable detection of both shallow and deep subsurface mass variations, and thus consists of closely spaced stations near points of interest (e.g., the South Mount Meager geothermal project area) and more widely spaced stations with increasing distance from the summit of Mount Meager. Measurements were collected with a relative LaCoste & Romberg gravity meter and corrected for temporal effects - such as tide and drift - with the suite of programs GTOOLS. Spatial corrections were performed using the Python-based program GSOLVE, which not only performs the simple Bouguer corrections (free air, latitude, and Bouguer slab correction), but also calculates Terrain corrections based on selected DEMs. The resulting preliminary Bouguer anomaly map presented here shows a region of relatively low gravity around the area of the South Mount Meager geothermal project, as well as a stronger anomaly (-44.45 mGal) on the northern flank below Plinth Peak. A positive gravity anomaly (maximum 136.04 mGal) was also detected on the mountains south Mount Meager. These results will be further explored and more detailed corrections will be applied in order to clearly visualize any relevant anomalies: this includes varying the density of the bouguer slab and terrain corrections taking into account collected samples from site, as well as varying the reach of terrain corrections with different resolution DEMs.

After these corrections have been refined, the results will be inverse modelled to properly identify the possible causes of gravity anomalies. These models will be informed by results from other geophysical methods surveyed alongside the gravity measurements. The results will be finally modelled and integrated with the software Leapfrog Geothermal, in order to present a result easy to visualize and to manipulate.

Data

Table 1. Gravity differences between reference and survey stations collected during the Summer 2019 survey at the MVC, corrected for temporal effects. The "absolute gravity" values refer to the relative gravity differences between survey stations and reference station BASE.

Name	Absolute Gravity	Standard Error	Number of Observations	Latitude	Longitude	Elevation
BASE	0	0.007	32	50.63557	-123.406	473.662
G001	-66.969	0.011	1	50.68509	-123.478	722.2353
G002	15.26	0.01	1	50.62249	-123.4	409.5758
G003	-0.711	0.011	1	50.63869	-123.414	456.5915
G004	-6.25	0.011	1	50.6436	-123.43	447.3578
G005	-17.649	0.011	1	50.65093	-123.438	464.246
G006	-33.536	0.011	1	50.66036	-123.446	532.2078
G007	-160.472	0.01	1	50.57771	-123.52	1365.233
G008	-151.968	0.01	1	50.5766	-123.521	1320.087
G009	-147.506	0.01	1	50.57607	-123.52	1297.27
G010	-59.919	0.011	1	50.68349	-123.492	671.7593
G011	-366.509	0.011	1	50.62411	-123.54	2332.443
G012	-239.339	0.01	1	50.58383	-123.537	1756.376
G013	-203.396	0.01	1	50.51427	-123.436	1718.323
G014	24.107	0.011	1	50.57851	-123.293	328.3443
G015	-112.584	0.011	1	50.57496	-123.513	1102.603
G016	-103.572	0.01	1	50.573	-123.515	1061.711
G017	-87.037	0.01	1	50.57136	-123.527	971.236
G018	-75.78	0.01	1	50.56827	-123.527	919.0518
G019	-67.786	0.011	1	50.56599	-123.526	875.0318
G020	-303.538	0.011	1	50.62384	-123.487	2085.292
G021	-294.202	0.011	1	50.62415	-123.481	2036.736
G022	-289.062	0.01	1	50.62522	-123.477	2007.659
G023	16.891	0.011	1	50.59281	-123.354	358.3093
G024	-251.242	0.011	1	50.60403	-123.484	1820.425
G025	-258.998	0.01	1	50.60382	-123.49	1862.84
G026	-266.479	0.01	1	50.6041	-123.494	1892.158
G027	-307.29	0.01	1	50.60369	-123.505	2076.252
G028	-305.396	0.01	1	50.60353	-123.502	2059.672
G029	-223.516	0.011	1	50.60081	-123.482	1702.723
G030	-216.97	0.011	1	50.60144	-123.478	1669.982
G031	-193.7	0.011	1	50.54742	-123.558	1596.699
G032	-93.073	0.011	1	50.57117	-123.519	1008.116
G033	-87.089	0.01	1	50.57137	-123.514	968.4273
G034	-80.657	0.01	1	50.57223	-123.511	930.2308
G035	-54.174	0.011	1	50.56807	-123.514	788.5718
G036	-172.637	0.011	1	50.60027	-123.671	1630.33
G037	-157.222	0.011	1	50.58003	-123.62	1476.15
G038	-58.801	0.01	1	50.73261	-123.707	804.266
G039	-148.971	0.01	1	50.73546	-123.471	1200.008
G040	-81.863	0.01	1	50.68141	-123.513	785.5313
G041	-58.317	0.011	1	50.56726	-123.518	809.7928
G042	-51.568	0.011	1	50.56582	-123.513	773.5608
G043	-149.865	0.011	1	50.58455	-123.491	1336.328
G044	-131.304	0.01	1	50.58049	-123.491	1239.381
G045	-116.811	0.01	1	50.57916	-123.488	1163.521
G046	-3.97	0.01	1	50.57616	-123.488	1093.649

G047	-340.767	0.011	1	50.63137	-123.515	2232.769
G048	-329.955	0.011	1	50.64436	-123.526	2156.431
G049	-257.836	0.011	1	50.638	-123.535	1830.544
G050	-277.143	0.011	1	50.73388	-123.578	1962.811
G051	-349.477	0.01	1	50.61807	-123.572	2330.456
G052	-287.997	0.01	1	50.64209	-123.554	1984.067
G053	-65.419	0.01	1	50.68523	-123.528	725.022
G054	-215.493	0.01	1	50.66009	-123.51	1553.296
G055	-156.085	0.01	1	50.6494	-123.477	1270.867
G056	-179.5	0.01	1	50.63887	-123.477	1451.149
G057	14.505	0.01	1	50.61428	-123.383	391.575
G058	14.731	0.01	1	50.60365	-123.372	387.2448
G059	-281.401	0.011	1	50.63764	-123.528	1944.754
G060	-47.809	0.011	1	50.561	-123.536	747.5735
G061	-35.991	0.01	1	50.56173	-123.505	672.533
G062	-26.844	0.01	1	50.5593	-123.489	640.712
G063	-20.548	0.01	1	50.56869	-123.475	601.5966
G064	-59.677	0.011	1	50.66873	-123.452	685.846
G065	-91.584	0.011	1	50.67572	-123.464	863.0023
G066	-217.065	0.011	1	50.48557	-123.498	1791.487
G067	-312.696	0.009	2	50.56184	-123.417	2216.87
G068	-261.559	0.01	1	50.59461	-123.501	1872.504
G069	-244.863	0.01	1	50.59485	-123.497	1793.741
G070	-228.81	0.011	1	50.59433	-123.494	1719.044
G071	-238.778	0.01	1	50.69609	-123.354	1823.061
G072	-6.209	0.009	2	50.59981	-123.435	510.4035
G073	-59.465	0.01	1	50.5648	-123.533	825.1448
G074	-85.243	0.01	1	50.65785	-123.427	925.2078
G075	-62.994	0.01	1	50.5711	-123.505	837.4265
G076	-42.187	0.011	1	50.56271	-123.496	738.4495
G077	-83.092	0.01	1	50.60471	-123.448	966.7476
G078	-104.467	0.01	1	50.5882	-123.47	1100.757
G079	-219.438	0.011	1	50.58035	-123.423	1716.554
G080	-69.416	0.01	1	50.57124	-123.568	893.33
G081	-93.303	0.011	1	50.62372	-123.426	1029.842

Table 2. Raw averaged gravity readings as collected by the LaCoste & Romberg alongside their time and date of acquisition, as well as the calculated tide effect and residual from drift correction.

Name	Dial	Day	Month	Year	Hour	Minute	Tidal Effect	Loop	Residual
BASE	4338.646	10	7	2019	15	20	-0.03253	1	1.05E-08
G001	4271.667	10	7	2019	16	32	-0.03805	1	-1.2E-11
G002	4353.953	10	7	2019	21	30	0.033073	1	-9.1E-13
G003	4337.991	10	7	2019	22	22	0.04376	1	-9.1E-13
G004	4332.456	10	7	2019	23	6	0.049456	1	-9.1E-13
G005	4321.057	10	7	2019	23	35	0.051569	1	9.09E-13
G006	4305.17	11	7	2019	0	2	0.052501	1	-9.1E-12

BASE	4338.704	11	7	2019	0	33	0.05251	1	-1.1E-08
BASE	4338.88	11	7	2019	14	5	-0.01307	2	3.05E-07
G007	4178.355	11	7	2019	16	35	-0.06184	2	-1.8E-12
G008	4186.857	11	7	2019	18	2	-0.06023	2	0
G009	4191.332	11	7	2019	19	1	-0.04611	2	-9.1E-13
G010	4278.971	11	7	2019	21	21	0.010957	2	-1.5E-11
BASE	4338.922	11	7	2019	22	52	0.045469	2	-3E-07
BASE	4338.8	12	7	2019	15	32	-0.0493	3	7.73E-07
G011	3972.279	12	7	2019	18	18	-0.08416	3	1.82E-12
G012	4099.458	12	7	2019	18	52	-0.07912	3	1.82E-12
G013	4135.413	12	7	2019	19	22	-0.07125	3	9.09E-13
G014	4363.062	12	7	2019	23	18	0.042437	3	-1.3E-11
BASE	4339.011	13	7	2019	1	50	0.078936	3	-7.7E-07
BASE	4338.9	13	7	2019	14	4	0.013025	4	-1.9E-08
G015	4226.232	13	7	2019	16	28	-0.06935	4	3.64E-12
G016	4235.213	13	7	2019	18	16	-0.10045	4	-4.5E-12
G017	4251.749	13	7	2019	19	3	-0.09929	4	2.73E-12
G018	4263.038	13	7	2019	20	44	-0.06698	4	-2.7E-12
G019	4271.055	13	7	2019	21	28	-0.0434	4	-8.2E-12
BASE	4338.921	13	7	2019	23	44	0.036791	4	1.86E-08
BASE	4338.855	14	7	2019	14	6	0.031235	5	3.08E-07
G020	4035.266	14	7	2019	15	35	-0.02361	5	6.37E-12
G021	4044.568	14	7	2019	16	34	-0.06018	5	-5E-12
G022	4049.676	14	7	2019	17	45	-0.09453	5	-5.9E-12
BASE	4338.887	15	7	2019	0	21	0.037007	5	-3.1E-07
BASE	4338.898	15	7	2019	14	6	0.050439	6	1.18E-06
G023	4355.712	15	7	2019	15	52	-0.01294	6	1.27E-11
G024	4087.548	15	7	2019	16	32	-0.03912	6	-3.6E-12
G025	4079.749	15	7	2019	17	30	-0.07447	6	1.18E-11
G026	4072.244	15	7	2019	18	10	-0.09398	6	9.09E-13
G027	4031.411	15	7	2019	19	1	-0.1102	6	-7.3E-12
G028	4033.295	15	7	2019	19	45	-0.11485	6	5E-12
G029	4115.188	15	7	2019	21	36	-0.08683	6	-2.7E-12
G030	4121.756	15	7	2019	22	25	-0.05983	6	0
G031	4145.058	15	7	2019	23	26	-0.0203	6	-7.3E-12
BASE	4338.787	16	7	2019	0	20	0.015838	6	-1.2E-06
BASE	4338.842	16	7	2019	14	6	0.066459	7	7.74E-07
G032	4245.71	16	7	2019	16	23	-0.00897	7	-1.8E-12
G033	4251.632	16	7	2019	18	26	-0.08451	7	0
G034	4258.049	16	7	2019	20	19	-0.11332	7	-9.1E-13
G035	4284.601	16	7	2019	22	52	-0.06209	7	-6.4E-12
BASE	4338.825	16	7	2019	23	57	-0.01981	7	-7.7E-07
BASE	4338.847	18	7	2019	13	14	0.083561	8	8.71E-07
G036	4166.211	18	7	2019	14	29	0.077471	8	-2.7E-12

G037	4181.614	18	7	2019	15	28	0.060566	8	3.64E-12
G038	4279.96	18	7	2019	18	13	-0.02827	8	0
G039	4189.766	18	7	2019	19	1	-0.05562	8	9.09E-13
G040	4256.856	18	7	2019	19	51	-0.07793	8	-2.7E-12
G041	4280.391	18	7	2019	21	7	-0.09492	8	-2.7E-12
G042	4287.154	18	7	2019	22	22	-0.08702	8	-7.3E-12
BASE	4338.758	18	7	2019	23	37	-0.05695	8	-8.7E-07
BASE	4338.847	19	7	2019	14	10	0.077663	9	-5.1E-07
G043	4188.97	19	7	2019	15	51	0.060978	9	0
G044	4207.496	19	7	2019	17	25	0.021072	9	0
G045	4221.938	19	7	2019	19	10	-0.035	9	2.73E-12
G046	4334.752	19	7	2019	20	19	-0.06461	9	-2.7E-12
G047	3997.944	19	7	2019	21	31	-0.07949	9	0
G048	4008.757	19	7	2019	21	59	-0.0799	9	-4.1E-12
G049	4080.881	19	7	2019	22	32	-0.07646	9	2.27E-12
BASE	4338.729	19	7	2019	23	14	-0.06594	9	5.14E-07
BASE	4338.843	20	7	2019	14	9	0.068274	10	-0.0043
G050	4061.705	20	7	2019	15	17	0.06748	10	1.36E-12
G051	3989.356	20	7	2019	16	41	0.051215	10	-2.3E-12
G052	4050.771	20	7	2019	19	20	-0.01516	10	5.91E-12
G053	4273.327	20	7	2019	20	16	-0.03832	10	1.82E-12
G054	4123.241	20	7	2019	20	53	-0.05036	10	-5.5E-12
G055	4182.641	20	7	2019	21	29	-0.05837	10	0
G056	4159.223	20	7	2019	22	3	-0.06203	10	1.82E-12
BASE	4338.74	20	7	2019	22	34	-0.06182	10	0.016696
G057	4353.234	20	7	2019	23	16	-0.05623	10	0
G058	4353.489	21	7	2019	0	41	-0.0286	10	-8.2E-12
BASE	4338.768	21	7	2019	1	29	-0.0066	10	-0.0124
BASE	4338.796	21	7	2019	13	39	0.05048	11	1.47E-06
G059	4057.402	21	7	2019	14	39	0.055897	11	1.36E-12
G060	4290.996	21	7	2019	16	20	0.05432	11	-2.7E-12
G061	4302.79	21	7	2019	18	23	0.025597	11	2.73E-12
G062	4311.901	21	7	2019	20	14	-0.01406	11	-1.8E-12
G063	4318.175	21	7	2019	21	55	-0.03944	11	2.73E-12
G064	4279.057	22	7	2019	0	6	-0.03255	11	-3.6E-12
G065	4247.159	22	7	2019	0	37	-0.02417	11	-3.6E-12
BASE	4338.755	22	7	2019	1	8	-0.01383	11	-1.5E-06
BASE	4338.755	22	7	2019	13	5	0.030629	12	-0.00776
G066	4121.705	22	7	2019	13	49	0.033087	12	-3.6E-12
G067	4026.105	22	7	2019	15	21	0.041108	12	0.010028
G068	4077.245	22	7	2019	18	43	0.028102	12	-7.7E-12
G069	4093.933	22	7	2019	20	5	0.008345	12	9.09E-13
G070	4109.977	22	7	2019	21	45	-0.01419	12	-3.6E-12
BASE	4338.788	22	7	2019	23	7	-0.02153	12	-0.00227

BASE	4338.753	23	7	2019	14	11	0.015373	13	-0.00681
G071	4100.004	23	7	2019	16	12	0.024609	13	-3.6E-12
G072	4332.598	23	7	2019	17	1	0.027897	13	0.015843
G067	4026.098	23	7	2019	19	35	0.024057	13	-0.01003
G073	4279.337	23	7	2019	21	39	0.00814	13	-1.8E-12
BASE	4338.808	23	7	2019	23	31	0.000101	13	0.000991
BASE	4338.744	24	7	2019	13	46	-0.00177	14	0.00643
G074	4253.52	24	7	2019	16	42	0.003597	14	0
G072	4332.549	24	7	2019	17	23	0.008694	14	-0.01584
G075	4275.79	24	7	2019	18	12	0.0148	14	2.73E-12
G076	4296.606	24	7	2019	18	48	0.018716	14	-4.5E-12
BASE	4338.814	24	7	2019	19	51	0.023469	14	0.009412
BASE	4338.698	27	8	2019	13	37	0.028	15	2.27E-07
G077	4255.504	27	8	2019	16	17	-0.07366	15	9.09E-13
G078	4234.113	27	8	2019	16	50	-0.08984	15	1.82E-12
G079	4119.124	27	8	2019	18	59	-0.10711	15	-7.3E-12
BASE	4338.583	27	8	2019	20	0	-0.08635	15	-2.3E-07
BASE	4338.693	29	8	2019	14	35	0.073431	16	1.33E-06
G080	4269.219	29	8	2019	16	15	0.006617	16	-4.5E-12
G081	4245.31	29	8	2019	16	48	-0.01881	16	-6.4E-12
BASE	4338.588	29	8	2019	17	27	-0.04707	16	-1.3E-06

Table 3. Spatial (free air and latitude) corrections calculated for base and survey stations, alongside their coordinates. All the coordinates and corrections use the NAD83 CSRS datum.

Name	Latitude	Longitude	Elevation	Ellipsoidal gravity	Free air effect	Free air anomaly
BASE	50.63557	-123.406	473.662	981126.9	-146.172	-980981
G001	50.68509	-123.478	722.2353	981131.3	-222.882	-980975
G002	50.62249	-123.4	409.5758	981125.8	-126.395	-980984
G003	50.63869	-123.414	456.5915	981127.2	-140.904	-980987
G004	50.6436	-123.43	447.3578	981127.7	-138.055	-980996
G005	50.65093	-123.438	464.246	981128.3	-143.266	-981003
G006	50.66036	-123.446	532.2078	981129.1	-164.239	-980998
G007	50.57771	-123.52	1365.233	981121.8	-421.311	-980861
G008	50.5766	-123.521	1320.087	981121.7	-407.379	-980866
G009	50.57607	-123.52	1297.27	981121.7	-400.338	-980869
G010	50.68349	-123.492	671.7593	981131.2	-207.305	-980984
G011	50.62411	-123.54	2332.443	981125.9	-719.792	-980773
G012	50.58383	-123.537	1756.376	981122.3	-542.018	-980820
G013	50.51427	-123.436	1718.323	981116.2	-530.274	-980789
G014	50.57851	-123.293	328.3443	981121.9	-101.327	-980996
G015	50.57496	-123.513	1102.603	981121.6	-340.263	-980894
G016	50.573	-123.515	1061.711	981121.4	-327.644	-980897

G017	50.57136	-123.527	971.236	981121.2	-299.723	-980909
G018	50.56827	-123.527	919.0518	981121	-283.619	-980913
G019	50.56599	-123.526	875.0318	981120.8	-270.035	-980919
G020	50.62384	-123.487	2085.292	981125.9	-643.521	-980786
G021	50.62415	-123.481	2036.736	981125.9	-628.537	-980792
G022	50.62522	-123.477	2007.659	981126	-619.564	-980796
G023	50.59281	-123.354	358.3093	981123.1	-110.574	-980996
G024	50.60403	-123.484	1820.425	981124.1	-561.783	-980814
G025	50.60382	-123.49	1862.84	981124.1	-574.872	-980808
G026	50.6041	-123.494	1892.158	981124.1	-583.92	-980807
G027	50.60369	-123.505	2076.252	981124.1	-640.731	-980791
G028	50.60353	-123.502	2059.672	981124.1	-635.615	-980794
G029	50.60081	-123.482	1702.723	981123.9	-525.46	-980822
G030	50.60144	-123.478	1669.982	981123.9	-515.357	-980826
G031	50.54742	-123.558	1596.699	981119.1	-492.741	-980820
G032	50.57117	-123.519	1008.116	981121.2	-311.105	-980903
G033	50.57137	-123.514	968.4273	981121.2	-298.857	-980909
G034	50.57223	-123.511	930.2308	981121.3	-287.069	-980915
G035	50.56807	-123.514	788.5718	981120.9	-243.353	-980932
G036	50.60027	-123.671	1630.33	981123.8	-503.12	-980793
G037	50.58003	-123.62	1476.15	981122	-455.54	-980824
G038	50.73261	-123.707	804.266	981135.6	-248.196	-980946
G039	50.73546	-123.471	1200.008	981135.8	-370.322	-980914
G040	50.68141	-123.513	785.5313	981131	-242.415	-980970
G041	50.56726	-123.518	809.7928	981120.9	-249.902	-980929
G042	50.56582	-123.513	773.5608	981120.7	-238.721	-980934
G043	50.58455	-123.491	1336.328	981122.4	-412.391	-980860
G044	50.58049	-123.491	1239.381	981122	-382.473	-980871
G045	50.57916	-123.488	1163.521	981121.9	-359.063	-980880
G046	50.57616	-123.488	1093.649	981121.7	-337.5	-980788
G047	50.63137	-123.515	2232.769	981126.6	-689.032	-980778
G048	50.64436	-123.526	2156.431	981127.7	-665.475	-980792
G049	50.638	-123.535	1830.544	981127.2	-564.906	-980820
G050	50.73388	-123.578	1962.811	981135.7	-605.723	-980807
G051	50.61807	-123.572	2330.456	981125.4	-719.179	-980756
G052	50.64209	-123.554	1984.067	981127.5	-612.283	-980803
G053	50.68523	-123.528	725.022	981131.4	-223.742	-980973
G054	50.66009	-123.51	1553.296	981129.1	-479.347	-980865
G055	50.6494	-123.477	1270.867	981128.2	-392.19	-980892
G056	50.63887	-123.477	1451.149	981127.2	-447.825	-980859
G057	50.61428	-123.383	391.575	981125	-120.84	-980990
G058	50.60365	-123.372	387.2448	981124.1	-119.504	-980990
G059	50.63764	-123.528	1944.754	981127.1	-600.151	-980808
G060	50.561	-123.536	747.5735	981120.3	-230.701	-980937

G061	50.56173	-123.505	672.533	981120.4	-207.544	-980949
G062	50.5593	-123.489	640.712	981120.2	-197.724	-980949
G063	50.56869	-123.475	601.5966	981121	-185.653	-980956
G064	50.66873	-123.452	685.846	981129.9	-211.652	-980978
G065	50.67572	-123.464	863.0023	981130.5	-266.323	-980956
G066	50.48557	-123.498	1791.487	981113.6	-552.853	-980778
G067	50.56184	-123.417	2216.87	981120.4	-684.126	-980749
G068	50.59461	-123.501	1872.504	981123.3	-577.855	-980807
G069	50.59485	-123.497	1793.741	981123.3	-553.548	-980815
G070	50.59433	-123.494	1719.044	981123.3	-530.497	-980822
G071	50.69609	-123.354	1823.061	981132.3	-562.597	-980808
G072	50.59981	-123.435	510.4035	981123.8	-157.511	-980972
G073	50.5648	-123.533	825.1448	981120.7	-254.64	-980925
G074	50.65785	-123.427	925.2078	981128.9	-285.519	-980929
G075	50.5711	-123.505	837.4265	981121.2	-258.43	-980926
G076	50.56271	-123.496	738.4495	981120.5	-227.886	-980935
G077	50.60471	-123.448	966.7476	981124.2	-298.338	-980909
G078	50.5882	-123.47	1100.757	981122.7	-339.693	-980888
G079	50.58035	-123.423	1716.554	981122	-529.729	-980812
G080	50.57124	-123.568	893.33	981121.2	-275.682	-980915
G081	50.62372	-123.426	1029.842	981125.9	-317.809	-980901

Table 4. Spatial corrections (Bouguer slab and Terrain corrections) calculated for the base and survey stations at Mount Meager. Final Anomaly refers to the total corrections that will be applied to the "absolute gravity" from Table 1, and is the combination of all the other calculated spatial anomalies. TerrCorrFinal refers to the combined values of the near and far terrain corrections, which are added to obtain the total effect from topography on the gravity signal for each station.

Name	Bouguer Slab (mGal)	TerrCorrNear (mGal)	TerrCorrFar (mGal)	TerrCorrFinal (mGal)	Final Anomaly (mGal)
BASE	-52.98999092	0.898662112	19.6799513	20.57861341	-980907.1991
G001	-80.79862866	0.830654068	16.98656861	17.81722268	-980876.8102
G002	-45.82047069	0.064889887	19.51911065	19.58400054	-980918.718
G003	-51.08026336	0.257067234	20.71572011	20.97278734	-980914.9706
G004	-50.04725441	0.57377649	23.13279339	23.70656988	-980922.0951
G005	-51.93659642	3.428229131	25.4079083	28.83613743	-980921.9145
G006	-59.53967915	0.656336388	24.87309526	25.52943165	-980913.3699
G007	-152.7327423	2.036488836	12.72837738	14.76486621	-980693.4621
G008	-147.6821243	2.832887103	12.44923751	15.28212461	-980703.3247
G009	-145.1294889	2.684802615	12.37799488	15.0627975	-980708.6289
G010	-75.15172563	0.089186724	16.83833947	16.9275262	-980891.7315
G011	-260.9374086	5.20284356	18.96138683	24.16423039	-980487.5369
G012	-196.491036	4.729258677	16.78757183	21.51683051	-980601.656
G013	-192.233949	N/A	8.423052124	8.423052124	-980588.6236

G014	-36.73285838	0.277030203	26.22038468	26.49741488	-980933.2055
G015	-123.3515085	4.203796613	12.82837855	17.03217516	-980753.4909
G016	-118.7767741	3.405463556	12.29121972	15.69668328	-980762.8345
G017	-108.6550876	2.440562627	13.51243983	15.95300246	-980783.9397
G018	-102.8170841	0.792442856	12.57160085	13.3640437	-980796.9394
G019	-97.89243248	0.491277357	12.51928927	13.01056663	-980807.6052
G020	-233.2878437	1.311118373	21.97813842	23.28925679	-980529.3376
G021	-227.8557213	1.753651353	23.89932322	25.65297458	-980538.0824
G022	-224.6028691	2.220112071	24.54626429	26.76637636	-980544.1497
G023	-40.08513242	0.05230143	28.79551002	28.84781145	-980926.7427
G024	-203.6563842	3.249366697	18.33399375	21.58336045	-980588.3565
G025	-208.4014818	2.61981579	17.24113683	19.86095262	-980579.9819
G026	-211.681401	4.055372007	16.45894207	20.51431408	-980574.5068
G027	-232.2765074	4.290902916	18.83444947	23.12535238	-980535.2647
G028	-230.4216444	5.365024084	19.65038581	25.01540989	-980538.4371
G029	-190.4887737	1.772687028	14.8397497	16.61243673	-980614.8061
G030	-186.8259298	1.518133262	15.13752375	16.65565701	-980622.0391
G031	-178.6275072	N/A	13.31854083	13.31854083	-980628.1187
G032	-112.7809371	3.212287157	12.18278085	15.39506801	-980775.0096
G033	-108.3408681	3.984902586	12.82433817	16.80924075	-980784.3171
G034	-104.0677074	2.906432033	14.36019345	17.26662548	-980793.5653
G035	-88.21989045	1.031764683	16.09302777	17.12479245	-980826.4182
G036	-182.3899081	N/A	12.40457813	12.40457813	-980598.5261
G037	-165.141329	0.065423136	8.307702376	8.373125512	-980650.1726
G038	-89.97565022	N/A	30.73859254	30.73859254	-980825.4485
G039	-134.248495	N/A	14.75491168	14.75491168	-980765.4565
G040	-87.87974436	2.192152176	16.01939428	18.21154645	-980864.3685
G041	-90.59394831	0.856793683	15.06796554	15.92475923	-980822.7661
G042	-86.54056637	0.175577482	15.21638548	15.39196296	-980831.6568
G043	-149.4990636	1.992294496	12.07515877	14.06745327	-980696.3142
G044	-138.6532549	1.639632574	11.6276042	13.26723677	-980718.9565
G045	-130.1665844	1.370691534	11.4582755	12.82896704	-980736.6802
G046	-122.3497453	1.583004773	11.33809292	12.92109769	-980652.8598
G047	-249.7865165	1.795385967	16.39797484	18.19336081	-980510.3217
G048	-241.2463677	3.916975755	21.11220272	25.02917848	-980525.9263
G049	-204.7884291	3.462090423	10.66860848	14.1306989	-980601.1672
G050	-219.585555	N/A	13.89544581	13.89544581	-980573.6096
G051	-260.7151102	2.166642184	15.91004836	18.07669054	-980476.8919
G052	-221.9635157	2.765881127	12.91856877	15.6844499	-980565.5853
G053	-81.11038998	0.236009039	14.12771424	14.36372328	-980877.5539
G054	-173.771913	2.308327549	15.73083493	18.03916247	-980673.4525
G055	-142.1756839	3.762939195	15.41390076	19.17683996	-980730.7118
G056	-162.3443701	2.04889195	15.2247195	17.27361145	-980679.2905
G057	-43.80667134	1.307281899	24.12949539	25.43677729	-980920.4599

G058	-43.32223544	0.157036175	24.90668353	25.0637197	-980921.4835
G059	-217.5654811	1.121850151	12.40066077	13.52251092	-980577.2856
G060	-83.63329546	0.89612206	18.72269535	19.61881741	-980834.169
G061	-75.23828655	2.552411669	19.35123239	21.90364406	-980851.6839
G062	-71.67837762	1.866060367	17.77219434	19.63825471	-980857.9659
G063	-67.30241169	1.517928106	20.09059764	21.60852575	-980866.9814
G064	-76.72765049	1.659069298	20.69806978	22.35713908	-980878.8262
G065	-96.54665847	3.374016126	13.99633166	17.37034779	-980841.8507
G066	-200.4190252	N/A	6.694728451	6.694728451	-980570.7048
G067	-248.0079379	1.095548818	24.89959578	25.9951446	-980474.9544
G068	-209.4826158	2.040954329	16.78692184	18.82787617	-980578.6945
G069	-200.6711695	2.939093221	15.46796525	18.40705847	-980595.5586
G070	-192.3145623	3.359031651	14.60219497	17.96122662	-980611.3134
G071	-203.9513033	N/A	16.83867113	16.83867113	-980587.7067
G072	-57.10037455	0.536032711	25.01585641	25.55188912	-980889.809
G073	-92.31142146	0.438980559	14.0369716	14.47595216	-980818.6889
G074	-103.5057681	1.583087987	16.8026553	18.38574329	-980806.7521
G075	-93.68541636	0.843518752	15.62662695	16.47014571	-980815.6199
G076	-82.61256359	0.208514851	13.88504579	14.09356064	-980838.0609
G077	-108.1529496	4.395743923	14.45831004	18.85405396	-980781.9444
G078	-123.1449422	2.49882219	12.80101309	15.29983528	-980749.0596
G079	-192.036027	2.624993524	23.01861835	25.64361187	-980594.0634
G080	-99.93950709	0.011787884	16.11207491	16.1238628	-980798.8945
G081	-115.2115187	4.391333873	16.35147567	20.74280954	-980765.4266

Table 5. Complete Bouguer anomalies (in relation to the BASE station), as plotted in Figure 13. The final anomaly is algebraically added to the absolute gravity. Note that station G046 is a clear outlier that was removed from the plotted Bouguer Anomaly map.

Name	Absolute Gravity (mGal)	Final Anomaly (mGal)	Spatial Corrected Gravity (mGal)	Bouguer Anomalies (mGal)
BASE	0	-980907.1991	-980907.1991	0
G001	-66.969	-980876.8102	-980943.7792	-36.5801
G002	15.26	-980918.718	-980903.458	3.7411
G003	-0.711	-980914.9706	-980915.6816	-8.4825
G004	-6.25	-980922.0951	-980928.3451	-21.146
G005	-17.649	-980921.9145	-980939.5635	-32.3644
G006	-33.536	-980913.3699	-980946.9059	-39.7068
G007	-160.472	-980693.4621	-980853.9341	53.265
G008	-151.968	-980703.3247	-980855.2927	51.9064
G009	-147.506	-980708.6289	-980856.1349	51.0642
G010	-59.919	-980891.7315	-980951.6505	-44.4514
G011	-366.509	-980487.5369	-980854.0459	53.1532

G012	-239.339	-980601.656	-980840.995	66.2041
G013	-203.396	-980588.6236	-980792.0196	115.1795
G014	24.107	-980933.2055	-980909.0985	-1.8994
G015	-112.584	-980753.4909	-980866.0749	41.1242
G016	-103.572	-980762.8345	-980866.4065	40.7926
G017	-87.037	-980783.9397	-980870.9767	36.2224
G018	-75.78	-980796.9394	-980872.7194	34.4797
G019	-67.786	-980807.6052	-980875.3912	31.8079
G020	-303.538	-980529.3376	-980832.8756	74.3235
G021	-294.202	-980538.0824	-980832.2844	74.9147
G022	-289.062	-980544.1497	-980833.2117	73.9874
G023	16.891	-980926.7427	-980909.8517	-2.6526
G024	-251.242	-980588.3565	-980839.5985	67.6006
G025	-258.998	-980579.9819	-980838.9799	68.2192
G026	-266.479	-980574.5068	-980840.9858	66.2133
G027	-307.29	-980535.2647	-980842.5547	64.6444
G028	-305.396	-980538.4371	-980843.8331	63.366
G029	-223.516	-980614.8061	-980838.3221	68.877
G030	-216.97	-980622.0391	-980839.0091	68.19
G031	-193.7	-980628.1187	-980821.8187	85.3804
G032	-93.073	-980775.0096	-980868.0826	39.1165
G033	-87.089	-980784.3171	-980871.4061	35.793
G034	-80.657	-980793.5653	-980874.2223	32.9768
G035	-54.174	-980826.4182	-980880.5922	26.6069
G036	-172.637	-980598.5261	-980771.1631	136.036
G037	-157.222	-980650.1726	-980807.3946	99.8045
G038	-58.801	-980825.4485	-980884.2495	22.9496
G039	-148.971	-980765.4565	-980914.4275	-7.2284
G040	-81.863	-980864.3685	-980946.2315	-39.0324
G041	-58.317	-980822.7661	-980881.0831	26.116
G042	-51.568	-980831.6568	-980883.2248	23.9743
G043	-149.865	-980696.3142	-980846.1792	61.0199
G044	-131.304	-980718.9565	-980850.2605	56.9386
G045	-116.811	-980736.6802	-980853.4912	53.7079
G046	-3.97	-980652.8598	-980656.8298	250.3693
G047	-340.767	-980510.3217	-980851.0887	56.1104
G048	-329.955	-980525.9263	-980855.8813	51.3178
G049	-257.836	-980601.1672	-980859.0032	48.1959
G050	-277.143	-980573.6096	-980850.7526	56.4465
G051	-349.477	-980476.8919	-980826.3689	80.8302
G052	-287.997	-980565.5853	-980853.5823	53.6168
G053	-65.419	-980877.5539	-980942.9729	-35.7738
G054	-215.493	-980673.4525	-980888.9455	18.2536
G055	-156.085	-980730.7118	-980886.7968	20.4023

G056	-179.5	-980679.2905	-980858.7905	48.4086
G057	14.505	-980920.4599	-980905.9549	1.2442
G058	14.731	-980921.4835	-980906.7525	0.4466
G059	-281.401	-980577.2856	-980858.6866	48.5125
G060	-47.809	-980834.169	-980881.978	25.2211
G061	-35.991	-980851.6839	-980887.6749	19.5242
G062	-26.844	-980857.9659	-980884.8099	22.3892
G063	-20.548	-980866.9814	-980887.5294	19.6697
G064	-59.677	-980878.8262	-980938.5032	-31.3041
G065	-91.584	-980841.8507	-980933.4347	-26.2356
G066	-217.065	-980570.7048	-980787.7698	119.4293
G067	-312.696	-980474.9544	-980787.6504	119.5487
G068	-261.559	-980578.6945	-980840.2535	66.9456
G069	-244.863	-980595.5586	-980840.4216	66.7775
G070	-228.81	-980611.3134	-980840.1234	67.0757
G071	-238.778	-980587.7067	-980826.4847	80.7144
G072	-6.209	-980889.809	-980896.018	11.1811
G073	-59.465	-980818.6889	-980878.1539	29.0452
G074	-85.243	-980806.7521	-980891.9951	15.204
G075	-62.994	-980815.6199	-980878.6139	28.5852
G076	-42.187	-980838.0609	-980880.2479	26.9512
G077	-83.092	-980781.9444	-980865.0364	42.1627
G078	-104.467	-980749.0596	-980853.5266	53.6725
G079	-219.438	-980594.0634	-980813.5014	93.6977
G080	-69.416	-980798.8945	-980868.3105	38.8886
G081	-93.303	-980765.4266	-980858.7296	48.4695

Citations

- Atef, H., Abd El-Gawad, A.M.S., Abdel Zaher, M., Farag, K.S.I., 2016. The contribution of gravity method in geothermal exploration of southern part of the Gulf of Suez–Sinai region, Egypt. *NRIAG J. Astron. Geophys.* 5, 173–185. <https://doi.org/10.1016/j.nrjag.2016.02.005>
- Barnaba, C., Marello, L., Vuan, A., Palmieri, F., Romanelli, M., Priolo, E., Braitenberg, C., 2010. The buried shape of an alpine valley from gravity surveys, seismic and ambient noise analysis. *Geophys. J. Int.* 180, 715–733. <https://doi.org/10.1111/j.1365-246X.2009.04428.x>
- Battaglia, M., Poland, M.P., Kauahikaua, J.P., 2012. GTOOLS: an Interactive Computer Program to Process Gravity Data for High-Resolution Applications, in: American Geophysical Union, Fall Meeting 2012, Abstract #GP43B-1143.
- Eckhardt, E.A., 1940. A brief history of the gravity method of prospecting for oil. *Geophysics* 5, 231–242. <https://doi.org/10.1190/1.1441806>
- Hackney, R.I., Featherstone, W.E., 2003. Geodetic versus geophysical perspectives of the “gravity anomaly.” *Geophys. J. Int.* 154, 35–43. <https://doi.org/10.1046/j.1365-246X.2003.01941.x>

- Juniper Systems, 2019. Geode Owner's Manual. Boston, MA.
- Longman, I.M., 1959. Formulas for computing the tidal accelerations due to the moon and the sun. *J. Geophys. Res.* 64, 2351–2355. <https://doi.org/10.1029/JZ064i012p02351>
- Lowrie, W., 2007. *Fundamentals of Geophysics*, Cambridge University Press. Cambridge University Press, Cambridge. <https://doi.org/10.1017/CBO9780511807107>
- McCubbine, J., Tontini, F.C., Stagpoole, V., Smith, E., O'Brien, G., 2018. Gsolve, a Python computer program with a graphical user interface to transform relative gravity survey measurements to absolute gravity values and gravity anomalies. *SoftwareX* 7, 129–137. <https://doi.org/10.1016/j.softx.2018.04.003>
- Milano, M., Pierri, I., Florio, G., Cella, F., Fedi, M., 2019. Bouguer gravity field of the Tuscan Archipelago (central Italy). *J. Maps* 15, 751–758. <https://doi.org/10.1080/17445647.2019.1669499>
- Miller, C.A., Williams-Jones, G., Fournier, D., Witter, J., 2017. 3D gravity inversion and thermodynamic modelling reveal properties of shallow silicic magma reservoir beneath Laguna del Maule, Chile. *Earth Planet. Sci. Lett.* 459, 14–27. <https://doi.org/10.1016/j.epsl.2016.11.007>
- Moritz, H., 1980. Geodetic reference system 1980. *Bull. Géodésique* 54, 395–405. <https://doi.org/10.1007/BF02521480>
- Nagy, D., 1966. The gravitational attraction of a right rectangular prism. *Geophysics* 31, 362–371. <https://doi.org/10.1190/1.1439779>
- Putiska, R., Kusnirak, D., Dostal, I., Lacny, A., Mojzes, A., Hok, J., Pasteka, R., Krajnak, M., Bosansky, M., 2014. Integrated Geophysical and Geological Investigations of Karst Structures in Komberek, Slovakia. *J. Cave Karst Stud.* 76, 155–163. <https://doi.org/10.4311/2013ES0112>
- Seigel, H.O., 1995. *A guide to high precision land gravimeter surveys*. Concord.
- Van Camp, M., de Viron, O., Watlet, A., Meurers, B., Francis, O., Caudron, C., 2017. Geophysics From Terrestrial Time-Variable Gravity Measurements. *Rev. Geophys.* 55, 938–992. <https://doi.org/10.1002/2017RG000566>
- Wilcox, L.E., 1989. Gravity anomalies: Interpretation, in: *Geophysics*. Springer, Boston, MA, pp. 601–617. https://doi.org/10.1007/0-387-30752-4_75
- Zurek, J., Williams-Jones, G., Trusdell, F., Martin, S., 2015. The origin of Mauna Loa's Nīnole Hills: Evidence of rift zone reorganization. *Geophys. Res. Lett.* 42, 8358–8366. <https://doi.org/10.1002/2015GL065863>

Acknowledgements

Our gratitude goes to Dr. Jeffrey Zurek, for expert advice and conversations during processing of the data.

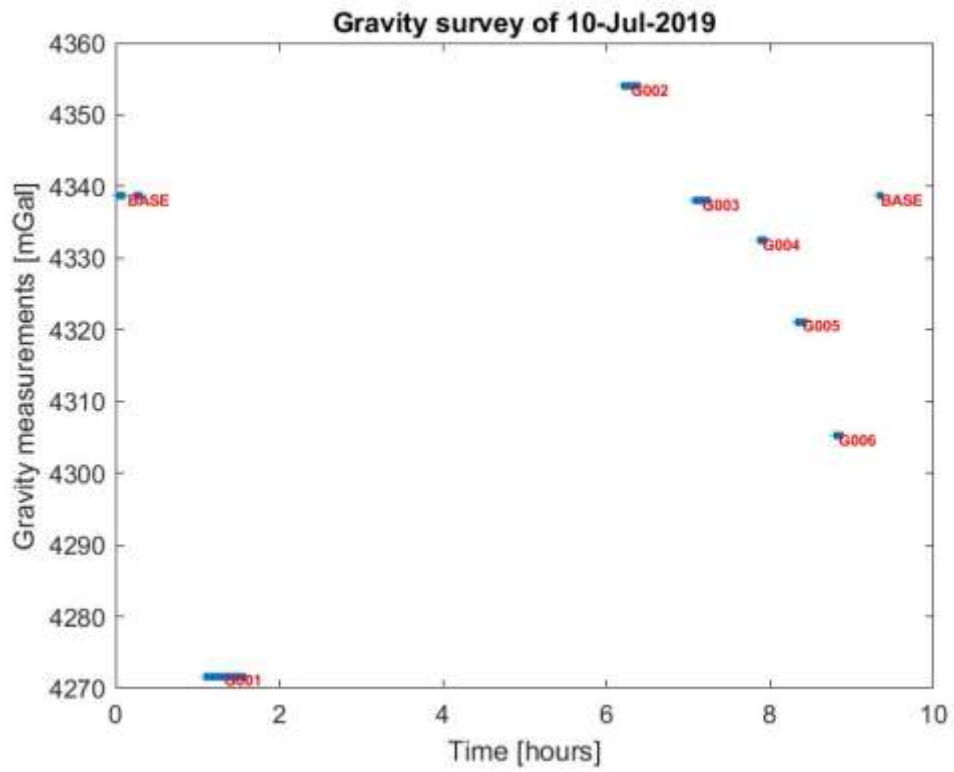


Figure 1. An example of how the program GTOOLS imports and reads a daily loop of relative gravity data.

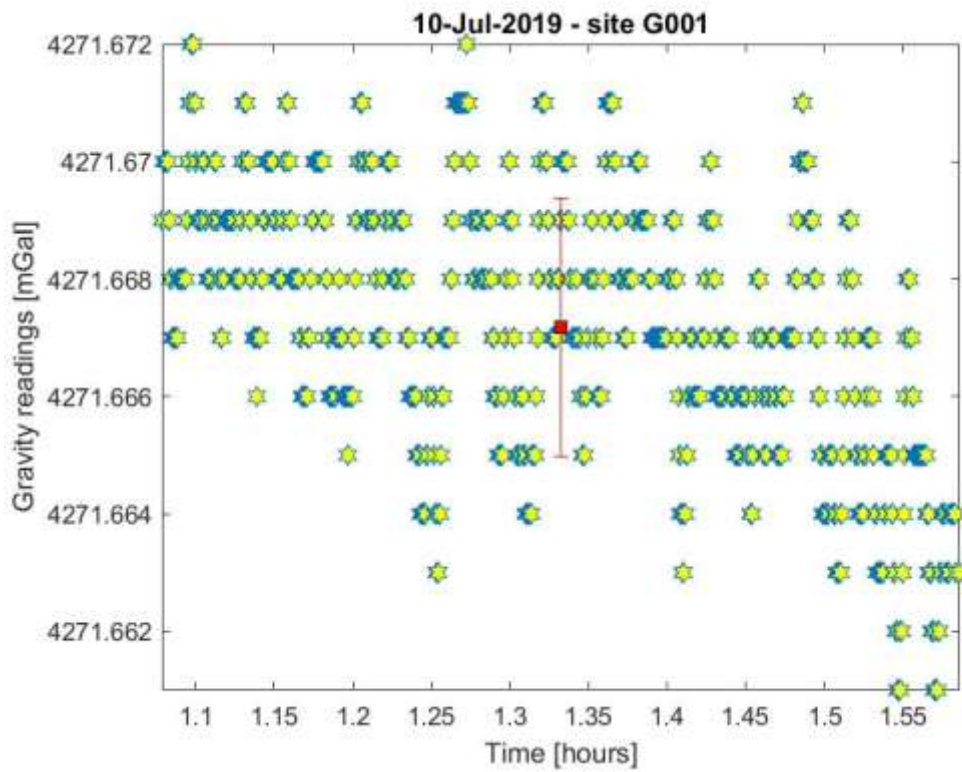


Figure 2. Relative gravity data for station G001. The data presented here is raw, as measured by the gravity meter.

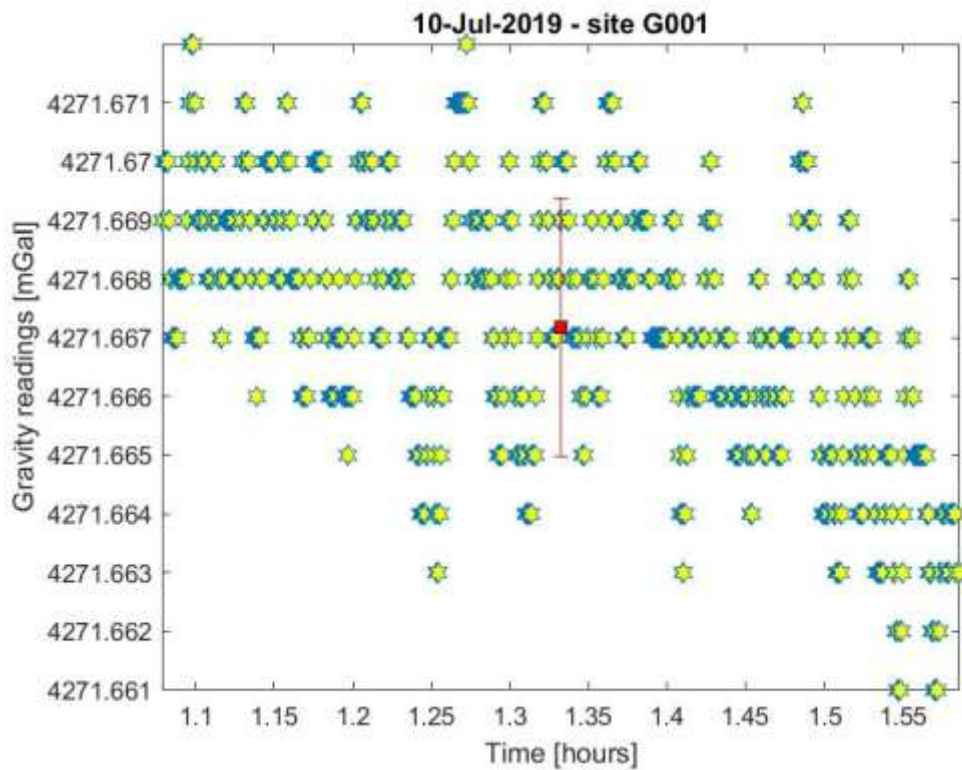


Figure 3. Raw gravity data for station G001 filtered by GTOOLS. Since no visible outliers were present in the original data, the program has not influenced the result significantly.

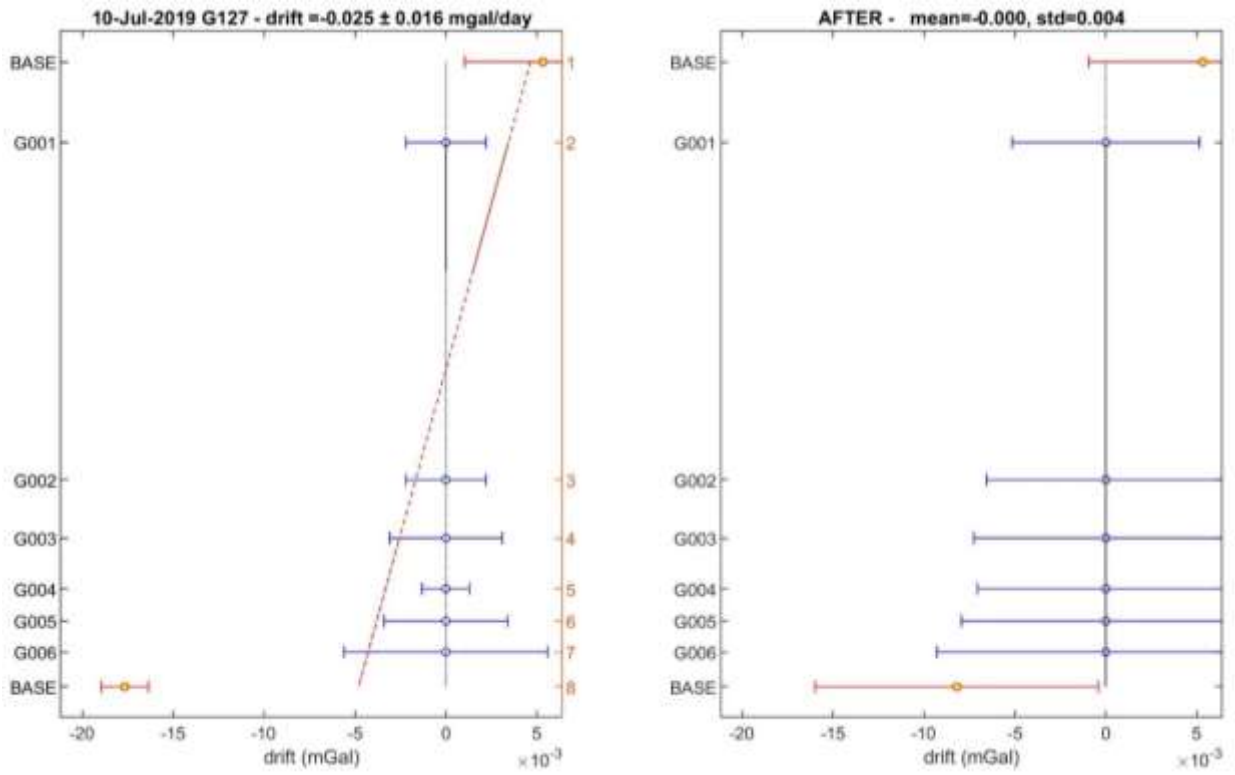


Figure 4. An example of daily drift correction in a daily loop of gravity measurements. The uncorrected survey gravity data is presented on the left, while the drift corrected data and the deviations from the linear regression are presented on the right.

Map of Bouguer Survey Gravity Stations - Mt. Meager Volcanic Complex

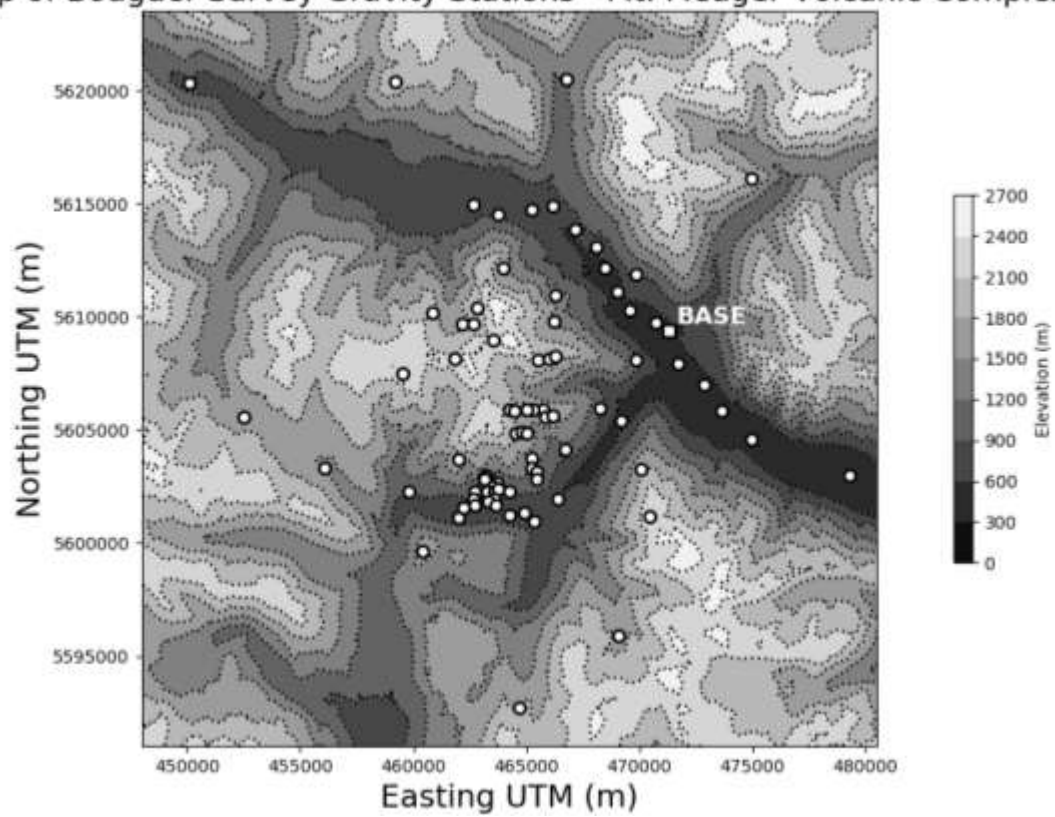


Figure 5. Map of surveyed gravity stations around the Mount Meager volcanic complex. The survey reference station is shown as a white square.



Figure 6. Calahorrano-Di Patre performing a gravity measurement at one of the stations on the MVC. This figure portrays the typical set-up for the gravity survey measurements. (Photo by S. Grasby)

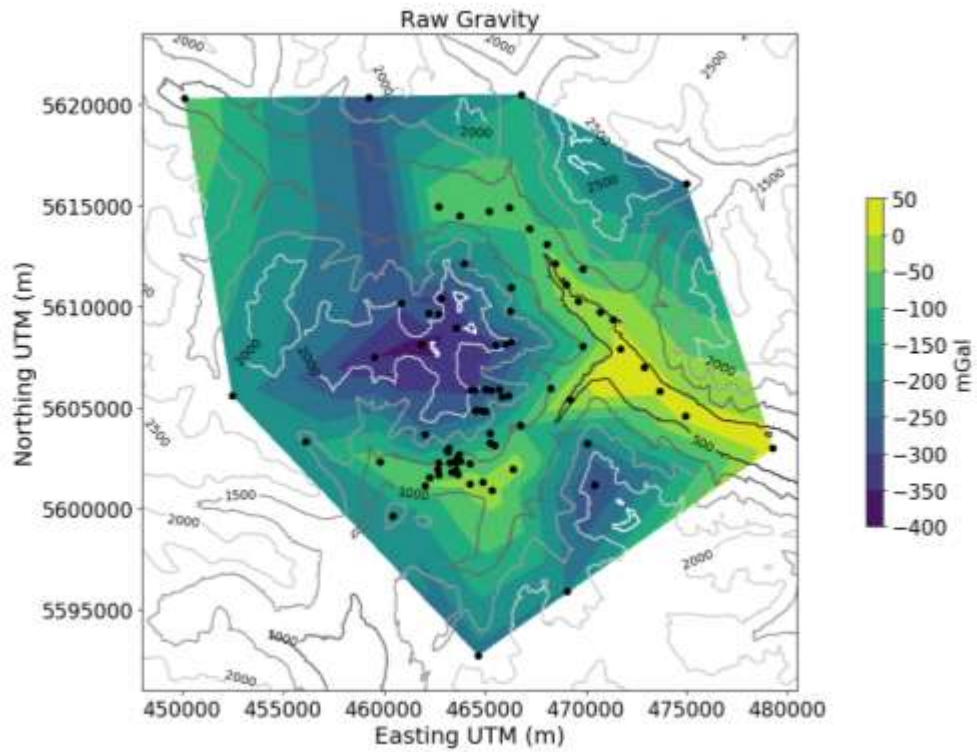


Figure 7. Relative gravity differences, corrected for temporal but not spatial effects.

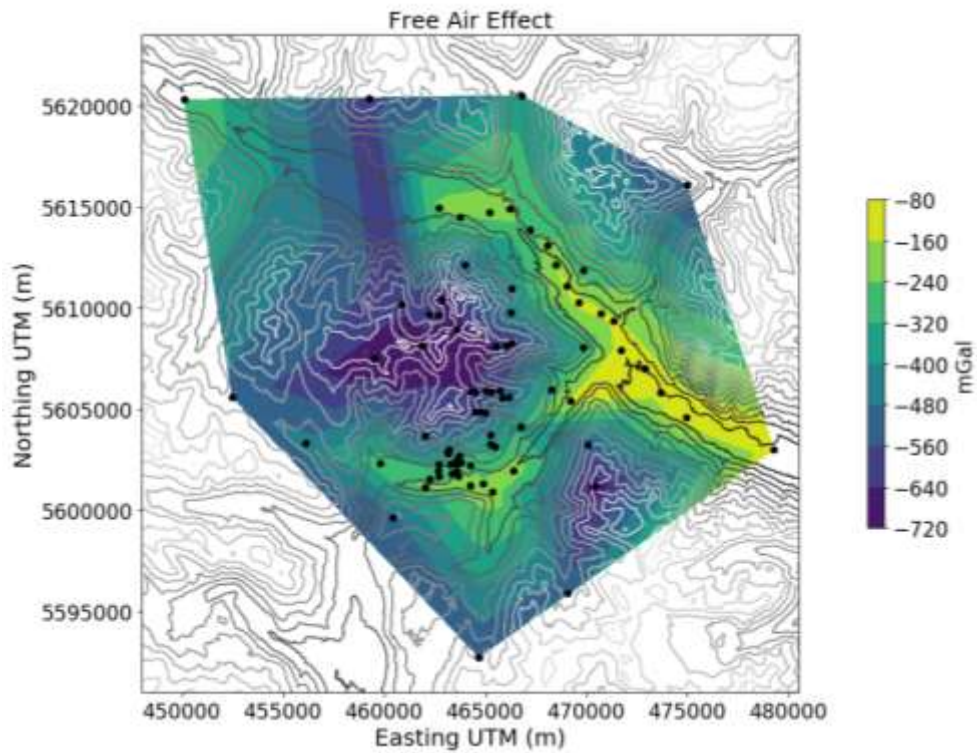


Figure 8. Plotted free air correction for survey stations at Mount Meager.

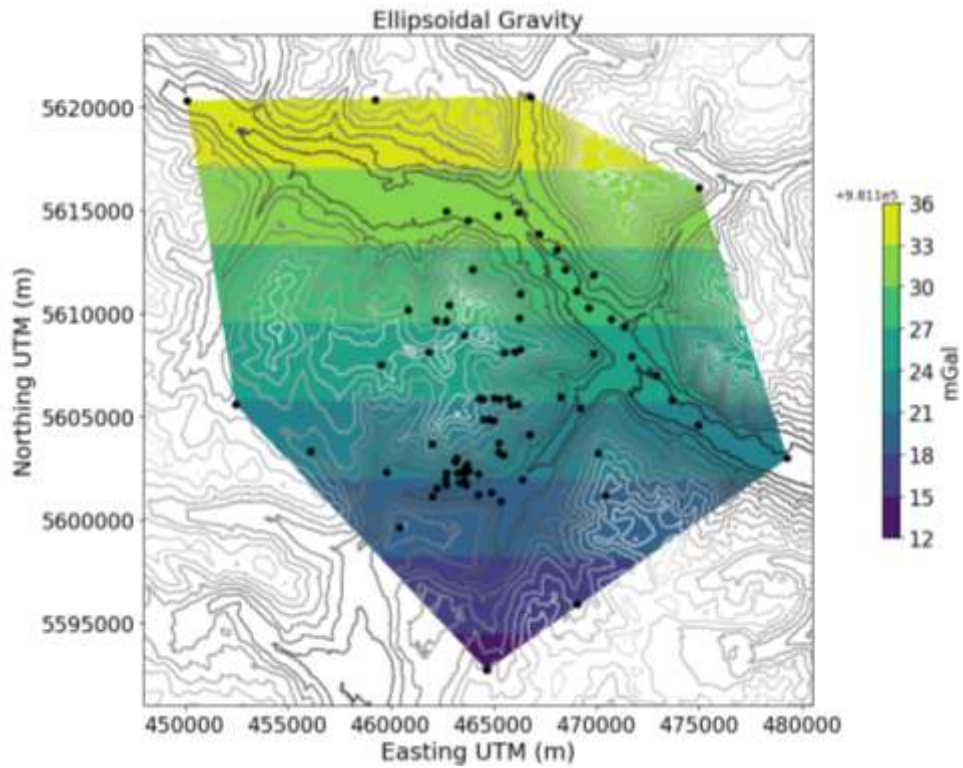


Figure 9. Plotted latitude correction for survey stations at Mount Meager.

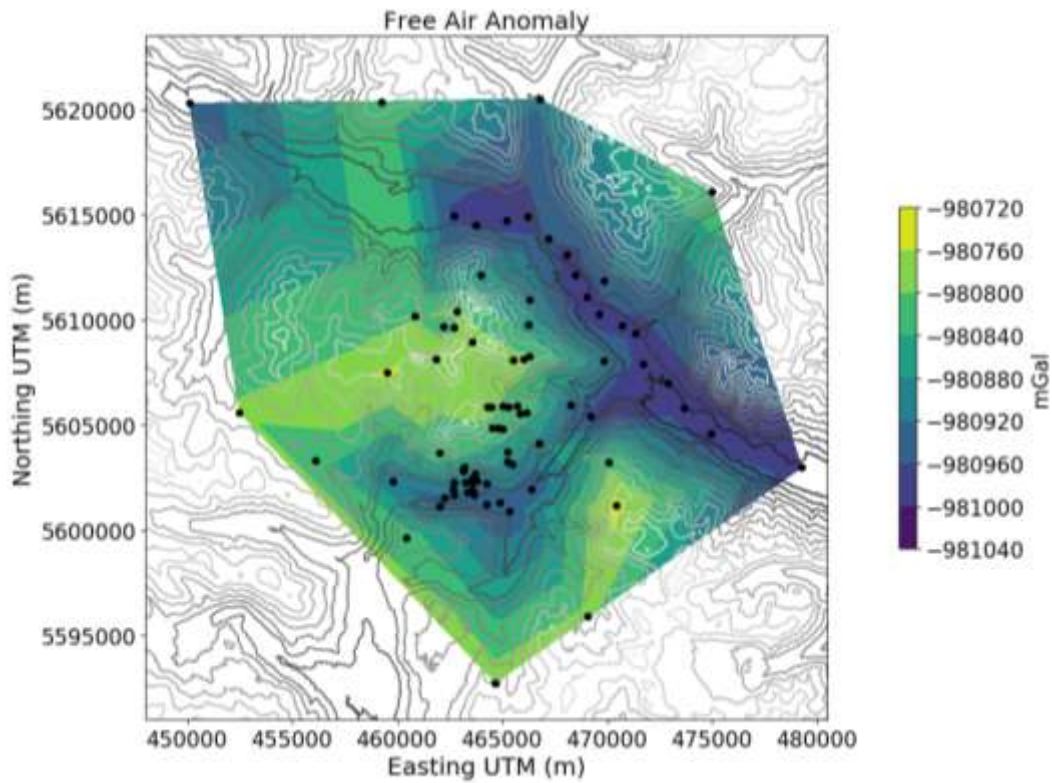


Figure 10. Free air anomaly correction, a combination of free air and ellipsoidal gravity, plotted for stations around Mount Meager. This free air anomaly is algebraically summed to the absolute gravity.

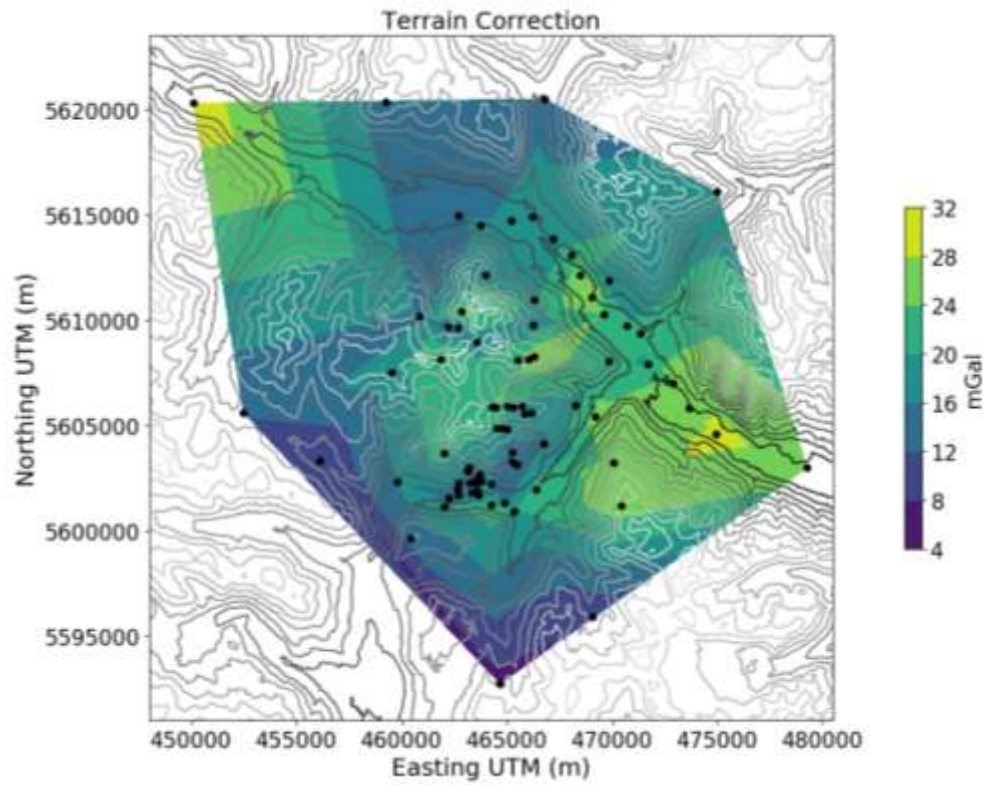


Figure 11. Calculated Terrain correction, including the Near Terrain using a LiDAR-derived 1m DEM and the Far Terrain using a coarser 30m DEM.

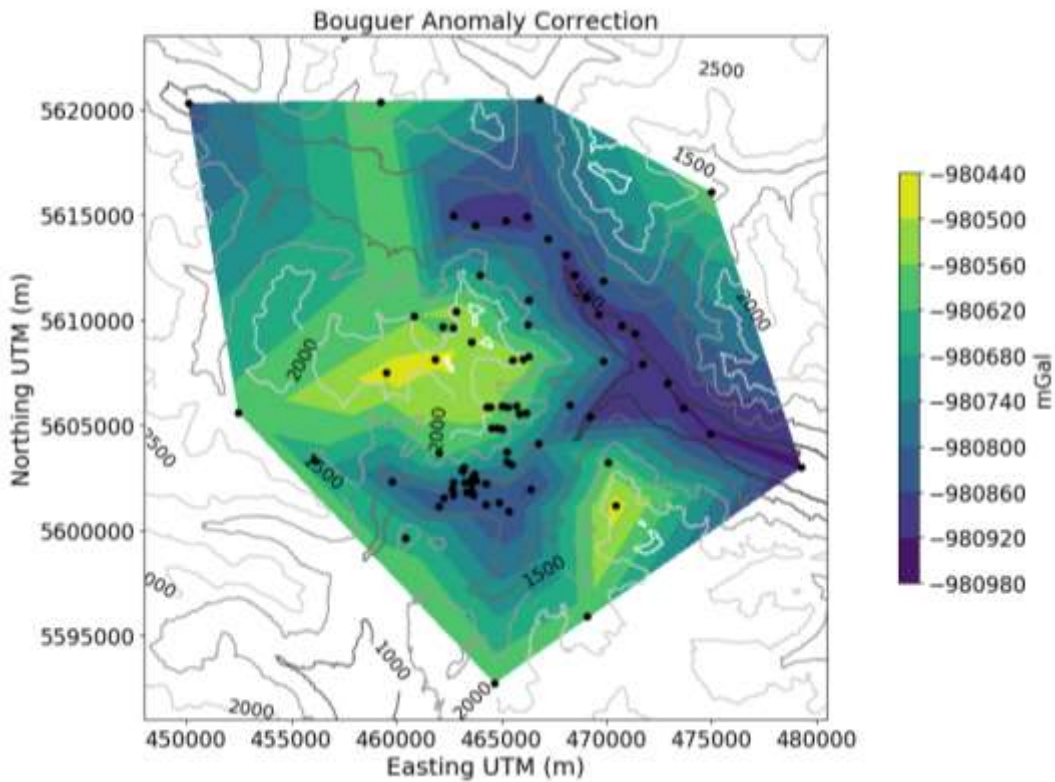


Figure 12. Calculated Bouguer correction, a combination of all the spatial corrections previously shown.

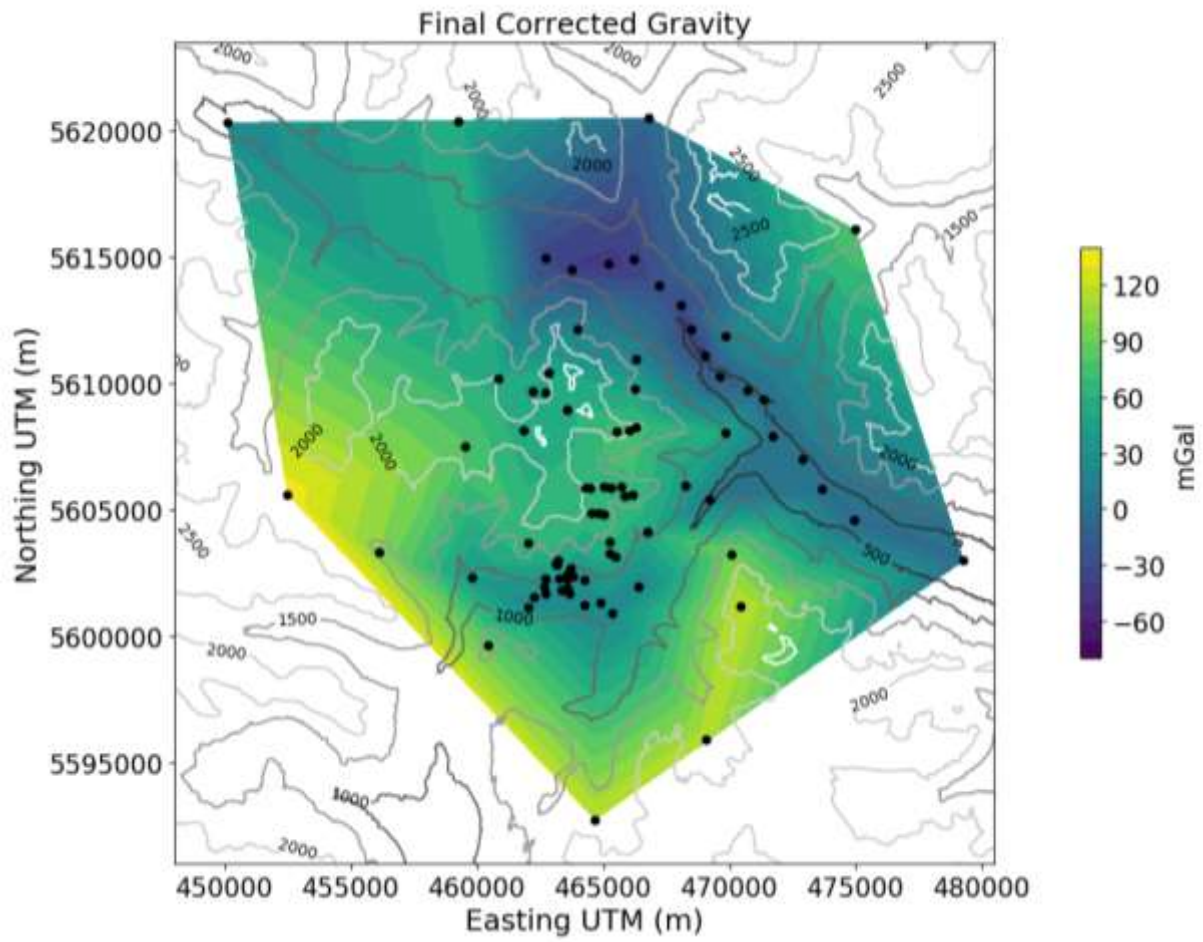


Figure 13. Preliminary Bouguer anomaly map for the Mount Meager volcanic complex area.

Chapter 5 - Broadband magnetotelluric study at Mount Meager to investigate the hydrothermal and magmatic system

Unsworth, M.J.¹; Hanneson, C.S.¹, Williamson A.R.¹

¹Department of Physics, University of Alberta, Edmonton, Alberta, Canada

Introduction

Magmatism is a fundamental geological process that is important in many areas of Earth science. It occurs when crustal or mantle rocks melt to form partially molten rock, which rises owing to its low density. The majority of the molten rock solidifies below the surface of the Earth to form plutonic, or intrusive, rocks. Molten rock that reaches the surface and erupts produces a volcano with associated extrusive or volcanic rocks. Magmatic systems are characterized by complicated interactions between the host rock, magma and hydrothermal fluids. It is important to understand these systems for a number of scientific and practical reasons.

A number of fundamental scientific questions can be addressed by studying magmatism. A key question is how magmatic systems can transform mafic input into volcanic rocks with a broad range of compositions. Over geological time, this process has produced the bimodal distribution of crust observed on Earth today.

From a practical point of view, there are a number of compelling reasons for studying magmatic systems, with a specific focus on volcanoes. These are important for understanding the nature of future eruptions, landslides and the potential to generate geothermal energy from the hot water found in the hydrothermal system. Information to address these questions can be obtained from surface observations of erupted lavas, hydrothermal fluids and gases. However, these methods are limited in what they can tell us about the structure of a volcanic system at depth. Geophysical methods are required to investigate the subsurface structure of these regions and a range of techniques can be used, as described elsewhere in this report. Each geophysical method measures a specific parameter that can be used to characterize the subsurface rock structure.

Electrical resistivity is a particularly useful parameter in this regard, because it is highly sensitive to the presence of magma, hydrothermal fluids and the clay alteration produced by interactions of fluids with the host rock. A range of geophysical methods can be used to measure electrical resistivity. Electrical methods, such as direct current (DC) resistivity, uses the injection of electric currents from metal electrodes, and has been used to image the near surface structure of many volcanos and geothermal systems worldwide (Eysteinnsson et al., 1994). Exploration at Mount Meager in the 1970s and 1980s included a number of DC resistivity surveys (Shore, 1975; Shore, 1981). A challenge of the DC resistivity method is that the depth of exploration is proportional to the length of the dipoles used. Thus deeper sounding requires the deployment of large dipoles, and this can be challenging in rugged terrain. Deeper exploration is most efficient with electromagnetic (EM) methods that probe the resistivity structure with either naturally occurring electromagnetic signals, or electromagnetic signals generated by a transmitter. The depth of exploration in these studies is controlled by the frequency of the signal, with the depth of investigation increasing as frequency decreases. For imaging structure below a depth of 1-2 km, EM

methods using natural signals are the most efficient, since it is expensive and logistically complicated to generate powerful, low-frequency EM signals. The most suitable natural source EM method is magnetotellurics (MT), which is an established method that measures electric and magnetic fields at survey points on the surface.

These questions need to be addressed in order to fully understand (1) the hazards associated with future volcanic eruptions and landslides and (2) the nature of the geothermal resource that could be developed from the high temperature reservoir that was discovered in the 1980s. The following three questions are all important for Mount Meager, the most recently active volcano in the Garibaldi Belt of British Columbia. Questions that need to be answered are:

(1) What is the nature of geothermal resources that can be used for energy production?

It is important to quantify the geothermal resources beneath a volcano to determine how much energy could be extracted, either for direct use or electricity generation. Using geophysical data to characterize the geothermal reservoir and the pathways that feed it can assist the development of a power plant by reducing the exploration risk.

(2) What is the size, location and composition of the magma body beneath Mount Meager?

Determining the size and composition of magma bodies beneath the volcano can give information about size of future eruptions, on timescales from days to millennia. The last eruption at Mount Meager occurred 2400 years ago, and recently active fumaroles indicate that the volcano is certainly not extinct. Understanding this assists the development of geothermal energy by defining the deeper source of heat and fluids feeding the present day reservoir. It could also lead to the discovery of concealed geothermal systems.

(3) Are there structures within the volcanic edifice that could cause major landslides?

Volcanic processes, such as hydrothermal circulation, can greatly decrease the strength of a volcanic edifice, and lead to sector collapses and major landslides. Mount Meager was the location of the largest recorded landslide in Canadian history in 2010 (Guthrie et al., 2012). Understanding the internal structure of the volcanic edifice is essential to determine the long term risk for large events. This is also relevant to geothermal development, as it can guide plans to construct infrastructure on a restless volcano.

In the following sections, it will be shown that MT exploration can make significant contributions to answering these three questions.

Magnetotelluric studies at Mount Meager – past and present

The magnetotelluric (MT) method was developed in the 1950's and 1960s and has become a widely used tool in volcano studies and geothermal exploration worldwide (Pellerin et al., 1996; Spichak and Manzella, 2009; Munoz, 2014). A number of prior studies have used MT exploration at Mount Meager.

The first MT studies at Mount Meager were reported from a program of exploration described by Pham (1977), Pham (1978) and Pham (1980). In total 17 MT soundings were collected and it was proposed that a shallow conductor was present at a depth of 2-4 km and likely partial melt. MT exploration continued with a survey of 7 MT soundings in 1982 reported by Flores-Luna, (1986). A combination of 1-D, 2-D and 3-D analysis was undertaken and reported a north dipping conductor (Flores-Luna, 1986). This study discounted the presence of the shallow conductor at a depth of 2-4 km reported by Pham (1978). Jones and Dumas (1993) presented a more detailed analysis of the previously collected MT data, combined with new Lithoprobe data that were collected in the in the Garibaldi Belt. This study applied

novel techniques to remove galvanic distortion from the MT data and gave evidence for both a shallow conductor that was possibly a geothermal reservoir and a deeper regional conductor at 10-15 km depth.

In all these prior studies, MT instruments were bulky, thus limiting the number of stations collected to vehicle accessible locations mostly along Meager Creek. The MT data analysis techniques available were hampered by the small number of stations, but reported a low resistivity layer that was identified as a geothermal reservoir. A more recent analysis of the Lithoprobe MT data, combined with more recent MT measurements made in 2006 gave the 2-D model shown in Rippe et al. (2013). This ABC-N profile passes close to Mount Meager.

In 2001 a more detailed commercial MT survey collected 30 stations on the south slope of the Mount Meager volcanic complex (Candy, 2001). This gave a clearer impression of the geometry of the low resistivity layer. However, the combined MT dataset from surveys in the 1980's and 2001 is insufficient to reliably image the 3-D structure of the geothermal system, the magmatic system or image subsurface structures that may control the strength of the volcanic complex.

To address the shortcomings of the previously collected data, the 2019 research program that is described in this report included a systematic component of MT exploration. This was motivated by the fact that (1) previous studies had identified a significant low resistivity target, but had insufficient station coverage to adequately define the geometry of the target and (2) since 2001 the MT method has advanced greatly and can now generate fully 3-D resistivity models because of improved instrumentation, new inversion algorithms, and accessibility to greater computer processing power.

Two types of MT were conducted at Mount Meager in 2019:

- (1) A detailed survey of the geothermal reservoir previously detected on the south side of Pylon Peak was carried out using higher frequency audio-magnetotelluric (AMT) data by the group from Natural Resources Canada and is described in Chapter 6. The goal of the survey was to use the new MT data to determine permeability variations in the subsurface and link these to flow rates observed at the surface and in boreholes. Since the target was in the upper 1-2 km, this only requires high frequency MT measurements in the band 10000 – 1 Hz. These are referred to as AMT data.
- (2) A more regional MT survey, aimed at studying the deeper parts of the geothermal system, and magmatic system was undertaken by the University of Alberta using broadband MT instruments. This is described in detail in this Chapter. The University of Alberta MT research group has used this approach on a number of active volcanos in the Andes in recent years and been able to define the location, size and composition of magma bodies (Comeau et al., 2015; Cordell et al., 2018). At Mount Meager the broadband MT survey was designed to image fluid pathways that carried fluids to the geothermal reservoir and the fumaroles on the Job Glacier. It was also planned that these measurements might define the size and content of any magma bodies present beneath the volcano. With the deeper exploration targets, lower frequencies were used in the broadband magnetotelluric (BBMT) survey than in the AMT survey.

Methods

Broadband MT data recording

The investigation of the hydrothermal and magmatic system at Mount Meager by the University of Alberta used broadband MT data. The value of this exploration method in this context was outlined in the previous section. This geophysical method measures resistivity, a rock property sensitive to the presence of magma, hydrothermal fluids and clay alteration. The deep exploration required in this study (0-20 km) requires the use of low frequency EM signals that are most efficiently used in the magnetotelluric method.

Details of the magnetotelluric method are described by Vozoff (1991) and Simpson and Bahr (2005), and a brief summary is provided here.

As shown in Figure 1, EM waves originate in the atmosphere and travel downwards towards the Earth. At the Earth's surface, most of the energy is reflected back into the atmosphere, but a small fraction of the energy enters the Earth. The depth to which this transmitted signal travels in the Earth depends on both the resistivity of the Earth and frequency of signal through the skin depth equation. It can be shown mathematically that the resistivity of the Earth can be calculated from the ratio of the horizontal electric field and orthogonal horizontal magnetic field at the surface. This gives a value of resistivity that is an average from the surface to a depth equal to one skin depth. By measuring the EM signals at different frequencies, the depth variation of resistivity can be determined.

The instrument used in MT is basically a sensitive radio receiver that measures the electric and magnetic field components of these natural EM signals at the surface of the Earth. The instrument is shown schematically in Figure 2. At Mount Meager the electric fields were measured with dipoles 40-90 metres in length and connected to the ground with porous pot electrodes. One pair of electrodes measured the north-south electric field component and a second pair measured the east-west electric field component. The three orthogonal components of the magnetic field were measured with induction coils. Figures 3 and 4 show the University of Alberta field crew installing and operating the broadband MT instruments at Mount Meager in July 2019.

The duration of the measurement depends on the frequencies to be recorded. Logistics makes it efficient to record MT data for one day at each site, with recording continuing overnight. This typically gives measurements in the frequency band 1000 – 0.001 Hz. From the physics of EM signal propagation in the Earth, these frequencies typically sample from the surface to a depth of 30 – 60 km. Commercial MT instruments are manufactured by a number of companies and have been developed to be very efficient. All MT data collection at Mount Meager in July 2019 used instruments manufactured by Phoenix Geophysics, a Canadian company based in Toronto. The Natural Resources Canada group used the recently introduced MTU-5C system, while the University of Alberta used the older MTU-5A system.

Time series analysis

After MT data collection was completed, a series of standard processing steps were applied to the time series data. The first was that the time series were processed to calculate the spectra of the electric and magnetic field components as a function of frequency. This used the statistically robust method of Egbert and Booker (1986). Since measurements were always made at multiple stations, the remote reference method of Gamble et al. (1979) was used to separate signal from noise. The spectra were then used to compute the apparent resistivity and phase, as a function of frequency. These quantities are important because they depend only on Earth resistivity structure, and not on the characteristics of the EM signals.

Inversion of MT data to produce a resistivity model

The second stage of data analysis was to convert the apparent resistivity and phase data into a model of subsurface resistivity. This used a computer algorithm to implement a process called inversion, which seeks a resistivity model whose response fits the measured MT data to a given statistical tolerance. This process is non-unique, meaning that many resistivity models can be found which all fit a given dataset to within the same statistical tolerance. To overcome this limitation, conditions are imposed on the resistivity model. The most common approach is to require the resistivity model to be as spatially smooth as possible. However other approaches can be used, such as imposing constraints from other geophysical

surveys or geological information from drilling. Depending on the characteristics of the measured MT data, this can be done in 1-D, 2-D or 3-D. In the past, only 1-D and 2-D inversions were practical because of limitations in computer speed and memory. However, in recent years fully 3-D inversions have become practical for large MT datasets. Given the expected 3-D nature of a volcano such as Mount Meager, the focus was on 3-D inversion.

Resistivity model interpretation

The final stage in data analysis is to interpret the resistivity values observed in the resistivity model. Typically, this stage of analysis infers quantities such as the concentration of certain minerals, the porosity of a geothermal reservoir or the fraction of molten rock present in a magma body. There are always multiple explanations for a low resistivity region, which introduces another stage of non-uniqueness into the analysis of MT data. This non-uniqueness can be reduced significantly by using (1) other types of geophysical data collected at the same location and (2) laboratory experiments that measure the resistivity of rocks in the laboratory.

This stage of analysis for the Mount Meager broadband MT data is at an early stage, so detailed results will not be presented in this initial report. Both approaches (1) and (2) will be used to reduce the non-uniqueness of interpretation of 3-D models derived for Mount Meager.

MT data collection and analysis

MT data recording at Mount Meager

The project began with instrument calibration that is an important check on the functioning of the instruments and induction coils. Calibrations were repeated at the end of the survey to confirm that the instrument responses had not changed. The calibration files are included in the data archive, and figures showing the responses are included in Appendix B.

During the broadband MT survey, data were collected at 23 points in July 2019. Standard MT data collection techniques were used, generally without problems. High contact resistances were obtained at some sites, as expected with high resistivity crystalline rocks or ice present in the subsurface.

A total of 20 stations were accessed by helicopter while 3 were accessed by vehicle. The station deployment is shown in Figure 5 and details of each station are listed in Table 1. Time series data were recorded at each station for 1 or 2 days as shown in Figure 6. In the field the MT data were recorded in geomagnetic coordinates with the x-axis oriented to geomagnetic north and the y-axis oriented geomagnetic east.

Since MT is a natural source EM method, the data quality will depend on the signal strength which is out of the control of the user. During the survey, the signal levels were generally low as shown by the K-indices plotted in Figure 6. These low signal levels are as expected, since 2019 was when the minimum activity level in the approximately 11-year solar cycle occurred. However, given the low levels of human-caused electromagnetic noise in the study area, the MT data were generally of good quality, as explained in the following section.

Time series analysis for the Mount Meager data

Time series data from the 23 stations were processed using the statistically robust algorithm of Egbert and Booker (1986). Two typical soundings are shown in Figure 7 and all 23 soundings are shown in Appendix A.

Characteristics of the Mount Meager apparent resistivity and phase data

Apparent resistivity can be considered as an average resistivity of the Earth from the surface to the maximum depth to which the EM signal penetrates. Thus when apparent resistivity is plotted as a function of decreasing frequency, this corresponds to increasing depth in the Earth.

In each sounding there are two curves for apparent resistivity. The first is calculated from the north-south electric field and the east-west magnetic field, and is referred to as the XY component of the data. The second is calculated from the east-west electric field and the north-south magnetic field, and is referred to as the YX component of the data. By looking at both the XY and YX components of the data, information can be determined about whether the subsurface resistivity structure is 1-D, 2-D or 3-D.

Inspection of MT sounding curves can determine the quality of the data. A number of tests can be applied to the data.

- (1) The apparent resistivity and phase curves should be smooth, as a function of frequency. This is generally the case for the Mount Meager data in the frequency band 100 – 0.001 Hz. The accuracy of the apparent resistivity and phase decreases as frequency decreases. This is because for a given recording time, there will be less estimates of the low frequency signals than the high frequency signals. Only station MGR117 has very poor quality data at low frequency, and there are several explanations for this. This recording was made on a day with weak signal levels, with the K-index in the range 0-1. This may also have occurred because this MT station was placed on a rock glacier located just below the summit of Mount Meager. In this case, the high resistivity of the glacial ice may have caused problems with the electric field measurements, or motion of the glacier may have caused magnetic field noise.
- (2) The apparent resistivity and phase should be mutually consistent. It can be shown mathematically that when apparent resistivity increases with decreasing frequency, the phase angle should be in the range 0-45°. Similarly, when the apparent resistivity decreases with decreasing frequency, the phase angle should be in the range 45-90°. This observation provides a self consistency test for MT data and it can be seen to be valid for all the 23 stations collected in July 2019 at Mount Meager.

Visual inspection of the apparent resistivity curves in Appendix A shows a number of features.

- (1) The first is that at high frequency (100 – 1 Hz) the apparent resistivity is quite variable. These high frequency signals measure near surface structure, implying that the actual resistivity is spatially quite variable. This is as expected in volcanic environments where materials with a wide range of resistivity are found. Regions with recently extruded lava can have a resistivity in excess of 1000 Ωm . In contrast, an area where the rock has undergone hydrothermal alteration to form clay minerals can have a resistivity less than 1 Ωm .
- (2) At low frequency (1 – 0.001 Hz) all of the MT curves show a decreasing apparent resistivity in both the XY and YX components. This implies that there is a low resistivity layer at depth beneath the entire survey area. The preliminary 3-D resistivity model presented later in this report confirms this observation. An inversion of the MT data is needed to determine the actual depth of the layer.
- (3) Electric and magnetic fields are each measured in two orthogonal directions. Thus apparent resistivity / phase can be computed from the E_x and H_y components OR from the E_y and H_x

components. These are referred to as the XY and YX data components in Figure 7 and Appendix A. If the XY and YX components are identical for all co-ordinate systems, then this would imply that the subsurface resistivity structure was 1-D. This is clearly not the case for the MT data collected at Mount Meager and presented in Figure 7. The sounding curves shown in Appendix A give evidence of a 3-D resistivity structure, that requires a 3-D approach to inversion.

- (4) The XY and YX curves are often offset and parallel at high frequency (100-1 Hz) showing the presence of complicated effects due to 3-D resistivity structure in the near-surface. These offsets are sometimes referred to as static shifts, and can greatly complicate MT data analysis in volcanic environments (Arnason, 2015).

Apparent resistivity at a given frequency can also be plotted as a map to illustrate spatial variations. Figure 8 shows apparent resistivity and phase at two frequencies in map view. In this figure the average of the XY and YX apparent resistivity is plotted. At the relatively high frequency of 4 Hz shown in Figure 8(a-b), the EM signals are only penetrating to a depth of 1-2 km and a pronounced low in the apparent resistivity can be seen, centered beneath Mount Meager. At the lower frequency of 0.032 Hz shown in Figure 8(c-d) the EM signals are penetrating deeper and a similar pattern of low resistivity is observed.

Characteristics of the Mount Meager induction vector data

MT instruments also measure the vertical component of the magnetic field. Measurement of the vertical magnetic field at Mount Meager is illustrated in Figure 4(a). This quantity is sensitive to horizontal changes in resistivity structure and complements the apparent resistivity and phase data described above. The vertical magnetic field data at a set of stations is conveniently plotted as induction vectors. When plotted in the Parkinson convention, the in-phase component of induction vectors point at conductors (regions of low resistivity). If plotted in the Weise convention, the in-phase component of these vectors points away from conductors. Figure 9 shows the in-phase components of the induction vectors in the Weise convention.

At a frequency of 4 Hz, the EM signals sample the near surface resistivity structure, and the induction vectors plotted in Figure 9(a) illustrate a radial pattern, pointing away from Mount Meager. This indicates that the Mount Meager complex has a low resistivity close to the surface. This is likely caused by hydrothermal fluids and extensive near-surface clay alteration.

At a lower frequency of 0.02 Hz, the EM signals sample deeper resistivity structure, and the induction vectors plotted in Figure 9(b) generally point southwest. This indicates that the resistivity at depth is relatively low to the northeast of the survey area.

3-D magnetotelluric inversion of the Mount Meager broadband MT data

The MT soundings collected in 2019 were combined with selected stations from the 1982 and 2001 surveys to give the array of 30 stations shown in Figure 10. These data were then edited to remove noisy points and interpolated onto a set of 32 frequencies in the bandwidth 0.0005-500 Hz. The ModEM inversion algorithm of Kelbert et al., (2014) was then used to generate a 3-D resistivity model that fits the measured MT data to within a specified tolerance. This is a complicated process, with many inversion runs needed to explore how the final 3-D model depends on the control parameters used, and the degree of model smoothing. Each run typically takes several weeks on a high performance computer cluster. This is a task that is currently in progress at the University of Alberta.

However, some initial 3-D resistivity models have been obtained, and they are starting to show a consistent set of features. Figures 11, 12 and 13 shows a typical resistivity model as both horizontal and vertical slices.

Results

High quality broadband MT data were collected at 23 stations around Mount Meager. This represents the first MT dataset to be able to image mid-crustal depths beneath this restless volcano. The preliminary 3-D resistivity model for Mount Meager is shown in Figures 11, 12 and 13. While this is a preliminary model, some significant model features can be identified as follows.

- (1) From the surface to sea-level the resistivity of the Mount Meager complex is generally high, with a number of low resistivity features with resistivity in the range 1-10 Ωm . These appear to correlate with the location of the fumaroles on the north side of the massif, and with the geothermal resources on the south side above Meager Creek.
- (2) From sea level to a depth of 5 km the crust has a relatively high resistivity in the range 100-1000 Ωm . A few isolated conductors are observed within this layer.
- (3) From 5 – 10 km a pronounced low resistivity layer is observed under most of the Mount Meager Massif with a resistivity in the range 1-10 Ωm . The lowest resistivities are centered beneath the geothermal reservoir in Meager Creek. The cause of this low resistivity is likely a combination of saline fluids, clay alteration and partial melt. A careful analysis constrained by laboratory experiments on rock resistivity is needed to determine the cause of low resistivity. This work is currently in progress.

Summary and Future Work

Summary

The results above have presented the first 3-D resistivity models of the crustal structure beneath Mount Meager. The model shows a low resistivity layer at a depth of 5 km below sea level that is caused by a combination of saline fluids, clay alteration and partial melt. A number of shallower low resistivity features can be identified and interpreted as shallow geothermal reservoirs or zones of hydrothermal alteration.

Ongoing data analysis

Additional data analysis is required and will include the following tasks.

- (1) Additional 3-D MT inversions to investigate how well the measured MT data can resolve the various resistivity features. This will include editing the 3-D resistivity model and restarting the inversion from the edited model. The statistical approach introduced by Lee et al. (2020) for the Krafla geothermal field will be used. Synthetic MT inversions will be used to test 3-D resistivity model resolution.
- (2) Determine the cause of the regions with low resistivity using laboratory studies of rock resistivity. A key aspect of the data analysis will be to address the cause of zones of high and low resistivity found beneath Mount Meager. Resistivity contrasts in this type of environment can be caused by

saline fluids, molten rock or minerals formed by hydrothermal alteration. External constraints are often needed to distinguish between these alternatives. It was once assumed that both geothermal reservoirs and magma bodies always had a low resistivity. However careful laboratory experiments in recent years have shown that these assumptions are not always valid (Pommier and Le Trong, 2011). The resistivity of molten rock depends on the composition, and a high silica content can often produce molten rock with a relatively high resistivity making detection with electromagnetic methods challenging (Cordell et al., 2018; Lee et al., 2020). Similarly, in high temperature geothermal fields, the clay alteration minerals formed do not necessarily have a low resistivity, resulting in a reservoir that can be relatively resistive compared to the surrounding rock (Arnason et al., 2000). Analysis of the new 3-D resistivity models from Mount Meager will benefit greatly from the other geological and geophysical datasets available – both those collected in the 2019 field campaign, and in previous exploration.

- (3) Systematic comparison of the 3-D resistivity model with other available geophysical datasets. This will include the resistivity models obtained from DC resistivity exploration (Shore, 1981) and the seismic and gravity studies that took place in 2019.

Need for additional data

The MT data collected at Mount Meager were generally good in quality, and will give a reliable inversion model. However, a major limitation was the relatively large station spacing, and the irregular grid caused by the lack of MT stations in the Upper Lillooet Provincial Park. Developing a more complete model of the 3-D resistivity structure will require additional stations in key areas. Synthetic inversions will be used to investigate the optimum MT station layout.

Data

The measured MT time series data have been provided as requested and consist of the following files :

- (a) A summary of the data acquisition is provided in an Excel file listing recording dates, locations and recording parameters.
- (b) The time series data files are sorted by recording date, with one folder being provided for each day. This means that synchronous recordings are in the same folder, and facilitates the use of remote reference processing to improve the quality of the response. For each recording, there are four files:

The run information data is contained in a file with extension TBL. Data were recorded with three sample rates and each is contained in a single file with extension TS3, TS4 or TS5

- (c) The calibration files recorded at the start and end of the survey. The instrument calibrations are contained in the files with extension CLB. Induction coil calibrations are contained in files with the extension CLC.

These data can be viewed using the program SyncTSV provided by Phoenix Geophysics. The data files can be processed using the SSMT software package, also produced by Phoenix Geophysics.

References

- Arnason K, The Static Shift problem in MT Soundings, Proceedings of the World Geothermal Congress, Melbourne, Australia, 19-25 April 2015
- Arnason K, Karlsdottir R, Eysteinnsson H, Flovenz OG, Gudlaugsson ST, The resistivity structure of high-temperature geothermal systems in Iceland, World Geothermal Congress, 2000.
- Comeau M, MJ Unsworth, F Ticona, M Sunagua, Magnetotelluric images of magma distribution beneath Volcan Uturuncu, Bolivia : Implications for magma dynamics, *Geology*, 43(3), 243-246, March 2015.
- Candy C, Crew Development Corporation report on a magnetotelluric survey : South Meager Geothermal Project, Pemberton, British Columbia, Frontier Geosciences project FG1-581, 2001.
- Cordell DR, MJ Unsworth, D Diaz, Imaging the Laguna del Maule Volcanic Field, central Chile using magnetotellurics: Evidence for crustal melt regions laterally-offset from surface vents and lava flows, *Earth and Planetary Science Letters*, 488, 168-180, 10.1016/j.epsl.2018.01.007, 2018 (accepted January 9 2018)
- Egbert GD, and J. R. Booker, Robust estimation of geomagnetic transfer functions, *Geophysical Journal of the Royal Astronomical Society*, 87, 173-194, 1986.
- Eysteinnsson H, K Arnason and OG Flovenz, Resistivity methods in geothermal prospecting in Iceland, *Surveys in Geophysics*, 15, 263-275, 1994.
- Flores-Luna CF, Electromagnetic induction studies over the Meager Creek Geothermal Area, British Columbia: Research in Applied Geophysics No. 37, University of Toronto, 1986
- Gamble TB, WM Goubau, J Clarke, Magnetotellurics with a remote reference, *Geophysics*, 44, 53-68, 1979
- Guthrie RH et al., The 6 August 2010 Mount Meager rock slide-debris flow, Coast Mountains, British Columbia: characteristics, dynamics, and implications for hazard and risk assessment, *Nat. Hazards Earth Syst. Sci.*, 12, 1277–1294, 2012
- Jones, A.G., and I. Dumas, Electromagnetic images of a volcanic zone, *Physics of the Earth and Planetary Interiors*, 81, 289-314, 1993.
- Kelbert A, N Meqbel, GD Egbert, K Tandon, ModEM : A modular system for inversion of electromagnetic geophysical data, *Computers and Geosciences*, 66, 40-53, 2014
- Lee BM, Unsworth MJ, Arnason K, Cordell DR, Imaging the magmatic system beneath the Krafla geothermal field, Iceland : A new 3-D electrical resistivity model from inversion of magnetotelluric data, *Geophysical Journal International*, 2020.
- Munoz G, Exploring for Geothermal Resources with Electromagnetic Methods, *Surveys in Geophysics*, 35, 101-122, 2014.
- Pellerin L, JM Johnston and GW Hohmann, A numerical evaluation of electromagnetic methods in geothermal exploration, *Geophysics*, 61, 121-130, 1996.
- Pommier A, E Le Trong, SIGMELTS : A web portal for electrical conductivity calculations in geosciences, *Computers and Geosciences*, 37, 1450-1459, 2011.
- Rippe D, MJ Unsworth and CA Currie, Magnetotelluric constraints on the fluid content of the upper mantle beneath the southern Canadian Cordillera: implications for rheology, *Journal of Geophysical Research*, 118(10), doi:10.1002/jgrb.50255, October 2013

Shore GA, Deep Resistivity Surveys and Supplementary Geophysics at Meager Creek selected area, Pemberton BC, report prepared for British Columbia Hydro and Power Authority, report G.T. 4, 1975

Shore GA, Report on DC resistivity survey in the Meager Creek Geothermal Area 1980, report prepared for British Columbia Hydro and Power Authority, report G.T. 26, 1981

Simpson F and K Bahr, Practical magnetotellurics, Cambridge University Press, 2005

Spichak V and A Manzella, Electromagnetic sounding of geothermal zones, Journal of Applied Geophysics, 68, 459-478, 2009.

Pham van Ngoc, Magnetotelluric reconnaissance survey in the Lilloet Valley, BC, Earth Physics Branch Open File 77-20, Earth Physics Branch, Department of Energy, Mines and Resources, Ottawa, 40 pp., 1977.

Pham van Ngoc, Magnetotelluric prospecting in the Mount Meager Geothermal Region, Earth Physics Branch Open File 78-6E, Earth Physics Branch, Department of Energy, Mines and Resources, Ottawa, 31 pp., 1977.

Pham van Ngoc, Magnetotelluric survey of Mount Meager and the region of the Squamish Valley, Earth Physics Branch Open File 80-8E, Earth Physics Branch, Department of Energy, Mines and Resources, Ottawa, 77 pp., 1980.

Vozoff K, The magnetotelluric method, in Electromagnetic Methods in Applied Geophysics, Vol2B 641-711, Society of Exploration Geophysicists, 1991

Acknowledgements

This research was supported by an NSERC Discovery Grant to Martyn Unsworth, and an award from the Future Energy Systems program at the University of Alberta. The 3-D inversions were performed on the high performance computer clusters operated by Compute Canada. Gary Egbert, Anna Kelbert and Naser Meqbel are thanked for allowing the use of the ModEM inversion program. Jim Craven at the Geological Survey of Canada is thanked for his help in preparing the MT instruments for use in the field at Mount Meager. Steve Grasby is thanked for his leadership of the project and assistance in securing funding and planning field logistics. Cliff Candy at Frontier Geosciences is thanked for making the 2001 Geosystem data available for this research.

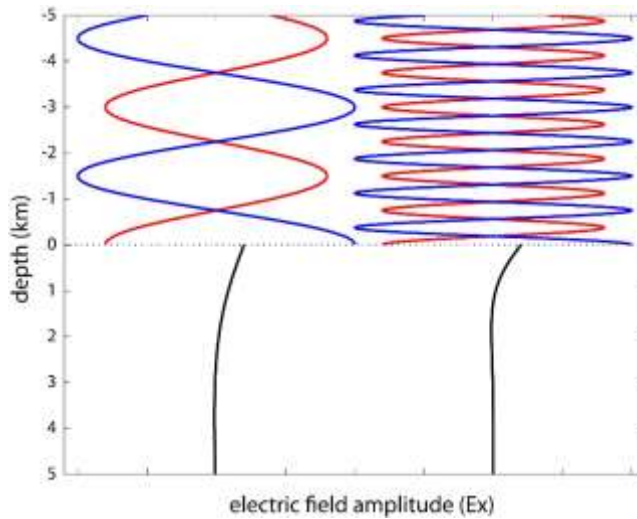


Figure 1 : Schematic of the electromagnetic (EM) signals used in magnetotelluric exploration. The blue lines show a low frequency signal (left) and high frequency signal (right) incident on the surface of the Earth. Most of the energy is reflected back into the atmosphere (red), and a small fraction is transmitted into the Earth (black). Within the Earth the EM energy travels by diffusion. Note that the low frequency signal travels deeper into the Earth than the high frequency.

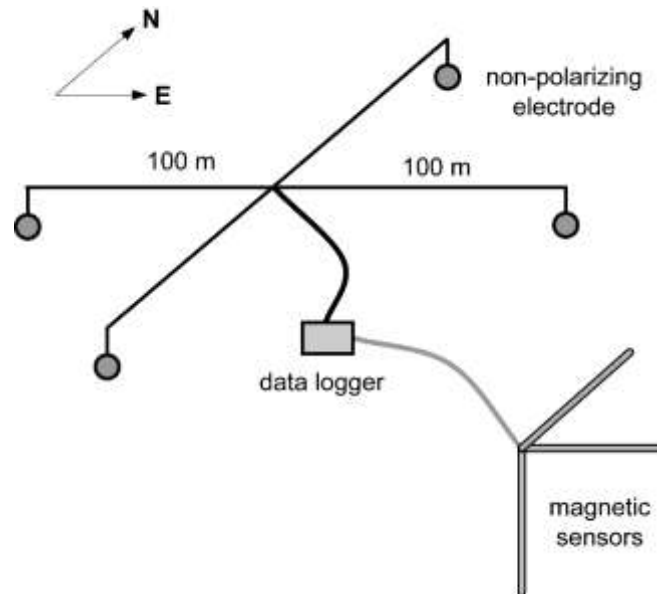


Figure 2 : Schematic diagram of a broadband magnetotelluric station used to measure the electric and magnetic fields. The electric fields are measured in the north-south and east-west directions using pairs of non-polarizing electrodes. The magnetic fields are measured in north-south, east-west and vertical directions using induction coils.



Figure 3: Photographs of the University of Alberta field crew installing and operating Phoenix Geophysics MT instruments at Mount Meager in July 2019. (a) Helicopter departing from station MGR108 (b) Data being recorded at station MGR108 with a Phoenix Geophysics MTU5A instrument (c) Field crew at station MGR 116 (d) Data collection from the instrument at station MGR116.



Figure 4 : (a) Installation of the induction coil measuring the vertical magnetic field at station MGR111
(b) field camp at the foot of Mount Meager.

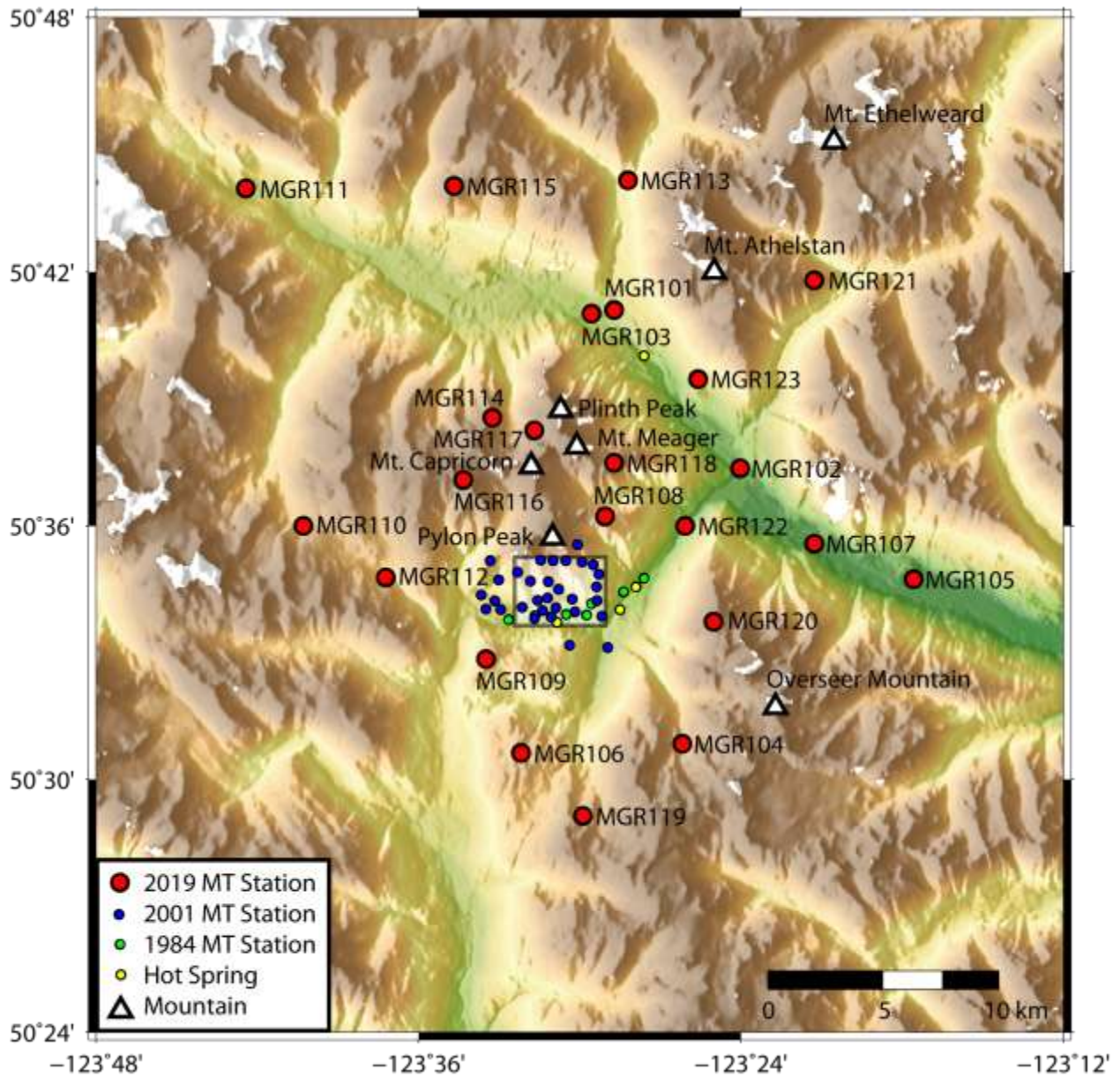


Figure 5 : Map of the Mount Meager area showing previously collected MT data, and data collected in 2019 by the University of Alberta. Rectangle shows the approximate extent of the South Meager geothermal area.

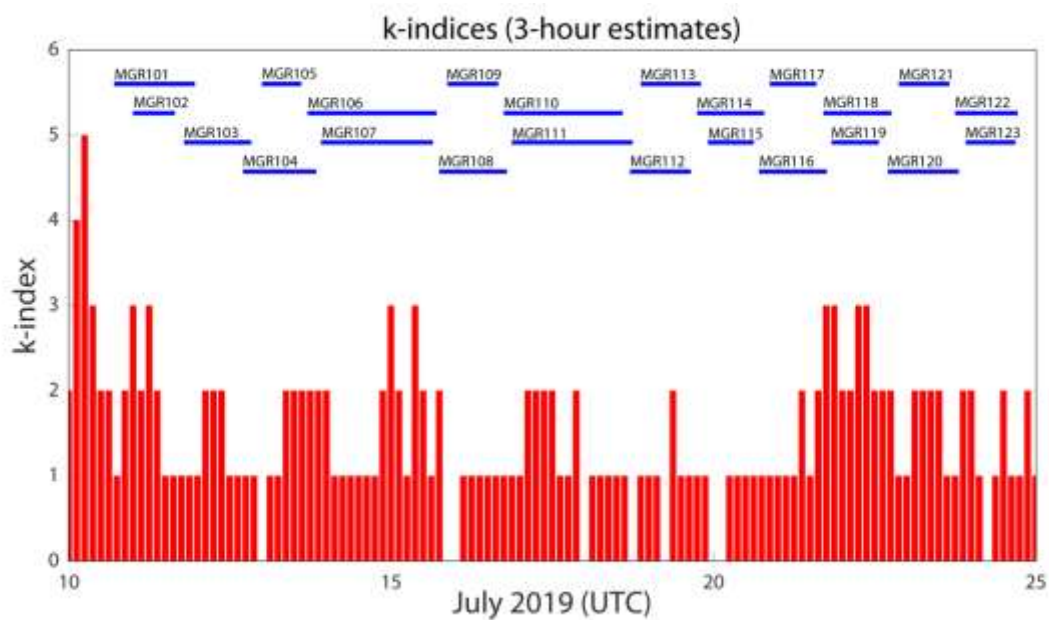
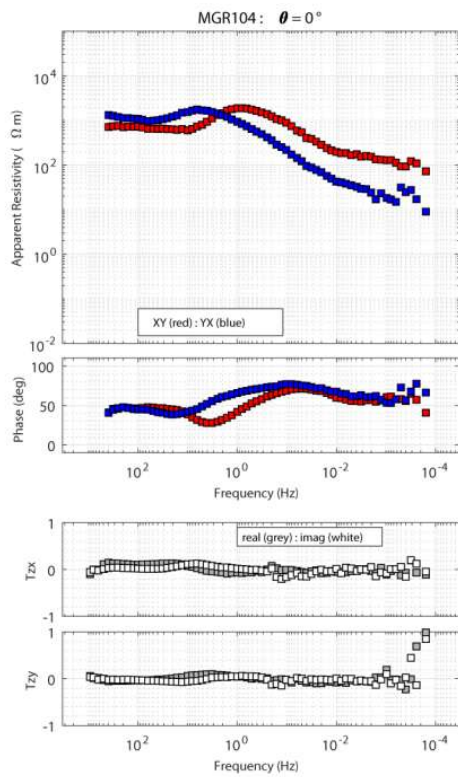
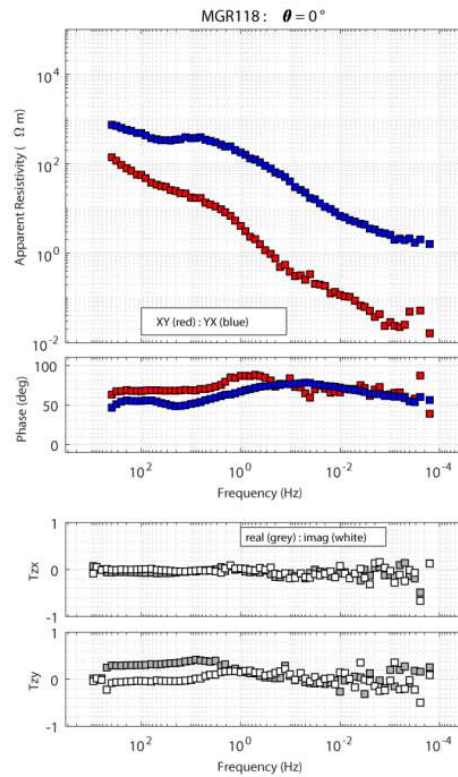


Figure 6 : K-index as a function of date during the July 2019 survey at Mount Meager. The recording times of the 23 magnetotelluric stations are also shown.



(a)



(b)

Figure 7 : Apparent resistivity and phase curves at two representative stations recorded in July 2019 at Mount Meager by the University of Alberta. (a) MGR104 and (b) MGR118

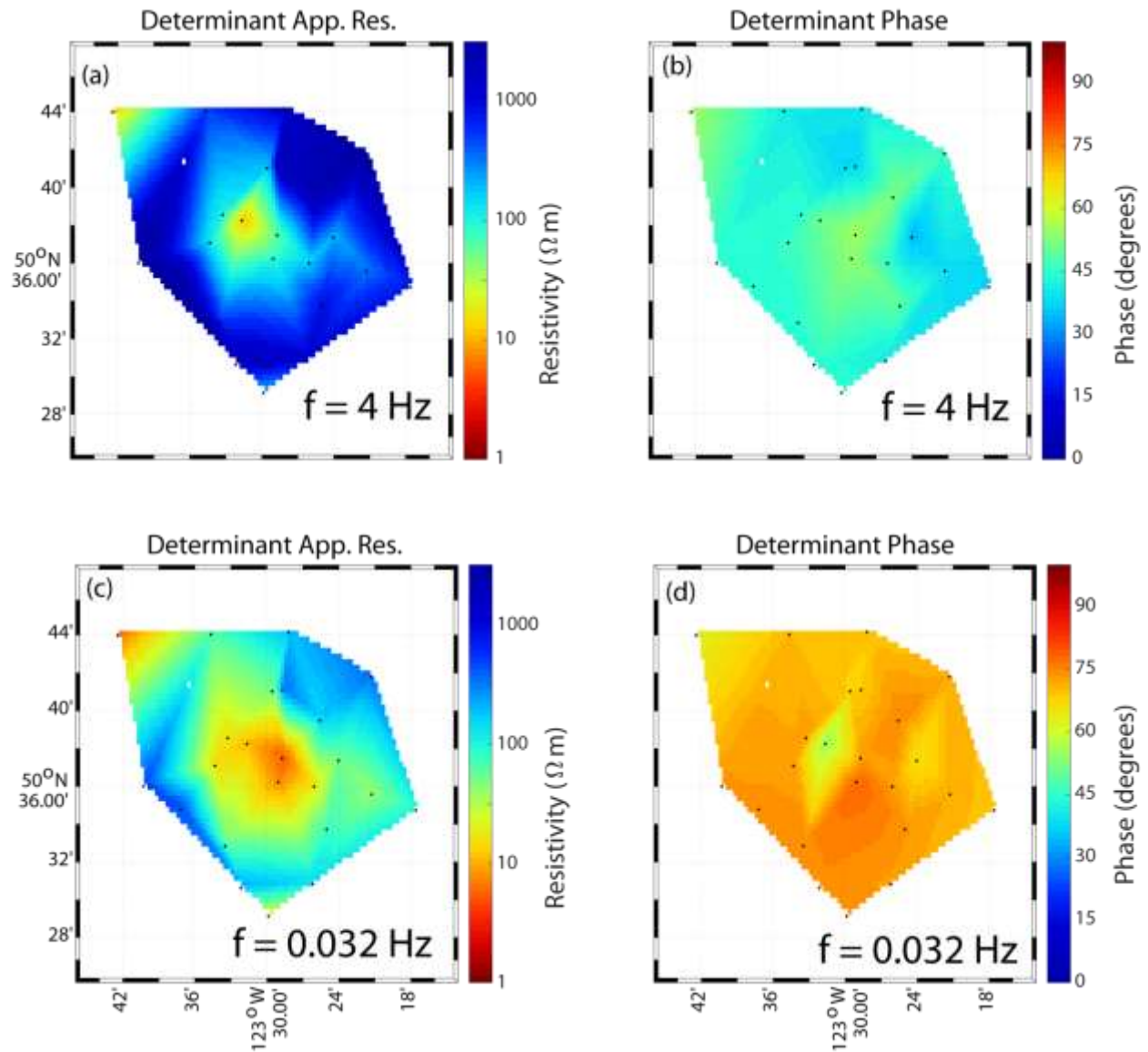


Figure 8 : Map of apparent resistivity and phase at two representative frequencies. (a) and (c) show the average value of the apparent resistivity computed from the north-south and east-west electric fields. (b) and (d) show the corresponding phases.

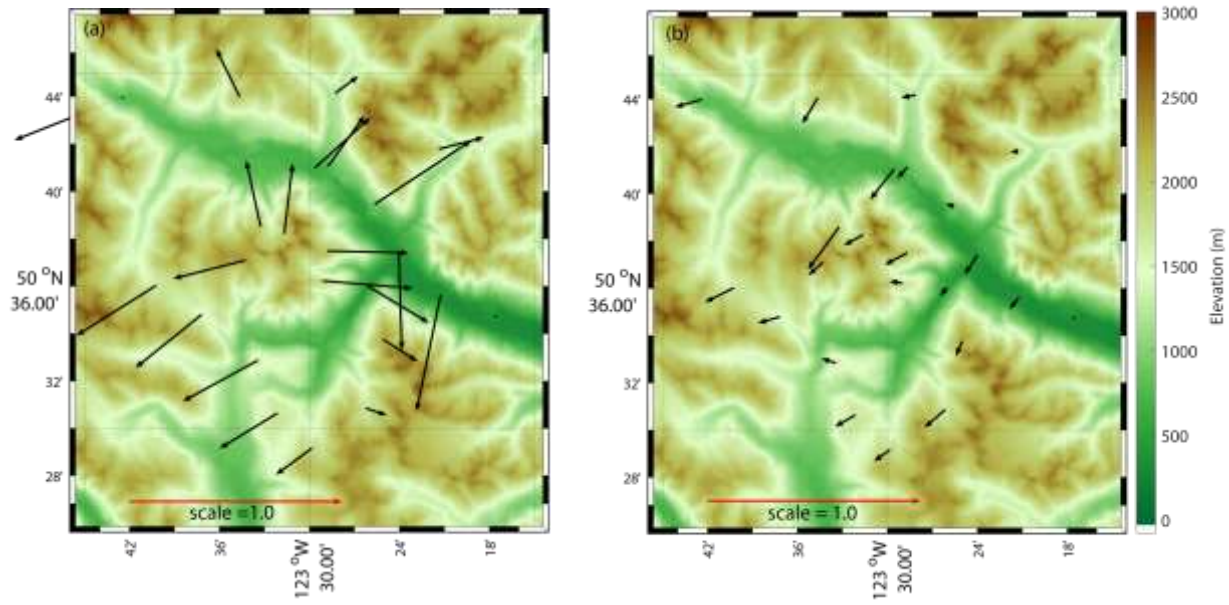


Figure 9 : Map of induction vectors at two representative frequencies. Induction vectors are plotted in the Weise convention and point away from zones of low resistivity (high conductivity). (a) shows data at a frequency of 4 Hz and most vectors point away from the Mount Meager volcanic complex, showing that at shallow depth it is characterized by low resistivity. (b) show induction vectors at a lower frequency of 0.02 Hz which penetrate deeper into the Earth. These vectors consistently point southwest, indicating that conductivity increases to the northeast.

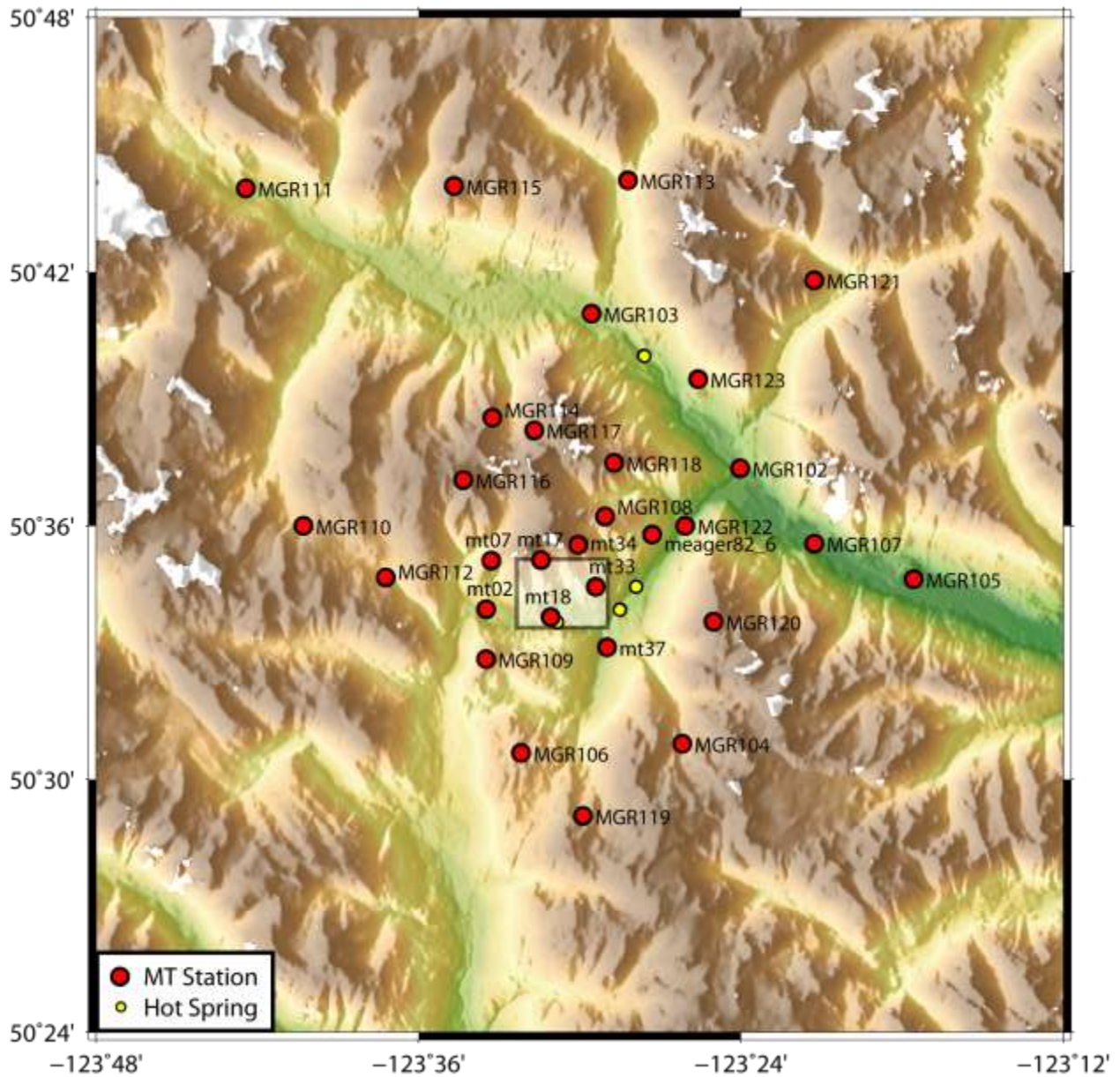


Figure 10 : Map of all MT stations used in the 3-D inversion. This uses a combination of the three broadband MT datasets collected in 1982, 2001 and 2019 that were shown in Figure 5. Rectangle shows the approximate extent of the South Meager geothermal area.

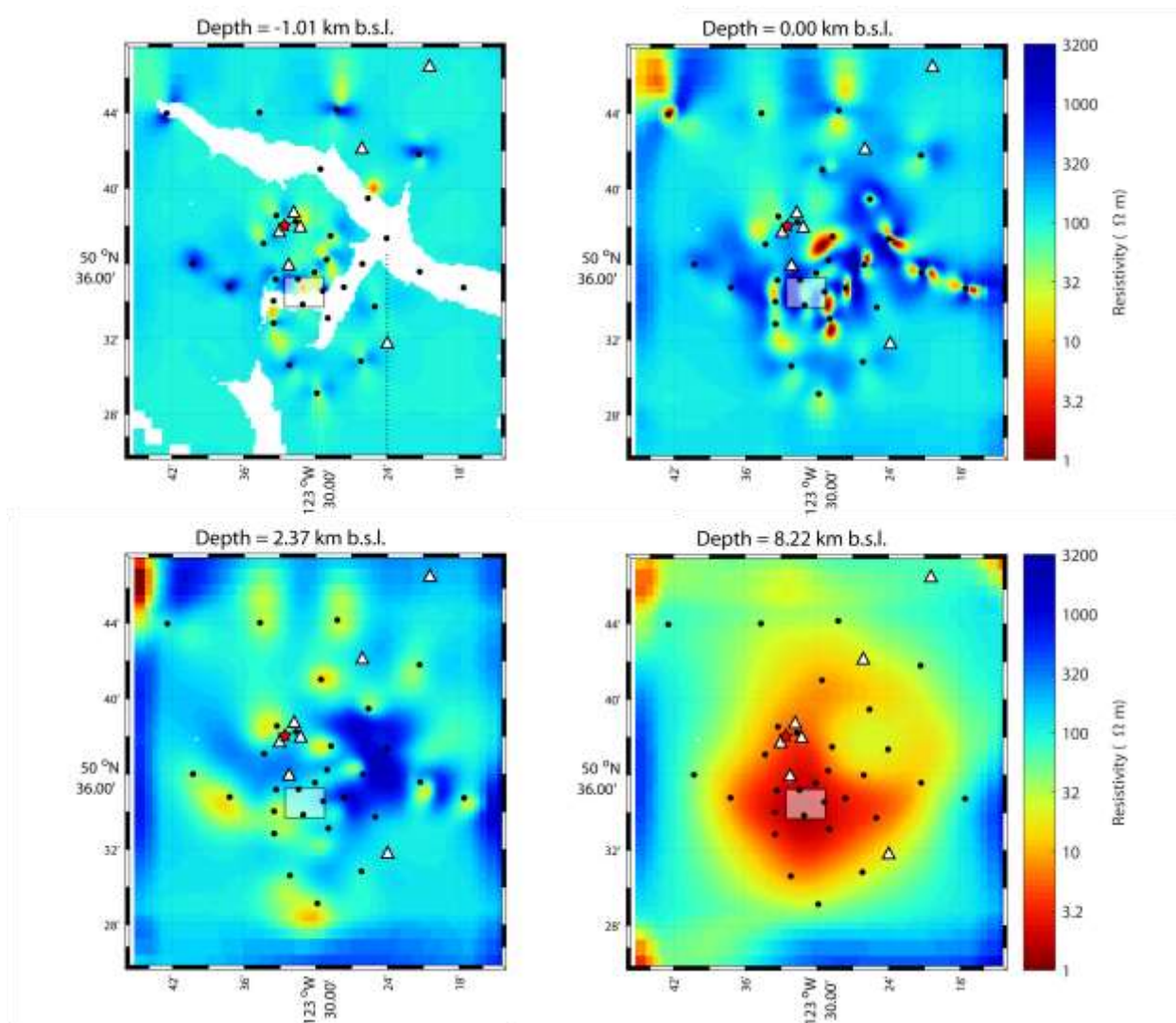


Figure 11: Horizontal slices of the preliminary 3-D resistivity model obtained by inversion of the Mount Meager broadband MT dataset using the 3-D ModEM inversion. Inversion files from folder s30p32r8-Topo2-run6-iter041. (a) 1 km above sea level (b) sea level (c) 2.37 below sea level and (d) 8.21 km below sea level. Fumaroles on Job Glacier are shown by the star. Rectangle shows the approximate extent of the South Meager geothermal area.

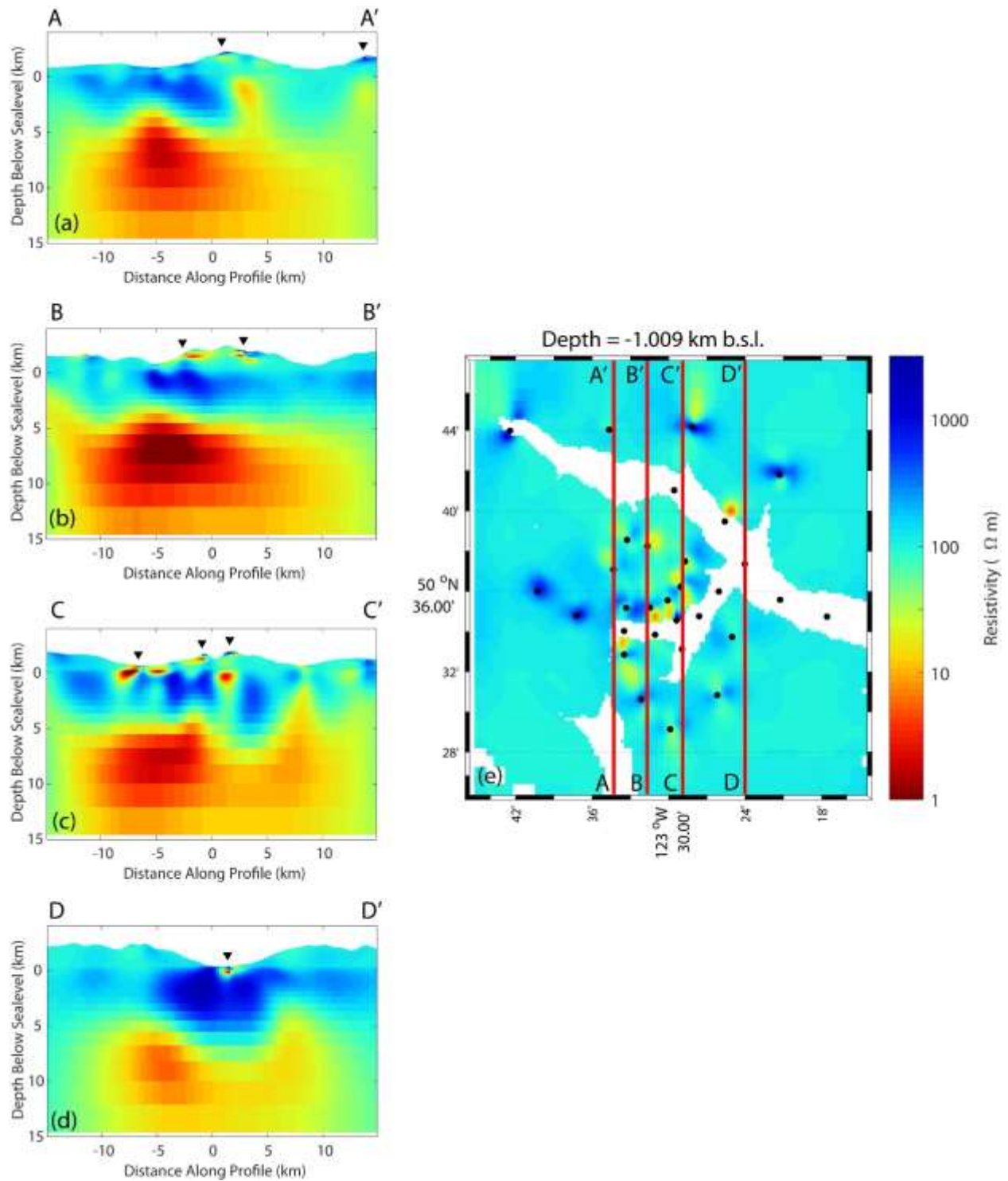


Figure 12: Vertical north-south slices of the preliminary 3-D resistivity model obtained by inversion of the Mount Meager broadband MT dataset using the 3-D ModEM inversion. Inversion files from folder s30p32r8-Topo2-run6-iter041. (a)-(d) show four north-south transects with locations show in (e).

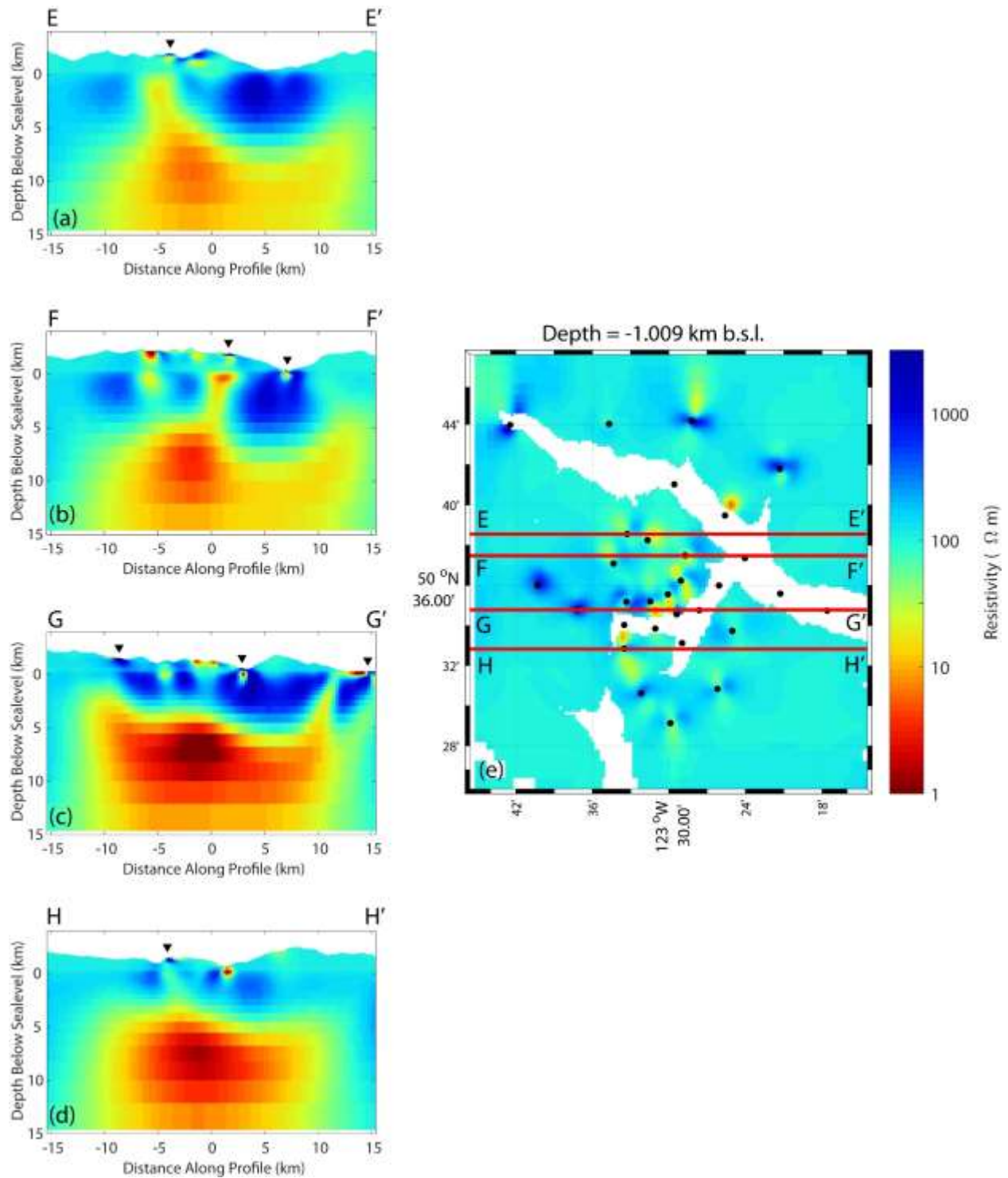


Figure 13: Vertical east-west slices of the preliminary 3-D resistivity model obtained by inversion of the Mount Meager broadband MT dataset using the 3-D ModEM inversion. Inversion files from folder s30p32r8-Topo2-run6-iter041. (a)-(d) show four north-south transects with locations show in (e).

Date of Deployment	Station Name	Latitude (°N)	Longitude (°W)	Elevation (m)	N-S Line (m)	E-W Line (m)	Helicopter or Truck
2019/07/10	MGR101	50.685	123.478	726	27	35	T
2019/07/10	MGR102	50.623	123.401	411	53	58	T
2019/07/11	MGR103	50.684	123.493	675	60	77	H
2019/07/12	MGR104	50.514	123.436	1713	57	51	H
2019/07/12	MGR105	50.579	123.293	343	52	57	T
2019/07/13	MGR106	50.510	123.536	1613	47	75	H
2019/07/13	MGR107	50.593	123.354	363	53	59	H
2019/07/15	MGR108	50.604	123.484	1827	52	57	H
2019/07/15	MGR109	50.547	123.558	1597	52	75	H
2019/07/16	MGR110	50.600	123.671	1628	64	54	H
2019/07/16	MGR111	50.733	123.707	805	53	62	H
2019/07/18	MGR112	50.580	123.620	1484	53	88	H
2019/07/18	MGR113	50.736	123.470	1200	61	52	H
2019/07/19	MGR114	50.643	123.554	1970	52	52	H
2019/07/19	MGR115	50.734	123.578	1960	55	54	H
2019/07/20	MGR116	50.618	123.572	2335	40	52	H
2019/07/20	MGR117	50.638	123.528	1946	66	47	H
2019/07/21	MGR118	50.625	123.479	2028	52	73	H
2019/07/21	MGR119	50.486	123.498	1789	63	56	H
2019/07/22	MGR120	50.562	123.417	2213	57	54	H
2019/07/22	MGR121	50.697	123.355	1823	54	88	H
2019/07/23	MGR122	50.600	123.434	508	88	54	H
2019/07/23	MGR123	50.658	123.427	925	44	38	H

Table 1 : Details of MT soundings recorded at Mount Meager in July 2019 by the University of Alberta

Appendix A : MT sounding curves from Mount Meager

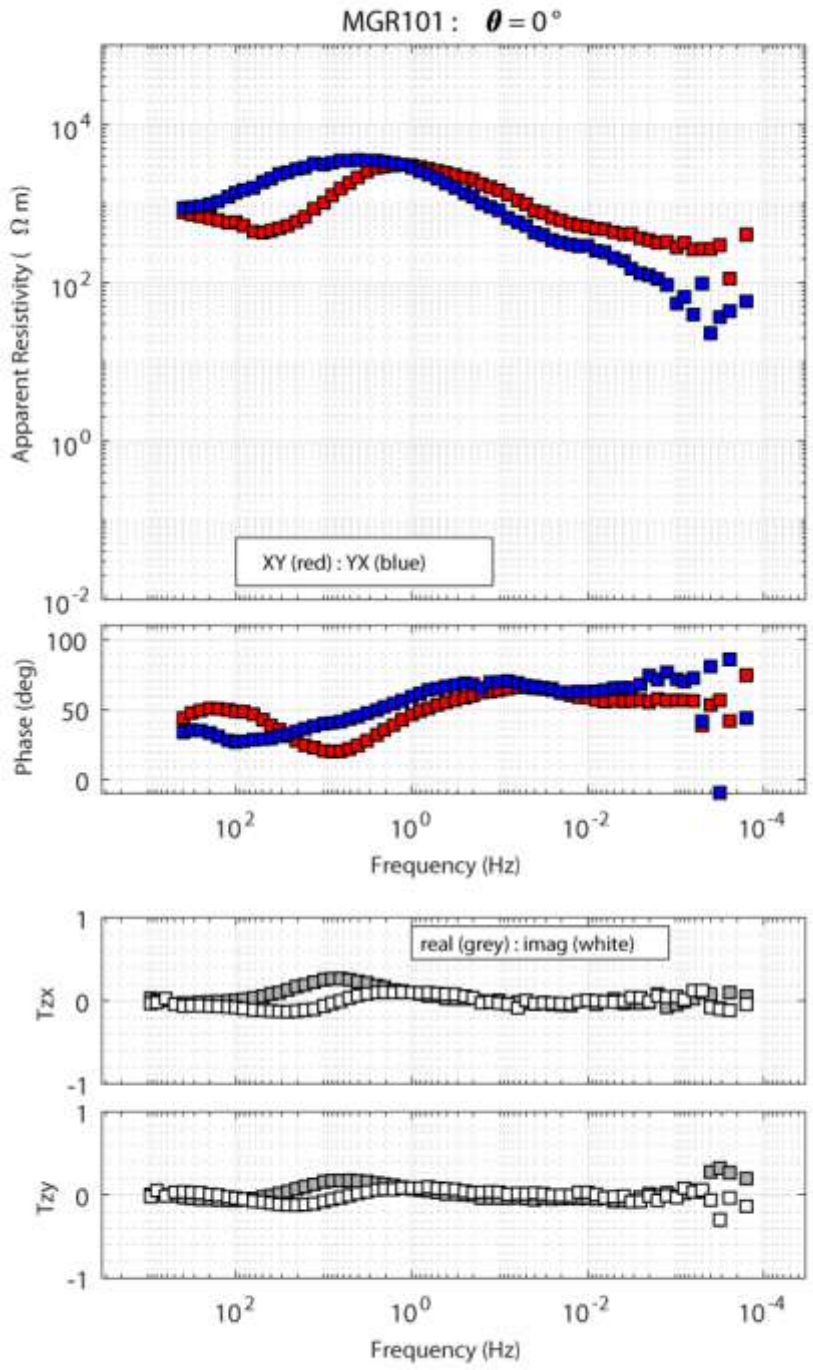


Figure A1 : MT sounding MGR101

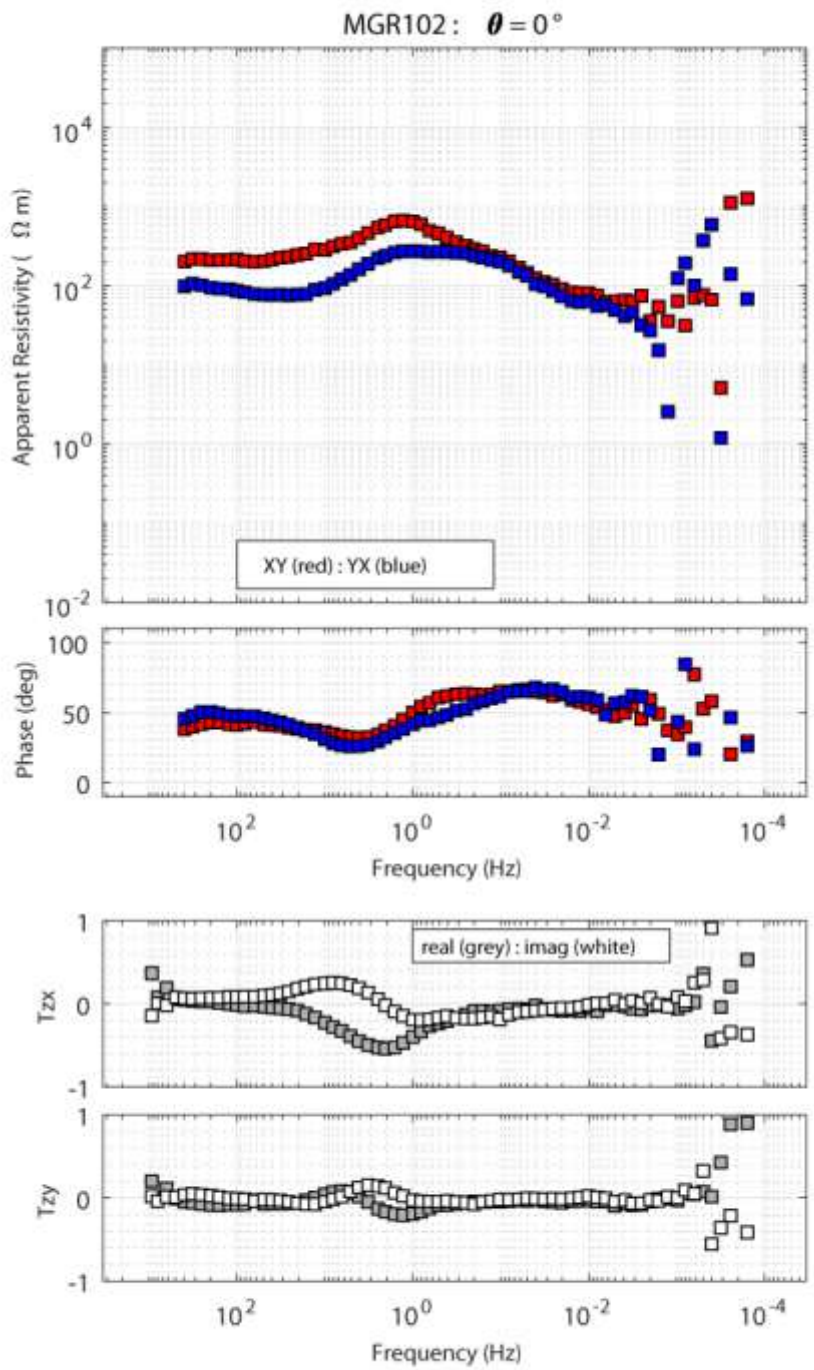


Figure A2 : MT sounding MGR102

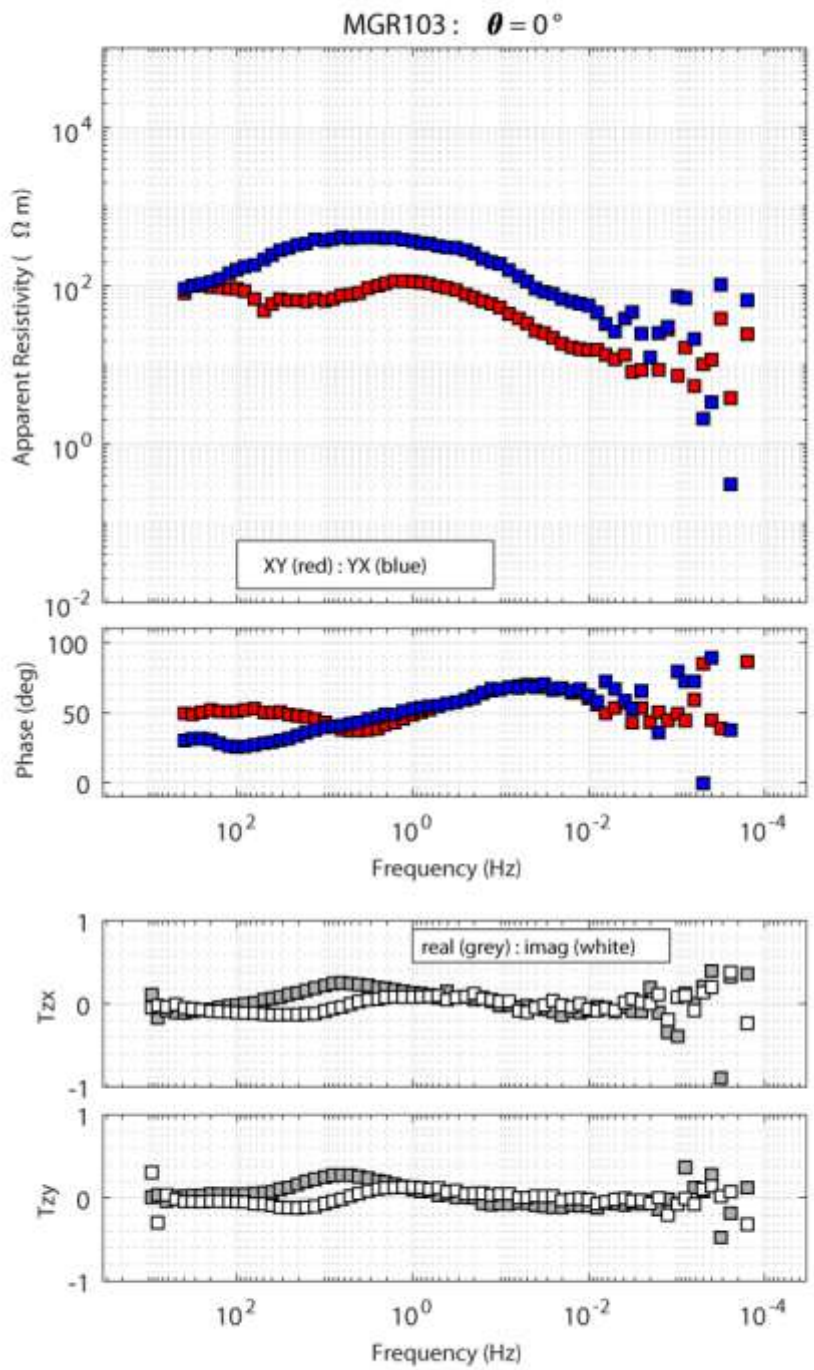


Figure A3 : MT sounding MGR103

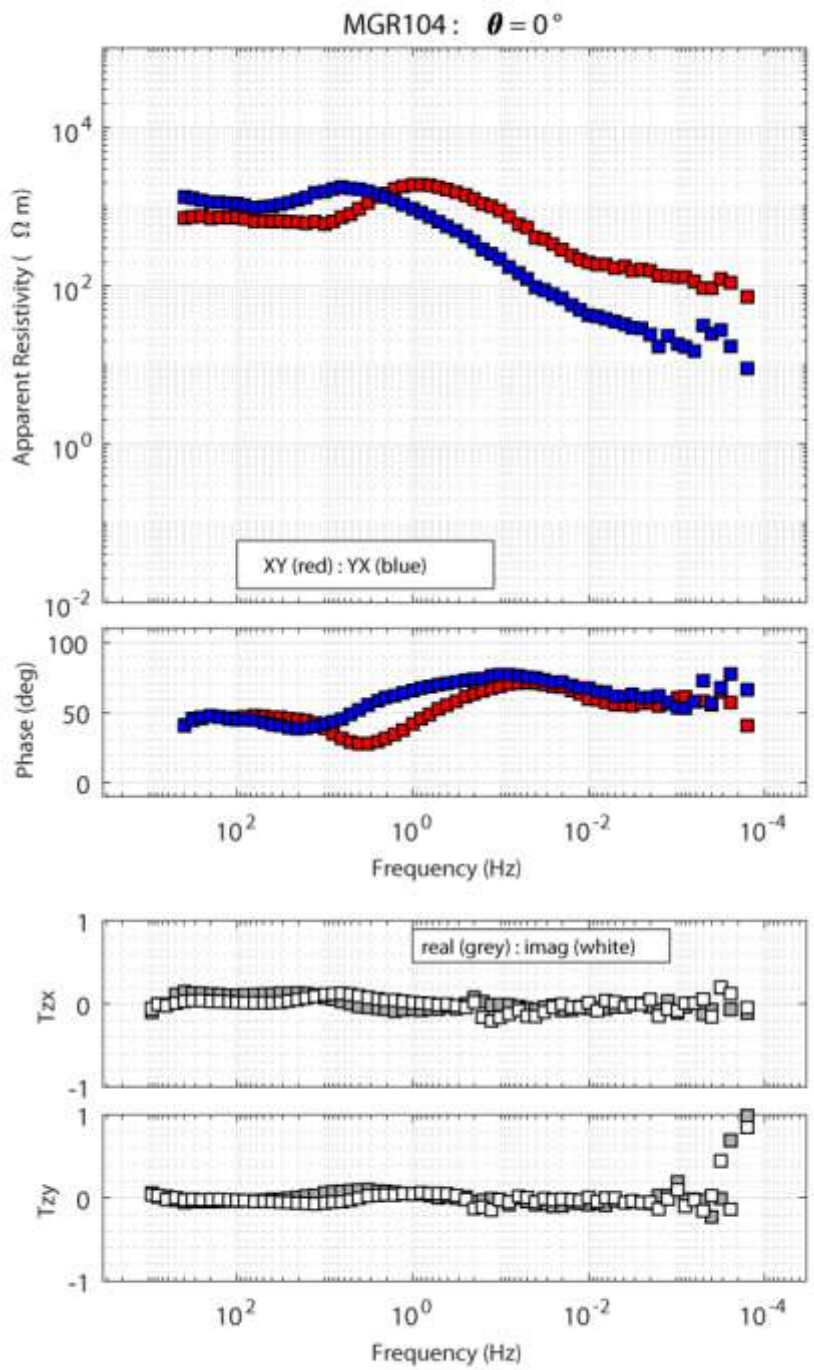


Figure A4 : MT sounding MGR104

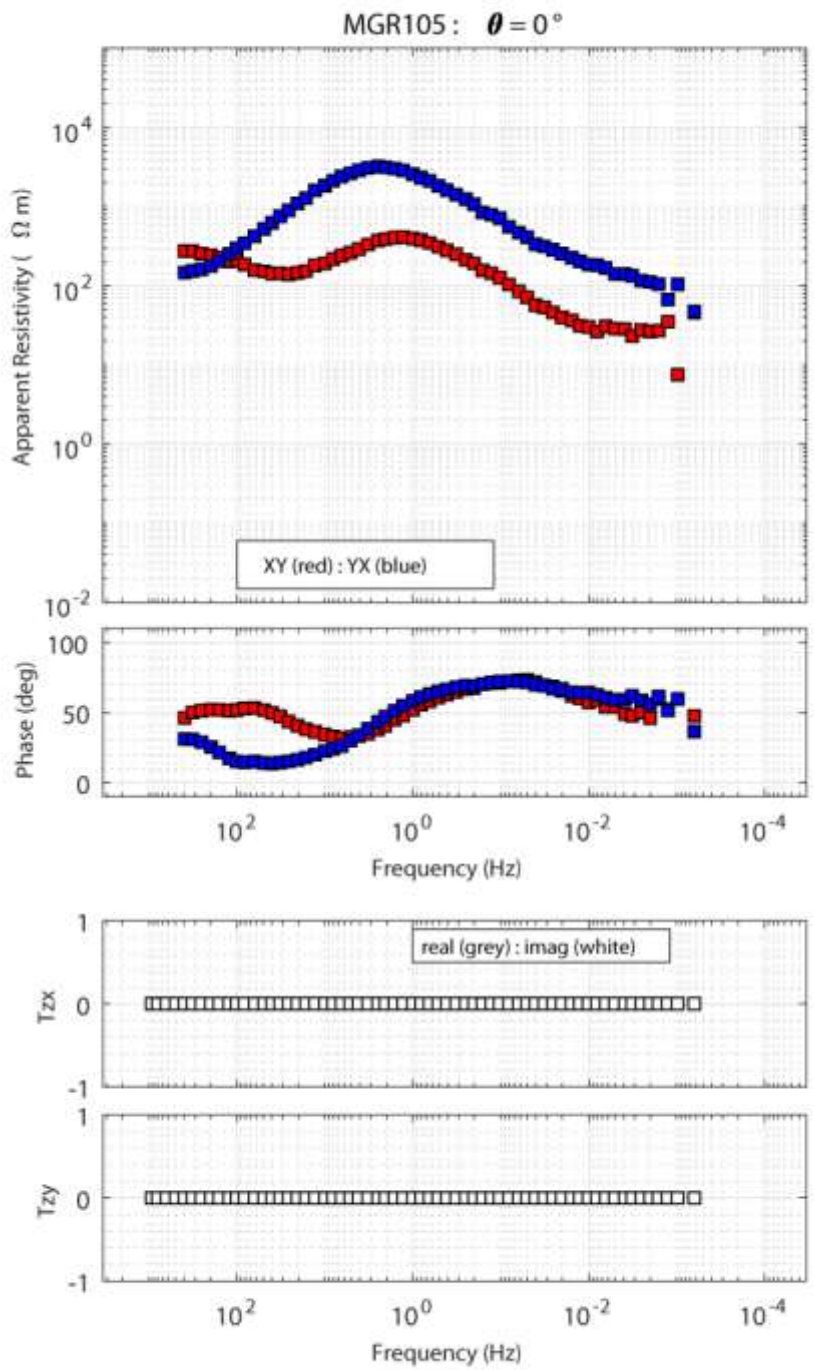


Figure A5 : MT sounding MGR105

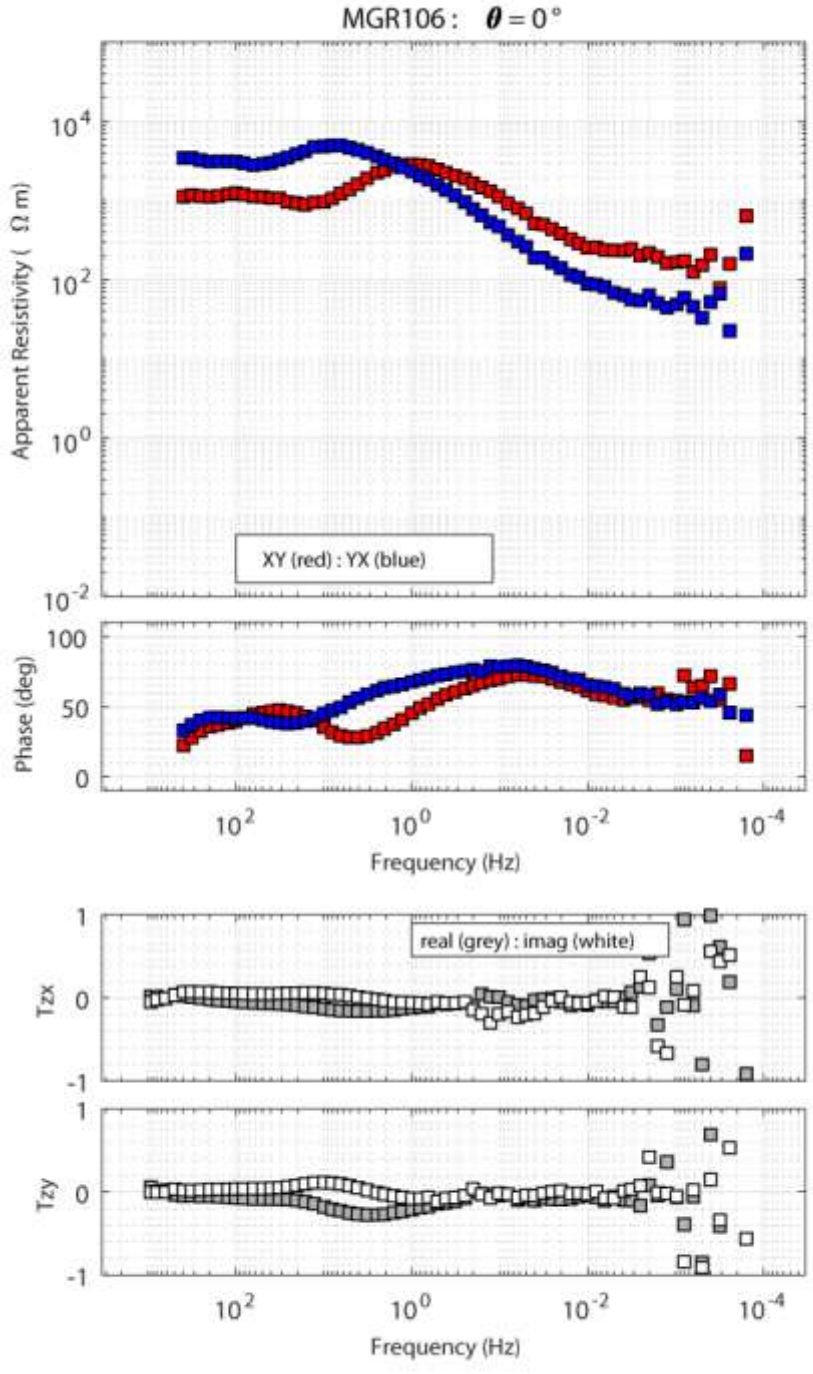


Figure A6 : MT sounding MGR106

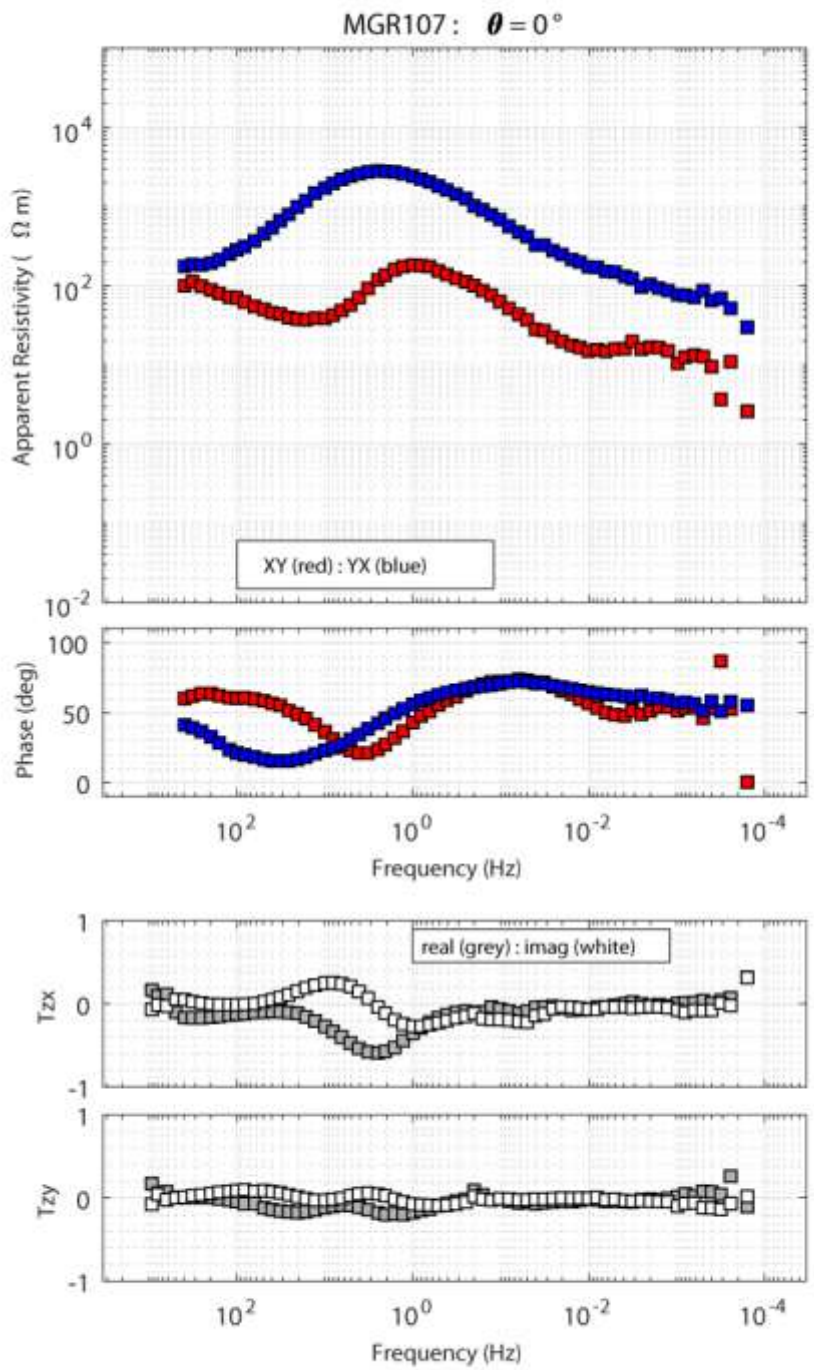


Figure A7 : MT sounding MGR107

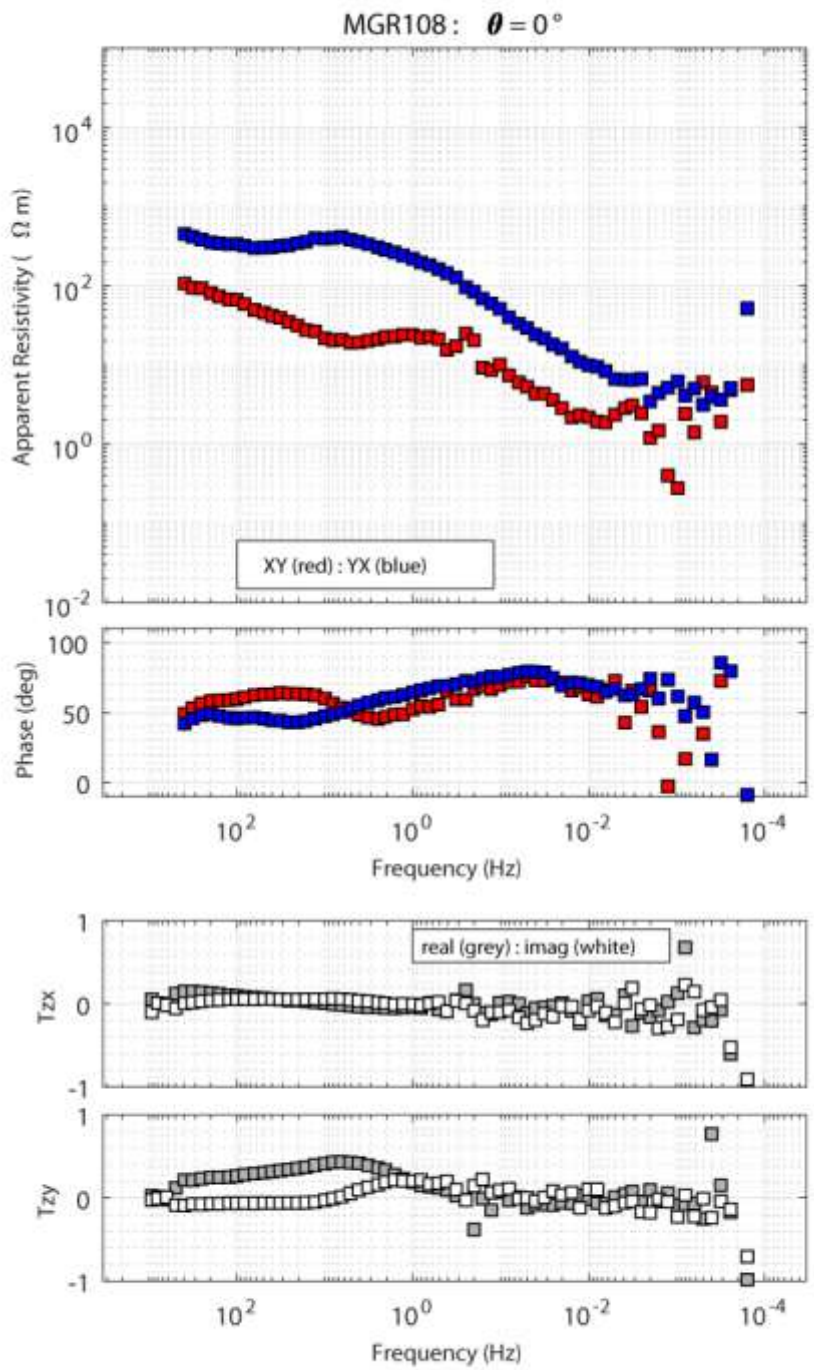


Figure A8 : MT sounding MGR108

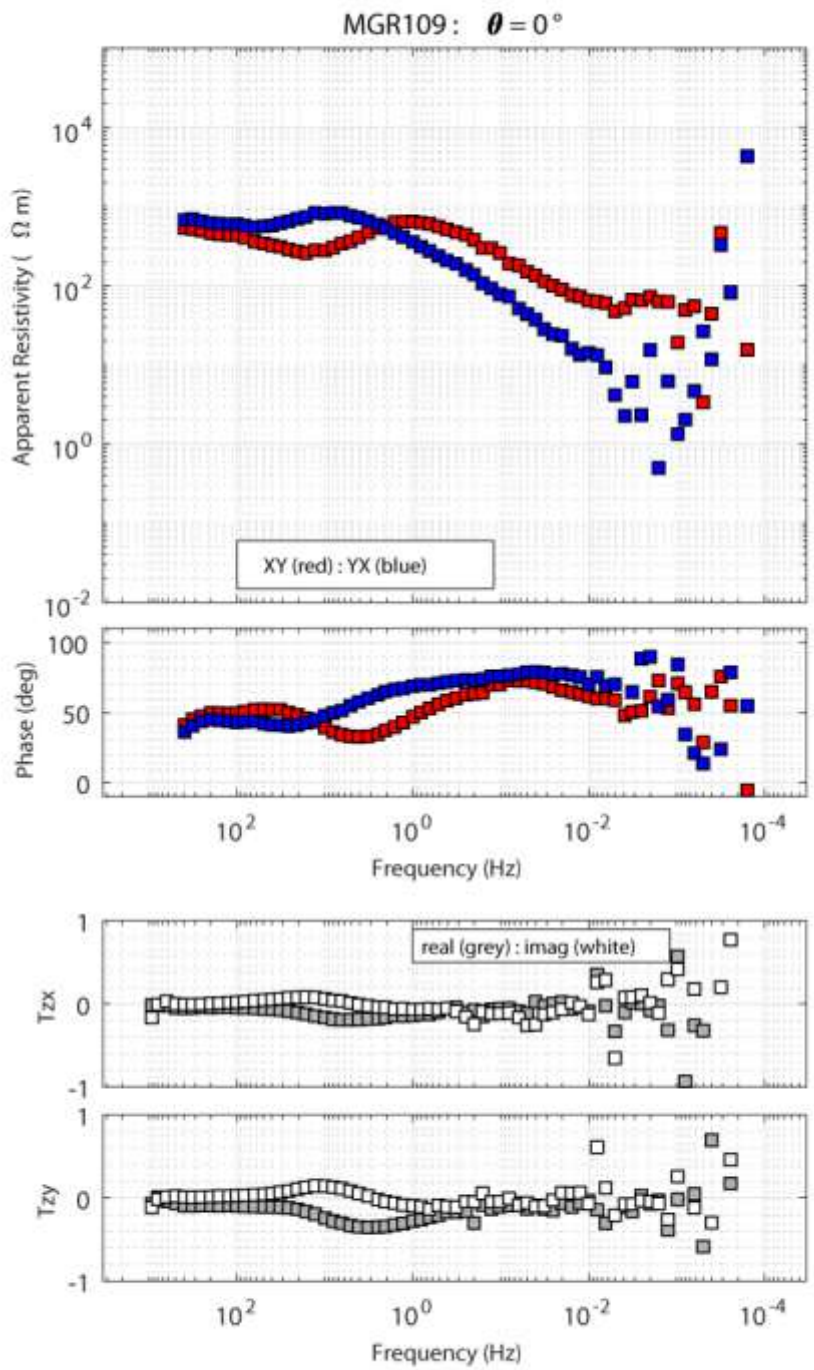


Figure A9 : MT sounding MGR109

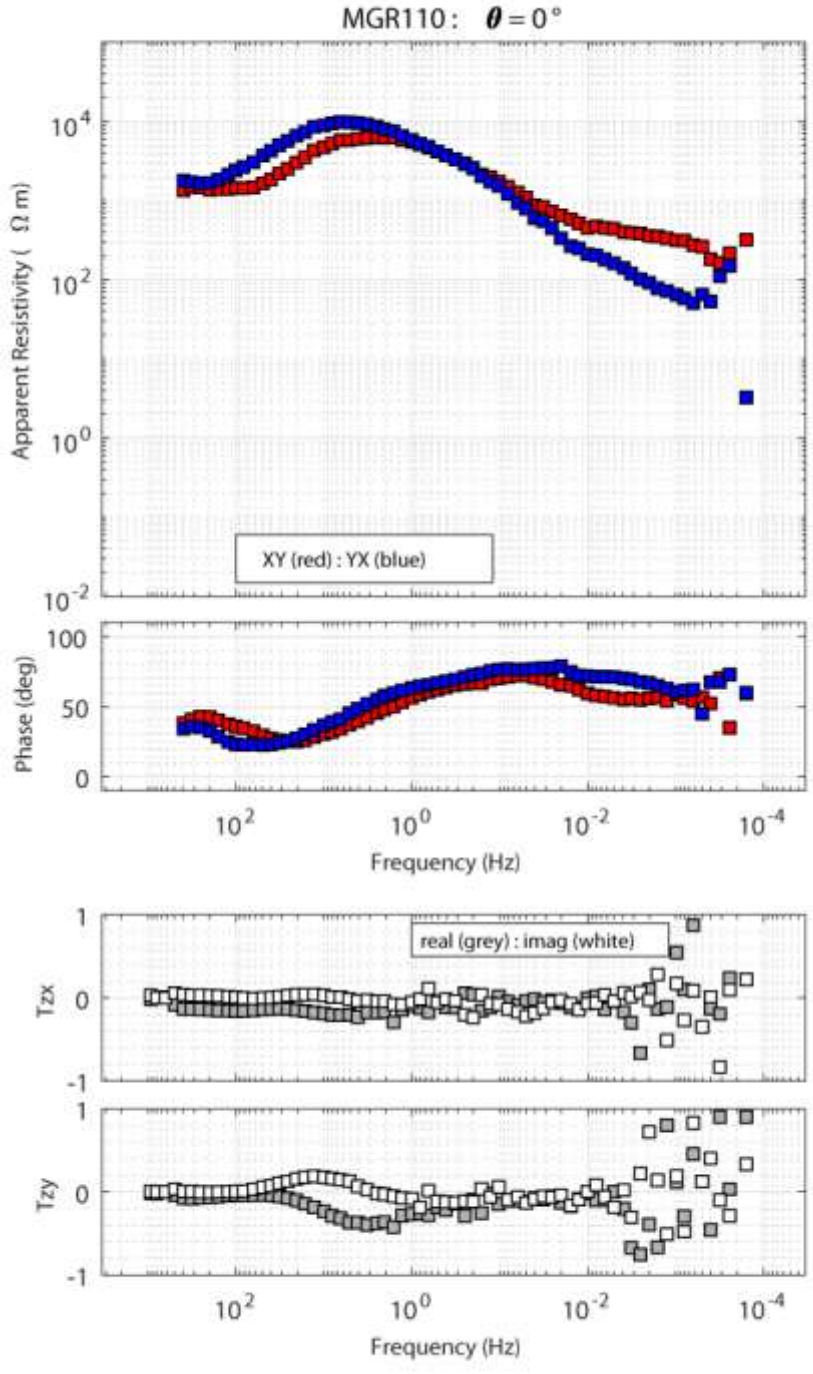


Figure A10 : MT sounding MGR110

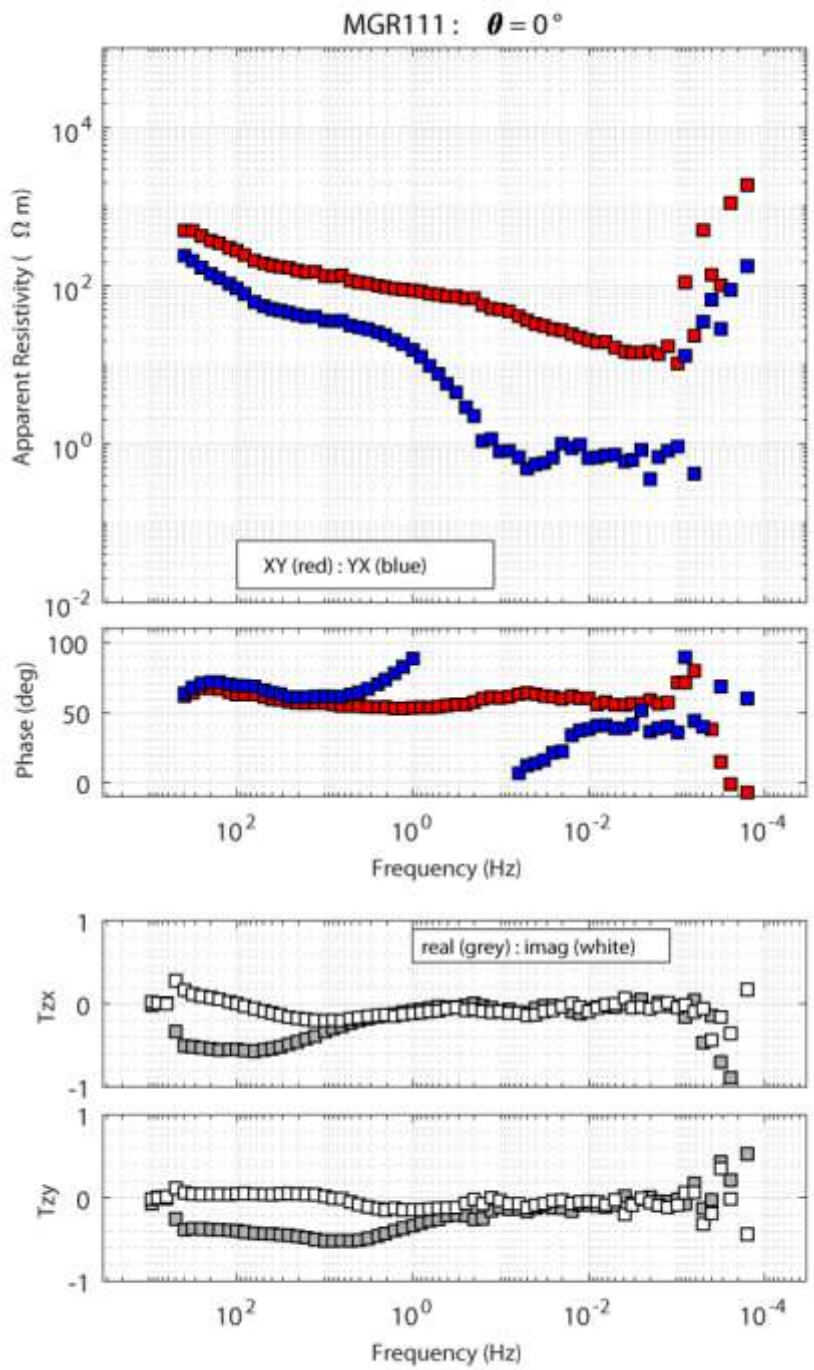


Figure A11 : MT sounding MGR111

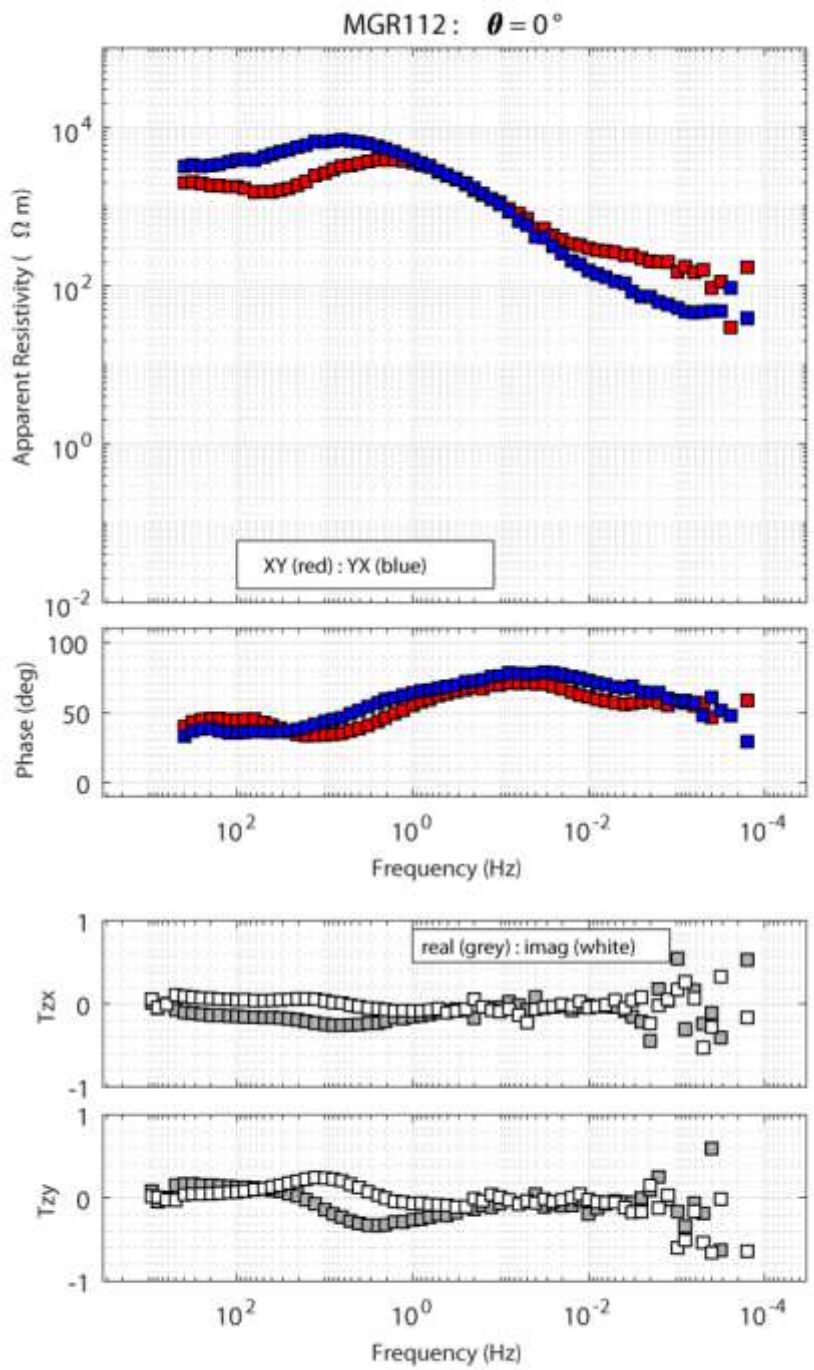


Figure A12 : MT sounding MGR112

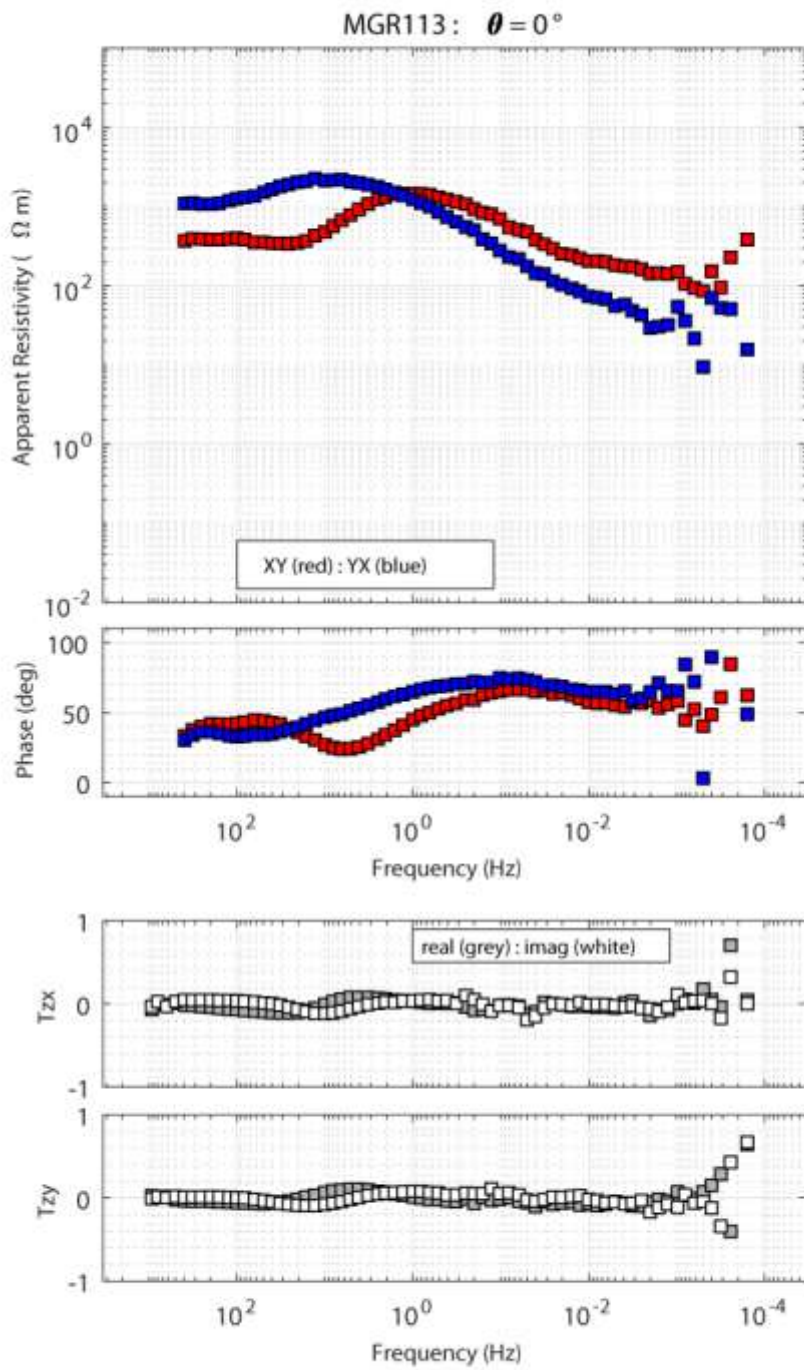


Figure A13 : MT sounding MGR113

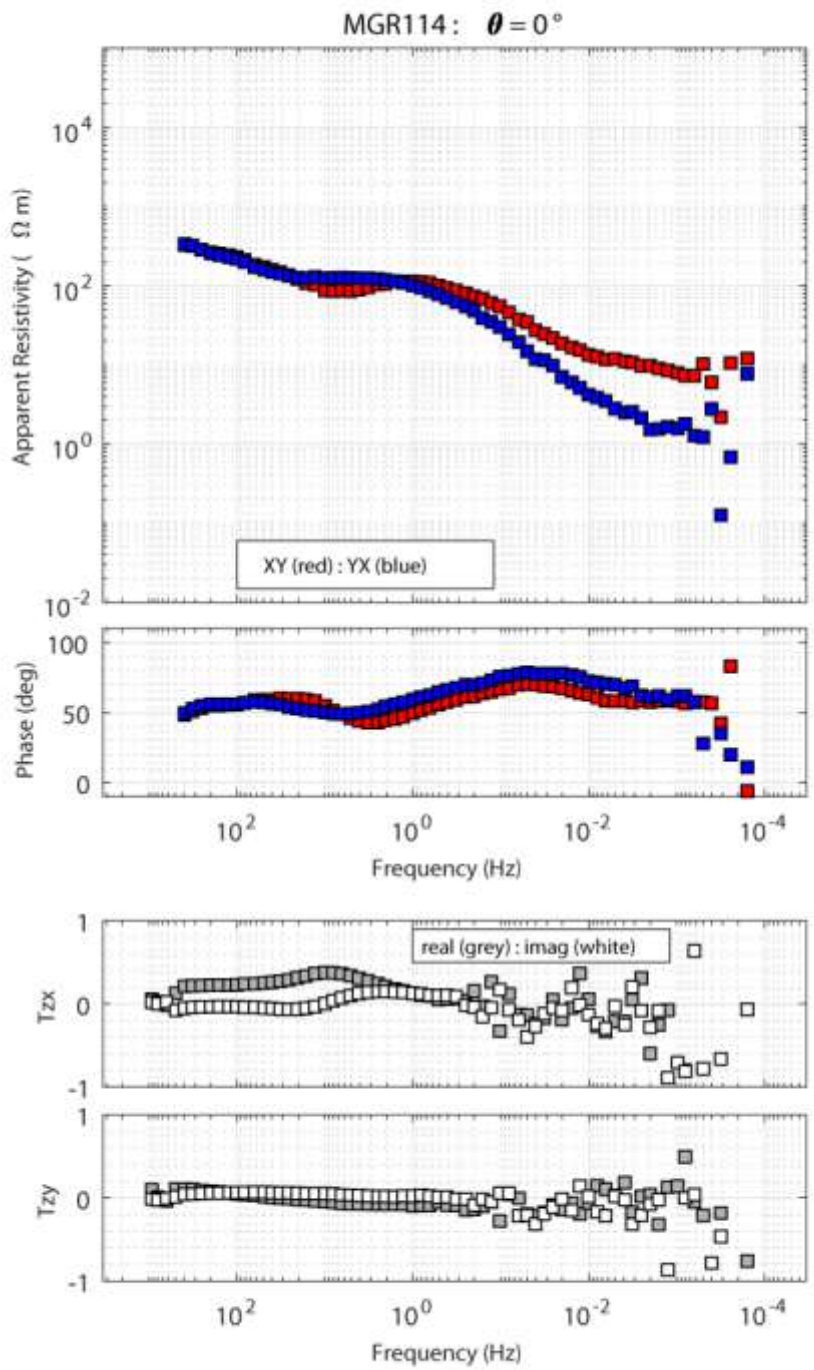


Figure A14 : MT sounding MGR114

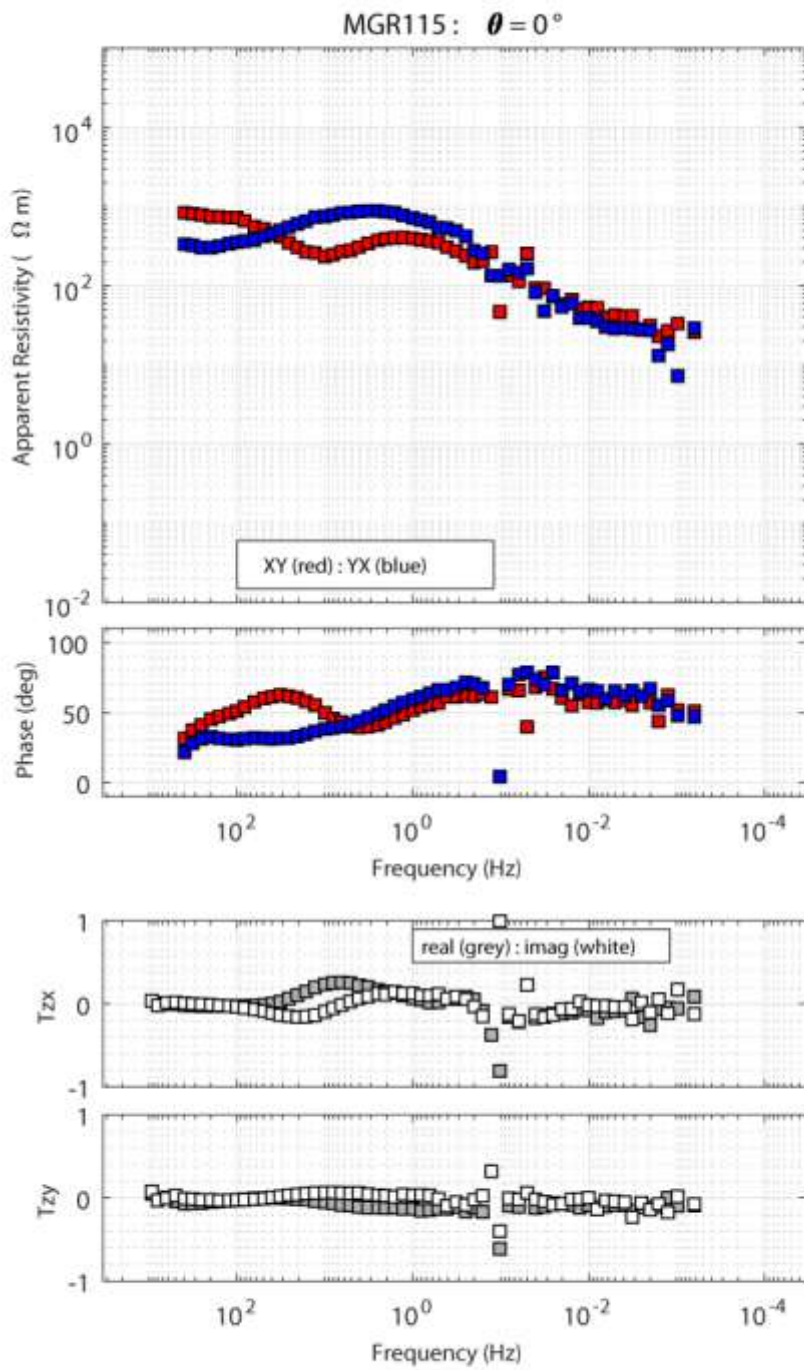


Figure A15 : MT sounding MGR115

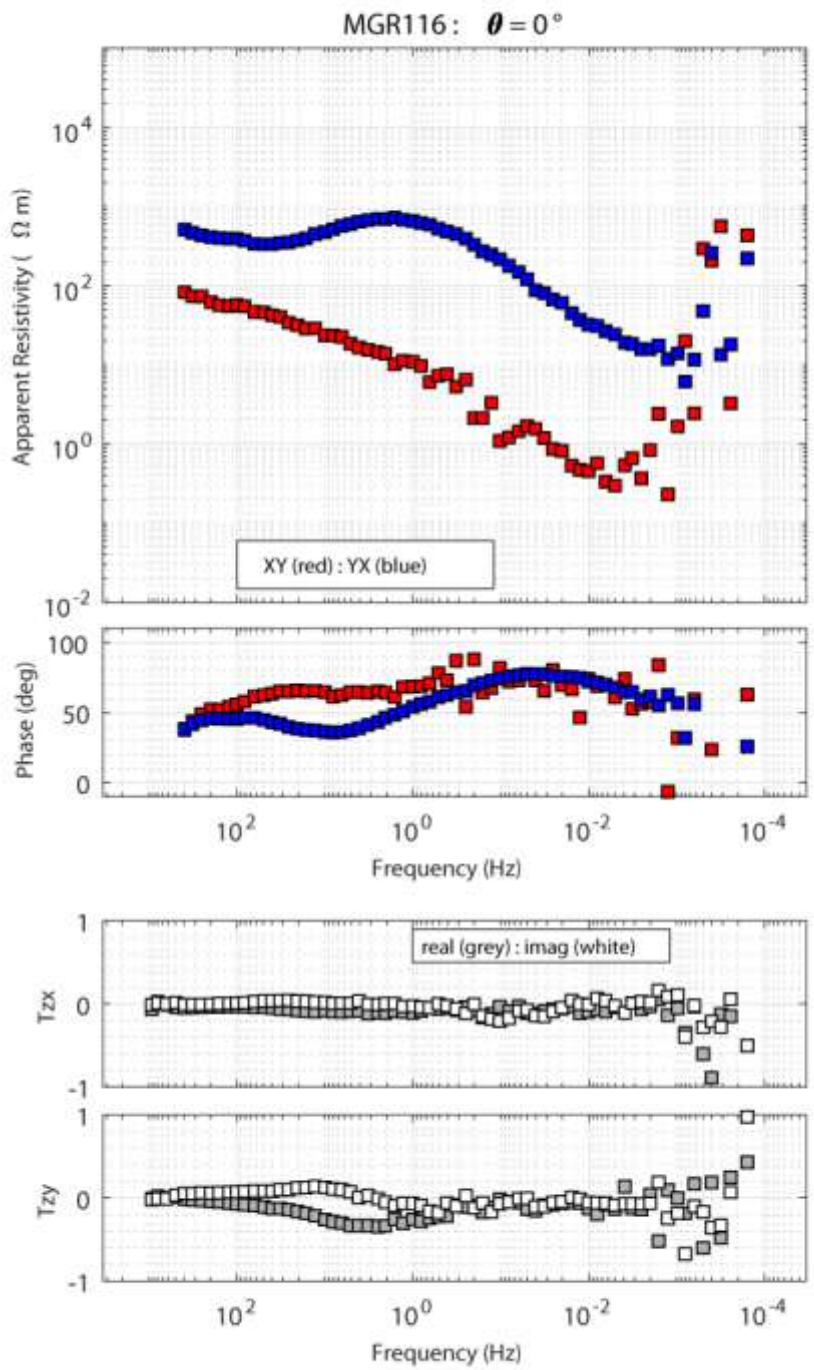


Figure A16 : MT sounding MGR116

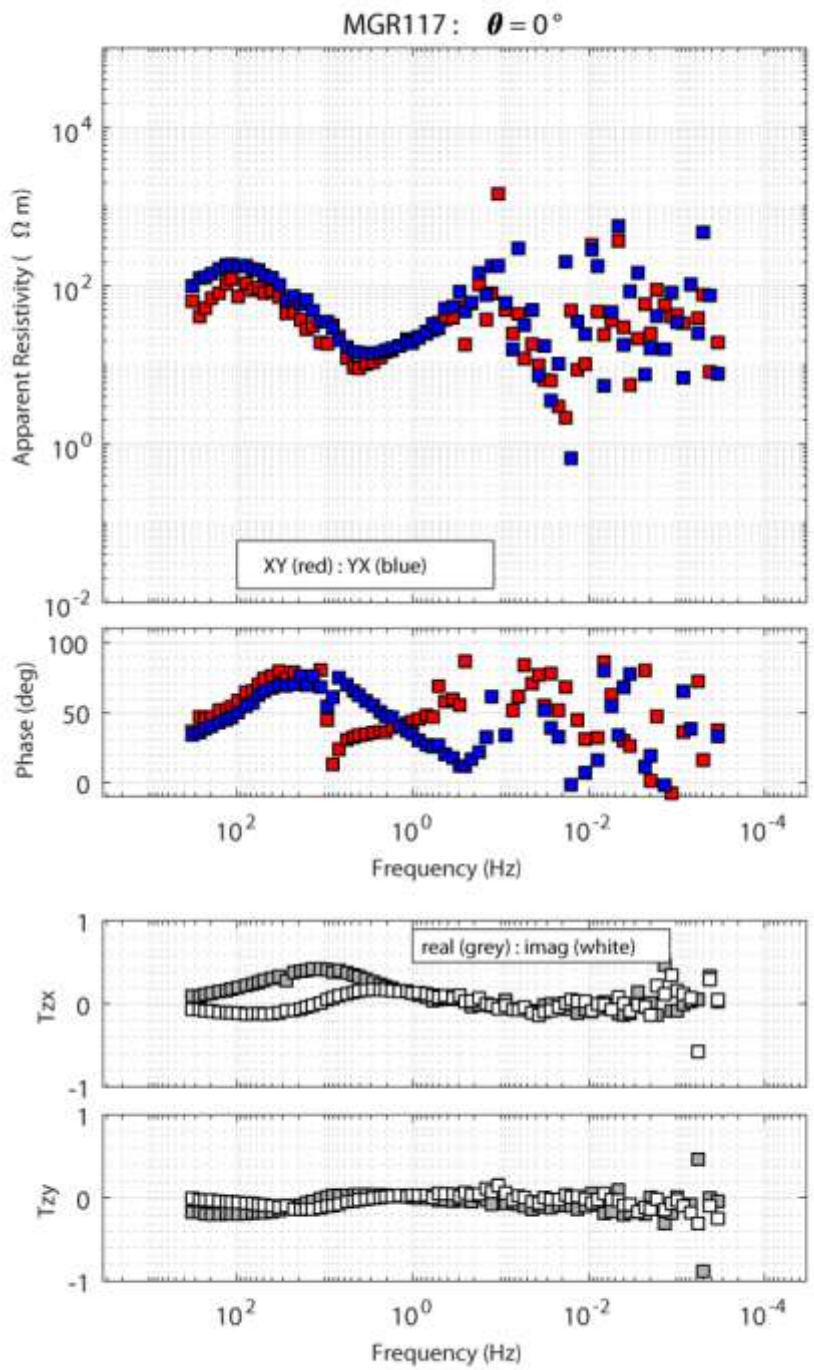


Figure A17 : MT sounding MGR117

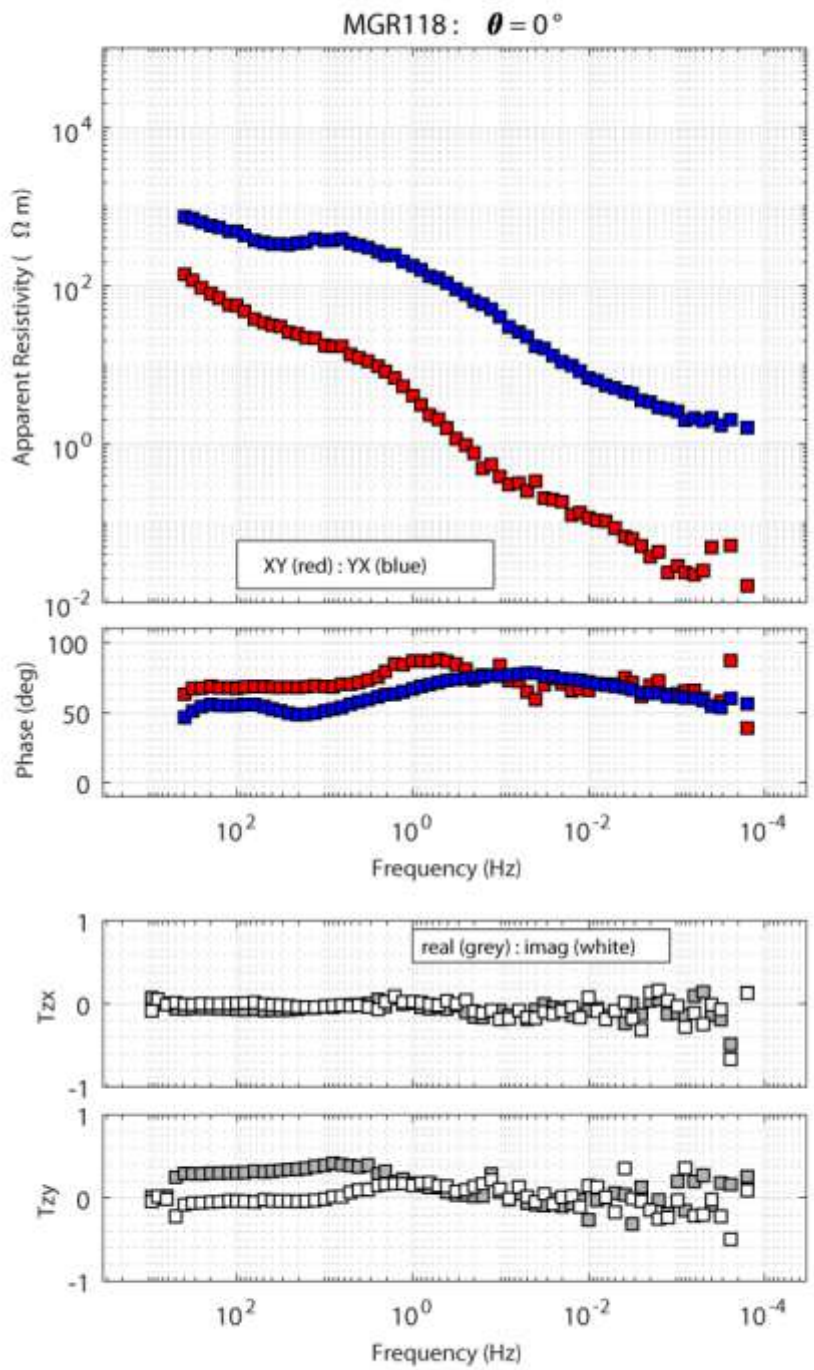


Figure A18 : MT sounding MGR118

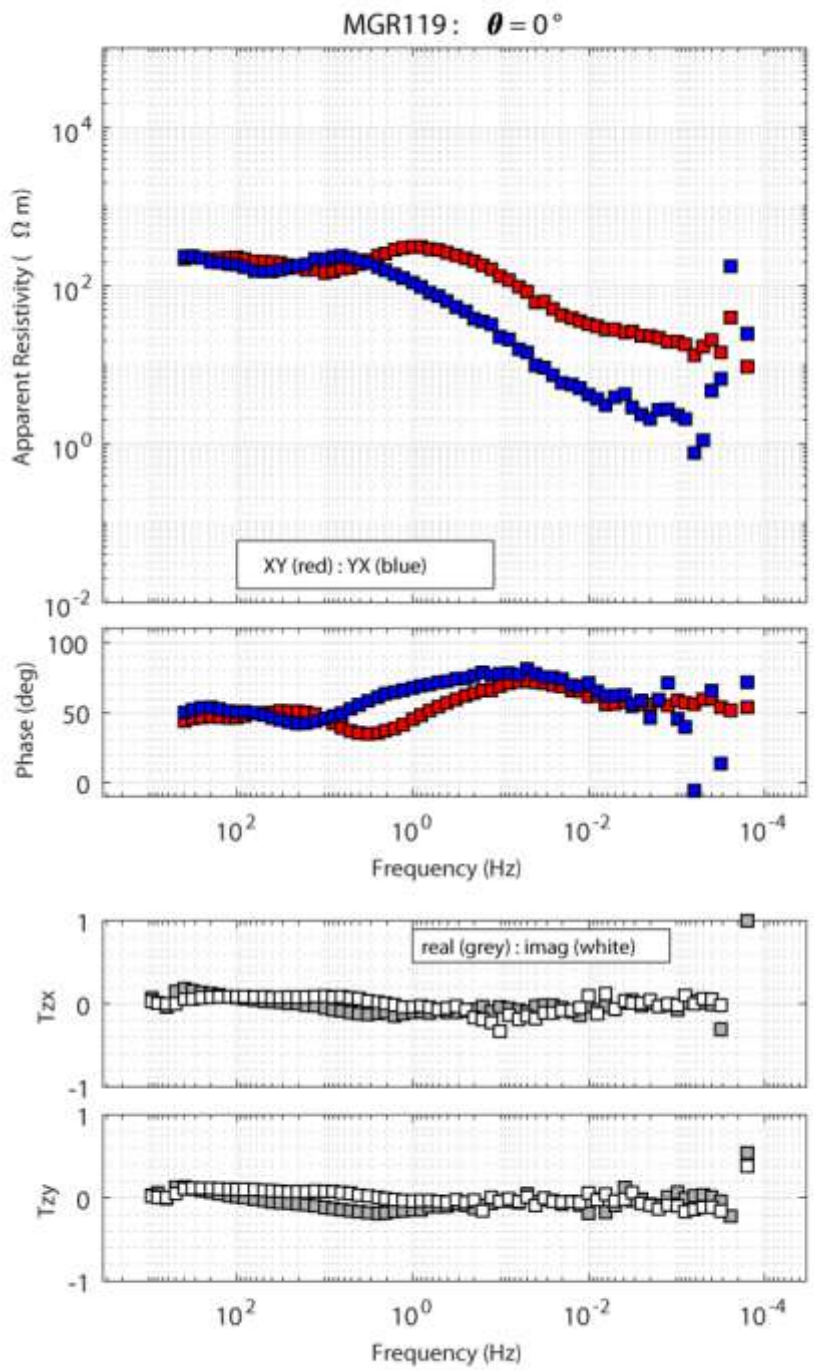


Figure A19 : MT sounding MGR119

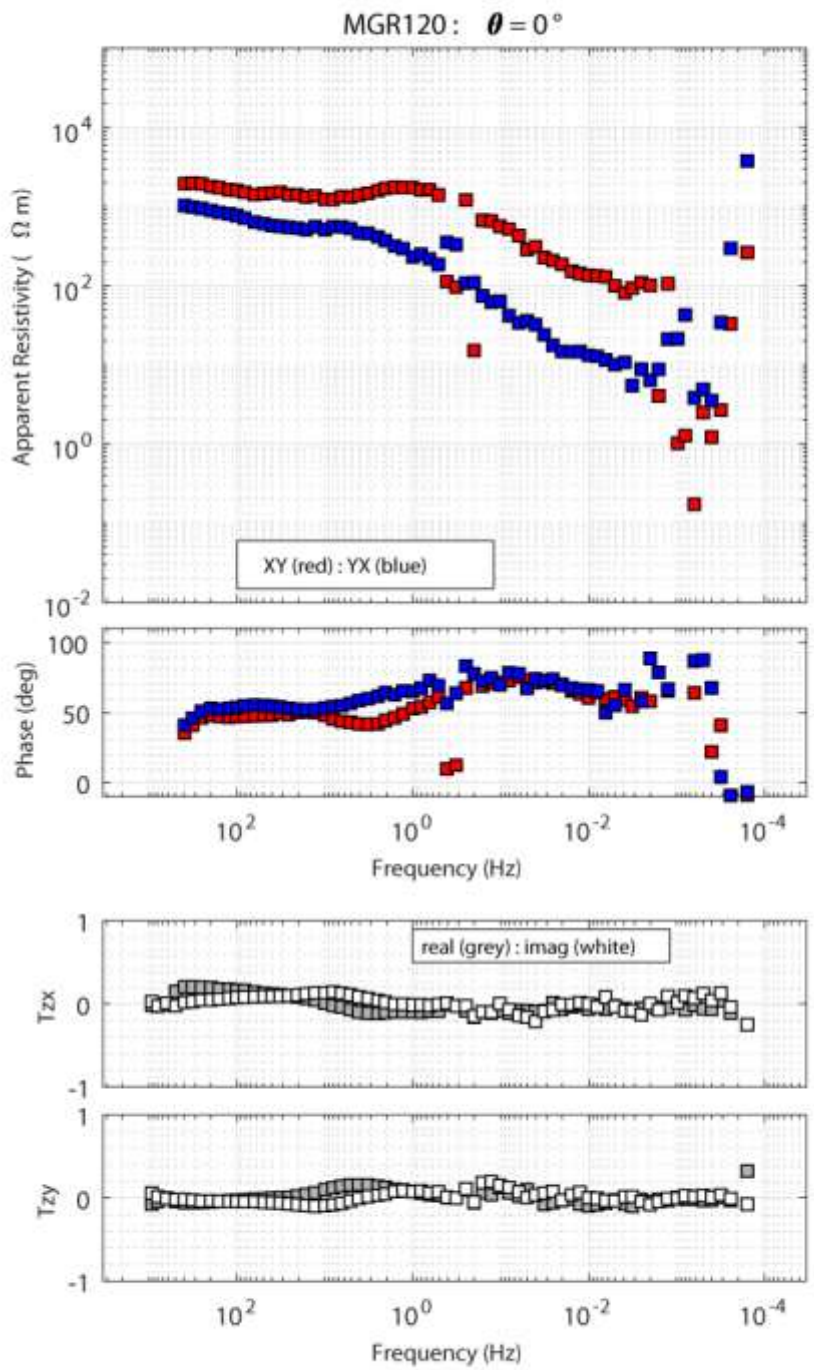


Figure A20 : MT sounding MGR120

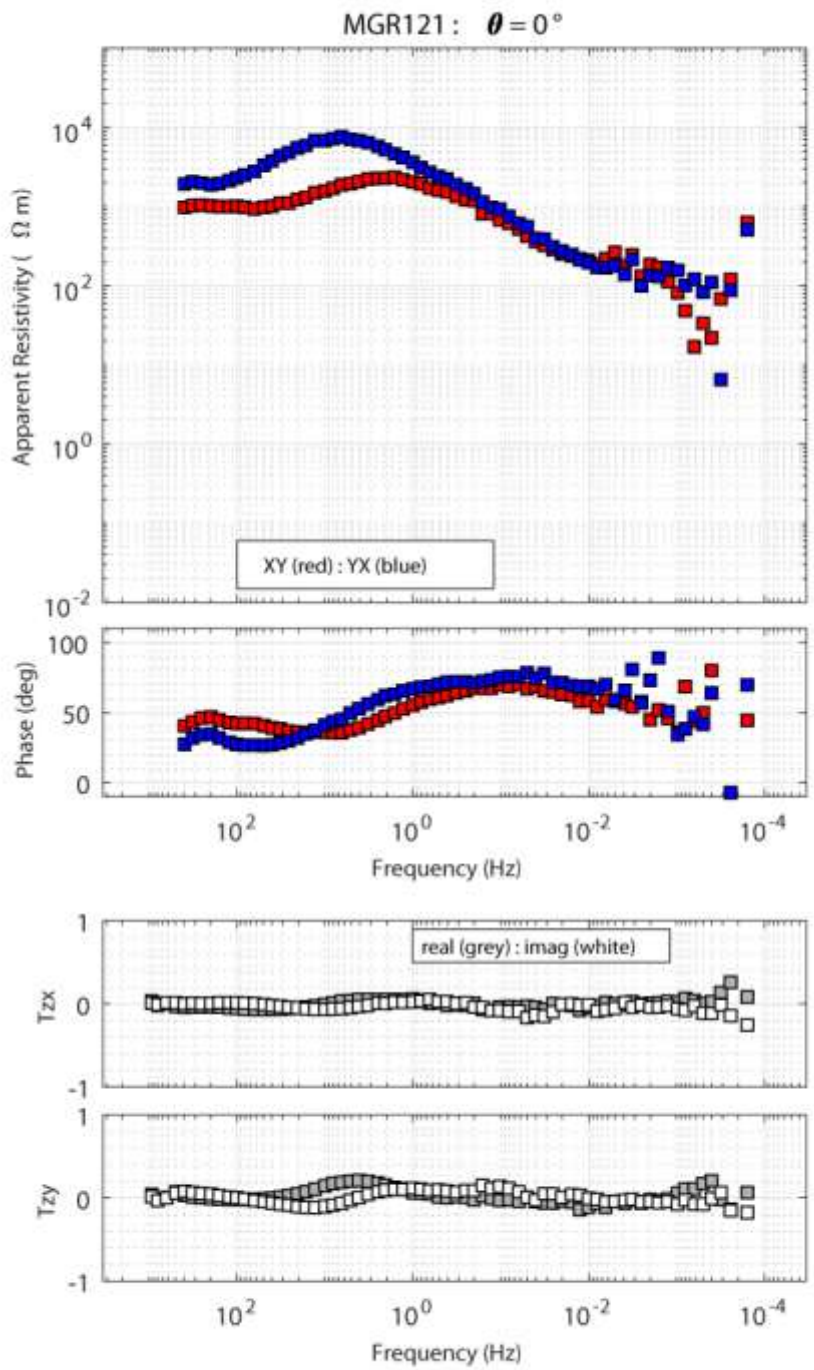


Figure A21 : MT sounding MGR121

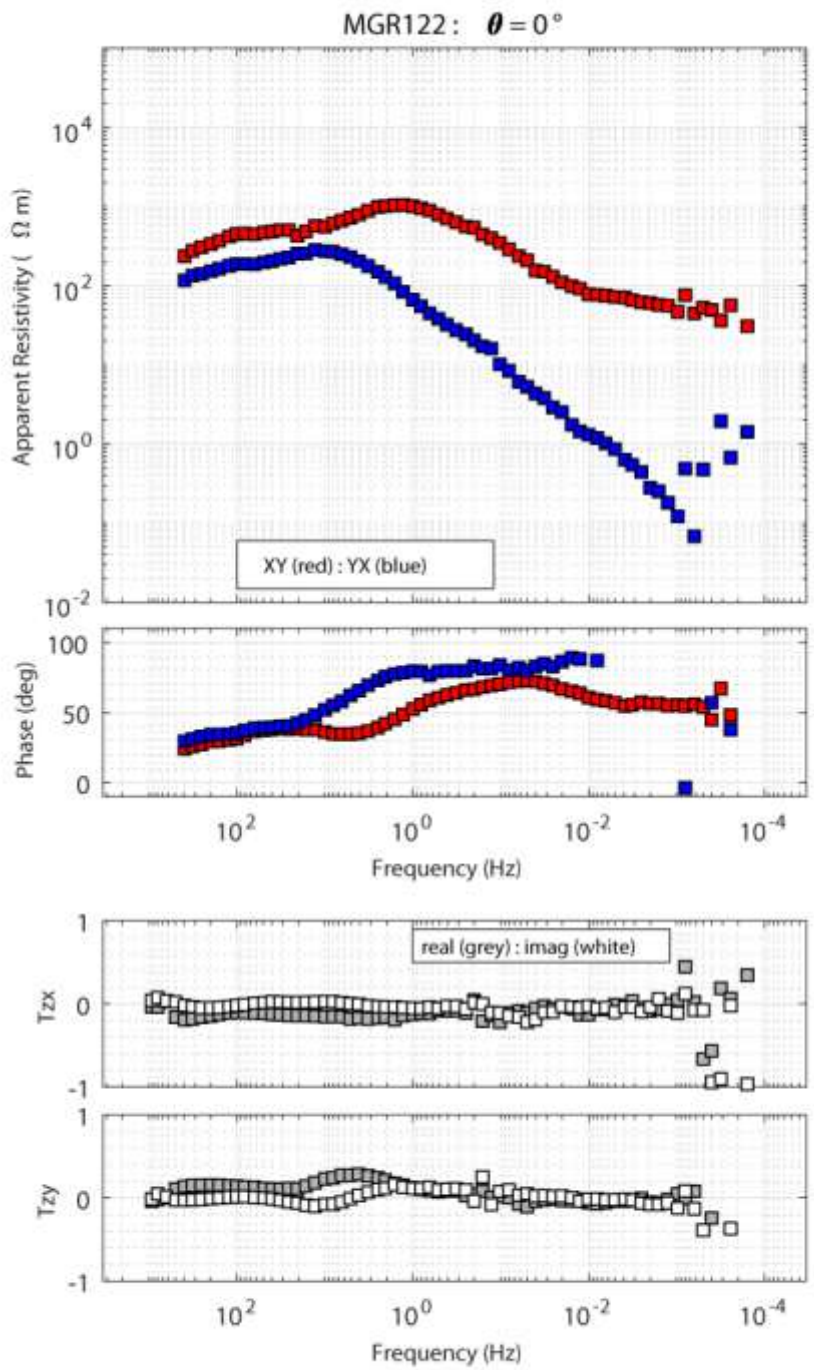


Figure A22 : MT sounding MGR122

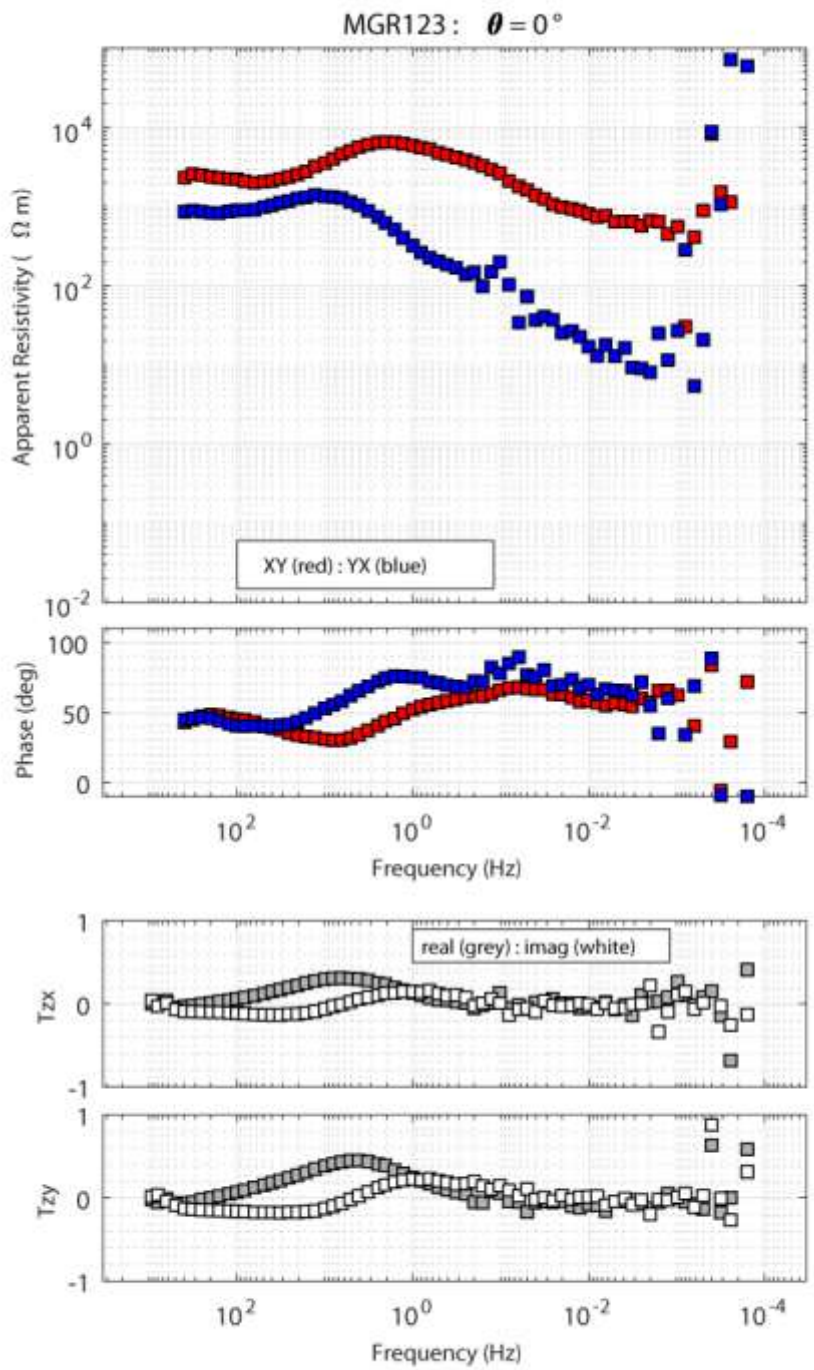


Figure A23 : MT sounding MGR123

Appendix B : MT instrument calibration

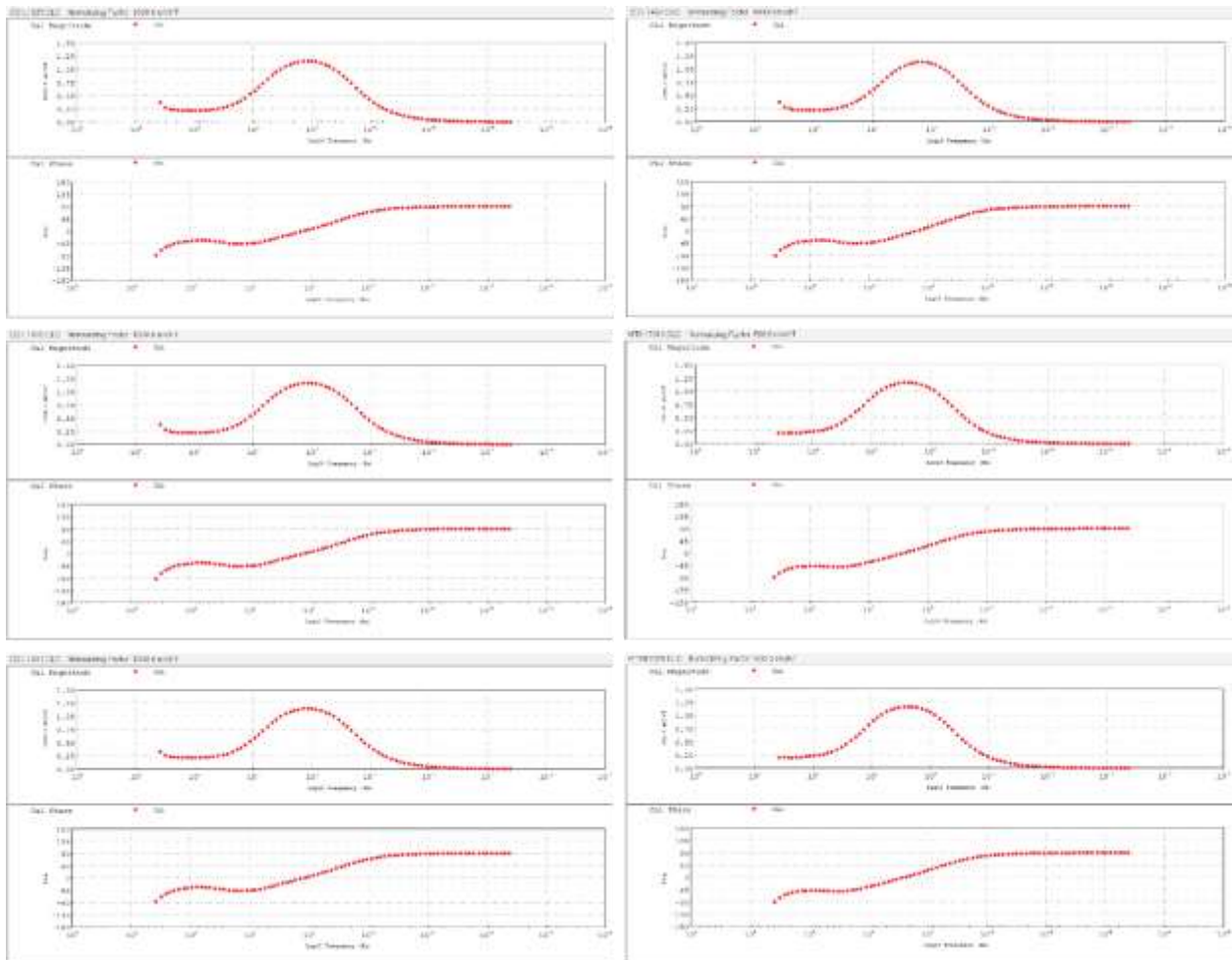


Figure B1 : Calibration responses of the MTC50 induction coils on July 24 2019. These responses are provided in the CLC files provided as part of this report.

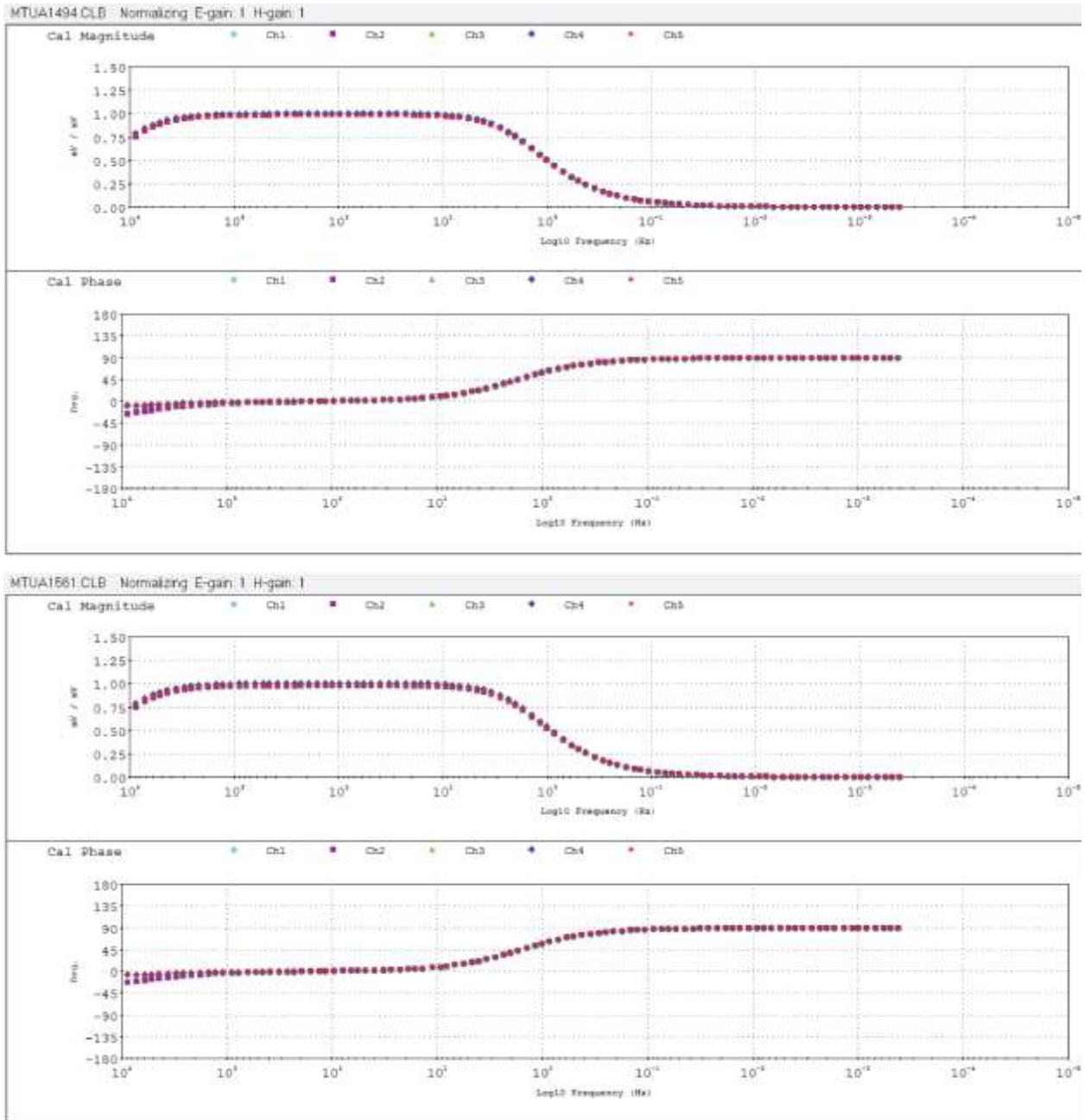


Figure B2 : Calibration responses of the electric fields of the MTU5A instruments on July 24 2019. These responses are provided in the CLB files provided as part of this report.

Chapter 6 - Overview of the 2019 Audiomagnetotelluric Survey of the Mount Meager Geothermal Reservoir

Craven, J.A.¹; Hormozzade, F.^{1,2}, Tschirhart, V.¹; Ansari, M.¹, Bryant, R.¹, and Montezadian, D.²

¹Geological Survey of Canada

²Carleton University

Introduction

Magnetotellurics (MT) is an electromagnetic exploration method used in both geothermal exploration and studies of the magmatic systems of active volcanoes (Chave and Jones, 2009). Ambient low frequency electromagnetic (EM) waves act as a (natural) transmitter in a typical active source EM geophysical survey. MT amplitude and phase properties associated with the diffusion of the ambient fields into the subsurface can be measured by comparatively easy to deploy receivers and used to infer the resistivity of the subsurface. The resistivity is a property of a rock matrix that is also sensitive to the presence of fluids within interconnected pore spaces (i.e., permeability) and to any clay alteration products commonly found in geothermal reservoirs. In addition, because temperature is a strong control on the presence of key clay alteration products, a subsurface map of resistivity can also be a proxy for a subsurface temperature map.

Geothermal exploration at Mount Meager using magnetotellurics began in the 1980s. At that time MT instruments were bulky requiring AC power sources that lengthened installation times to upwards of ½ day per site and constrained the stations collected to vehicle accessible locations primarily along Meager Creek (Flores Luna et al, 1982) and van Ngoc (1977). Unfortunately, the MT data from four widely spaced sites documented by van Ngoc (1977) has been lost. The analysis of the eight road sites from the 1982 survey was compromised by the small number of sites, a problem compounded by the data analysis techniques available at the time that were limited to simple 1-D layered earth models, low resolution 2-D models, or unrealistic thin sheet 3-D models. Even so, careful analysis of the data detected a dipping low resistivity layer identified as a fault controlled geothermal reservoir (Flores Luna et al, 1982) and later when aided by off-line legacy data the reservoir was shown to be affected by clay alteration (Jones and Dumas, 1993). Important geometrical information and fundamental relationships to the permeability of the reservoir was not established. In 2001, a more detailed industry MT survey collected 30 stations on the south slope of the volcanic complex to provide better areal coverage. Due to instrument limitations these earlier data sets do not include the higher sampling rates required to image at reservoir depths and therefore are not discussed herein.

Research at Mount Meager in 2019 included MT data collection aimed at greatly expanding coverage using modern instruments. When combined with recently developed 3-D inversion techniques, it is planned that this will allow a fully 3-D subsurface resistivity model to be developed. Our goal is to examine the characteristics of the reservoir and the distribution of fault and fracture systems on the local and regional circulation of geothermal reservoirs, based on MT responses in each site. The overarching objective of this study is to ascertain the spatial and genetic relationships between fluid flow and permeability to subsurface alteration and conduits such as fault systems in order to lower the risk developing geothermal resources.

Methods

MT surveys involve the measurement of natural electric and magnetic fields at the surface of the Earth. In general, electromagnetic geophysical surveys utilize a generator and complicated grounded electrodes or antennas to form transmitters, but the use of natural signals by MT as a transmitter avoids these complications. Because the depth of investigation of EM surveys depends on the frequency of the fields and the natural spectrum covers a broad range of frequencies, the same instrument can measure the subsurface resistivity at different depths simply by recording different ranges of frequencies. Typical MT measurements are made in the range 10000 – 0.001 Hz. When exclusively in the higher frequency range of 1000- 1Hz the data is often referred to as audiomagnetotellurics (AMT). The frequency range of approximately 400-0.001 Hz is often referred to as broadband MT (BBMT). In general, results from AMT surveys are often at higher resolution than BBMT, but are less depth penetrating.

As stated earlier, MT uses ambient or natural EM fields as effective sources. This has advantages as pointed out above, but also some disadvantages. One disadvantage is that times of low ambient signal may dominate a particular recording interval. MT data are typically acquired overnight when signal strength is higher to ensure high quality data. During the Meager project, to maximize the number of sites steel electrodes and a comparatively short ½ hour daytime AMT recording interval was utilized. Any resulting decrease in data quality was minimized through careful data editing (described in detail below) and the installation of a permanent site recording (only) daytime broadband magnetic fields. The broadband magnetic field data at the permanent could be processed with the local electric fields collected at each AMT site to enable better AMT processing down to frequencies where AMT and BBMT recording overlap at 1 Hz or so (when the response of the electrodes used for the AMT starts to fall-off). Such processing is possible at only the longer periods because of the planar nature of the fields. This recording method whilst able to produce high quality AMT data does generate a large data set requiring considerable manual editing to remove bursts of high frequency noise plus subsequent manual merging of the locally processed AMT data with the permanent MT coil processed data.

Prior to editing, the MT metadata were evaluated. In this step, the dipole length, declination, azimuth and calibrations were checked. In order to ensure high data quality data unaffected by man-made or non-planar natural noise sources, the MT data from the survey were processed and edited manually using the EMPower software utilizing a consistent workflow and parameters. The time series were converted to impedances, apparent resistivity and phase; all of which are functions of frequency. To get the final responses, the cross powers were edited such that inconsistent data from different recordings was removed from the calculations of resistivity, phase and other geophysical parameters. The key tools utilized in the EMPower software were the Polar Editor and Time Editor, in which masks were created to remove the bad data selected by visual inspection. This procedure was used on both the BBMT and AMT processed data sets and the combined dataset was exported from the EMPower software.

Data Collection

The collection of the MT data at 84 sites was conducted in the summer 2019. The recordings were made using AMT sensors and steel electrodes connected to newly acquired MTU-5C recorders. Two sites were also collected using MTC-5A recorders and remain to be processed. This report documents solely the data collected with MTU-5C systems. Declination was calculated using online calculators and found to vary between 16.37 to 16.41 degrees. Direct site access was generally impossible via truck, quad or helicopter and so the sites had to be backpacked. The AMT coils were cumbersome to carry and so the crews switched to open top portage style bags. The sites recorded along the Lillooet River were made primarily to test varying bags for portability and to train crews on data acquisition prior to deployment on the mountainside. As mentioned above, to ensure high quality at the bottom end of the AMT frequency end, broadband MT sensors were deployed at a permanent site to be processed with the local AMT electric field data. A summary of AMT recording is presented in Tables 1 and 2 below. The permanent magnetic field-only recordings are listed in Table 3. For completeness, similar information for the two MTU-5A sites is provided in Table 4.

Results

The primary result at this stage is simply the vetting, checking, editing and basic processing of the AMT time series data collected in the summer of 2019 at Mount Meager and the creation of an edited merged high quality data set consisting of impedances in the AMT frequency domain. The impedance data set can be used for the 3D modeling as described in the next section.

Summary and Future Work

The processed data can be used to formulate models of subsurface structure, both in terms of the geothermal reservoir and the underlying magmatic systems. These models will provide important information about subsurface electrical resistivity structure which can be used to address question related to the viability of the geothermal resource, and possible eruption potential of Mount Meager.

A key aspect of the AMT data analysis will be to address the cause of zones on high and low resistivity found beneath Mount Meager. Resistivity contrasts in this type of environment can be caused by saline fluids, molten rock or minerals formed by hydrothermal alteration. External constraints are often needed to distinguish between these alternatives. It was once assumed that geothermal reservoirs always demonstrated a low resistivity associated with the presence of fluids in interconnected porosity. However, careful laboratory experiments in recent years have shown that these assumptions are not always valid. In high temperature geothermal fields, the clay alteration minerals formed do not necessarily have a low resistivity, resulting in a reservoir cap created by clay alteration that can be relatively resistive compared to the surrounding rock.

Analysis of the new resistivity 3-D models from Mount Meager will benefit greatly from the other geological and geophysical datasets available – both those collected in the 2019 field campaign, and in previous exploration.

Data

The raw data consist of time series (.JSN) and calibration (.CAL) files. More information about the format of time series can be found [here](#).

After manual editing and merging, EDI files were exported from the EMPower software for further use in modeling and interpretation. The 200 GB data set will be made available as a vetted data set in a subsequent GSC Open File report.

Citations

- Chave, A., & Jones, A. (2012). *The magnetotelluric method: theory and practice*. Cambridge;: Cambridge University Press.
- Flores-Luna, C., Kurtz, R.D., DeLaurier, J. (1985). Magnetotelluric exploration in the Meager Mountain Geothermal Area, Canada. *Acta Geodaet, 20, Geophys. Mont. Acad. Sci*, pp. 165-171.
- Flores-Luna, C. (1986). *Electromagnetic induction studies over the Meager Creek geothermal area, British Columbia*. PhD Thesis, Department of Physics, University of Toronto. 221 pp.
- Jones, A. G. and Dumas, I. (1993). Electromagnetic images of a volcanic zone, *Phys. Earth and Planet. Inter.* 81, pp. 289–314.
- Van Ngoc, P., 1977. Magneto-Telluric survey of the Mount Meager region of the Squamish Valley, Earth Physics Branch, Open File Number 77-20-E, pp. 64, <https://doi.org/10.4095/314797>.

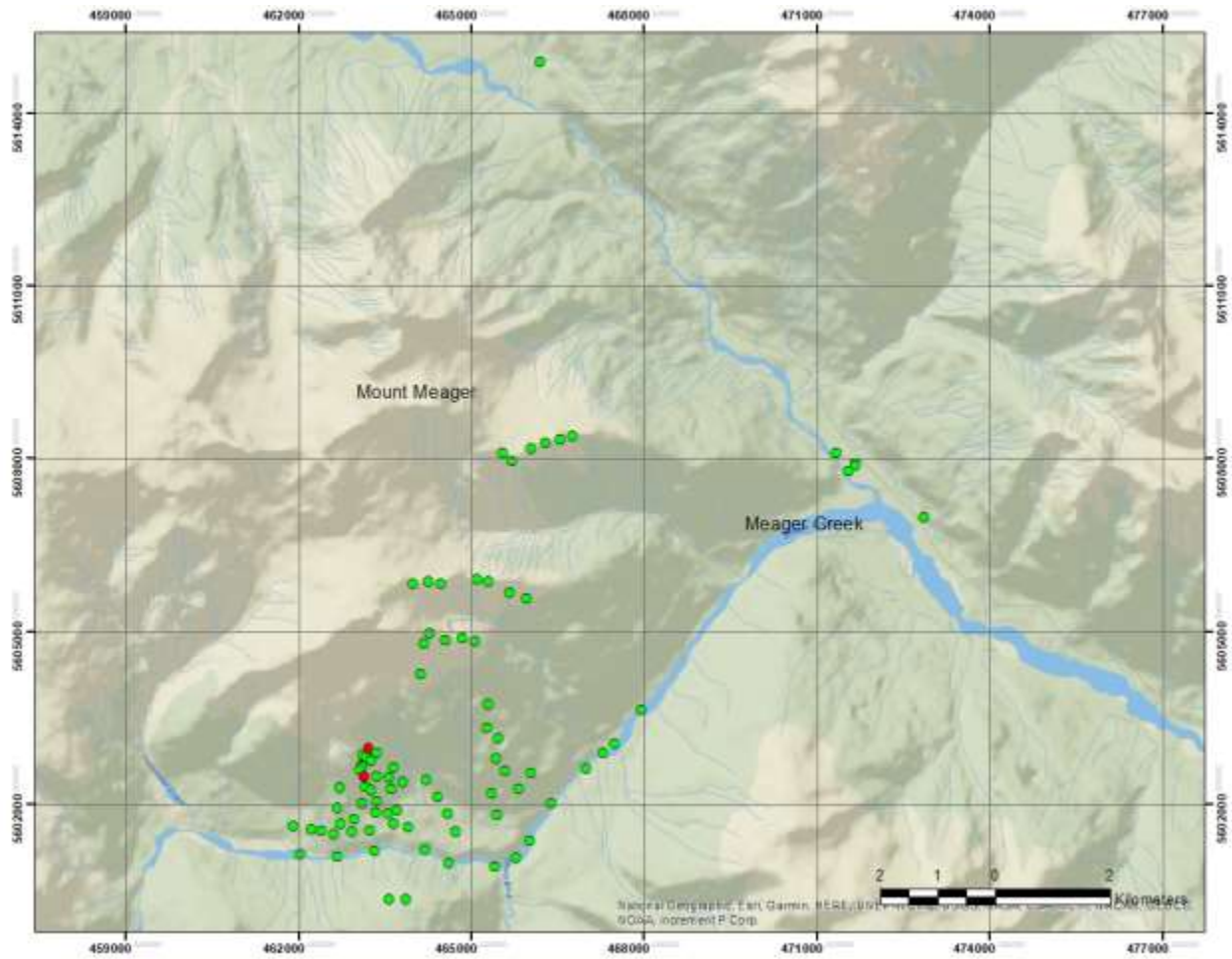


Figure 1. Station locations for the 84 AMT MTU-5C sites. The MTU-5A AMT sites are shown in red.

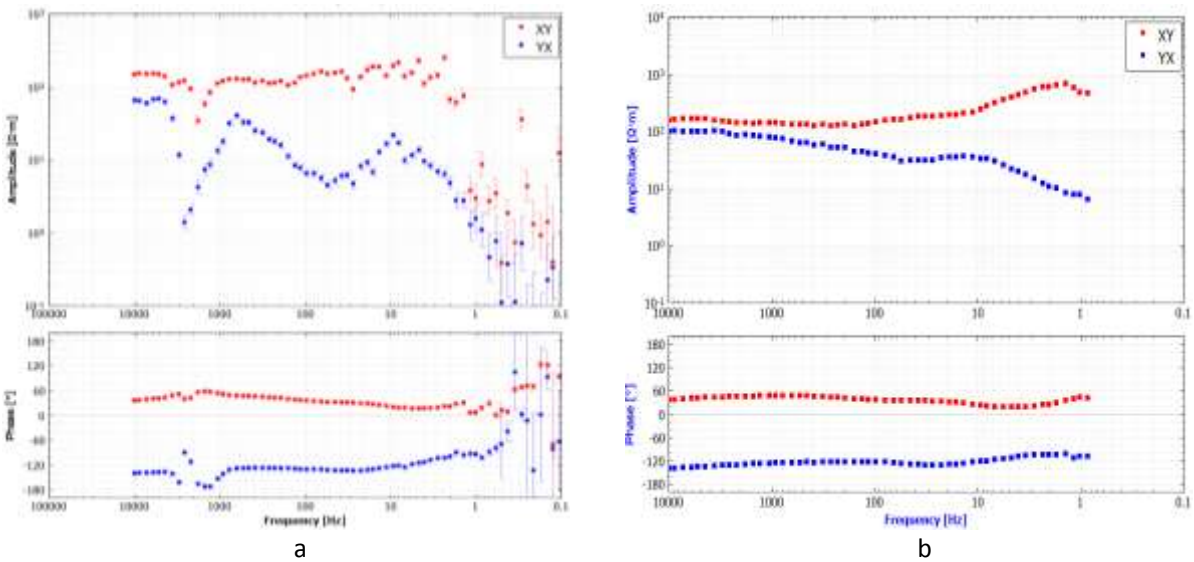


Figure 2. AMT apparent resistivity and phase responses of Z_{xy} (red dots) and Z_{yx} (blue dots) for site number 84, a) before editing and b) after editing.

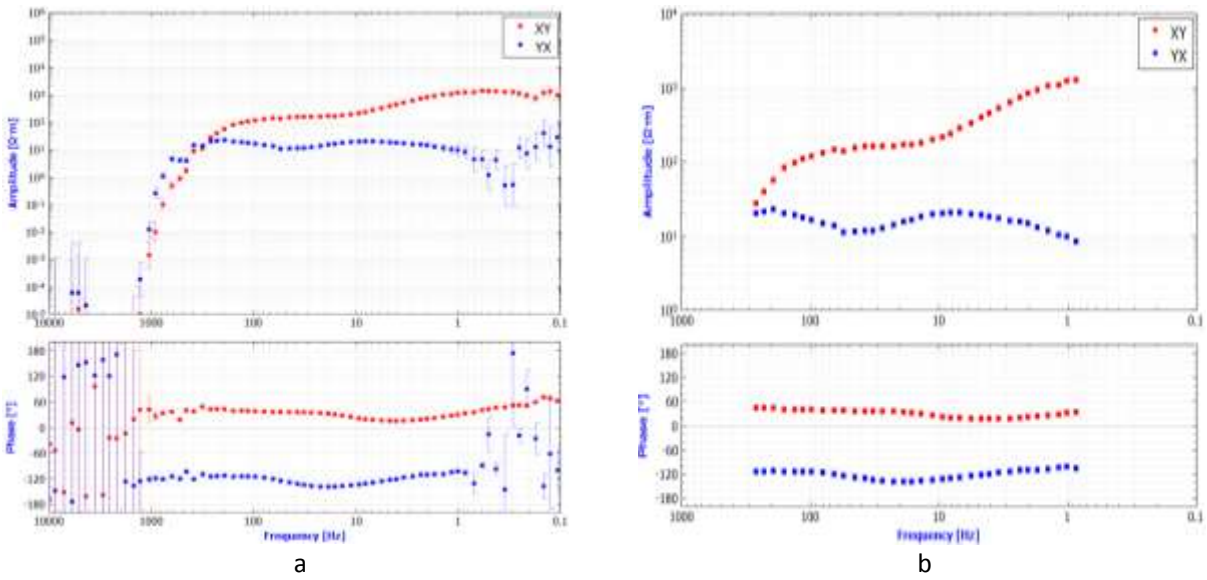


Figure 3. MT apparent resistivity and phase responses of Zxy (red dots) and Zyx (blue dots) for site number 84, a) before editing and b) after editing.

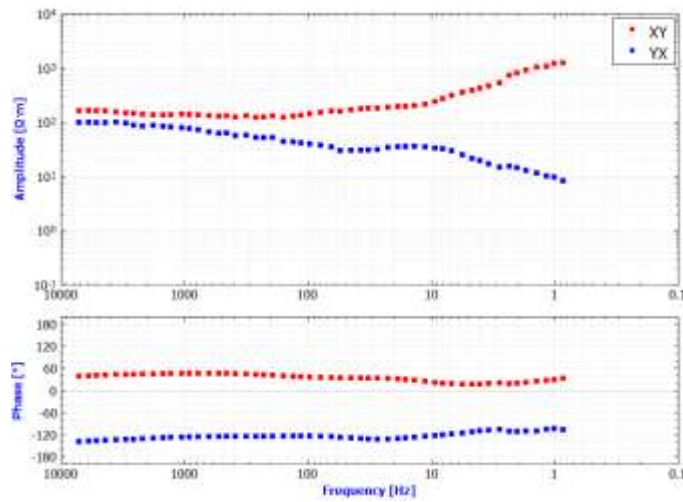


Figure 4. MT apparent resistivity and phase responses of Zxy (red dots) and Zyx (blue dots) for site number 84 (Merged)

Table 1. Site coordinates and configurations of the Mount Meager MT survey

Site Name	Latitude	Longitude	Elevation (m)	Hz azimuth (°)	Ex azimuth (°)	Declination (°)
01	50.62262	-123.4006	393.516674	0	0	16.39
01b	50.62227	-123.4006	390.657858	0	0	16.39
02	50.62131	-123.4021	394.649283	0	0	16.38
03	50.62424	-123.4052	395.127848	0	0	16.39
04	50.68503	-123.4786	705.010088	0	0	16.41
06	50.57658	-123.5208	1303.957128	0	0	16.39
07	50.57694	-123.5177	1317.964034	0	0	16.39
08	50.57627	-123.5201	1294.815007	0	0	16.39
09	50.5756	-123.5189	1263.50623	0	0	16.39
10a	50.57489	-123.5213	1231.130754	0	0	16.39
10b	50.57486	-123.5211	1234.050084	0	0	16.39
11	50.57428	-123.5218	1197.923076	0	0	16.39
13	50.57318	-123.5176	1095.395138	0	20	16.39
14	50.57469	-123.5133	1080.166357	0	0	16.39
15	50.57296	-123.5146	1049.414719	0	0	16.39
16	50.57153	-123.5203	1016.039198	0	0	16.39
17	50.57132	-123.5267	1005.012571	0	0	16.39
18	50.56817	-123.5273	906.876575	0	0	16.39
19	50.56583	-123.5263	859.448098	0	0	16.39

Site Name	Latitude	Longitude	Elevation (m)	Hz azimuth (°)	Ex azimuth (°)	Declination (°)
20	50.62386	-123.4872	2069.493576	0	0	16.4
21	50.62457	-123.4802	2028.923018	0	0	16.4
22	50.62268	-123.485	2063.22173	0	0	16.4
23	50.62543	-123.4766	1991.358404	0	0	16.4
24	50.62595	-123.4732	1983.236051	0	0	16.39
25	50.62649	-123.47	1897.97168	0	0	16.39
26	50.60339	-123.509	2161.918937	0	0	16.39
27	50.60404	-123.4934	1871.827809	0	10	16.39
28	50.60372	-123.5051	2065.118357	0	30	16.39
29	50.60375	-123.4904	1847.917505	0	0	16.39
30	50.60328	-123.5021	2036.358392	0	0	16.39
31	50.60206	-123.4852	1764.996737	0	0	16.39
32	50.60125	-123.4811	1678.366567	0	0	16.39
33	50.56645	-123.5229	842.104667	0	0	16.39
34	50.57106	-123.5188	991.706354	0	0	16.39
35	50.56453	-123.5235	827.787039	0	0	16.39
36	50.57134	-123.514	954.445102	0	30	16.39
37	50.56483	-123.5191	787.993877	0	0	16.39
38	50.57238	-123.5113	920.069013	0	0	16.39
39	50.56528	-123.5098	762.699639	0	0	16.38

Site Name	Latitude	Longitude	Elevation (m)	H _z azimuth (°)	Ex azimuth (°)	Declination (°)
40	50.56905	-123.521	863.277112	0	0	16.39
41	50.56576	-123.5132	764.776517	0	0	16.39
42	50.56926	-123.5176	870.880817	0	0	16.39
43	50.56795	-123.5125	781.913085	0	30	16.39
44	50.56762	-123.5176	800.961316	0	0	16.39
45	50.58457	-123.4904	1308.875694	0	0	16.39
46	50.56743	-123.5148	779.654134	0	0	16.39
47	50.58084	-123.4905	1230.23032	0	0	16.38
48	50.57926	-123.4877	1149.420276	0	0	16.38
49	50.57608	-123.4883	1084.146812	0	0	16.38
50	50.57421	-123.486	977.751247	0	0	16.38
51	50.57398	-123.4796	879.325601	0	0	16.38
52	50.57136	-123.4826	840.89468	0	0	16.38
53	50.57068	-123.4894	887.855708	0	0	16.38
54	50.56737	-123.4878	735.966065	0	0	16.38
55	50.61429	-123.3835	388.993311	0	0	16.37
56	50.56066	-123.5271	707.043132	0	0	16.38
57	50.56103	-123.5361	734.115083	0	0	16.38
58	50.56157	-123.518	689.920022	0	0	16.38
59	50.56176	-123.5056	664.237897	0	0	16.38

Site Name	Latitude	Longitude	Elevation (m)	H _z azimuth (°)	Ex azimuth (°)	Declination (°)
60	50.55976	-123.4996	645.484607	0	0	16.38
61	50.55933	-123.4883	624.672987	0	0	16.38
62	50.56067	-123.4831	612.469875	0	0	16.38
63	50.56912	-123.4746	586.999872	0	0	16.38
64	50.56338	-123.4799	604.924088	0	0	16.38
65	50.58921	-123.5069	1813.951535	0	30	16.38
66	50.59398	-123.5063	1991.654962	0	0	16.38
67	50.55405	-123.5102	1261.817131	0	0	16.38
68	50.59556	-123.5047	1974.529782	0	0	16.38
69	50.5541	-123.5144	1243.562765	0	0	16.38
70	50.59466	-123.5009	1854.255011	0	0	16.39
71	50.57706	-123.462	540.825906	0	0	16.38
72	50.59501	-123.4969	1777.553747	0	0	16.39
73	50.58388	-123.4526	516.950066	0	0	16.39
74	50.59446	-123.4938	1702.225255	0	0	16.39
75	50.56413	-123.528	817.660964	0	0	16.38
76	50.57469	-123.4661	561.961008	0	0	16.39
77	50.56464	-123.5309	813.770478	0	0	16.38
78	50.57851	-123.4592	530.709255	0	0	16.39
79	50.56746	-123.5002	751.807959	0	0	16.39

Site Name	Latitude	Longitude	Elevation (m)	H _z azimuth (°)	Ex azimuth (°)	Declination (°)
80	50.56535	-123.5378	797.376991	0	0	16.38
81	50.56458	-123.4981	749.238919	0	0	16.38
82	50.56486	-123.5334	816.772403	0	0	16.38
84	50.57274	-123.5055	845.321417	0	0	16.38
86	50.57015	-123.5027	809.924889	0	0	16.38

Table 2. Detailed configuration of the Magnetic and Electric field measurements of sites named in Table 1.

Data File	Site Name	Start Time	End Time	MTU box number	Hx id	Hy id	Hz id	Ex line length	Ey line length	Processing note comment
10227_2019-07-07-231456	01	Sun Jul 07 2019 23:14:56 UTC	Mon Jul 08 2019 00:14:08 UTC	227	1148	1146	1173	28.1	28.3	
10229_2019-07-07-231300	01b	Sun Jul 07 2019 23:13:00 UTC	Mon Jul 08 2019 00:18:23 UTC	229	1141	1142	1143	25.87	29	
10227_2019-07-08-185238	02	Mon Jul 08 2019 18:52:38 UTC	Mon Jul 08 2019 20:03:15 UTC	227	1141	1142	1143	22.25	21.38	
10230_2019-07-08-185715	03	Mon Jul 08 2019 18:57:15 UTC	Mon Jul 08 2019 19:56:27 UTC	230	1170	1171	1173	24.9	24.8	
10229_2019-07-09-183437	04	Tue Jul 09 2019 18:34:37 UTC	Tue Jul 09 2019 20:42:01 UTC	229	1141	1142	None	27.5	38.5	
10230_2019-07-11-194326	06	Fri Jul 12 2019 00:53:26 UTC	Fri Jul 12 2019 03:56:36 UTC	230	1170	1173	None	21.3	20.9	
10227_2019-07-11-171743	07	Thu Jul 11 2019 17:17:43 UTC	Thu Jul 11 2019 18:50:43 UTC	227	1141	1142	1143	24.7	21.8	
10229_2019-07-11-184750	08	Fri Jul 12 2019 00:31:50 UTC	Fri Jul 12 2019 03:42:19 UTC	229	1148	1146	1327	22.43	23.08	
10229_2019-07-12-170419	09	Fri Jul 12 2019 17:04:19 UTC	Fri Jul 12 2019 18:04:40 UTC	229	1148	1146	1327	27.8	23.2	
10227_2019-07-11-202714	10a	Fri Jul 12 2019 00:31:14 UTC	Fri Jul 12 2019 03:54:24 UTC	227	1141	1142	None	24.6	23.05	
10227_2019-07-12-184456	10b	Fri Jul 12 2019 18:44:56 UTC	Fri Jul 12 2019 19:48:48 UTC	227	1141	1142	None	24.6	23.05	

Data File	Site Name	Start Time	End Time	MTU box number	Hx id	Hy id	Hz id	Ex line length	Ey line length	Processing note comment
10230_2019-07-12-170609	11	Fri Jul 12 2019 17:06:09 UTC	Fri Jul 12 2019 18:46:52 UTC	230	1170	1171	1173	25.2	27.3	
10229_2019-07-12-203316	13	Fri Jul 12 2019 20:33:16 UTC	Fri Jul 12 2019 21:41:30 UTC	229	1170	1171	1173	13.1	14.1	
10227_2019-07-13-170047	14	Sat Jul 13 2019 17:00:47 UTC	Sat Jul 13 2019 18:03:56 UTC	227	1141	1142	1143	15.5	11.76	
10230_2019-07-13-163351	15	Sat Jul 13 2019 16:33:51 UTC	Sat Jul 13 2019 17:32:48 UTC	230	1148	1146	1327	20.2	18.4	
10230_2019-07-13-184937	16	Sat Jul 13 2019 18:49:37 UTC	Sat Jul 13 2019 19:50:31 UTC	230	1148	1146	None	18.4	19.4	
10227_2019-07-13-194535	17	Sat Jul 13 2019 19:45:35 UTC	Sat Jul 13 2019 20:50:40 UTC	227	1141	1142	1143	27.3	30.3	Hx installed backwards
10230_2019-07-13-210600	18	Sat Jul 13 2019 21:06:00 UTC	Sat Jul 13 2019 22:06:16 UTC	230	1148	1146	1327	19.5	17.8	
10227_2019-07-13-215820	19	Sat Jul 13 2019 21:58:20 UTC	Sat Jul 13 2019 22:45:10 UTC	227	1142	1141	1143	18.55	28.64	
10227_2019-07-14-160715	20	Sun Jul 14 2019 16:07:15 UTC	Sun Jul 14 2019 17:15:24 UTC	227	1141	1142	1143	24.19	32.17	
10230_2019-07-14-161300	21	Sun Jul 14 2019 16:13:00 UTC	Sun Jul 14 2019 17:12:55 UTC	230	1148	1146	1327	30	30.8	
10227_2019-07-14-181854	22	Sun Jul 14 2019 18:18:54 UTC	Sun Jul 14 2019 19:19:25 UTC	227	1141	1142	1143	27.7	25.56	
10230_2019-07-14-181532	23	Sun Jul 14 2019 18:15:32 UTC	Sun Jul 14 2019 19:15:58 UTC	230	1148	1146	1327	31.2	23.7	

Data File	Site Name	Start Time	End Time	MTU box number	Hx id	Hy id	Hz id	Ex line length	Ey line length	Processing note comment
10230_2019-07-14-210330	24	Sun Jul 14 2019 21:03:30 UTC	Sun Jul 14 2019 22:03:05 UTC	230	1141	1142	1143	21.5	28.6	
10230_2019-07-14-224200	25	Sun Jul 14 2019 22:42:00 UTC	Sun Jul 14 2019 23:41:44 UTC	230	1141	1142	1143	32	26.6	
10230_2019-07-15-154934	26	Mon Jul 15 2019 15:49:34 UTC	Mon Jul 15 2019 16:47:38 UTC	230	1148	1146	1327	21.8	28.75	
10227_2019-07-15-161626	27	Mon Jul 15 2019 16:16:26 UTC	Mon Jul 15 2019 17:14:19 UTC	227	1141	1142	1143	29.06	33.78	
10230_2019-07-15-174619	28	Mon Jul 15 2019 17:46:19 UTC	Mon Jul 15 2019 18:41:50 UTC	230	1148	1146	1327	19.39	24.56	
10227_2019-07-15-180236	29	Mon Jul 15 2019 18:02:36 UTC	Mon Jul 15 2019 19:04:57 UTC	227	1141	1142	1143	31.06	32.12	
10230_2019-07-15-193625	30	Mon Jul 15 2019 19:36:25 UTC	Mon Jul 15 2019 20:30:20 UTC	230	1148	1146	1327	26.3	19.7	
10227_2019-07-15-201345	31	Mon Jul 15 2019 20:13:45 UTC	Mon Jul 15 2019 21:19:12 UTC	227	1141	1142	1143	33.55	24.58	
10230_2019-07-15-213359	32	Mon Jul 15 2019 21:33:59 UTC	Mon Jul 15 2019 22:30:34 UTC	230	1148	1146	1327	24.1	25.2	
10230_2019-07-16-180821	33	Tue Jul 16 2019 18:08:21 UTC	Tue Jul 16 2019 19:15:31 UTC	230	1141	1142	1143	22.93	23.08	
10229_2019-07-16-165427	34	Tue Jul 16 2019 16:54:27 UTC	Tue Jul 16 2019 17:54:52 UTC	229	1170	1171	1173	10.98	22.1	
10230_2019-07-16-203307	35	Tue Jul 16 2019 20:33:07 UTC	Tue Jul 16 2019 21:28:36 UTC	230	1141	1142	1143	18.45	23.28	

Data File	Site Name	Start Time	End Time	MTU box number	Hx id	Hy id	Hz id	Ex line length	Ey line length	Processing note comment
10229_2019-07-16-184312	36	Tue Jul 16 2019 18:43:12 UTC	Tue Jul 16 2019 19:44:40 UTC	229	1170	1171	None	15.8	11.4	
10230_2019-07-16-221551	37	Tue Jul 16 2019 22:15:51 UTC	Tue Jul 16 2019 22:29:47 UTC	230	1141	1142	None	17.14	14.92	
10229_2019-07-16-202850	38	Tue Jul 16 2019 20:28:50 UTC	Tue Jul 16 2019 21:29:13 UTC	229	1170	1171	1173	26.07	15.11	
10227_2019-07-18-171319	39	Thu Jul 18 2019 17:13:19 UTC	Thu Jul 18 2019 18:08:30 UTC	227	1141	1142	1143	16.29	28.63	
10229_2019-07-18-170502	40	Thu Jul 18 2019 17:05:02 UTC	Thu Jul 18 2019 17:58:31 UTC	229	1170	1171	1173	12.2	25	
10227_2019-07-18-185221	41	Thu Jul 18 2019 18:52:21 UTC	Thu Jul 18 2019 19:48:39 UTC	227	1141	1142	1143	24.57	31.26	
10229_2019-07-18-183603	42	Thu Jul 18 2019 18:36:03 UTC	Thu Jul 18 2019 19:33:38 UTC	229	1170	1171	1173	14.3	18.45	
10227_2019-07-18-204045	43	Thu Jul 18 2019 20:40:45 UTC	Thu Jul 18 2019 21:38:58 UTC	227	1141	1142	1143	26.1	23.89	
10229_2019-07-18-203426	44	Thu Jul 18 2019 20:34:26 UTC	Thu Jul 18 2019 21:32:18 UTC	229	1170	1171	None	29.25	15.67	
10229_2019-07-19-155042	45	Fri Jul 19 2019 15:50:42 UTC	Fri Jul 19 2019 16:30:15 UTC	229	1141	1142	1143	26.46	20.6	
10229_2019-07-18-221107	46	Thu Jul 18 2019 22:11:07 UTC	Thu Jul 18 2019 22:49:57 UTC	229	1170	1171	1173	27.6	27.6	
10229_2019-07-19-173035	47	Fri Jul 19 2019 17:30:35 UTC	Fri Jul 19 2019 18:10:17 UTC	229	1141	1142	1143	18.11	10.91	

Data File	Site Name	Start Time	End Time	MTU box number	Hx id	Hy id	Hz id	Ex line length	Ey line length	Processing note comment
10229_2019-07-19-190217	48	Fri Jul 19 2019 19:02:17 UTC	Fri Jul 19 2019 19:40:31 UTC	229	1141	1143	1142	11.23	19.23	
10229_2019-07-19-201917	49	Fri Jul 19 2019 20:19:17 UTC	Fri Jul 19 2019 20:50:26 UTC	229	1141	1142	1143	19.77	25.93	
10229_2019-07-19-213734	50	Fri Jul 19 2019 21:37:34 UTC	Fri Jul 19 2019 22:14:55 UTC	229	1141	1142	1143	21.65	18.72	
10229_2019-07-20-175841	51	Sat Jul 20 2019 17:58:41 UTC	Sat Jul 20 2019 18:41:23 UTC	229	1141	1142	1143	19.1	21.4	
10229_2019-07-20-192633	52	Sat Jul 20 2019 19:26:33 UTC	Sat Jul 20 2019 20:08:36 UTC	229	1141	1142	1143	20.33	13.06	
10229_2019-07-20-205918	53	Sat Jul 20 2019 20:59:18 UTC	Sat Jul 20 2019 21:38:19 UTC	229	1141	1142	1143	24.26	27.67	
10229_2019-07-20-223614	54	Sat Jul 20 2019 22:36:14 UTC	Sat Jul 20 2019 23:18:11 UTC	229	1141	1142	None	13.03	20.61	
10227_2019-07-21-002259	55	Sun Jul 21 2019 00:22:59 UTC	Sun Jul 21 2019 01:01:06 UTC	227	1170	1171	1173	19	25.6	
10229_2019-07-21-164745	56	Sun Jul 21 2019 16:47:45 UTC	Sun Jul 21 2019 17:27:08 UTC	229	1170	1171	1173	21.69	24.01	
10227_2019-07-21-163530	57	Sun Jul 21 2019 16:35:30 UTC	Sun Jul 21 2019 17:16:58 UTC	227	1141	1142	1143	26.56	26.96	
10229_2019-07-21-180858	58	Sun Jul 21 2019 18:08:58 UTC	Sun Jul 21 2019 18:49:12 UTC	229	1170	1171	1173	28.73	31.06	
10227_2019-07-21-184337	59	Sun Jul 21 2019 18:43:37 UTC	Sun Jul 21 2019 19:29:50 UTC	227	1141	1142	1143	26.35	31.85	

Data File	Site Name	Start Time	End Time	MTU box number	Hx id	Hy id	Hz id	Ex line length	Ey line length	Processing note comment
10229_2019-07-21-193505	60	Sun Jul 21 2019 19:35:05 UTC	Sun Jul 21 2019 20:17:28 UTC	229	1170	1171	1173	14.12	25.66	
10227_2019-07-21-201822	61	Sun Jul 21 2019 20:18:22 UTC	Sun Jul 21 2019 21:00:28 UTC	227	1141	1142	1143	21.34	28.48	
10229_2019-07-21-210517	62	Sun Jul 21 2019 21:05:17 UTC	Sun Jul 21 2019 21:43:53 UTC	229	1170	1171	1173	31.73	27.36	
10227_2019-07-21-220724	63	Sun Jul 21 2019 22:07:24 UTC	Sun Jul 21 2019 22:48:20 UTC	227	1141	1142	1143	27.92	18.68	
10229_2019-07-21-222418	64	Sun Jul 21 2019 22:24:18 UTC	Sun Jul 21 2019 23:05:26 UTC	229	1170	1171	1173	29.3	22.64	
10229_2019-07-22-150925	65	Mon Jul 22 2019 15:09:25 UTC	Mon Jul 22 2019 15:51:45 UTC	229	1170	1171	1173	17.93	13.03	
10227_2019-07-22-150100	66	Mon Jul 22 2019 15:01:00 UTC	Mon Jul 22 2019 15:40:38 UTC	227	1141	1142	1143	24.06	13.8	Hx installed backwards
10229_2019-07-22-181916	67	Mon Jul 22 2019 18:19:16 UTC	Mon Jul 22 2019 19:03:57 UTC	229	1170	1171	1173	20.69	18.25	
10227_2019-07-22-162235	68	Mon Jul 22 2019 16:22:35 UTC	Mon Jul 22 2019 17:06:30 UTC	227	1141	1142	1143	20.1	17.21	
10229_2019-07-22-195223	69	Mon Jul 22 2019 19:52:23 UTC	Mon Jul 22 2019 20:33:07 UTC	229	1170	1171	1173	7.99	12.43	
10227_2019-07-22-184338	70	Mon Jul 22 2019 18:43:38 UTC	Mon Jul 22 2019 19:24:53 UTC	227	1141	1142	1143	23.43	23.02	
10229_2019-07-23-155738	71	Tue Jul 23 2019 15:57:38 UTC	Tue Jul 23 2019 16:58:00 UTC	229	1141	1142	1143	17.92	19.08	

Data File	Site Name	Start Time	End Time	MTU box number	Hx id	Hy id	Hz id	Ex line length	Ey line length	Processing note comment
10227_2019-07-22-201716	72	Mon Jul 22 2019 20:17:16 UTC	Mon Jul 22 2019 21:01:04 UTC	227	1141	1142	1143	23.3	14.58	
10229_2019-07-23-175120	73	Tue Jul 23 2019 17:51:20 UTC	Tue Jul 23 2019 18:33:10 UTC	229	1141	1142	1143	25.99	24.46	
10227_2019-07-22-214849	74	Mon Jul 22 2019 21:48:49 UTC	Mon Jul 22 2019 22:17:23 UTC	227	1141	1142	1143	19.23	18.32	
10229_2019-07-23-200523	75	Tue Jul 23 2019 20:05:23 UTC	Tue Jul 23 2019 21:07:32 UTC	229	1141	1142	1143	11.64	24.96	
10227_2019-07-23-154701	76	Tue Jul 23 2019 15:47:01 UTC	Tue Jul 23 2019 16:43:34 UTC	227	1170	1171	1173	20.13	26.26	
10229_2019-07-23-215354	77	Tue Jul 23 2019 21:53:54 UTC	Tue Jul 23 2019 22:47:12 UTC	229	1141	1142	None	15.22	22.81	
10227_2019-07-23-172728	78	Tue Jul 23 2019 17:27:28 UTC	Tue Jul 23 2019 18:27:00 UTC	227	1170	1173	1171	23.87	23.29	
10229_2019-07-24-153403	79	Wed Jul 24 2019 15:34:03 UTC	Wed Jul 24 2019 16:31:47 UTC	229	1141	1142	1143	18.03	16.57	
10227_2019-07-23-193856	80	Tue Jul 23 2019 19:38:56 UTC	Tue Jul 23 2019 20:40:18 UTC	227	1170	1171	1173	17.8	21.53	
10229_2019-07-24-172440	81	Wed Jul 24 2019 17:24:40 UTC	Wed Jul 24 2019 18:13:37 UTC	229	1141	1142	1143	12.98	9.55	
10227_2019-07-23-211852	82	Tue Jul 23 2019 21:18:52 UTC	Tue Jul 23 2019 22:26:42 UTC	227	1170	1171	None	12.68	17.29	
10227_2019-07-24-152346	84	Wed Jul 24 2019 15:23:46 UTC	Wed Jul 24 2019 16:23:03 UTC	227	1170	1171	1173	20.02	16.13	

Data File	Site Name	Start Time	End Time	MTU box number	Hx id	Hy id	Hz id	Ex line length	Ey line length	Processing note comment
10227_2019-07-24-165932	86	Wed Jul 24 2019 16:59:32 UTC	Wed Jul 24 2019 17:56:49 UTC	227	1170	1171	1173	13.15	16.33	

Table 3. Detailed configuration of the Magnetic field measurements at the permanent site.

Data File	Site Name	Start Time	End Time	Latitude (°)	Longitude (°)	Elevation (m)	MTU box number	Hx id	Hy id	Hz id	Ex line length	Ey line length	Hz azimuth	Ex azimuth	Declination (°)
10227_2019-07-16-175805	MT Magonly 1	Tue Jul 16 17:58:05 2019 GMT	Tue Jul 16 23:20:25 2019 GMT	50.567	-123.523	847.215	227	1501	1494	None	Not installed	Not installed	0	0	16.39
10230_2019-07-18-161149	MT Magonly 2	Thu Jul 18 16:11:49 2019 GMT	Thu Jul 18 23:17:11 2019 GMT	50.567	-123.523	842.938	230	1501	1494	None	Not installed	Not installed	0	0	16.39
10230_2019-07-19-150815	MT Magonly 3	Fri Jul 19 15:08:15 2019 GMT	Fri Jul 19 23:07:30 2019 GMT	50.567	-123.523	842.47	230	1501	1494	None	Not installed	Not installed	0	0	16.39
10230_2019-07-20-160909	MT Magonly 4	Sat Jul 20 16:09:09 2019 GMT	Sun Jul 21 00:03:55 2019 GMT	50.567	-123.523	843.352	230	1501	1494	None	Not installed	Not installed	0	0	16.39
10230_2019-07-21-154727	MT Magonly	Sun Jul 21 15:47:27 2019 GMT	Sun Jul 21 23:25:55 2019 GMT	50.567	-123.523	843.19	230	1501	1494	None	Not installed	Not installed	0	0	16.39
10230_2019-07-22-140407	MT Magonly 5	Mon Jul 22 14:04:07 2019 GMT	Mon Jul 22 22:30:32 2019 GMT	50.567	-123.523	843.474	230	1501	1494	None	Not installed	Not installed	0	0	16.38

Data File	Site Name	Start Time	End Time	Latitude (°)	Longitude (°)	Elevation (m)	MTU box number	Hx id	Hy id	Hz id	Ex line length	Ey line length	Hz azimuth	Ex azimuth	Declination (°)
10230_2019-07-23-151812	MT Magonly 6	Tue Jul 23 15:18:12 2019 GMT	Tue Jul 23 23:18:13 2019 GMT	50.567	-123.523	843.666	230	1501	1494	None	Not installed	Not installed	0	0	16.38
10230_2019-07-24-143210	MT Magonly 7	Wed Jul 24 14:32:10 2019 GMT	Wed Jul 24 19:04:15 2019 GMT	50.567	-123.523	843.09	230	1501	1494	None	Not installed	Not installed	0	0	16.38

Table 4. Measurement information for MTU-5A sites.

Site Name	Data File	Start Time	End Time	Latitude	Longitude	Elevation (m)	Hx id	Hy id	Hx id	Ex line length	Ey line length	Hx azimuth	Ex azimuth
5	1495711A	2019-07-11 17:47	2019-07-11 20:34	50:34.660,N	123:31.175,W	1400	1147	1172	1174	19.9	21.7	0	0
12	1495712A	2019-07-12 19:36	2019-07-12 20:41	50:34.395,N	123:31.237,W	1126	1147	1174	1172	12.8	14.04	0	20

Chapter 7 - Mount Meager Passive Seismic Monitoring

Hersh Gilbert, Jan Dettmer, Genevieve Savard, and Hongyi Su

Department of Geoscience, University of Calgary

Introduction

Our investigation of the subsurface structure of the Mount Meager geothermal system included the deployment of an array of 59 earthquake monitoring sensors. The seismic sensors were arrayed in a configuration designed to attain uniform sampling of Mount Meager in the area between Meager Creek and the Lillooet River, just outside of the Upper Lillooet Provincial Park (Fig. 1). Sampling Mount Meager in its entirety allows us to characterize crustal structures associated with the area of high geothermal heat and how those vary across the mountain. Specifically, the observations from this array will be used to identify the distribution of low seismic wavespeeds that can mark the pathways of geothermal fluids as well as magma chambers. The snapshot of local seismicity attained by our brief earthquake monitoring deployment will provide additional constraints on the pattern of faults and fractures within Mount Meager that allow for fluid circulation through this geothermal system. Knowledge of the locations of potential geothermal heat sources and the plumbing system through which that heat is transported to the surface will aid future efforts in geothermal exploration.

The sensors themselves are compact and only require a small 0.5 x 0.5 m² and a small amount of soil to install the instrument and ensure it is well coupled to the ground. We distributed these instruments as evenly as possible across the extent of Mount Meager. However, due to challenges of accessing steep hillsides and areas with dense vegetation, we were not able to place instruments on some portions of the mountain.

During installation, the instruments were almost completely buried to protect them from animals and the environment. The instruments were occasionally visited, and moved, by wildlife (likely bears based on claw marks). Although this disturbed the sensor once it was moved, for all cases we were able to retrieve the instrument and make use of the data from the recording period prior to the sensor being disturbed.

Methods

The local earthquakes we detected were too small to be identified by networks that relied on more sparsely spaced stations for event detection. The events we detected were identified using the Fingerprint And Similarity Thresholding (FAST) approach, which is a machine learning tool designed to recognize similar “earthquake fingerprints”. The FAST method involves creating a spectrogram from the continuous seismic time series and extracting spectral images. Each spectral image is then converted to a binary fingerprint based on selected wavelet coefficients (Bergen et al., 2016). By recognizing patterns of similar wavelet coefficients, the FAST method is able to discern subtle signals in the seismic time series that may have been produced by earthquakes. Through this approach earthquakes can be detected in noisy records with very low signal-to-noise ratio that may otherwise go unnoticed.

Data Collection

Our earthquake monitoring spanned three recording intervals from the beginning of July until the middle of October, 2019. During this time, the instruments recorded several regional and distant earthquakes

from around the world. The array also detected small local earthquakes that were located within our recording array. The subtle signals associated with these local earthquakes was possible because the array of sensors was sufficient sensitivity to low-amplitude signals that we were able to identify the pulse of faint seismic energy propagating across the array. Initial locations for a handful of these earthquakes place them directly below the recording array between Capricorn Mountain and Pylon Peak at a depth of just over 4km (Fig. 1). Part of our ongoing analysis is devoted to calculating the magnitude of these local events. Based on their signal duration and frequency content, it appears their magnitudes would be less than 1.

Results

Of particular interest for a number of the earthquakes detected here, multiple events that occurred on July 13th, 2019 exhibited nearly identical waveforms (Fig. 2). Such similarities in earthquake records is indicative of repeating events where a single asperity repeatedly ruptures. Future efforts will be devoted to identifying whether more of these repeating events occurred by using template matching techniques that are well suited for detecting highly similar waveforms.

Summary and Future Work

The sound of rocks tumbling down the side of the mountain was a constant reminder during the installation and removal of the seismic network that the landscape around Mount Meager is highly unstable. The seismic sensors picked up several of these rock fall events and they appear to have distinct signatures that distinguishes them from the earthquakes we recorded. Instead of exhibiting clear abrupt P- and S-waves arrivals, as observed for the earthquakes (**Fig. 2**), the rock falls show up as a much more emergent signal. Constraining the source of these low-frequency signals is an area of our ongoing efforts.

Our ongoing analysis is focused on examining the correlated signals in the ambient seismic noise recorded by the monitoring array. These correlated signals in the ambient noise possess information about the structure of the subsurface and will allow us to constrain the sources of heat in the geothermal system.

Data

Our passive earthquake monitoring network recorded close to 650 Gb of three-component continuous seismic data during the summer and fall of 2019. In addition to the short-period Inova Hawks, that comprised the majority of the monitoring network, we also collected six weeks of broadband data on the peak of Mount Meager.

Citations

Bergen, K., C. Yoon, G. C. Beroza, 2016, Scalable Similarity Search in Seismology: A New Approach to Large-Scale Earthquake Detection. Proceedings of the 9th International Conference on Similarity Search and Applications (SISAP), Lecture Notes in Computer Science. Tokyo, Japan, 24-26 October 2016.

Acknowledgements

We are grateful to University of Calgary graduate students Jackie Smale and Katie Biegel who assisted in the deployment and removal of the seismic monitoring array.



Figure 1. Google Earth map of Mount Meager earthquake monitoring stations (yellow circles) and detected events that (red dots) occurred on July 13, 2019. The events appear to have occurred at a depth of just over 4 km.

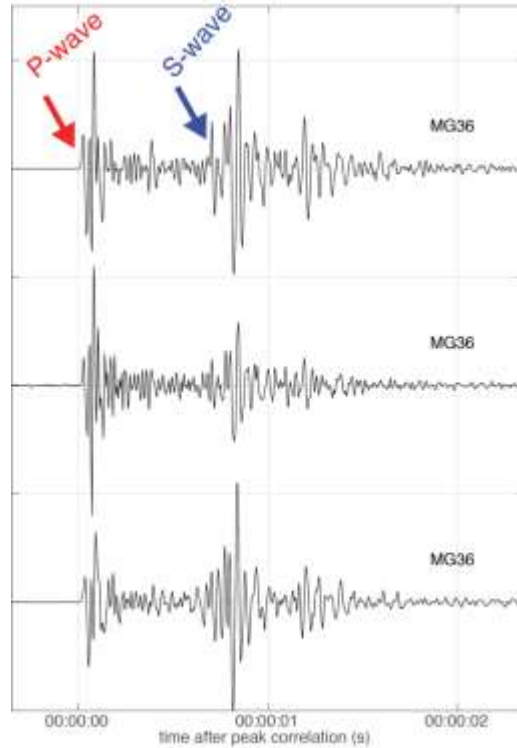


Figure 2. Seismograms illustrating repeating earthquake signals from events that occurred on July 13, 2019. Example waveforms from a station near Job Glacier on the north side of Mount Meager. These well recorded events were located towards the central portion of the Mount Meager array (locations noted on Figure 1). The short time between the arrivals of the P and S waves exhibited on these waveforms (less than 1 s) support our findings that these are indeed local events and are located within the recording array.